From silicen to Si films and clusters : silicon growth on Ag and layered materials studied by STM, GIXD and DFT

Alberto Curcella

To cite this version:

Alberto Curcella. From silicen to Si films and clusters : silicon growth on Ag and layered materials studied by STM, GIXD and DFT. Materials Science [cond-mat.mtrl-sci]. Sorbonne Université, 2018. English. NNT : 2018SORUS410 . tel-02612244v2

HAL Id: tel-02612244
https://theses.hal.science/tel-02612244v2

Submitted on 19 May 2020

Sorbonne Université

École doctorale
Physique et chimie des matériaux
ED397

Laboratoire - Equipe de recherche
Institut des nanosciences de Paris
Physico-chimie et dynamique des surfaces

From silicene to Si films and clusters: silicon growth on Ag and layered materials studied by STM, GIXD and DFT

Par Mr. Alberto Curcella

Thèse de doctorat de physique

Dirigée par Dr. Geoffroy Prévot

Co-dirigée par Dr. Michele Lazzeri

Présentée et soutenue publiquement le 5 Octobre 2018

Devant un jury composé de :

Dr. Isabelle Berbezier	Directrice de recherche	Rapporteuse
Dr. Marie-Christine Hanf	Maître de conference	Rapporteuse
Pr. Abhay Shukla	Professeur	Président du jury
Pr. Laurence Masson	Professeure	Examinatrice
Pr. Vincent Repain	Professeur	Examinateur
Dr. Geoffroy Prévot	Chargé de recherche	Directeur de Thése
Dr. Michele Lazzeri	Directeur de recherche	Co-Directeur de Thése

And all of a sudden I’m relatively sane,
With everything to lose and nothing to gain.
Or something like that...

Acknowledgements

I would like to spend few words to thank the people who helped me and supported me during this three-years journey. First of all, Geoffroy Prévot and Michele Lazzeri, who have supervised my PhD project, for their scientific teachings, but also for having motivated me all along the PhD. I am also particularly grateful to the other people who have directly contributed to the advancement of this research project, Romain Bernard and Yves Borensztein. A special thank to all the people in the research unit "PHYSUF" for having contributed to a nice and serene working environment. I would like to personally acknowledge Hervé Cruguel and Sébastien Royer for their help and their extra-scientific advices. I cannot forget to mention three colleagues with whom I have shared this journey since its beginning: William Watkins, Léo Bossard-Giannesini and Danilo Longo. Clément Livache, I hope we will have the chance to climb together several more times. I would like to thank also Bernard Croset, for the interesting and fruitful discussions concerning the French language, and Max Marangolo, fellow citizen and friend.

Many, countless thanks to my friends, all the naturalized citizens of Paris and my lifetime friends from Ravenna. I convey my respects to the "Peacock Tranguel" association and to "Maison del Can".

I express my gratitude to Silvia, for her support and her affection.

I would like to conclude thanking my family and in particular my mother and my father, Chiara and Giuseppe, for all the support someone could ask for, and my brother, Carlo, the person I will always look up to.

Contents

SORBONNE UNIVERSITÉ

Abstract

ED397

Institut des nanosciences de Paris

Doctor of Physics

From silicene to Si films and clusters: silicon growth on Ag and layered materials studied by STM, GIXD and DFT

by Alberto CURCELLA

The present Thesis is organized as follows.

In the Introduction I give the context in which this work takes shape. I describe the advent of graphene, the bidimensional (2D) allotrope of carbon, its properties and how this material has triggered the research of new bidimensional materials. Among them, *silicene*, which is the silicon counterpart of graphene, is the material that I have studied during my PhD.

Chapter 1 constitutes a non-exhaustive summary about the state-of-the-art of silicene research. I mainly focus on the basic knowledge necessary to understand what is silicene, which are its ideal theoretical properties, on which substrates it has been synthesized up-to-date and which are the differences between expected properties and experimental evidences.

In Chapter 2, I introduce the two experimental techniques that I have employed to obtain the results of this Thesis, i.e. *scanning tunneling microscopy* (STM) and *grazing incident X-ray diffraction* (GIXD).

In Chapter 3, I explain the basic principles of *density functional theory* (DFT).

Chapter 4 reports the first part of the original results of this Thesis. In this chapter, I present the outcomes of a combined experimental and theoretical study, based on GIXD measurements and DFT simulations, aimed to determine the exact atomic arrangement of the *silicene monolayer structures on Ag(111)*.

Chapter 5 concerns the *atomic structure of Si thin films on Ag(111)*. I will show, by means of GIXD measurements, that the Si film has a diamond bulklike structure with stacking faults.

Chapter 6 is a very dense chapter. Firstly, I determine the atomic structure of the reconstruction observed on top of the previously described diamond bulklike Si film by GIXD measurements. Then, by combined STM and DFT studies I give an original picture for *Si growth on Ag(111) above 1 ML of Si coverage*.

Chapter 7 reports STM studies regarding *Si evaporation on several layered materials*: HOPG, MoS_2, $TiTe_2$ and $ZrSe_2$. I will show that on each of these substrates and both for room temperature and high temperature growth, Si evaporation results in the formation 3D Si nanoclusters.

In the last Chapter I will summarize all the results previously reported and I will give the perspectives on future works and projects.

Résumé

Dans cet ouvrage, je résume les études menées au cours de ma thèse, concernant la synthèse des couches de silicène et des couches minces de Si sur Ag(111) et de Si sur des matériaux lamellaires. Je présente des résultats originaux qui peuvent dévoiler des phénomènes physiques intéressants associés au système étudié.

Ici, je vais rendre compte des principaux résultats, en essayant d'illustrer le fil conducteur de ce travail.

Dans l'introduction, je définis le contexte de la recherche sur les matériaux bidimensionnels (2D). Je montre que le graphene, l'allotrope 2D du carbone, a stimulé l'intérêt vers la synthèse d'autres couches monoatomique. Des études théoriques ont prédit qu'un arrangement 2D hexagonale métastable d'atomes de Si pourrait exister. Ce nouveau matériau, appelé par la suite *silicène*, peut être considéré comme l'équivalent en silicium du graphène (Fig. 1).

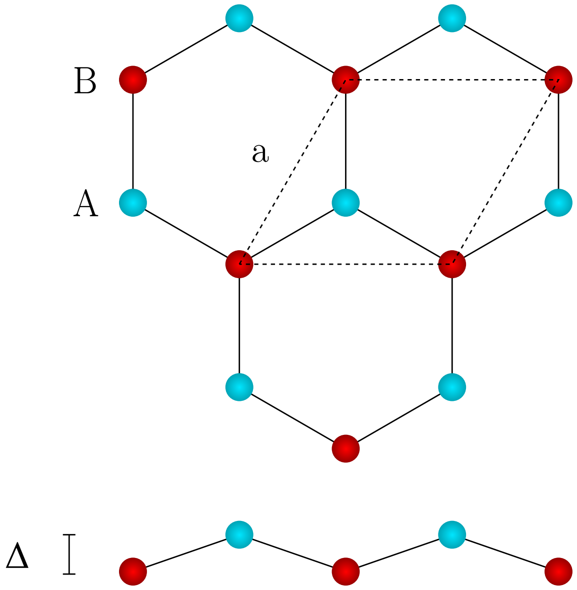

FIGURE 1: Vue de dessus (a) et latérale (b) de la structure du "free-standing" silicène. La structure d'équilibre présente une corrugation à niveau atomique (Δ), différemment du graphene qui est complètement plat.

Les propriétés très intéressantes prédites pour la forme "free-standing" de ce nouveau matériau ont donné l'élan initial à la recherche de sa réalisation expérimentale. Contrairement au graphène, ce matériau ne peut pas être exfolié à partir de sa forme allotropique en couches, mais il doit être déposé sur un substrat.

Ag(111) a été étudié au cours des dernières années par des nombreux groupes de recherche. Plusieurs études ont rapporté la synthèse des arrangements 2D de Si sur ce matériau. Cependant, les propriétés rapportées pour la couche de silicène/Ag(111) sont différentes de celles prédites pour le free-standing silicène, en raison de l'interaction entre le substrat et la couche.

Dans le chapitre 4, je étude la structure des monocouches de silicène sur Ag(111). Je mets en évidence la déformation induite dans le substrat par la présence du silicène, qui peut être considéré comme une signature de l'interaction entre les deux matériaux. Les couches de silicène sur Ag(111) sont déposées à $T_{croissance}$=500-570 K et sont toujours composées par plusieurs reconstructions de surface. Des expérimentes de diffraction rasante des rayons X (GIXD) et des simulations de théorie de la fonctionnelle de la densité(DFT) ont permis de déterminé l'arrangement atomique exacte de la structure de surface (4 × 4) du silicène (Fig. 2).

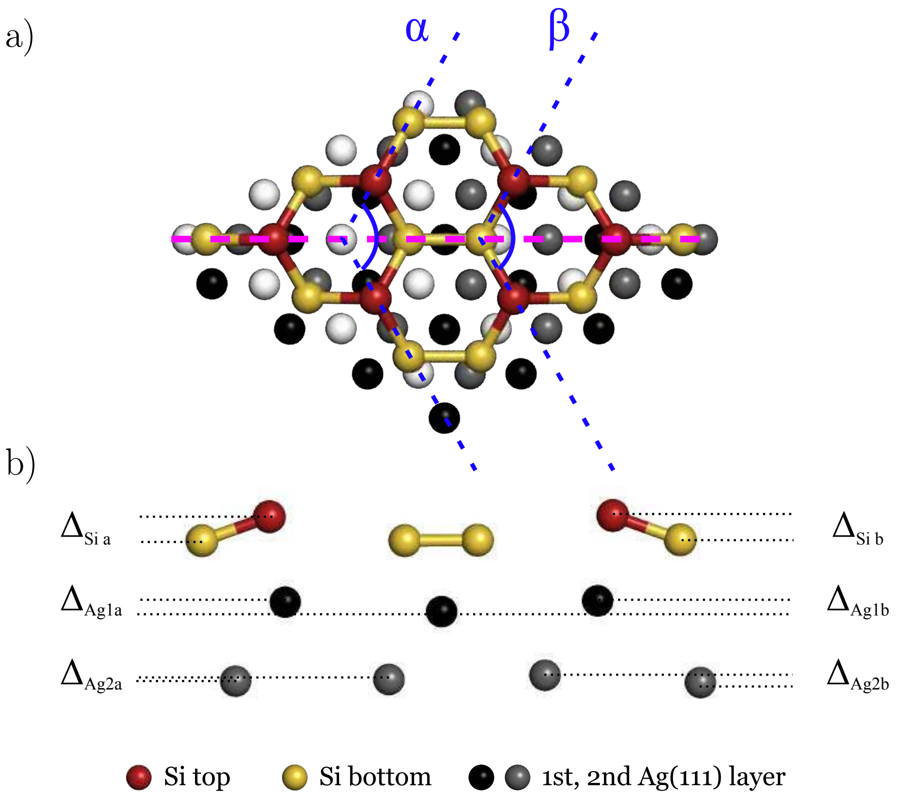

FIGURE 2: Vue de dessus (a) et latérale (b) de la reconstruction (4 × 4) sur Ag(111). α et β sont les angles indiqués par les lignes bleus. La représentation latérale correspondes à la ligne pointillée rose en (a).

		d (Å)	$\Delta_{Si\ a/b}$ (Å)	$\Delta_{Ag1a/b}$ (Å)	$\Delta_{Ag2a/b}$ (Å)	α	β
Free standing silicène	DFT-LDA [1]	2.25	0.44				
(4 × 4) Si/Ag(111)	DFT-GGA [2]	2.35	0.8	0.4			
	DFT-GGA [3]	2.32	0.75			110°	118°
	LEED [4]	2.29-2.31	0.77/0.74	0.29/0.31	0.10/0.21		
	RHEPD [5]		0.83			112°	119°
	DFT-GGA/GIXD	2.30-2.33	0.76	0.25/0.27	0.05/0.24	108.6°	111.1°
	DFT-GGA+vdW	2.30-2.34	0.78/0.79	0.23/0.25	0.04/0.17	108.0°	110.5°
	DFT-LDA	2.33-2.37	0.90/0.91	0.29/0.32	0.07/0.27	105.6°	109.3°

TABLE 1: Comparaison entre les caractéristiques structurales obtenues pour la structure (4 × 4) du silicène/Ag(111), simulée dans trois approximations différentes. On reporte aussi les résultats présentes en littérature.

Trois approximations différentes sont utilisées dans les calculs DFT: local density approximation (LDA), generalized gradient approximation (GGA), aussi avec corrections de type van der Waals (GGA+vdW). Les caractéristiques structurales obtenues pour les structures d'équilibre sont montrées en Tab 1.

Les facteurs de structure théoriques obtenus à partir des positions atomique d'équilibre sont très proches des ceux obtenus expérimentalement par GIXD. On montre que notre simulations DFT-GGA donnent le meilleure accord avec les mesures de diffraction. Les mesures GIXD sont également utilisées pour déterminer la relaxation du substrat Ag(111). La déformation élastique est atténuée dans les premières couches de la surface de l'Ag.

On a utilisé le même approche théorique et expérimentale pour étudier les structures $(2\sqrt{3} \times 2\sqrt{3})R30^\circ$ et le $(\sqrt{13} \times \sqrt{13})R13.9^\circ$ du silicène. La première, observée en coexistence avec la structure (4×4) pour $T_{croissance} = 570$ K, est n'a pas exactement l'orientation attendue de 30° par rapport au substrat d'Ag. Les facteurs de structure théoriques de la structure $(2\sqrt{3} \times 2\sqrt{3})R30^\circ$, qu'on a obtenus avec les simulations de DFT, sont en bon accord avec les expériences. La structure d'équilibre présente une corrugation de 1.10 Å et des distances inter-atomiques de l'ordre de 2.25-2.33 Å. En ce qui concerne la reconstruction $(\sqrt{13} \times \sqrt{13})R13.9^\circ$, observée à $T_{\ croissance} = 500$ K, j'ai simulé toutes ses configurations inéquivalentes pour les structures dites *type I* et *type II*. Les facteurs de structure expérimentaux peuvent être reproduits prenant en considération un mélange des configurations $type\ II - t_1h_2t_3$ et $type\ II - t_1t_2h_3$ (pour la notation j'envoie le lecteur à sec. 4.4). Je n'ai trouvé aucune preuve de la présence de la structure *type I* dans la couche de silicène.

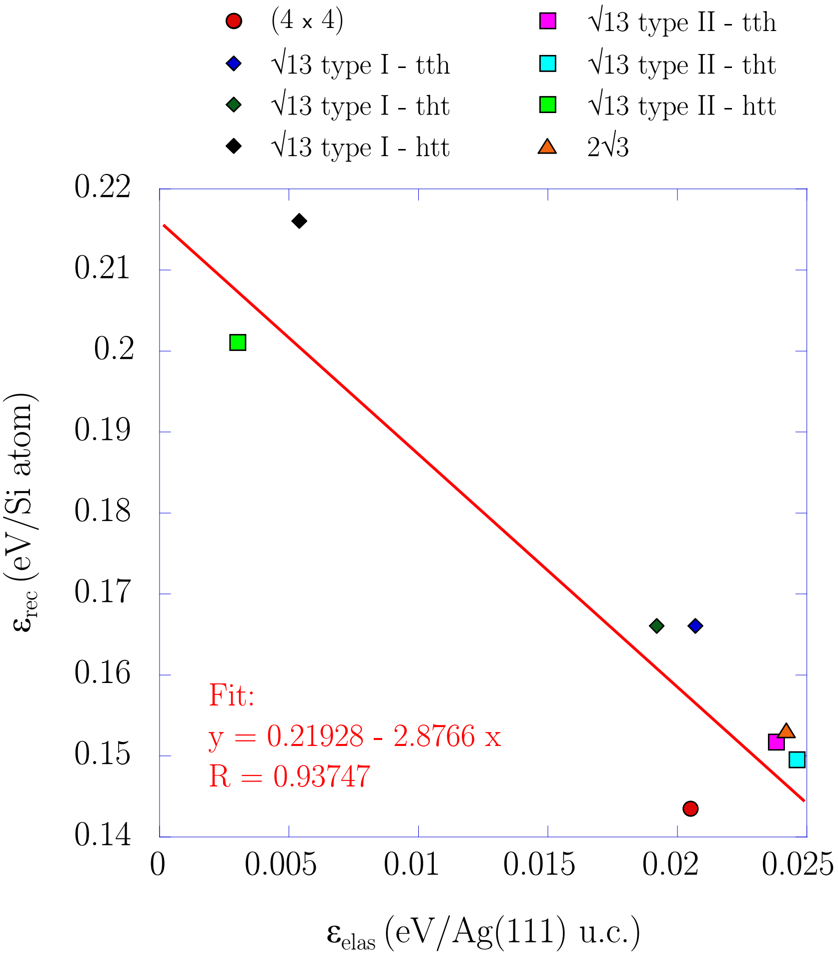

FIGURE 3: Graphique de l'énergie associée à la déformation élastique du substrat (ϵ_{el}) en fonctionne de l'énergie associée aux atomes de Si (ϵ_{rec}) dans les différentes structures de silicène.

Je conclu le Chapitre 4 avec des considérations énergétiques sur la stabilité des différentes structure observées dans la monocouche de silicène et sur la déformation qu'elles induisent dans le substrat de Ag(111). Je montre que les structures induisant la déformation élastique (ϵ_{el}) plus importante dans le substrat d'Ag sont également celles qui ont la plus faible énergie associée aux atomes de la couche de silicène (ϵ_{rec}), comme on montre en Fig. 3.

Comme déjàmentionné, la forte interaction entre la couche de silicène et le substrat Ag(111) cause la perte des proprietées intéressantes prévues pour le free-standing silicène. Les chercheurs ont alors commencéàse intéresser àla croissance des films épais de Si sur Ag(111), pour explorer la possibilitéque cette procédure pourrait conduire àla formation de la allotrope lamellaires du Si, appelé*silicite* (en analogie avec la graphite) ou *silicène multicouche*. La synthèse de cette nouvelle forme de silicium a étéreportépar De Padova *et al.* [6, 7]. Cependant, d'autres études ont remis en cause cette interprétation [8–10]. Afin de déterminer la nature des films de Si sur Ag (111), j'ai effectué des mesures GIXD sur un film dans la même plage de température dans laquelle la synthèse de silicite a été revendiquée.

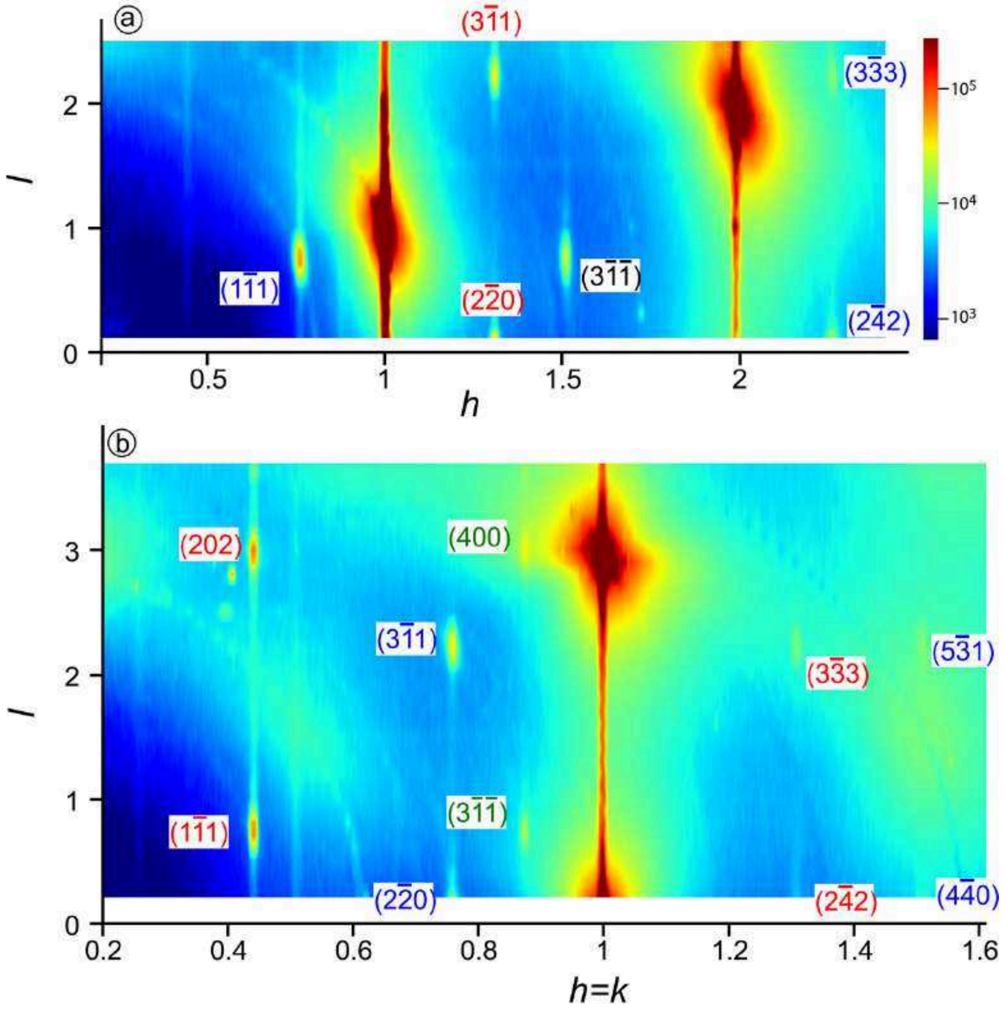

FIGURE 4: Cartes de l'intensité diffractée par 8 ML de Si évaporés sur Ag(111) à T $_{croissance}$=520 K. a) Carte correspondante àk=0. b) Carte correspondante àh = k. L'échelle des couleurs est la même pour les deux cartes. Les taches indexées appartiennent au film de Si et correspondent à une structure diamante avec quatre orientations différentes (étiquettes bleues, rouges, vertes). Les indexes h, k, l sont référées au substrat d'Ag.

Fig. 4 montre deux cartes de diffraction obtenues en performant des mesures de GIXD sur 8 ML de Si déposés sur Ag(111) àT$_{croissance}$=520 K. Elles correspondent à l'intensité mesurée pour des plans de l'espace réciproque perpendiculaires àla surface de l'échantillon. Les tiges de troncature du cristal d'Ag apparaissent aux valeurs entières de h et k. également, les taches à(101), (202), (110), (113) sont les spots de Bragg du cristal d'Ag. Des autres taches sont visibles, qui n'étaient pas présentes avant l'évaporation de Si. Elles sont associées au film épais de Si. Toutes ces taches peuvent être indexées en accord avec une structure diamant de Si massif. Cette évidence rejets toute interprétation de la croissance de silicite ou de silicène multicouche. Cependant, certaines taches de diffraction observées apparaissent décalées par rapport à leurs positions théoriques idéales. En utilisant le modèle Paterson, je attribue ces changements à la présence de fautes d'empilement. Dans le Chapitre 6 j'analyse le mécanisme de croissance du Si sur Ag(111) au delà de la monocouche de silicène. La croissance de la deuxième couche et des celles successives est caractérisée par l'apparition d'une structure $(\sqrt{3} \times \sqrt{3})R30^\circ$ à la surface de l'échantillon.

Des mesures de GIXD conduites sur un film de Si (épaisseur 2 ML, $T_{croissance}$=510 K) déposé sur Ag(111) ont montré que cette phase est compatible avec la terminaison $(\sqrt{3} \times \sqrt{3})R30^\circ$ de l'Ag sur le Si(111), décrite par le modèle "honeycomb chain triangle" (HCT) (Fig. 5).

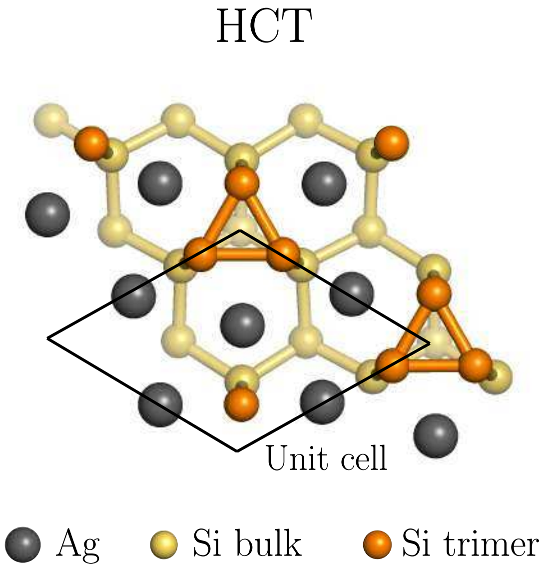

FIGURE 5: Configuration atomique du modèle "honeycomb chain triangle" (HCT).

En outre, notre mesures de STM montrent la présence de deux phases différentes de la reconstruction $(\sqrt{3} \times \sqrt{3})R30^\circ$ dans les premières étapes de la croissance de la deuxième couche de Si. Les deux phases sont étiquetées par α et β. Les mesures STM en temps réel montrent que la phase α est progressivement remplacée par la β lors du dépôt ultérieur (Fig. 6).

Après l'évaporation de 2 ML de Si, seule la phase β est observée àla surface de l'échantillon. Par conséquent, il est raisonnable d'affirmer que le $(\sqrt{3} \times \sqrt{3})R30^\circ$ précédemment déterminée par mesures de GIXD et coïncidant essentiellement avec la terminaison d'Ag du Si(111), est associé à cette phase β. Une interprétation pour la phase α manque toujours à ce stade.

Ensuite je présente les résultats des simulations DFT de plusieurs structure de surface avec une périodicité $(\sqrt{3} \times \sqrt{3})R30^\circ$. Au contraire du modèle HCT, ces structures n'ont pas des atomes d'Ag á la surface, mais sont composées exclusivement par du Si. L'objectif de ces simulations est de trouver une description pour la structure α. Les images STM simulées associées aux modèles théoriques SONT comparées aux images expérimentales. Un seul modèle peut reproduire les images expérimentales: Il se compose d'une seule couche de Si avec en plus une reconstruction $(\sqrt{3} \times \sqrt{3})R30^\circ$, ou les atomes de Si sont adsorbé en configuration "dumbbell". J'étiquette cette structure "ML+Si". Comme la phase β est décrite par le modèle HCT,

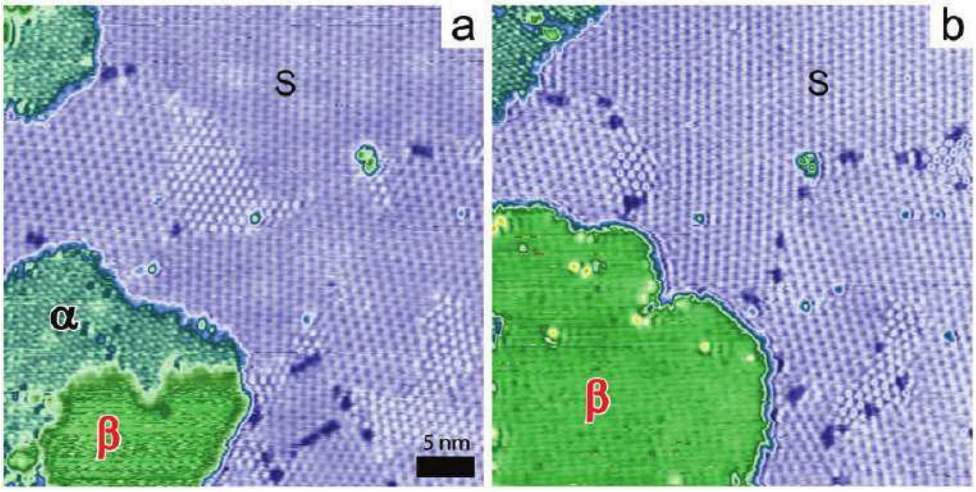

FIGURE 6: Images STM en temps réel (42 × 42 nm^2) montrant les premières étapes de la croissance de la deuxième couche de Si sur Ag(111). La partie bleue représente la monocuche de silicène avec différentes reconstructions de surface. Les îlots verts correspondent à la deuxième couche, caractérisée par les structure $(\sqrt{3} \times \sqrt{3})R30^\circ - \alpha$ and $(\sqrt{3} \times \sqrt{3})R30^\circ - \beta$.

la terminaison Ag-$(\sqrt{3} \times \sqrt{3})R30^\circ$ est simulée sur une seule couche de Si et vient appelée "ML+Si/Ag", de manière similaire au modèle "ML+Si". Comme prévu, son image STM simulée est en bon accord avec l'image expérimentale de la phase β.

àce stade, je introduis l'*énergie de surface grand canonique*. C'est une fonction de μ_{Si}, qui à l'équilibre thermodynamique coïncide avec le potentiel chimique du Si. Ainsi, en introduisant cette quantité, je peux comparer la stabilité des modèles "ML+Si" et "ML+Si/Ag" avec celle des reconstructions de la monocouches de silicène, i.e. "ML (4 × 4)" et ML $(\sqrt{13} \times \sqrt{13})$. Les résultat de ces considérations énergétique montrent que ni la structure "ML+Si" ni la "ML+Si/Ag" sont plus stables de la monocouche de silicène dans une large intervalle de μ_{Si}. Une nouvelle interprétation est nécessaire.

Je présente à ce point des autre évidences expérimentales basées sur des mesure STM en temps réel. Je montre que à partir de la croissance de la deuxième couche de Si, dans certaines zones de la surface de l'échantillon, proches des bords des marches, on observe que la monocouche de silicène vient soulevée de exactement 0.235 nm qui correspond à la hauteur d'un plan de Ag(111), en préservant dans ce processus sa structure de surface. Il y a une seule explication possible: des atomes d'Ag sont ségrégés à la surface de l'échantillon.

Afin de proposer une nouvelle interprétation alternative, je présente en suite d'autres mesures de STM en temps réel. Je montre qu'à partir de la croissance de la deuxième couche de Si, les zones de l'échantillon proches des bords des marches recouvertes par la monocouche de silicium sont soulevées exactement de la hauteur d'une couche d'Ag(111), conservant dans cette transition la structure de la surface (Fig. 7). La question naturelle à ce stade est: d'où viennent ces atomes d'Ag?

Je propose que les phases α et β sont en vrai des bicouches de Si terminées par les reconstruction $(\sqrt{3} \times \sqrt{3})R30^\circ$ reportées précédemment, c'est à dire les structure TDS (sans atomes d'Ag à la surface) et HCT (avec atomes d'Ag à la surface), respectivement. Ces deux nouveaux modèles sont étiquetés "BL+Si" and "BL+Si/Ag". Dans ce cas, la comparaison entre les énergies de surface grand canoniques montre que, dans une large gamme de μ_{Si}, les structures BL sont plus stables que les reconstructions monocouches de silicène ML (4 × 4) and ML $(\sqrt{13} \times \sqrt{13})$. Cela corrobore le processus proposé de la transition directe de la monocouche de silicène à la bicouche de Si (BL+Si and BL+Si/Ag). De plus, BL+Si/Ag est légèrement

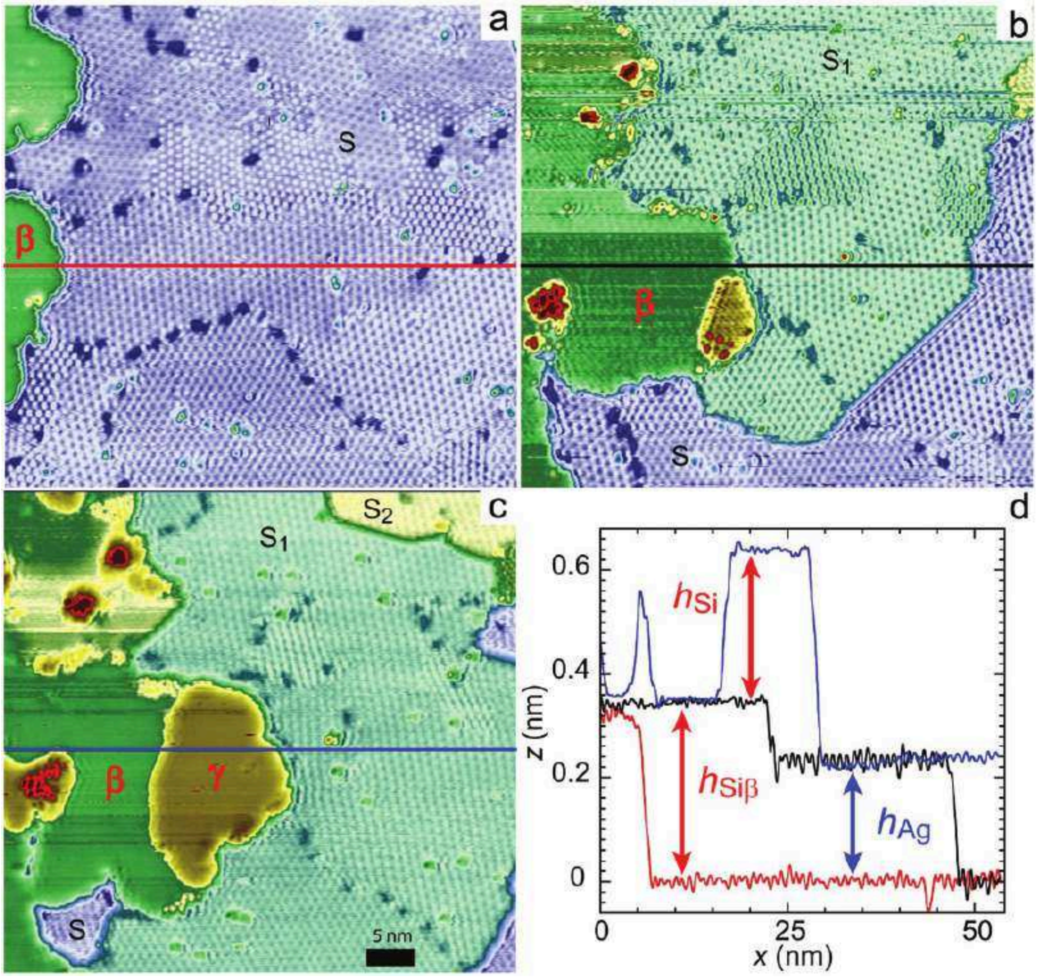

FIGURE 7: a-c) Une vue détaillée de l'évolution de la couche de silicène lors de l'évaporation du Si à 500 K. La région est exactement la même pour les images a-c. La taille de l'image est 53 × 52 nm^2. Évolution du profil de hauteur STM: les profils rouge, noir et bleu correspondent aux lignes horizontales dessinées respectivement dans les panneaux a, b et c.

énergétiquement favorisé par rapport à BL+Si, ce qui pourrait expliquer pourquoi, expérimentalement, la phase β (BL+Si/Ag) croît aux frais de la phase α (BL+Si). En plus de cela, les structures BL+Si et BL+Si/Ag sont toujours favorisées énergiquement par rapport à une simple bicouche de Si(111) avec un empilement AB. Je peux tirer quelques conclusions à ce stade. Alors que les bicouches de Si doivent être stabilisées par des reconstructions de surface similaires à celles observées pour la surface Si (111) (voir modèle HCT et modèle TDS), la monocouche de silène est une structure très stable qui ne nécessite pas de reconstruction énergie. Cela montre que le silicène se comporte différemment du Si massif, alors que les bicouches de Si peuvent être considérées comme deux couches de Si(111).

Dans la dernière partie du Chapitre 6, je présente des considérations sur l'énergétique de l'adsorption des atomes de Si dessus et dessous d'une couche de silicène (4 × 4) sur Ag(111). Je montre que, dans certains cas, il est même plus avantageux, pour un atome de Si, de s'insérer sous la couche de silicène et d'éjecter un atome d'Ag du substrat, en prenant sa place. Ceci confirme les preuves selon lesquelles les bicouches reconstruites BL+Si et BL+Si/Ag (associé à la phase α et β) se développent en creusant dans le substrat d'Ag.

Donnons à nouveau le processus général de la croissance de Si sur Ag(111) après le complètement achèvement de la monocouche de silicène. Les atomes de Si arrivants à la surface ne se déposent pas simplement sur la couche de silicène, mais ils préfèrent s'insérer au-dessous d'elle dans le substrat d'Ag. Ainsi, la monocouche de silicène se transforme directement en bicouche de Si, insérée dans le substrat d'Ag, montrant, dans un premier temps, une reconstruction $(\sqrt{3} \times \sqrt{3})R30^\circ$ sans atomes d'Ag à la surface (BL+Si, phase α). Les atomes d'Ag éjectés diffusent à la surface et peuvent soit se réinsérer au-dessous la couche de silicène, soit aller au-dessus de la surface et donner lieu à la phase $(\sqrt{3} \times \sqrt{3})R30^\circ - \beta$ (Fig. 8). Cette structure est interprétée comme une bicouche de Si insérée dans le substrat Ag et terminé par une reconstruction avec des atomes ségrégées à la surface (BL+Si/Ag). La phase β croît aux frais du α, étant énergétiquement plus favorable. Pour une couverture de Si égale à 2 ML, seule la phase β est observée à la surface.

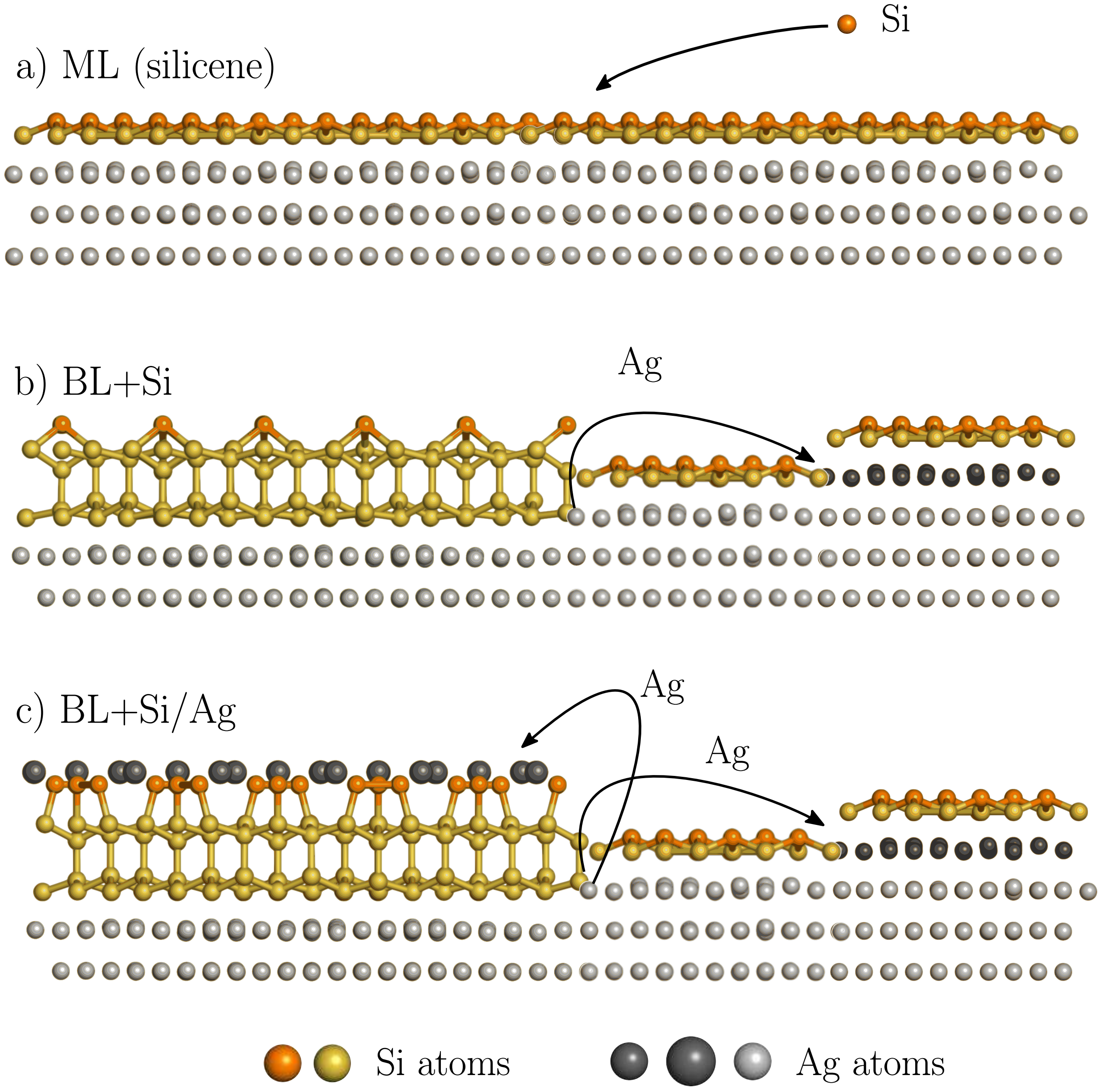

FIGURE 8: Monocouche de silicène complète (ML) recouvrante le substrat d'Ag(111); b) formation de la bicouche sans Ag terminée par la reconstruction TDS (BL+Si); c) la bicouche initiale est remplacée par la reconstruction riche en Ag HCT (BL+Si/Ag). Notez que dans (b) et (c) la bicouche est insérée dans le substrat, conduisant à l'expulsion des atomes d'Ag, qui soit se réinsèrent au-dessous de la couche de silicène (b) soit sont adsorbées au-dessus de la bicouche en croissance (c).

Dans le Chapitre 7 je présente une étude STM concernant le dépôt de Si sur plusieurs matériaux lamellaires: HOPG, MoS_2, $TiTe_2$ and $ZrSe_2$. Je montre que l'évaporation à température ambiante sur HOPG conduit à la formation de nanoclusters de Si entourés d'une reconstruction $(\sqrt{3} \times \sqrt{3})R30°$. Cela a été interprété dans la littérature par la présence d'une couche de silicène. Je montre que cette reconstruction de surface peut être interprétée en termes de ondes de densité de charge.

Certaines observations inattendues sont reportées pour le substrat de $TiTe_2$. Après un recuit à 360 °C du substrat nu, des structures hexagonales sont apparues, différentes de la surface vierge de $TiTe_2$. Ces structures sont probablement dues à la contamination par la laque d'Ag. L'évaporation de Si sur ce substrat "altéré" a entraîné la formation de structures 3D Si sur les parties de l'échantillon correspondant au substrat propre. Au contraire, des mesures de STM en temps réel au cours de l'évaporation montrent la croissance et l'évolution des îlots plats induits par l'évaporation du Si sur les structures hexagonales. Ces îlots ne sont pas stable: en fait ils demouillent après un recuit à 573 K.

Chapter 1

State of the art and presentation of the system under study

In this chapter I present a selection of the works reported in the literature, which helps building the context for the research on silicene, i.e. the bidimensional hexagonal allotrope of silicon. After a general discussion about the advent of 2D materials and the first theoretical predictions of metastable Si monolayers, I focus on those studies concerning low-dimensional Si allotrope synthesis. In particular, I describe silicon deposition on Ag(110), Ag(100) and Ag(111), which results in the formation of Si nanoribbons and siicene sheets, respectively. During my PhD I mainly studied the silicene and Si thin film on Ag(111). The original results that I have obtained are discussed in Chapters 4, 5, 6. To conclude this general overview, I present some works concerning silicene growth on other substrates. I would like to anticipate that the specific bibliographic information, necessary for the understanding of the results of this Thesis, is also discussed in the introduction of Chapters 4, 5, 6 and 7.

1.1 Free-standing silicene

Takeda and Shiraishi [11] were the first to investigate theoretically the possibility of 2D arrangement of Si atoms, by means of density functional theory (DFT) calculations. In analogy to the hexagonal arrangement of C atoms in graphite, they supposed that the Si monolayer may possess the same hexagonal structure, as illustrated in Fig. 1.1.

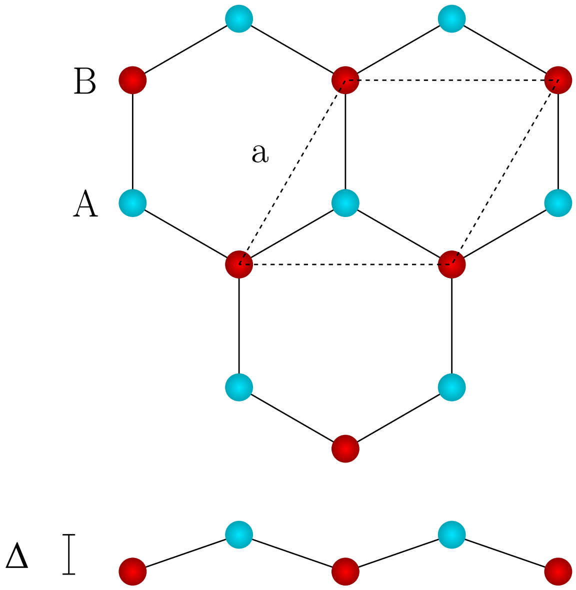

FIGURE 1.1: Top and lateral view of the low-buckled hexagonal structure predicted for free-standing silicene. "A" and "B" labels the two inequivalent sites in the silicene unit-cell, Δ is the buckling and "a" is the parameter of the unit cell (dotted rhombus).

As Si is not known to form flat sp_2 bonds, the calculations allowed the two inequivalent atoms inside the unit cell, "A" and "B", also to relax out-of-plane. Takeda and Shiraishi found that the most stable structure corresponds to a low-buckled hexagonal lattice of Si atoms and that the planar configuration is actually energetically unfavored. They reported that the equilibrium structure has a lattice parameter a=3.855 Å and a buckling Δ=0.53 Å. This atomic corrugation is substantially different from the one found in a plane of Si(111), in which the vertical displacement of Si atoms is equal to 0.78 Å. This evidence was interpreted in terms of mixed sp_2-sp_3 character of the Si single layers.

Despite the interesting results presented in Takeda's and Shiraishi's pioneer work, silicene, term which was coined by was coined by Guzmán-Verri and Lew Yan Voon in 2007 [12], was ignored for more than a decade. These interesting results were reproduced for the first time in 2009 by Cahangirov *et al.* [1]. In their work they found a buckling value close to the one already reported, i.e. Δ=0.44 Å. In this work the stability of the hexagonal buckled structure was thoroughly investigated by calculating the vibrational modes for both planar and buckled structure. In Fig. 1.2 shows whereas the buckled silicene structure has all the optical and acoustical branches with positive frequencies, the ZO (out-of-plane optical mode) mode of the planar silicene structure shows imaginary frequencies near the Γ point.

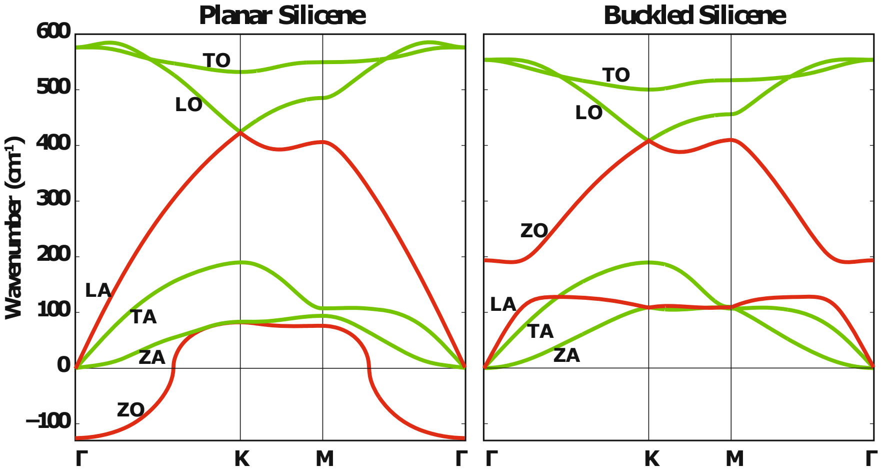

FIGURE 1.2: Comparison between the phonons calculated for buckled and planar silicene. The out-of-plane, transverse and longitudinal acoustic and optical modes are denoted by ZA, TA, LA, ZO, TO and LO, respectively. LA an ZO modes are those mostly affected by the presence of the buckling. Figure reproduced from ref. [13].

The ZO mode corresponds to the "A" and "B" atoms moving out-of plane in opposite directions, and the presence of the imaginary frequency for such a mode means that there is no restoring force acting against this kind of displacement. Thus, the negative frequency for the ZO mode is the signature of the instability of the planar structure; on the contrary the absence of negative frequencies for the low-buckled form shows the metastability of such a structure. From now on whenever I name the free-standing (FS) form of silicene I always refer to the buckled structure, unless otherwise stated. Nevertheless, this slightly-corrugated 2D allotropic form of silicon is less stable than its bulk form as it can be inferred by their cohesive energies 5.16 (FS silicene) and 5.16 (bulk Si) eV per atom [1].

In the same work, Cahangirov *et al.* discussed also the electronic properties of FS silicene. In Fig. 1.3 I report the electronic band structure and the density of state (DOS) of FS silicene calculated by Cahangirov. Similarly to graphene, the π and π^* bands crossing at the K-K$'$ point of the Brillouin zone at the Fermi level ($E = 0$) shows a semimetallic character. Near the crossing, the two bands have a linear dispersion, which means that charge carriers behave like massless Dirac fermions. By fitting the π and π^* bands in this region with:

$$v_f \simeq \frac{E(q)}{\hbar|q|} \tag{1–1}$$

it is possible to estimate the Fermi velocity v_f; in expression equation q is the electronic wavevector, E is the energy and $\hbar$ is the reduced Planck's constant. By doing so Cahangirov *et al.* obtained $v_f \sim 10^6$ m/s, comparable to the Fermi velocity measured in graphene [14].

Other interesting and exotic properties were predicted for silicene. For example, as Si has larger spin-orbit coupling than C, 0.036 eV and 0.008 eV respectively [15], it was hypothesized that silicene could display quantum spin Hall effect [16–18].

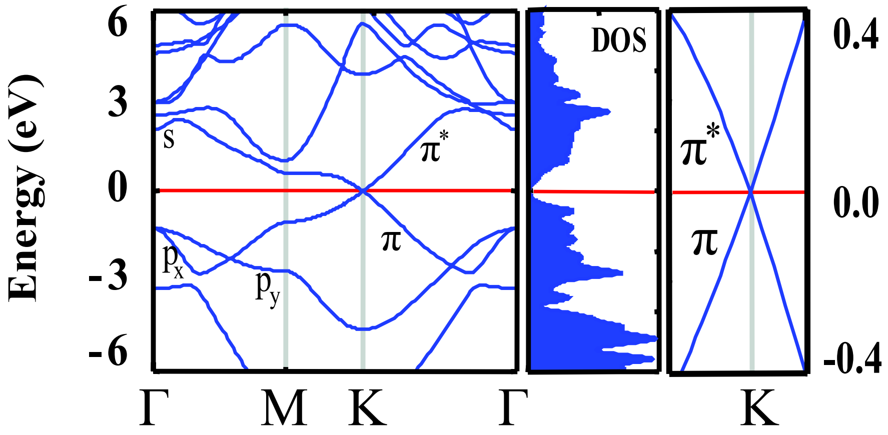

FIGURE 1.3: Energy band structure and density of states (DOS) of FS silicene. A magnification of the band structure around the K point is shown as well, in which the linear crossing of π and π^* bands can be seen. Adapted from ref. [1].

All these interesting theoretical predictions on silicene started the quest for its experimental realization. Not long after the publication of the predictions about the interesting exotic properties of silicene, the successful synthesis of 1D and 2D Si lattices was claimed on several substrates, for example Ag(110) [19, 20], Ag(111) [2, 3, 20–26], $ZrB_2(0001)$ [27], Ir(111) [28], HOPG [29, 30] and MoS_2 [31]. In the following sections I discuss the observations reported for silicene growth on some of these substrates.

1.2 Silicon nanoribbons on Ag(110)

The first experimental observation of silicene-like structures were reported on Ag substrates, due to its immiscibility with Si [32].

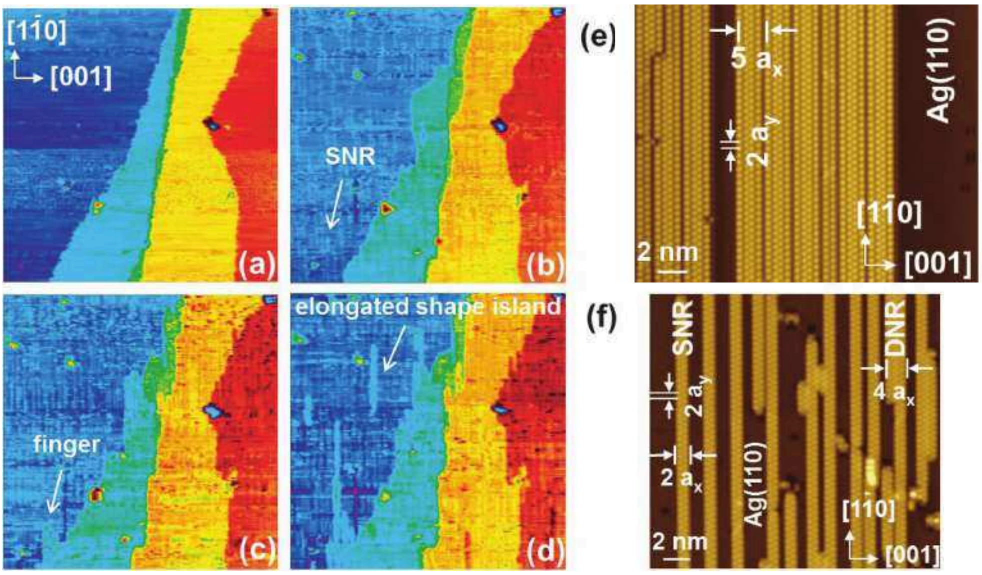

FIGURE 1.4: a-d) Sequence of STM images (234 × 234 nm^2) of the same sample area showing the evolution of the Ag(110) surface upon Si deposition at room temperature. (a) Bare silver surface. Each color corresponds to a different Ag terrace. (b)-(c)-(d) images correspond to increasing Si coverage, 0.1-0.2-0.3 ML. (e) Self-assembled NRs appearing after the evaporation of 0.5 monolayers of Si at 460 K. a_x and a_y are orthogonal vectors, expressed in the cubic basis of Ag (a_x=0.409 nm, a_y=0.205 nm). f) Si SNRs and DNRs appearing after Si evaporation at room temperature (0.3 ML coverage). Figures adapted from [33].

According to literature, submonolayer Si deposition at room temperature on Ag(110) results in the formation of one-dimensional (1D) Si nanoribbons (NRs) [19, 20, 34]. The nanoribbons observed on Ag(110) are randomly distributed on the surface and have a width of either 0.8 nm, in the case of single NRs (SNRs), or 1.6 nm for double NRs (DNRs) [35]. For deposition at higher temperature (460 K), it was observed that NRs self-assembl and form a (5×2) or $c(10 \times 2)$ 1D grating [34, 36]. The exact atomic structure of such NRs was debated for long, especially because it was claimed that this system possessed Dirac cones as predicted for FS silicene [37]. However, further studied attributed the linear dispersion observed by angular-resolved photemission spectroscopy (ARPES) to folded Ag bands induced by the adsorbed Si reconstruction [38]. Moreover, also the optical response of Si/Ag(110) showed features not compatible with those expected for FS silicene [39, 40].

In 2013 Bernard *et al.* identified the growth mechanism of the Si NRs on Ag(110) by means of scanning tunneling spectroscopy (STM) and grazing incidence X-ray diffraction (GIXD) [33]. In Fig. 1.4.a-d I show four STM images reported in their works in which the evolution of the Ag substrate can be seen during Si evaporation at room temperature. Fig. 1.4.a shows the bare Ag substrate, in which each color correspond to a different Ag terrace. After evaporating 0.1 monolayer (ML) of Si (1 ML corresponds to the Ag(110) surface density), the Ag steps undergo a transformation and the first NRs appear, parallel to the straight parts of the Ag steps (Fig. 1.4.b). After further Si evaporation (0.2 ML coverage) the evolution of the Ag step is even more pronounced: some features, called "fingers" because of their shape, start growing at the step edges. They have the same height as a Ag step and they have been interpreted as Ag atoms ejected from the substrate upon Si evaporation, which diffuse and stick to the Ag steps. The density of NRs increase as well. After another Si evaporation (total coverage 0.3 ML) also elongated shape islands appear, which are interpreted in the same way of the "finger" features. Based on quantity of Ag atoms released during Si deposition, Bernard *et al.* proposed a "missing-row" model which could take into account the nucleation and growth of the NRs, but also the ejection of Ag atoms out of the substrate during Si deposition.

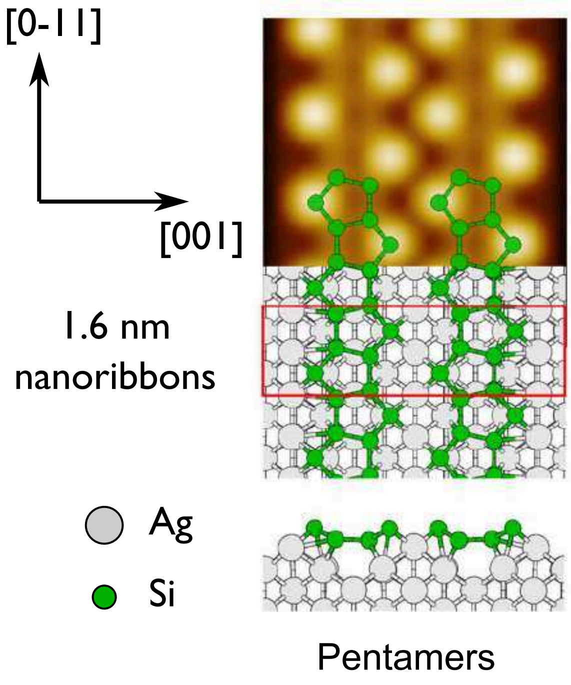

FIGURE 1.5: Schematic representation of the 1.6-nm-wide Si pentamer nanoribbon model on the "missing-row" reconstructed Ag surface and relative simulated STM image.

More recently, the exact structure of the Si NRs has been determined by combined GIXD and DFT calculations in a work by Prévot *et al.* [41]: by considering several theoretical models proposed in the literature [20, 41–48] they showed that the only one compatible with the diffraction data consisted of twin Si pentamer chains with alternate orientations grown on the "missing-row" reconstructed Ag surface, which is depicted in Fig. 1.5, along with the associated simulated STM image.

1.3 Silicon stripes and "complex structure" on Ag(100)

Si evaporation on Ag(100) at T_{growth} ∼500 K results in the formation of two superstructures. The first one is observed from the initial stages of Si up to the completion of the Si adlayer [49]. The low-energy electron diffraction (LEED) pattern show a $p(3 \times 3)$ reconstruction.

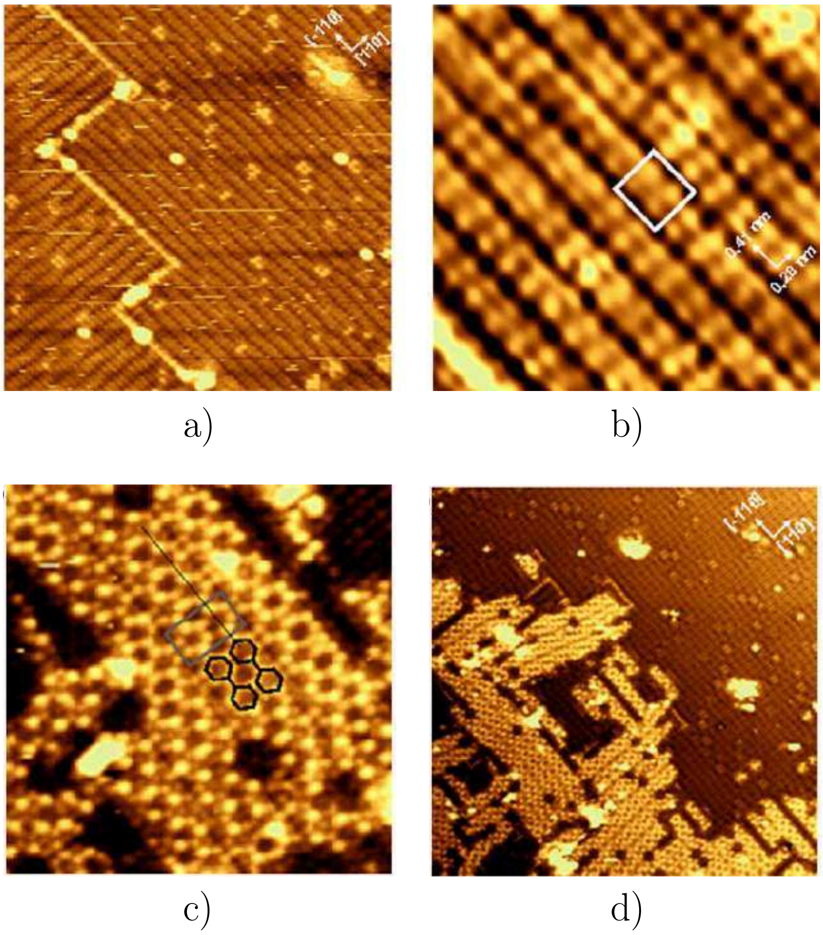

a) b) c) d)

FIGURE 1.6: a-b) STM images after 0.8 ML Si evaporation (T_{growth} ∼500 K) showing the $p(3 \times 3)$ reconstruction. The white rectangle indicates the superstructure unit cell. (23.4×23.4 nm$_2$; 6.4×6.1 nm$_2$). c-d) STM images after 1.6 ML Si evaporation (T_{growth} ∼500 K) showing the coexistence of the $p(3 \times 3)$ and "complex" reconstructions. The grey rectangle shows a local (7×4) periodicity; (22.3×22.3 nm$_2$; 6.4×6.4 nm$_2$). Figures reproduced from refs. [49].

The STM image in Fig. 1.6.a shows two orthogonal domains separated by sharp border lines. The Si-induced stripes are aligned along the [110] and [1$\bar{1}$0] substrate orientations and a modulation is visible along each line. This can be seen better in Fig. 1.6.b: the stripes have a width of ∼0.28 nm and the modulations show a periodicity of 0.41 nm. In a first moment this $p(3 \times 3)$ reconstruction was interpreted, by means of diffraction measurements, in terms of one dimensional chains of four Si atoms (tetramers) adsorbed on the topmost Ag(100) layer [49]. However, the stability of the model was put into question by density functional theory (DFT) calculations [46], and a better candidate, consisting in a hexagon-type atomic geometry of Si atoms at one monolayer coverage, was put forward.

Beyond one Si ML deposition the LEED pattern displays the so-called "complex phase". From the STM images in Fig. 1.6.c-d, one can see that new stripes appear (coverage *sim* 1.6 Si ML) running along the same [110] and [1$\bar{1}$0] substrate directions. These new stripes show several defects and are not perfectly straight. This "complex phase" was interpreted as a silicene-type layer with extra Si adatoms residing on top [46].

1.4 Single and multi-layer silicene on Ag(111)

The (111) surface of Ag crystals appears to be an ideal candidate for silicene synthesis for several reasons:

1. the (111) surface of transition metals in general is composed of hexagonal close packed array of atoms characterized by smooth surface potential [50];
2. the solid phases of Ag and Si are not miscible [32], as already said in the previous section. This is confirmed also by Ag deposition on Si, which result in the formation of sharp interfaces, without making silicide compounds [51];
3. Ag and Si lattice constants are in 3/4 ratio, which could reduce the stress in case of epitaxial growth;
4. their similar electronegativity ($\sim$1.9) should result in a small charge transfer between the Si layer and the substrate.

The first study to claim succesful silicene growth was published in 2010 [52], but the experimental work which lit the fuse of silicene synthesis is the one written by Vogt *et al.* in 2012 [3]. Since then many theoretical and experimental works have been published [3–5, 19, 21, 23–25, 52–66], with the aim of instigate this system and see if the silicene layer possesses or not FS properties. In the following I will focus its structure and electronic properties and finally I will describe the growth mode.

1.4.1 Silicene structure on Ag(111)

The growth temperature plays a fundamental role in the crystallization of the Si honeycomb lattice on Ag(111). Lee *et al.* thoroughly studied the exact composition of the silicene layer, in terms of surface reconstructions, as a function of both substrate temperature during the growth and Si coverage. Fig. 1.7.a reports their results compared to those already present in literature. The labels are explained in Fig. 1.7.b[1].

Several techniques were used to study the structure of silicene on Ag(111). By STM and LEED investigation it was possible to identify the different surface reconstructions such as the (4×4), $(\sqrt{13} \times \sqrt{13})R13.9^\circ$, $(2\sqrt{3} \times 2\sqrt{3})R30^\circ$, $(3.5 \times 3.5)R26^\circ$, "dotted phase", and many others as shown in Fig. 1.7. Observed for the first time by Vogt *et al.*, the (4×4) reconstruction is by far the most studied phase of the silicene monolayer on Ag(111) [3–5, 19, 21, 23–25, 52–60]. Three models were initially proposed in the literature. A schematic representation for all of them is given in Fig. 1.8. In the model independently proposed

---

[1] In this Thesis I will employ a common notation used to label surface reconstructions: the label $(n_{rec} \times n_{rec})R\gamma_{rec}$ means that the surface reconstruction I am referring to has a unit cell with a lattice parameter n_{rec} times that of the unit cell reference and it is rotated by an angle γ_{rec} with respect to the same reference. In the case of Si reconstructions on Ag(111) the reference is either the unit cell of Ag(111) or the one of Si(111), which are both hexagonal. In particular, the (4×4) and $(4/\sqrt{3} \times 4/\sqrt{3})$ reconstructions (referred to the Ag unit cell) are also called (3×3) and $(\sqrt{3} \times \sqrt{3})$ reconstructions (when referred to the unit cell of a Si plane).

a)

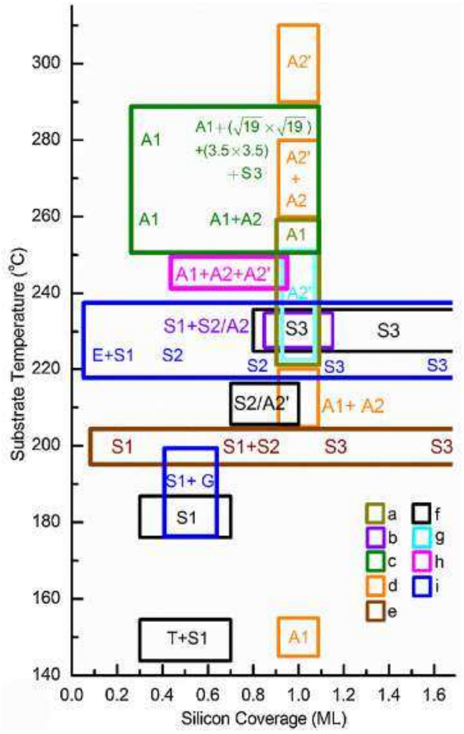

b)

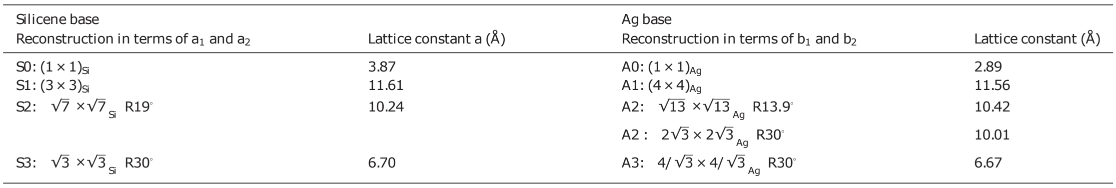

Silicene base Reconstruction in terms of a_1 and a_2	Lattice constant a (Å)	Ag base Reconstruction in terms of b_1 and b_2	Lattice constant (Å)
S0: $(1\times1)_{Si}$	3.87	A0: $(1\times1)_{Ag}$	2.89
S1: $(3\times3)_{Si}$	11.61	A1: $(4\times4)_{Ag}$	11.56
S2: $\sqrt{7}\times\sqrt{7}_{Si}$ R19°	10.24	A2: $\sqrt{13}\times\sqrt{13}_{Ag}$ R13.9°	10.42
		A2 : $2\sqrt{3}\times2\sqrt{3}_{Ag}$ R30°	10.01
S3: $\sqrt{3}\times\sqrt{3}_{Si}$ R30°	6.70	A3: $4/\sqrt{3}\times4/\sqrt{3}_{Ag}$ R30°	6.67

FIGURE 1.7: Phase diagram of the silicene superstructures as a function of Si coverage and the Ag(111) substrate temperature during the growth. The labels of the different reconstructions are explaind in (b). Moreover, *E* is a precursor phase observed at the step edges for low Si coverage; *G* is the so-called "dotted phase". The data *a-i* are the results reported in refs. [3, 23–25, 52, 56, 57, 66, 67] b) Labeling of the various supercells using a free silicene lattice ($\bar{a}_1/2$ cell parameters) and a Ag(111) surface lattice ($\bar{b}_1/2$ cell parameters) as bases. Figures reproduced from ref. [66].

by Vogt *et al.* and Lin *et al.* [3, 55], the (4 × 4) structure consists of 18 atoms arranged in a honeycomb lattice: six of them are displaced vertically giving a buckling of 0.7/0.75 Å, according to the two reaserch groups [3, 55]. Both of them were put forward on the basis of STM and LEED experiments, along with DFT calculations. A good agreement was found between the experimental and the simulated STM images, in which six protrusions are clearly visible and correspond to the high-lying Si atoms, represented by red spheres in Fig. 1.8. Vogt *et al.* reported more details about the structure: the average Si-Si distance is 2.2 Å and the distance between the bottom silicon atoms and the first Ag layer is 2.92 Å. The side of the triangular structures formed by protruding Si atoms is equal to 0.38 Å, in agreement with the value reported by Lin *et al.*.

The second model [24] interpreted the so-called *corner holes*, i.e. the circular black areas in Fig. 1.8.d, in terms of missing silicon rings. Note that, according to DFT calculations, The six Si atoms around the corner are hydrogenated to saturate the Si dangling bonds.

The last model was more recently deduced from the interpretation of extended x-ray absorption fine structure (EXAFS) [68]. The silicon atoms were confirmed to be in a *low-buckled* honeycomb network, with

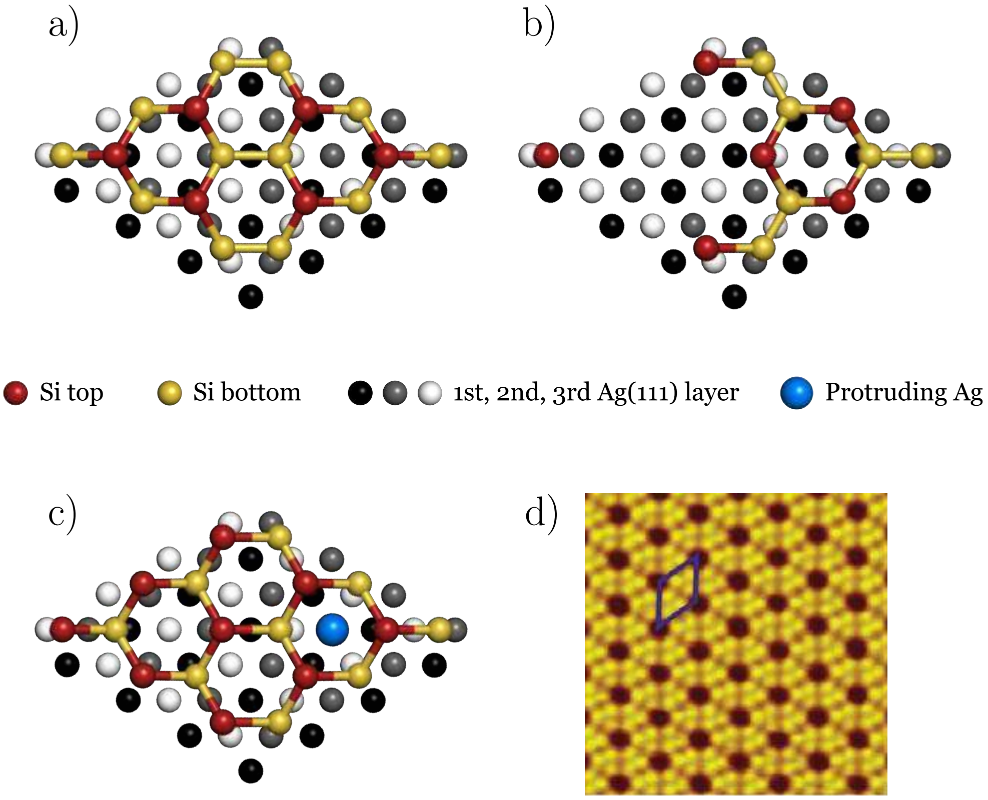

FIGURE 1.8: Top-view of the three models proposed in the literature. a) Model proposed independently by Lin *et al.* [55] and Vogt *et al.* [3]. The two other structures represent the models put forward by Feng *et al.* (b) and by Lagarde *et al.* (c) [24, 68]. d) High-resolution STM image (8.5×7.5 nm^2) of the (4×4) reconstruction taken from the literature [24]. The blue rhombus in (d) indicates the unit cell of the superstructure.

structural characteristics very similar to those found for a double Si(111) plane of crystalline silicon. Furthermore, it was proposed that a Ag adatom could be found below the silicene sheet, but 0.65 Å above the first Ag plane of the substrate (bluish atom in Fig. 1.8.c). The paper stated that the presence of this Ag atom could be due to the intermix of evaporated Si in the substrate, despite their reciprocal immiscibility.

A quantitative LEED study [4] and [5] reflection high-energy positron diffraction measurements confirmed the model independently proposed by Vogt *et al.* and Lin *et al.* [3, 55]. However, the two techniques which have been employed can lead to major uncertainties in the evaluation of the exact structural parameters. This issue will be tackled in Chapter 4.

As opposed to the case of the (4×4) reconstruction, literature lacks a quantitative diffraction studies, as already pointed out by Takagi *et al.* [69], aimed to determine the exact atomic structures of the $(2\sqrt{3} \times 2\sqrt{3})R30°$, $(\sqrt{13} \times \sqrt{13})R13.9°$ and other reconstructions of silicene/Ag(111), although several theoretical models have already been proposed [70–72]. In Chapter 4 I will present the first measurements of this kind ever reported up-to-date.

1.4.2 Electronic properties of silicene on Ag(111)

The electronic structure of silicene is probably the most appealing characteristic of this new material, both from the point of view of fundamental science and for the eventual realization of ground-breaking technological applications, such as high-frequency transistor.

The identification of the presence of massless Dirac fermions is not always straightforward. Arguably, the two most recognizable signatures of such particles are the quantum Hall effect (QHE) and the presence of linear bands in the electronic structure being studied. Usually, integer QHE is observed in 2D electron gases. In the case of an arbitrary material, when an external magnetic field is switched on, the orbital motion of the electrons in the studied system are quantized, i.e. they are confined in a parabolic potential well generated by the magnetic field. Thus, electrons can occupy only discrete eigenstates, known as Landau levels (LLs), which for conventional 2D systems are described as:

$$E_n = \hbar\omega\left(n + \frac{1}{2}\right) \tag{1–2}$$

$$\omega = \frac{eB}{m} \tag{1–3}$$

e is the elementary charge, $\hbar$ is the reduced Planck constant, B is the external magnetic field, n is the quantum number [73, 74]. Note that the energy spectrum is the same as that of a harmonic oscillator and the energy interval between two consecutive states is constant.

Considering that in systems possessing Dirac fermions the electrons obey the Dirac-Weyl equation, the energy spectrum writes differently:

$$E_n = \pm v_f\sqrt{2e\hbar Bn} \tag{1–4}$$

where v_f is the Fermi velocity [73, 74]. Note that the separation between the energy level is no more a constant, $E_n \propto \sqrt{n}$. Thus, the separation between LLs can determine the presence of Dirac fermions in the material under study.

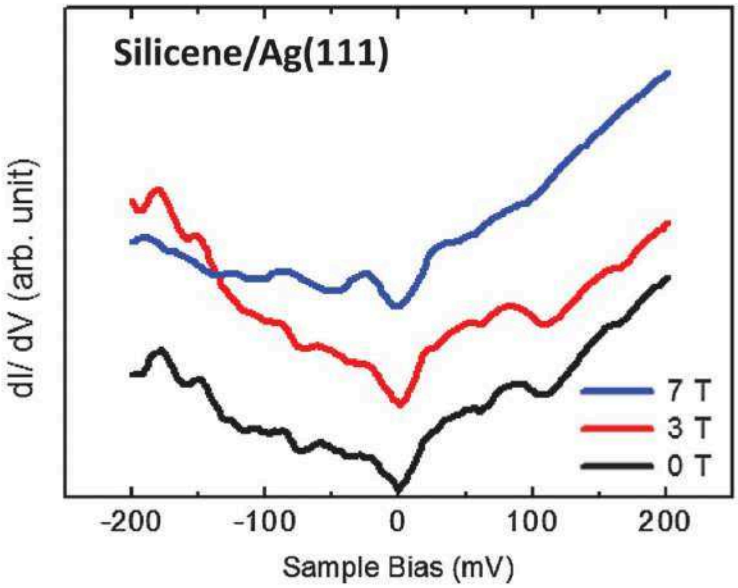

FIGURE 1.9: Evolution of STS spectra with increasing magnetic field applied perpendicular to the surface. No sign of the oscillations expected for the LLs are visible, rejecting the hypothesis of Dirac fermions.

Lin *et al.* measured the LL sequence using scanning tunneling spectroscopy with an external magnetic field. In Fig. 1.9 I report the spectral evolution of the (4 × 4) reconstructed silicene as a function of the magnetic field ($0 < B < 7$) obtained by Lin *et al.* [75]. Despite the V-shaped background, reminiscent of the Dirac cone, the features expected for LLs do not appear. Thus, Lin *et al.* concluded that the Si p_z orbitals, which should be responsible for the formation of the Dirac cones, are delocalized into the substrate because of strong hybridization with Ag states.

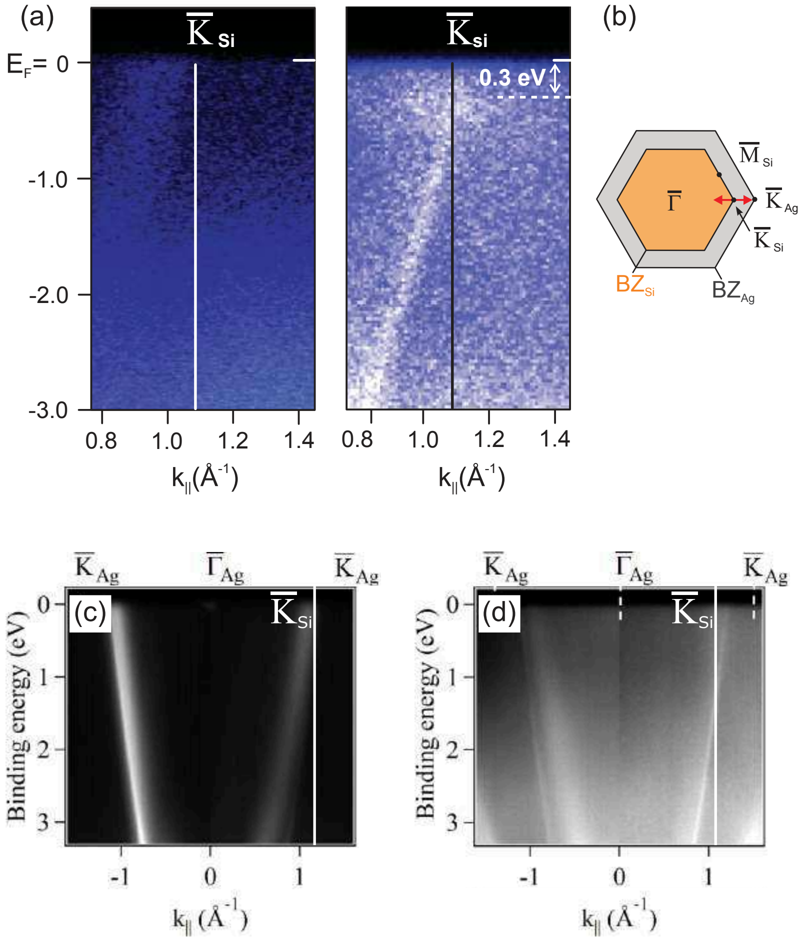

FIGURE 1.10: a-b) ARPES maps reported by Vogt *et al.* for the clean Ag surface and after the formation of the silicene layer, respectively, along the $\bar{\Gamma}_{Ag} - \bar{K}_{Ag}$ direction. The Brillouin zone (BZ) scheme for Ag and Si is depicted next to (b). The red arrow indicates the measurements direction. c-d) ARPES maps reported by Mahata *et al.* for bare Ag(111) and silicene/Ag(111), respectively, along the $\bar{\Gamma}_{Ag} - \bar{K}_{Ag}$ direction; the K_{Si} point is at $k_{\parallel}$=1.1 Å^{-1}. Figures reproduced from refs. [3, 76].

Concerning the presence of linearly dispersed bands, with ARPES it is possible to measure the kinetic energy of photoelectrons as a function of the momentum and determine the dispersion of the elctronic bands, as it was done for graphene [77]. Vogt *et al.* performed ARPES on a (4 × 4) reconstructed silicene monolayer on Ag(111) to determine its band structure [3]. They observed a linear band in proximity of the Fermi level and they associated it with the presence of Dirac cones in the system (Fig. 1.10).c-d) and they also reported a gap opening at K$_{Si}$ of ∼0.3 eV. However, further studies, both theoretical and experimental [55, 78, 79], drew a different conclusion. It was observed that the linear feature in the ARPES band is actually an Ag sp-bulk band, which remains substantially unaltered after the deposition of the silicene layer [76, 79]. From the comparison of Fig. 1.10.c and Fig. 1.10.d, Mahata *et al.* deduced that the bands crossing the Fermi level (E_F) in silicene are due to bulk states of the Ag substrate, since the bands display the same dispersion as in bare Ag(111). Moreover, they did not observe any gap-opening at K$_{Si}$.

It was also observed that the (4 × 4) silicene reconstruction, when it is not supported by the Ag(111) substrate, has a bandgap opening (∼0.3 eV) in proximity of the K point [55, 78], differently from the free-standing form calculated by Cahangirov *et al.* which is predicted to be semi-metallic [1]. When the Ag substrate is taken into account, the silicene monolayer becomes strongly metallic.

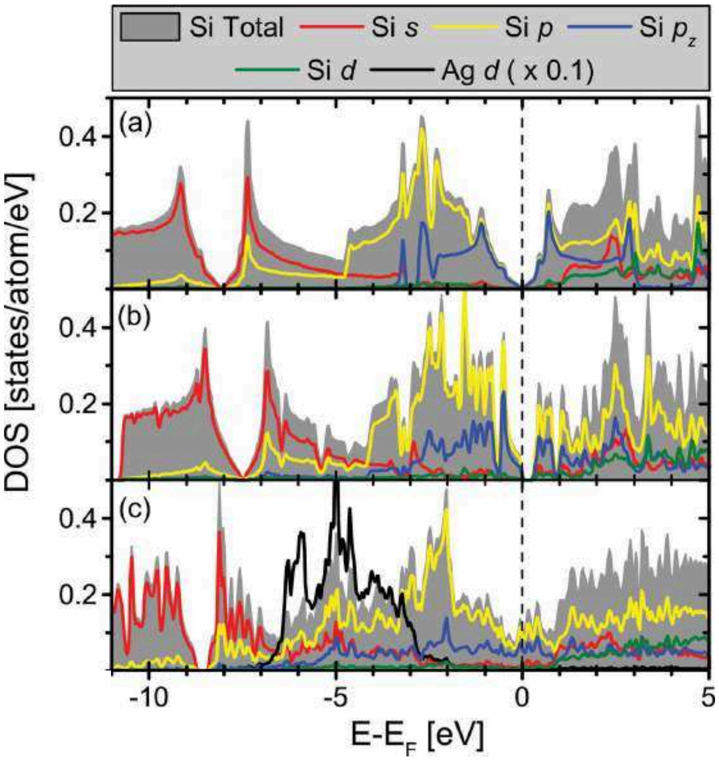

FIGURE 1.11: a) Calculated DOS of FS silicene showing the zero-bandgap electronic structure typical of semimetals. b-c) Calculated DOS of the (4 × 4) silicene structure unsupported and supported by the Ag(111) substrate. Figure adapted from ref. [78]

This effect is clearly visible in Fig. 1.11, which shows the calculated partial and total Si density of states (DOS) for FS silicene, (4 × 4) silicene structure in absence and presence of the Ag(111) substrate. In Fig. 1.11.a the semimetallic behavior of FS silicene can be clearly seen, as the total DOS becomes zero in one single point coinciding with the Fermi level. The trend for unsupported (4 × 4) reconstructed silicene (Fig. 1.11.b) shows the opening of the gap at the Fermi level. When the Ag substrate is inserted in the calculations (Fig. 1.11.c) the resulting total DOS is strongly metallic, with the contribution from the p_z orbital spreading across the Fermi level. This was interpreted by Johnson *et al.* in terms of strong hybridization between Si *p* and Ag *d* states, affecting irreversibly the electronic structure of the silicene sheet [78].

The same kind of measurements and considerations were done also for the other monolayer reconstructions, such as $(\sqrt{13} \times \sqrt{13})R13.9^\circ$ and $(2\sqrt{3} \times 2\sqrt{3})R30^\circ$ structures, arriving at the same conclusion, i.e. the silicene/Ag(111) system does not posses Dirac fermions.

1.4.3 Si thin films/multi-layer silicene on Ag(111)

It was noticed that the high silicon coverage regime is characterized by the appearance of a $(4/\sqrt{3} \times 4/\sqrt{3})$ reconstruction [2, 8, 10, 24, 54, 56, 57, 59, 80–82], as shown in Fig. 1.12.a. This reconstruction is also called $(\sqrt{3} \times \sqrt{3})$, in the case the notation refers to a silicene (1×1) cell. The high-resolution STM image reported in Fig. 1.12.b shows the surface appearance of this reconstruction. The lattice parameter associated with its unit cell was measured to be 0.64 nm. Whereas the growth of the second layer starts only after the completion of silicene monolayer, successive Si layers can grow before the completion of the second one as it is clearly visible from Fig. 1.12.a.

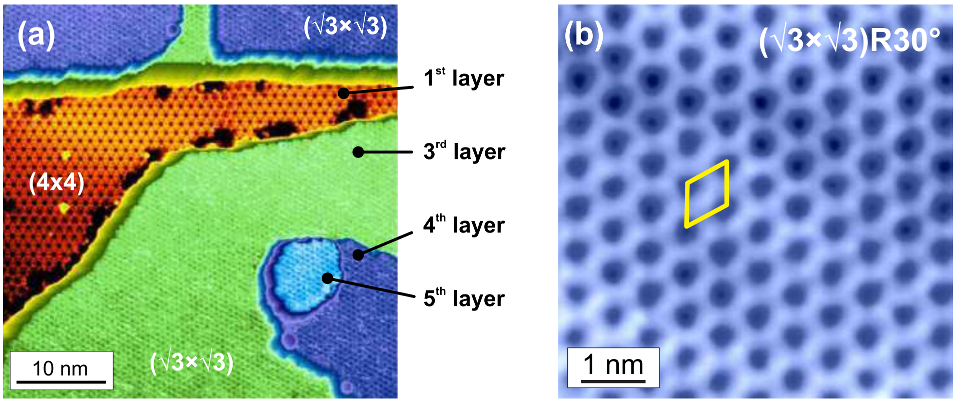

FIGURE 1.12: a) STM image after the evaporation of 1.5 ML of Si on Ag(111). Three different terraces show the ($\sqrt{3} \times \sqrt{3}$) reconstruction, while a region covered by the (4×4) silicene monolayer reconstruction is still visible. b) High-resolution STM image of the ($\sqrt{3} \times \sqrt{3}$) reconstruction, in which the unit cell is identified by the yellow rhombus. Images adapted from [83].

The interest in multilayer silicon deposition on Ag(111) resides in the fact that this system could result the formation of the so-called *multilayer silicene*, i.e. a stacking of silicene layers having a weak interaction among them and with the Ag(111) substrate. This could eventually leads to the decoupling between silicene layers and the substrate, recovering the electronic properties predicted for FS silicene. Several models have been proposed for the structure of the thin Si film on Ag(111) and the ($\sqrt{3} \times \sqrt{3}$) surface reconstruction associated with it, but the subject is still a matter of debate. This issue will be thoroughly discussed in Chapters 5 and 6.

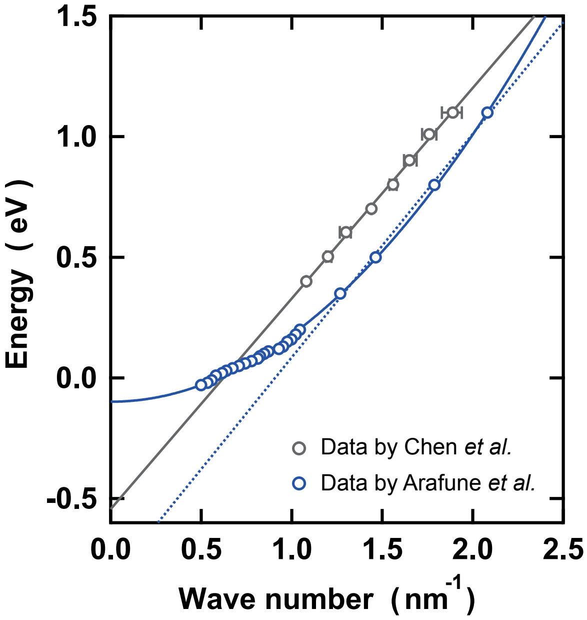

FIGURE 1.13: Comparison between the dispersion relations determined by dI/dV map obtained by Chen *et al.* (grey circles) and Arafune *et al.* (blue circles. The blue dotted line is obtained by fitting blue circles between 0.35 and 1.1 eV and it is similar to the trend observed for the grey dots.

The electronic structure of the thick Si films on Ag(111) was investigated, although its structure and the nature of its surface termination, i.e. the $(\sqrt{3} \times \sqrt{3})$ recosntruction, are still undetermined. Chen *et al.* [54, 82] attributed the presence of standing wave pattern on the $(\sqrt{3} \times \sqrt{3})$ reconstruction observed by STM to the presence of quasi-particles. In particular, by measuring the wavelength of the standing waves as a function of the applied voltage, they observed a linear band dispersion that they associated with the presence of Dirac fermions in the $(\sqrt{3} \times \sqrt{3})$ structure. However, Arafune *et al.* proved that the linear dispersion observed by Chen *et al.* was actually part of a larger parabolic dispersion [84], which could be due to a surface state intrinsic to the clean Ag(111) substrate, see Fig. 1.13, rejecting the hypothesis of Dirac fermions.

1.4.4 Si growth on Ag(111)

The growth mechanism of Si on Ag(111) at different temperatures was thoroughly studied by STM measurements and DFT calculations [65, 85]. Several growth regimes were identified depending on the temperature of the substrate during Si deposition (T_{growth}).

- T_{growth}=200 K

  As Si atoms are deposited on the surface, STM images, reported in Fig. 1.14.a, show the appearance of flat Si islands with an apparent height of 0.21 nm. It is not possible to identify an ordered arrangement at their surface. Some 3D clusters are visible, too.

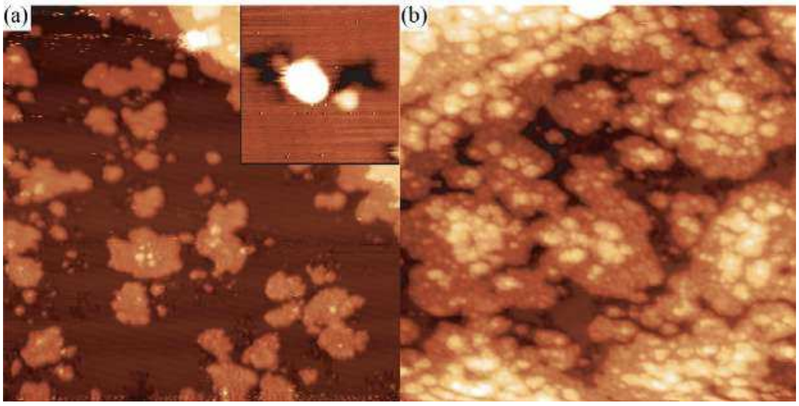

FIGURE 1.14: STM images showing Si growth on Ag(111) at 200 K for increasing Si coverage. (a) 86×86 nm^2 and 21×21 nm^2 (inset); (b)^{2}43×43 nm^2. Figures reproduced from ref. [65].

  Increasing Si coverage, Si islands begin to coalesce. Before the completion of the first layer, the second one starts to grow, resulting in an inhomogeneity of the Si coverage. The islands growing on top of the first (incomplete) Si layer, show an apparent height of 0.23 nm. The height of the Si islands is markedly different from the one expected between two Si planes (0.31 nm). However, this difference could be due to electronic effects to which STM is quite sensitive (see Sec. 2.3 and 3.10.

- T_{growth}=300 K

  Bernard *et al.* [33] showed that the evolution of the surface upon Si deposition is completely different from the previous case. As soon as Si evaporation begins, isolated dark spots appear and, upon further deposition of Si atoms, they act as nucleation centers for the growth of Si islands Fig. 1.15.a. The apparent height of these islands is lower than the one of the surrounding Ag substrate. Moreover, as clearly visible in Fig. 1.15.b, the substrate step edges undergo a significant evolution: at the same time as Si islands grow, "finger"-like features similar to those described in the case of Si/Ag(110) are observed. They have the same height as the Ag(111) step height. Thus, it was concluded that for Si evaporation at room temperature, Si atoms insert in the substrate and the ejected Ag atoms diffuse toward the step giving rise to these "fingers". The same picture was also confirm by Satta *et al.* [86], who also depicted the exact substitution mechanism of Si inside Ag(111) surface by a joint STM and DFT study.

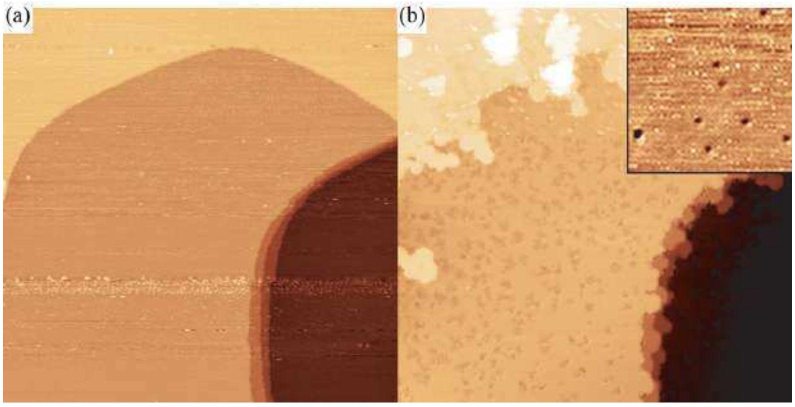

FIGURE 1.15: STM images showing Si growth on the same Ag(111) area at 300 K for increasing Si coverage. (a)-(b) 150×150 nm^2; inset: 21×21 nm^2. Figures reproduced from ref. [65].

- 400 K $< T_{growth} <$ 540 K

  Always by means of STM measurements, Prévot *et al.* showed the evolution of the surface during Si deposition in the specific case of growth at 440 K [87]. In this case, in the first stages of Si growth Si islands nucleate and, moreover, Ag step edges facet toward $\langle 110 \rangle$ directions (see Fig. 1.16.b) differently from what observed at 300 K (Fig. 1.15). The faceting is due to Si atoms which diffuse on the surface and then reach a step edge; here they give rise to a reconstruction of the step edge, with a periodicity equal to twice the Ag-Ag distance (inset Fig. 1.16.b). Upon further Si evaporation, the Si islands grow and elongated features, referred to as "fingers", appear at the step edges. Thus, the situation is similar to what observed at 300 K, in which Si atoms arrive on the substrate, eject Ag atoms which then migrate toward the step edges (Fig. 1.16.b-d). Finally, Si islands can nucleate also on the Ag "finger". This process continue until the completion of the silicon monolayer; the second Si layer begins to grow only afterwards.

- $T_{growth} >$ 540 K

  The growth mode observed until the ML completion is very similar to the previous one, but with the difference that Si islands preferentially nucleate and grow at the step edges. The major difference is that at the ML completion, the silicene layer dewets and the appearance of 3D islands is observed [3, 25, 59].

The growth of Si atoms by insertion in the Ag substrate was also supported by energetics considerations based on DFT calculations, reported in ref. [86].

1.5 Silicene synthesis on alternative substrates

As already said in Sec. 1.1, silicene synthesis has already been reported on several substrates different from Ag. In the following I give two other notable examples regarding the synthesis of hexagonal 2D Si

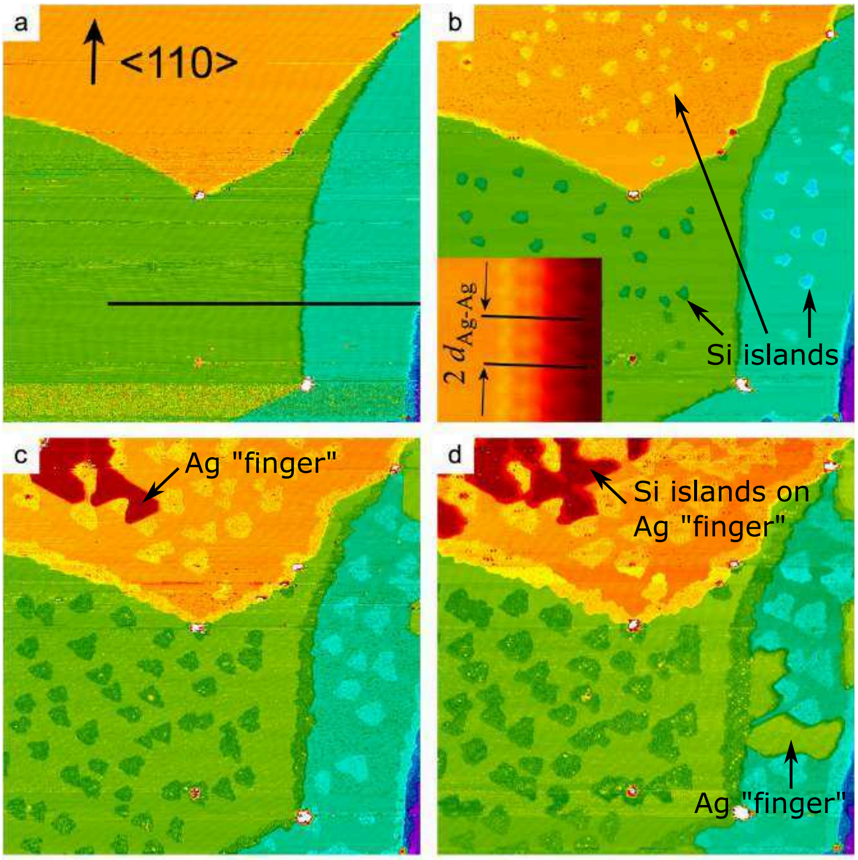

FIGURE 1.16: STM images showing Si growth on the same Ag(111) area at 440 K for increasing Si coverage. a) Bare Ag(111) susbtrate. Each color is assocated with a different Ag terrace. b) First stages of Si evaporation (coverage: 0.09 Si ML): nucleation of Si islands and faceting of the step edges toward ⟨110⟩ directions. Inset: step edge reconstruction of Si atoms. c) Growth of the Si islands and appearance of Ag "fingers" represented by the red features (coverage: 0.28 Si ML). d) New Ag "fingers appearing (green feature) and Si islands nucleating on Ag "fingers" (coverage: 0.49 Si ML). STM images dimensions: 325×325 nm^2; inset: 4.3×4.3 nm^2. Figures adapted from ref. [87].

lattices.

It was reported that ZrB_2 can be epitaxially grown onto Si(111) and act as a possible substrate for silicene synthesis. Air exposure of ZrB_2/Si(111) leads to the formation of a mixed B and Zr oxide layer, which can be removed by annealing at 800 C° [88]. The resulting surface is free from oxide compounds and shows a (2×2) reconstruction. This structure was associated with the presence of Si atoms segragating at the surface, as proven by photoemission spectroscopy measurements [27, 89]. Reported STM images showed that the (2×2) reconstruction consists of 1D arrays of stripe-shaped domains, aligned along one of the three equivalent $\langle 11\bar{2}0\rangle$ directions, see Fig. 1.17.a. The unit cell of the reconstruction contains only one protrusion. The domain boundaries are due to a shift of one unit cell between consecutive domains along the white lines ($\langle 11\bar{2}0\rangle$ directions) represented in Fig. 1.17.a. In the high resolution image reported in Fig. 1.17.b, it is possible to observe a honeycomb structure (blue hexagonal lattice) with a lattice parameter of 3.68 Å that have ascribed to a silicene lattice. Differently from silicene/Ag(111) no coexistence of multiple phases was observed. The observed surface reconstruction has a $(\sqrt{3} \times \sqrt{3})$ periodicity with respect to the silicene unit cell. Fleurence *et al.* [27] proposed the model in Fig. 1.17.c to interpret the structure. Concerning the electronic band structure, the Si atoms sitting on top of a Zr atom are those showing the strongest sp_2 character. Although a feature reminescent of a Dirac cone was observed by ARPES measurements, all the silicene-derived bands appear to be hybridized with Zr d orbitals [90]. Thus, the electronic behavior is different from the one expected for free-standing silicene.

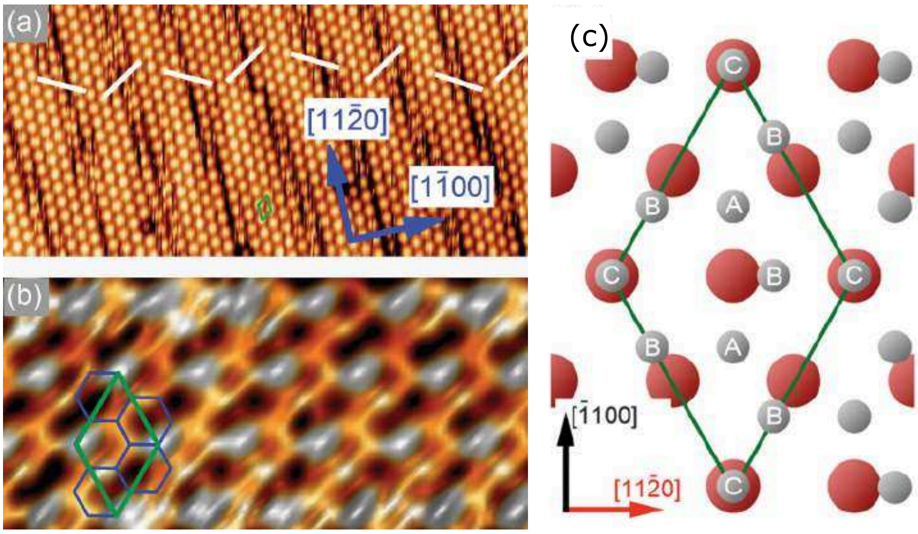

FIGURE 1.17: a) STM image (20×5 nm^2) of the (2 × 2) silicene reconstruction on ZrB_2. The green rhombus indicates the unit cell of the reconstruction and the white lines show the directions of the shift between the domains at the boundaries. b) STM image (4.2×2 nm^2) of the silicene honeycomb structure, emphasized by the blue hexagonal lattice. c) Model of the interface between silicon atoms (grey spheres) and the uppermost Zr atoms (red spheres). "A", "B" and "C" denote inequivalent atomic positions in the silicene unit cell. Images adapted from ref. [27].

The formation of a 2D hexagonal Si lattice was also observed onto Ir(111) [28]. After Si deposition on the (111) surface of Ir, the sample is annealed at 670 K in order to obtain a ($\sqrt{7} \times \sqrt{7}$) reconstruction with respect to the Ir substrate or a ($\sqrt{3} \times \sqrt{3}$) structure with respect to the hexagonal Si lattice unit cell. STM images (Fig. 1.18.a) showed the presence of an hexagonal lattice of protrusions with a lattice parameter of 7.2 Å, Fig. 1.18.a. A model was put forward based on DFT calculations(Fig. 1.18.b) [28], in which the six atoms of the ($\sqrt{3} \times \sqrt{3}$) unit cell of the silicene layer were found to be 2.0 Å above the Ir(111) surface, except for the Si atom exactly on top of a Ir atom (yellow sphere in Fig. 1.18.b) which is 0.63 Å higher. Two other atoms are sitting on the hcp and fcc hollow sites of the Ir(111) surface and the last three are on bridge sites. The calculated band structure which was calculated for silicene/Ir(111) is markedly different from the one of FS silicene [91]. The very strong hybridization with the Ir(111) substrate and the lack of Dirac-like features (as the one reported for silicene/ZrB_2) in the band structure, makes highly questionable the hypothesis of sp_2 character of the silicene layer.

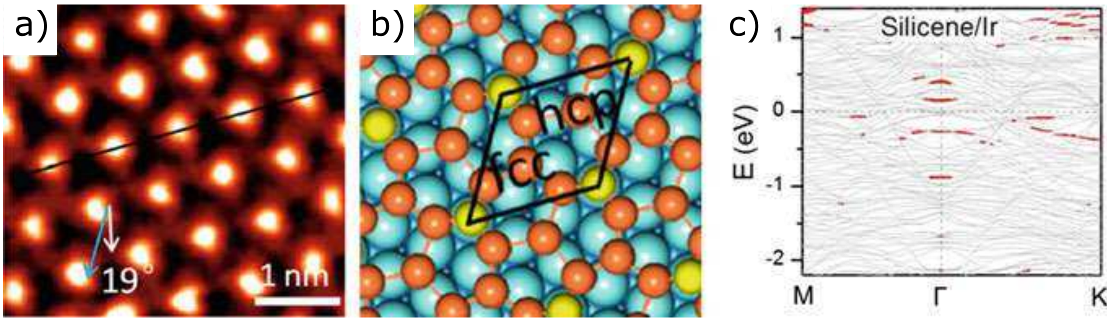

FIGURE 1.18: a) STM image of the (7 × 7) silicene reconstruction on Ir(111). b) DFT-base structural model: yellow and red spheres represent Si atoms, while light-blue spheres represent Ir atoms. c) Electronic band structure of silicene/Ir(111) represented in the ($\sqrt{3} \times \sqrt{3}$) unit cell. The contribution from the si atoms are highlighted in red. Figures reproduced from refs. [28] and [**quhe**].

To conclude, the synthesis of silicene monolayers on the materials I have taken as examples ends up with the hybridization of the silicene sheet with the substrate bands, resulting in the loss of the free-standing-like properties. Indeed, the ultimate goal would be the synthesis of a FS silicene layer on a semiconducting substrate. This kind of systems has been studied recently, and in particular the cases of silicene/HOPG [30] (HOPG is a zero gap semiconductor or semimetal) and silicene/MoS_2 [31] will be discussed in detail in Chapter 7.

Chapter 2

Experimental Methods

2.1 Introduction

In this section I present the experimental setups used for the measurements shown in Chapters 4, 5, 6 and 7. I will describe the physical principles of the different experiments as well as the procedures employed in the data analysis.

2.2 Sample preparation

As explained in Chapter 1, substrates with clean surfaces are needed for synthesizing silicene layers. Consequently, I have performed experiments in ultra-high vacuum (UHV) conditions (base pressure below 10^{-10} mbar), and I have used techniques to get rid of the contaminants found on the samples when they are inserted in the analysis chambers. Two types of materials have been used as possible substrates for silicene synthesis: single crystal Ag(111), and van der Waals layered materials, such as HOPG, MoS_2, $TiTe_2$ and $ZrSe_2$ belong, see Chapter 7.

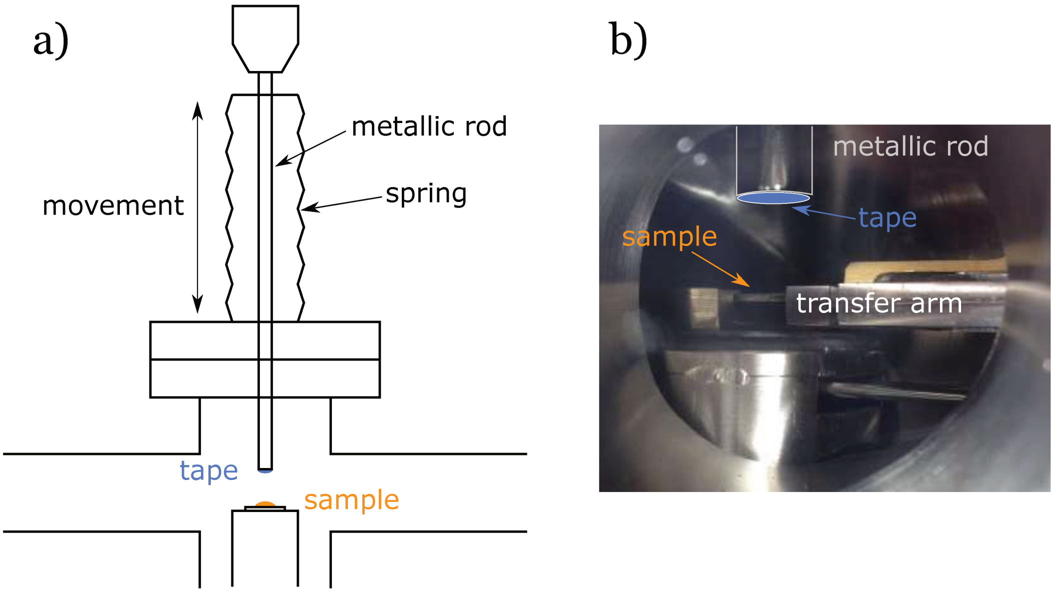

FIGURE 2.1: a) Schematics of the in-situ cleavage apparatus. b) Photo of the system inside the UHV chamber.

The Ag(111) sample and the layered materials need two different procedures to clean their surface. Ag(111) is prepared by standard cycle of Ar^+ ion bombardment ($P_{Ar} = 7 \times 10^{-5}$ mbar) and subsequent UHV annealing (T = 870 K). In case the silver sample is introduced in the chamber after being exposed to air, it is necessary to perform three cycles with a 45 min bombardment and 20 min annealing, trying to keep the maximum pressure below 10^{-9} mbar when heating. This is usually enough to remove the oxide layer from the Ag(111) surface and obtain large terraces of few hundreds of nanometers.

A different procedure is needed in the case of van der Waals materials. In this case, the best way to obtain a clean surface is to remove the first layers of the materials with the help of an adhesive tape, apt to this use. I have developed with the help of our research engineer Hervé Cruguel a simple system to perform *in-situ* cleavage. As represented in Fig. 2.1, the system is made of a metallic rod that can move vertically thanks to a translator. A piece of UHV-compatible adhesive tape (Supplier: Agar Scientific, Oxford Instruments) is applied to one extremity of the rod, which can be approached to the sample, so the tape comes touching the sample surface. When the rod is retracted, part of the sample remains attached to the tape and the sample left on the sample holder presents a clean surface. The material which remains stuck to the tape is usually in good conditions, so it can be often removed from the tape and fixed to another sample holder.

2.3 Scanning tunneling microscopy (STM)

Scanning tunneling microscopy (STM) is a powerful experimental tool which give an apparent topography of a solid surface with atomic resolution. It was conceived and developed by Gerd Binning and Heinrich Rohrher [92], who were awarded the Nobel Prize in 1986. In this section I describe the setup I have used as well as the physical principles of STM and the procedure for processing the STM images.

2.3.1 Description of STM

In STM measurements, a direct real space image of a surface is obtained by applying a voltage difference (chosen by the user) between the sample and a metallic tip, which is scanned over the sample surface. Due to the proximity of tip and surface a tunneling current can pass from one to the other, and the value of the tunneling current is recorded as a function of the tip position. The 2D map obtained in this way constitutes the STM image. In the setup designed by Binning and Rohrher, the tip is mounted on a piezodrive, which consists of three mutually perpendicular piezoelectric transducers. Upon applying a voltage the piezo materials expand or contract, moving the tip on the surface with a sensitivity of ∽10 pm. In the *constant current* acquisition mode the tunneling current is kept at a chosen constant value I_{set}, by changing the tip-sample distance. This task is accomplished by the *feedback loop*, Fig. 2.2.a. The voltage needed to adjust the z-position of the tip is recorded for each point scanned and it is then converted in an apparent height h_{STM}. One can adjust the *feedback loop* strength by tuning its *gain*. The choice of such a constant is subjected to a trade-off: a high value means a quick response of the piezodrive, but can eventually introduce high-frequency oscillations during the scan; on the other hand a too low value makes the response too slow, possibly causing the crash of the tip on a surface obstacle. The size of the image, the number of points scanned, the gain of the *feedback loop*, the scanning speed and the time of acquisition can be set by the user. Being an highly sensitive technique, isolation from ambient and external vibration plays a fundamental role. Mechanical vibrations can put in resonance the tip-sample ensemble causing fluctuations of their reciprocal distance, resulting in periodic noise. It is important to stress out that STM does not measure a structural height: as I will show in Sec. 2.3.4, the tunneling current is directly linked to the local density of states which can vary from one zone to another of the sample. Inhomogeneities, different phases, adsorbates, impurities, even beneath the first layer, can have dissimilar local density of states, resulting in tip-sample distance other than that of the substrate, for the same value of the tunneling current.

2.3.2 STM set-up

The STM measurements have been performed at the INSP with a commercial set-up provided by Omicron, Fig. 2.3. It consists of two mechanically-decoupled UHV chambers: the preparation chamber (PC) and the analysis chamber (AC). In the PC, standard sputtering and annealing cycles can be performed using the sputter gun, a leak valve for Ar introduction and a PNB (pyrolitic boron nitride) resistance to heat up the sample, the temperature of which is measure by a thermocouple. A system for direct-current heating of the tip is used to remove the thin oxide film usually found on the surface of tips, previously exposed to

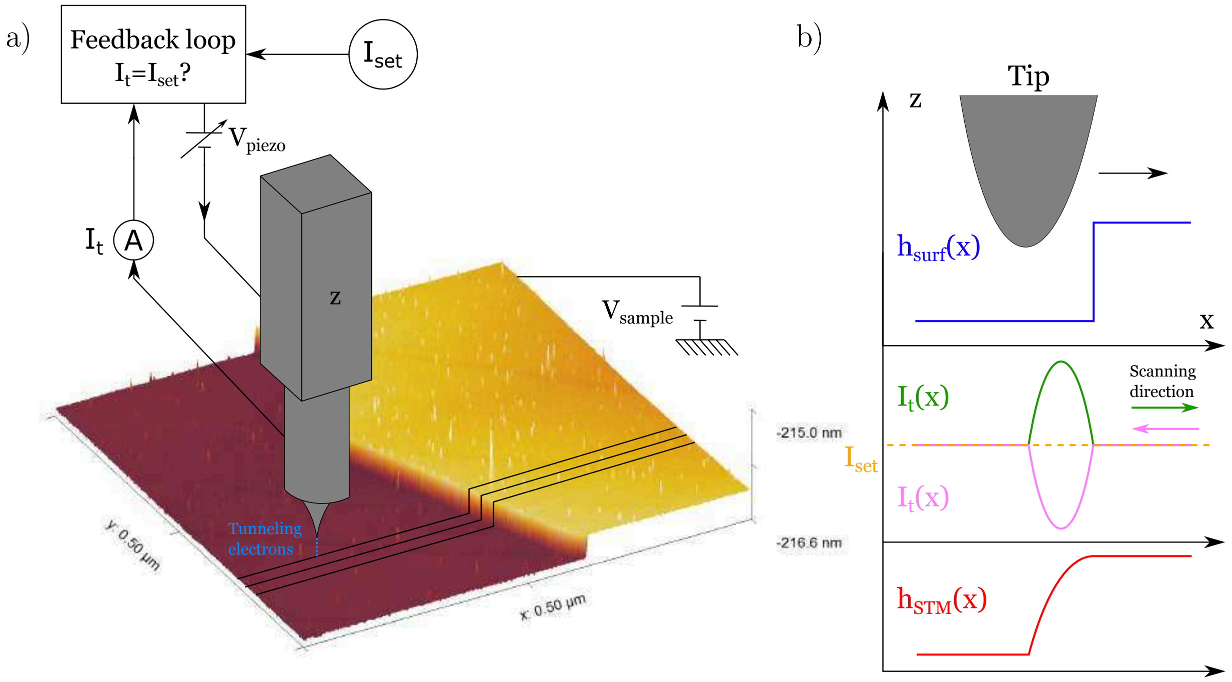

FIGURE 2.2: a) Schematic representation of the effect of the feedback loop. The tip is scanned along a line (black lines) parallel to the x-axis, one way and back; then it goes to the next line until the image is completed. For each point the voltage needed to the z-piezodrive to maintain the tip at the distance for which $I_t = I_{set}$ is recorded; I_t and I_{set} are respectively the tunneling current and the current requested by the user. b) STM images are always a convolution of the surface and the tip shape. In the drawn image, the tip encounters a step on the substrate: h_{surf} is the real height profile of the surface h_{STM} is the height measured by STM, in which the step is enlarged and smoothed by the tip shape.

air. This system consists of a Ta plate which can be translated inside the PC and put in direct contact with the tip, Fig. 2.4. Tip and Ta plate are than connected to an external power supply.

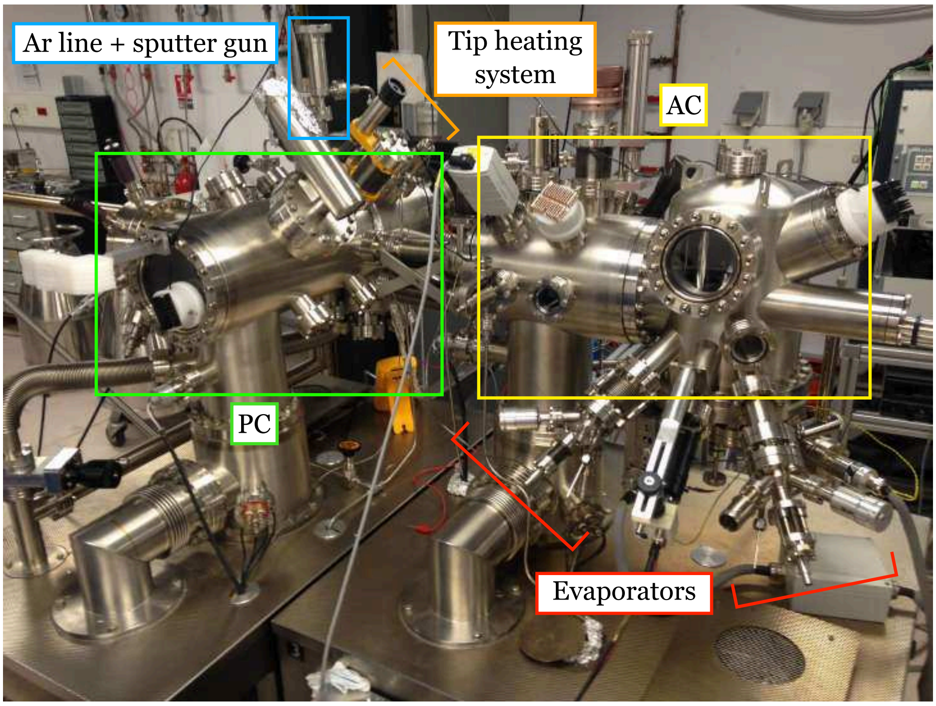

FIGURE 2.3: Photo of the STM experimental set-up.

Concerning the AC, the main system is the *Omicron VT-STM* , which can operate in a wide temperature range, i.e. 40-540 K, using a liquid N_2/He flow cryostat and a heating resistance. In order to achieve high resolution images below nanometric scale, the STM is stabilized by springs and by an *eddy current* damping system. When a non-magnetic conductive material is put in a time-varying magnetic field, eddy currents are formed in the material. These currents generate a magnetic field with an opposite direction to the applied one, inducing a force which slows down the system. The varying magnetic field is caused by the movement of the conductor in and out of a constant field. Two flanges pointing at the sample can be used for mounting evaporators. They can be oriented as shown in Fig. 2.4, with an angle of 30° between the axis of the evaporator and the sample holder plane. In this configuration, evaporation can be performed at the same time of STM scanning. This kind of real-time measurements permits to follow the evolution of the same area of the sample surface, during Si deposition, see Chapter 6.

In the next sections I give a description of the physical phenomena at the basis of STM measurements.

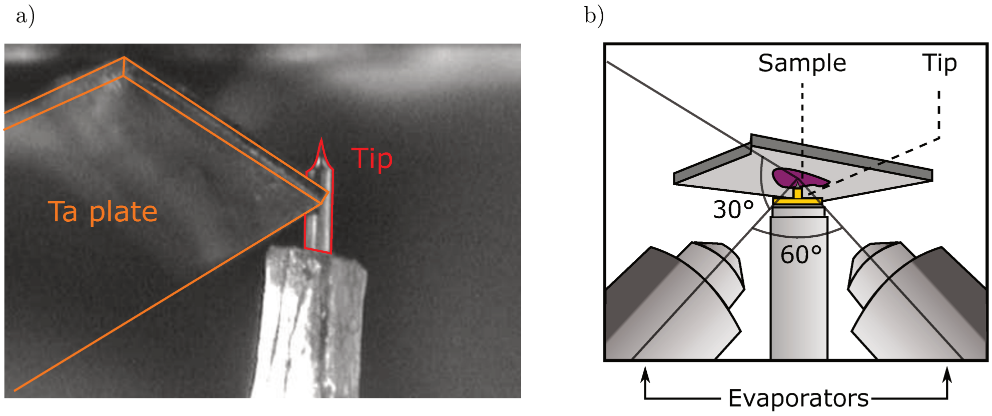

FIGURE 2.4: a) Photo of the STM tip in contact with the Ta plate for the direct-current heating procedure. b) Schematics of the orientation of the evaporators with respect to the sample and STM tip inside the AC. This geometry enables real-time measurements, i.e. scanning at the same time of evaoration.

2.3.3 Quantum Tunneling

Quantum tunneling is a phenomenon in which a particle of energy E has a non-zero probability of trespassing an energy barrier of height $U_0 > E$ and thickness a, as a consequence of the quantum-mechanical nature of particles. In this section I shall discuss the simple case of the collision of a particle against a 1-dimensional potential rectangular barrier, Fig. 2.5:

$$U(x) = \begin{cases} 0 & \text{for} \quad x < 0 \text{ and } x > a \\ U_0 & \text{for} \quad 0 < x < a \end{cases} \tag{2–1}$$

I am interested in the solutions of the time-independent Schrödinger equation $H\psi_k(x) = E\psi_k(x)$ for this potential, assuming a plane wave hitting the barrier:

$$\psi_k(x) = \begin{cases} e^{ikx} + a_k e^{-ikx} & \text{for} \quad x < 0 \\ b_k e^{ik'x} + c_k e^{-ik'x} & \text{for} \quad 0 < x < a \\ d_k e^{ikx} & \text{for} \quad x > a \end{cases} \tag{2–2}$$

where k and k' are the wavevectors:

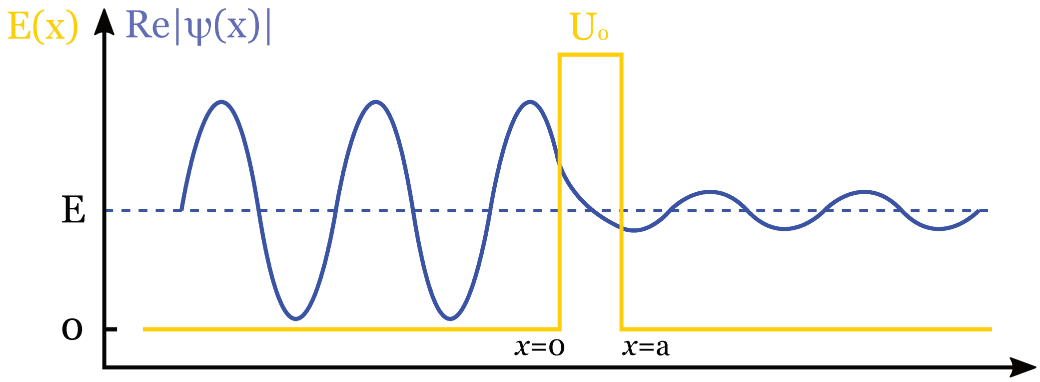

FIGURE 2.5: Representation of the real part of the wavefunction of a particle hitting a rectangular barrier of height U_0 and width a.

$$k = \frac{(2mE)^{1/2}}{\hbar}$$
$$k' = \frac{(2m(E-U_0))^{1/2}}{\hbar}$$

where m is the mass of the particles. In order to determine the coefficients a_k, b_k, c_k and d_k, the continuity equations for the wavefunctions and their first derivative at the points x=0 and x=a are imposed. The transmission coefficient, defined as the statistical fraction of electrons transmitted through the barrier, is written as:

$$T_k(E,a) = |d_k|^2 = \left[1 + (k\kappa)^2 \sinh^2(\kappa a)\right]^{-1} \tag{2–3}$$

where κ is the inverse of the *characteristic penetration length*:

$$\kappa = \sqrt{\frac{2m(U_0 - E)}{\hbar^2}} \tag{2–4}$$

The interesting case is obtained for strongly attenuating barriers, that is for $\kappa a \gg 1$, for which eq. 2–3 reduces to:

$$T_k \xrightarrow{\kappa a \gg 1} \frac{4}{(k\kappa)^2} e^{-2\kappa a} \tag{2–5}$$

In the case of STM, the tunneling of electrons occurs between a metallic tip and the sample surface, separated by vacuum acting as energetic barrier. It roughly roughly takes the value of the work function of a metal φ_m, which is of the order of 4 eV [93], corresponding to an attenuation length of ~1 Å. This means that a comparable variation of the barrier thickness changes the value of the transmission coefficient T_k of one order of magnitude, due to the exponential attenuation as a function of a. Thus, a precise measurement of the tunneling current, i.e. the number of electrons trespassing the vacuum barrier per unit time, allows the determination of the distance between tip and surface. This picture works only for a qualitative description, as it is based on the strong assumption that electrons before and after the barrier can be described by simple plane waves. In the next section a more specific approach is introduced which is widely-used in the description of tunneling current in STM.

2.3.4 Modeling of the tunneling current

The concept of tunneling introduced in the last section is now applied to the case of electrons tunneling from a metallic tip to the surface of a material through a vacuum gap.

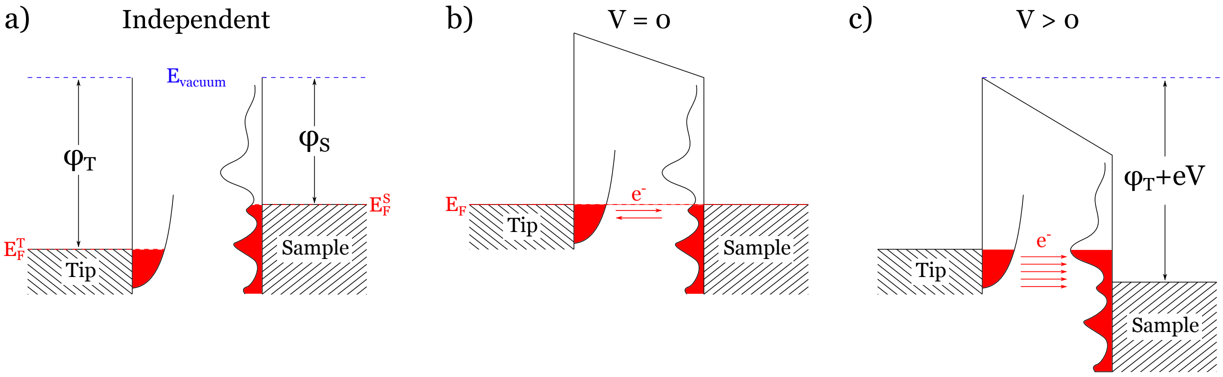

FIGURE 2.6: Tunneling process between a metallic tip and a metallic substrate. a) The Fermi levels of two independent electrodes. b) The electrodes are in tunneling condition; the alignment of the Fermi levels occurs. c) A positive voltage bias is applied to the sample inducing a shift of the Fermi levels. Electrons can flow from the tip to the sample filling and probing the empty states.

A simple picture of the tunneling process is depicted in Fig 2.6. When a metallic tip and a metallic surface are sufficiently distant, they are both characterized by their own independent workfunction (φ_T and φ_S) and Fermi energy (F_T and F_S) (Fig. 2.6.a). By approaching the tip to the sample, the two electrodes get in tunneling condition (Fig. 2.6.b). Thus, the electrons can flow from one electrode to the other, aligning in this way their Fermi levels. Eventually, it is possible to apply a bias voltage, positive in this case, between the sample and the tip, Fig. 2.6.c. This induces a shift between the Fermi levels, which allows the electrons to tunnel through the vacuum barrier, probing the empty energetic levels of the substrate. Nonetheless, STM can access the filled levels, too. This task is simply achieved by reversing the sign of the bias voltage. Note that in the case of a semiconductor substrate, the bias should be higher than the electronic gap.

Let us now introduce the formal theoretical description for this process. The model introduced by Bardeen [94] describes the tunneling as a one-particle process, in which an electron initially in a state of the electrode tip ψ_ν^T is transferred to a state of the electrode surface ψ_μ^S, and viceversa. The main approximations are that electrons do not interact during the tunneling and that no coupled sample-tip electronic states are taken into account. Moreover, *elastic tunneling* is assumed, i.e. electrons do not undergo any energy loss upon scattering with quasi particles of the surface, e.g. plasmons or phonons. Consistently, the time evolution of the Schrödinger equation containing the full potential, of both sample (S) and tip (T), can be treated in perturbation theory at first order. The calculations lead to the tip-sample probability transition for an electron, which is nothing less than the *Fermi's Golden Rule*:

$$P_{\mu\nu} = \frac{2\pi}{\hbar}\delta(E_\mu^S - E_\nu^T)\left|M_{\mu\nu}\right|^2 \tag{2–6}$$

in which $M_{\mu\nu}$ is the tunneling matrix element and E_μ^i is the eigen-energy of the electrode i (S=sample, T=tip) in the unperturbed state, i.e. sample and surface far apart. The tunneling current is proportional to $eP_{\mu\nu}$, where e is the value of the elementary charge. The elastic approximation is guaranteed by the delta-function. At this point, I shall consider the entire continuous spectrum of states for the tip and the substrate, which is achieved by summing on μ and ν and introducing the Fermi-Dirac distribution $f(E -$

$E_F) = (1 + exp[(E - E_F)/k_bT])^{-1}$, with E_F the Fermi energy. The tunneling current from tip to sample $I_{T\rightarrow S}$ and from sample to tip $I_{S\rightarrow T}$ can be written as:

$$\begin{aligned} I_{T\rightarrow S} &= \frac{4\pi e}{\hbar}\sum_{\mu\nu} f(E_\nu^T - E_F^T)\left[1 - f(E_\mu^S - E_F^S)\right]|M_{\mu\nu}|^2\delta(E_\nu^T - E_\mu^S - eV) \\ I_{S\rightarrow T} &= \frac{4\pi e}{\hbar}\sum_{\mu\nu} f(E_\mu^S - E_F^S)\left[1 - f(E_\nu^T - E_F^T)\right]|M_{\mu\nu}|^2\delta(E_\nu^T - E_\mu^S - eV) \end{aligned} \tag{2–7}$$

in which V is the bias voltage between tip and sample and the factor 2 accounts for electrons with opposite spin. The difference between the two currents give the net total tunneling current:

$$I = \frac{4\pi e}{\hbar}\sum_{\mu\nu}\left[f(E_\mu^S - E_F^S) - f(E_\nu^T - E_F^T)\right]|M_{\mu\nu}|^2\delta(E_\nu^T - E_\mu^S - eV) \tag{2–8}$$

The finite summation over the discrete states can be replaced by an integral over energies using the electronic density of states $n(E)$: $\sum_\mu \rightarrow \int n(E)dE$. It can be show that in the low-temperature limit Eq. 2–8 reduces to:

$$I = \frac{4\pi e}{\hbar}\int_0^{eV} n^T(E_F^T - eV + \epsilon)n^S(E_F^S + \epsilon)|M|^2 d\epsilon \tag{2–9}$$

and for small bias voltages:

$$I = \frac{4\pi e^2}{\hbar} V n^T(E_F^T)n^S(E_F^S)|M|^2 \tag{2–10}$$

where n^T and n^S are the density of states of the substrate and of the tip. Let us now discuss the tunneling matrix element $M_{\mu\nu}$. Its expression can be reduced to a surface integral only depending on the unperturbed wavefunctions of the two electrodes evaluated over the tip surface Σ. First of all, we can rearrange the unperturbed Schrödinger equation for the tip as follows:

$$\left\langle \psi_\nu^T \right| U_T = \left\langle \psi_\nu^T \right| \left(E_\nu^T + \frac{\hbar^2}{2m}\nabla^2\right) \tag{2–11}$$

and then use this expression in the definition of the tunneling matrix:

$$M_{\mu\nu} = \left\langle \psi_\nu^T \right| U_T \left|\psi_\mu^S\right\rangle = \int_{\Omega_T} \psi_\mu^S \left(E_\nu^T + \frac{\hbar^2}{2m}\nabla^2\right)\psi_\nu^{T*} d\mathbf{r} \tag{2–12}$$

being Ω_T the volume of the tip. Taking into account the elastic tunneling condition, i.e. $E_\nu^T = E_\mu^S$, and that the potential of the sample U_S has no effect inside the volume of the tip, it is possible to obtain, integrating on the tip-sample direction:

$$M_{\mu\nu} = \frac{\hbar^2}{2m}\int_\Sigma \left[\psi_\mu^S \nabla \psi_\nu^{T*} - \psi_\nu^{T*}\nabla\psi_\mu^S\right] d\mathbf{S} \tag{2–13}$$

It is worth making few considerations. Firstly, the two wavefunctions appearing in the expression are relative to the unperturbed electrodes. The potential barrier does not appear explicitly: only the value of the wavefunctions at the surface Σ is needed. Furthermore, the formula is symmetric with respect to the two electrodes, a property known as *reciprocity principle* of STM.

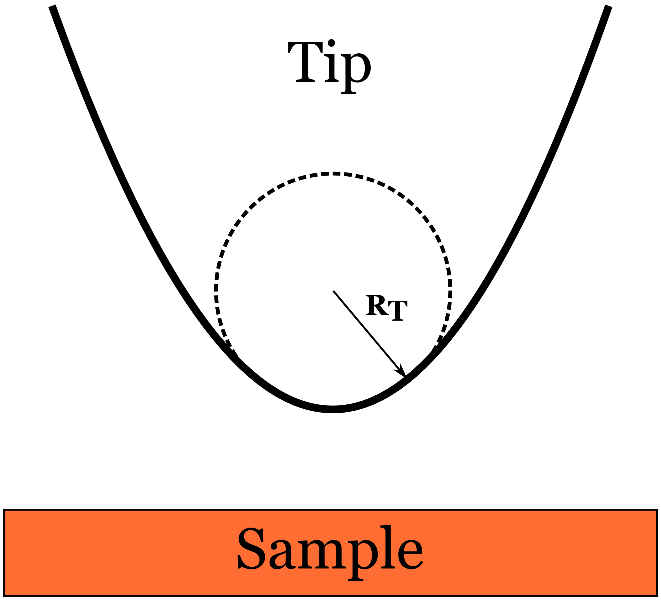

FIGURE 2.7: Schematic representation of the tip in *Tersoff-Haman model*. Locally it can be represented by a sphere of radius R_T, and it is described by a s-orbital wavefuntcion, thus neglecting angular dependence.

Eventually Bardeen's approach allows an estimation of the tunneling current given that the electronic structure of tip and sample are known. Although this requirement is not too constraining in the case of the sample, it gets much more challenging considering the tip, as its structure cannot be easily determined with precision. This obstacle is the driving argument behind the Tersoff-Haman (TH) model [95]. In fact, the two researchers proposed a simple model for the tip, in order to neglect, in first approximation, the contribution of its shape. Thus, in the TH model the STM current carries information only about the sample, and not the joint tip-surface system. The STM tip is modeled as a locally spherical tip with radius R_T (Fig. 2.7) described by a single s-orbital wavefunction. Assuming for simplicity the same workfunction φ for both sample and tip, both wavefunctions ψ^S_μ and ψ^T_ν satisfy the following Schrödinger equation in vacuum:

$$-\frac{\hbar^2}{2m}\nabla^2\psi = -\varphi\psi \qquad \mathit{or} \qquad \nabla^2\psi = \kappa^2\psi \tag{2–14}$$

where $\kappa = (2m\varphi)^{-1/2}/\hbar$ is the minimum inverse decay length in vacuum. Eq. 2–14 can be solved with modified Bessel functions, which substituted in Eq. 2–13 give, after some manipulations, the tunneling matrix element in the TH model:

$$M_{\mu\nu}(\boldsymbol{R}_T) = -\frac{2\pi C\hbar^2}{\kappa m}\psi^S_\mu(\boldsymbol{R}_T) \tag{2–15}$$

where C is a normalization constant. By taking Eq. 2–8 and substituting in it the expression for $M_{\mu\nu}$, I can write:

$$I(\boldsymbol{R}_T, V) = \frac{16\pi^3 C^2\hbar^3 e}{\kappa^2 m^2} n^T \int_0^{eV} n^S(\boldsymbol{R}_T, E^S_F + \epsilon)d\epsilon \tag{2–16}$$

where the density of state of the tip n_T is a constant, consistently with the assumption of the TH model. The integral includes all the states of the sample at the tip location between the Fermi energy and the Fermi energy shifted by the bias voltage: the tunneling current is proportional to the integrated *local density of states* of the sample surface. Finally, for small bias voltages:

$$I(\boldsymbol{R}_T, V) \approx \frac{16\pi^3 C^2 \hbar^3 e^2}{\kappa^2 m^2} V n^T n^S(\boldsymbol{R}_T, E_F^S) \tag{2–17}$$

This simple result relies on the basic assumption that the *s*-wave tip wavefunction is the only one playing a relevant role in the description of the tunneling and all the other tip wavefunctions can be neglected.

Thus, the TH model associate the current between a tip and a sample in STM experiments directly with the local density of the states of the sample. Despite relying on a quite simplistic approximation regarding the tip, the simulated STM images obtained by applying the TH model can nicely reproduce STM images in some cases (Chapter 4 and 6).

2.3.5 Image analysis

STM images can show several artifacts which can hamper a good analysis of the data. In order to tackle this problem I have used the Gwyddion software [96], which includes some built-in functions for the treatment of STM images. I have also employed a certain number of tools which have been developed in the team PHYSUF of INSP by Geoffroy Prévot and Axel Wilson [97, 98]. So as inferred from section 2.3.4, when performing STM in *constant-current mode*, the acquired image represents the bidimensional projection of a surface with a constant electronic density (*isosurface*), convoluted with the tip shape.

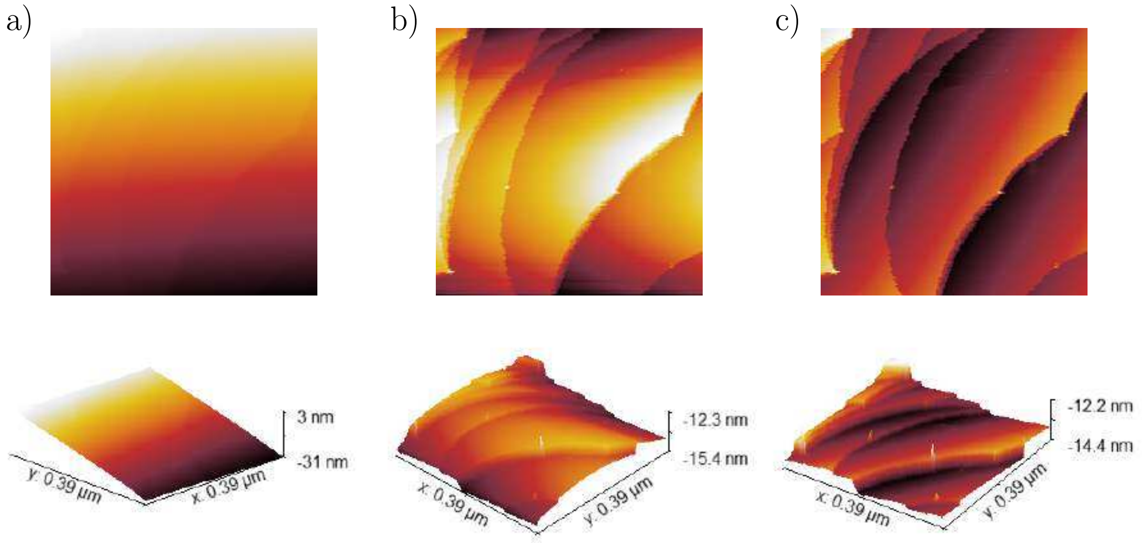

FIGURE 2.8: Standard correction procedure for STM images. a) Raw data: the only visible feature is the important inclination of the surface plane. The same image is shown after the subtraction of the plane (b) and after the application of the median filter (c).

For a reasonably good quality tip, i.e. atomically terminated, its "diameter" affects mainly the measurement of the corrugation the surface, for which a quantitative analysis is difficult to give. The response of the piezodrives plays a fundamental role. First of all, their deformation can be considered linear only for relatively small applied voltages, which is the case for images up to 100 × 100 nm^2. Another artifact due to the piezoelectric devices is the *creep*. It consists in a delay of the response following an abrupt change in the applied voltage bias. The effect is particularly important at the beginning of the scanning and after large displacements on the sample surface. A simple solution is just to wait a few seconds after high voltage changes. Another very common problem is the disorientation of the surface with respect to the z-direction. This disorientation, if not properly treated, is usually so important that it makes disappear, in perspective, all the other features of the surface (Fig. 2.8.a). It is straightforward to remove the plane identifying the z-disorientation. Eventually, the termination of the tip can change during the scanning. This can induce a sudden change in tip position, as it tries to recover the right value of the tunneling current. The tip can be modified upon the reorganization of the atoms at its extremity, or after the adsorption of molecules and atoms. This modification results in jumps of the value of z between two successive line scans.

The *median filter* adjusts the z-position of the $n+1$ line minimizing the quantity $\sum_i (z_{i,n+1} - z_{i,n})^2$, in which a component ξ is introduced in order to have $\sum_i \frac{\partial}{\partial \xi}(z_{i,n+1} + \xi - z_{i,n})^2$=0. The subtraction of the plane associated with the disorientation and the median filter have been applied as standard corrections to all the STM images analyzed; one example is given in Fig. 2.8. A useful filter which has been developed in our team is the *modulo filter*. The images are corrected so that the different atomic terraces of the bare substrate (separated by integer multiples of one step height) are all placed at the same height. As a result, islands forming after Si evaporation with the same thickness appear at the same z value, regardless of the Ag terrace where they have grown, as shown in Fig. 2.9.

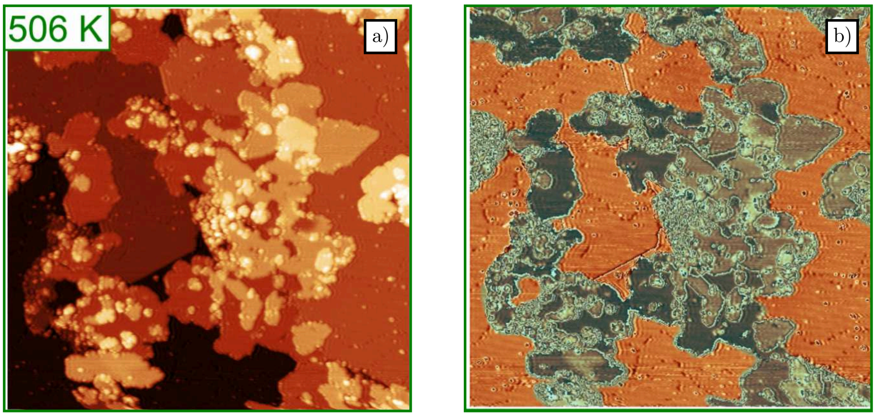

FIGURE 2.9: a) STM image of the Ag(111) surface after the evaporation of 2.2 ML of Si at 506 K. b) Apparent height of the surface modulo the Ag step height. Note that all Ag terraces have now the same height (color).

Another home-made tool can compensate for in-plane distortion. Let us consider two images, one acquired by scanning in the positive y direction and the other in the negative y direction: these two images are not necessarily identical because of thermal and piezoelectrics drift. However, by applying an opposite distortion to the two images one can obtain two matching figures which correspond to the unaltered surface appearance. Indeed, this procedure is correct only in the case of linear drift.

2.3.6 STM tips

In order to obtain high-resolution STM images it is of crucial importance to have atomically-sharp tips. In fact the lateral resolution is affected by the radius of the tip [95]. During my PhD, I have fabricated STM tips by chemical etching. A piece of W wire (purity 99.95%) is half dipped in a 2 molar solution of NaOH. An external bias voltage between the tip and the solution thanks to a half plunged metallic electrode. The induced current causes the dissolution of the wire. The etching takes place at the air-solution interface. The meniscus which forms around the wire when it is dipped plays a key role: the etching is slower at its top and becomes more important in the part right below. The electrolyte solution erodes the wire as depicted in Fig. 2.10, until the section of the wire at the interface is thin enough, so that the weight of the lower end causes the drop-off, i.e. the detachment of the etched part which leaves behind a sharp tip. At the end of the chemical attack, the reaction must be arrested by plunging the tip in water and ethanol. The process is monitored through an oscilloscope measuring the voltage between the tip and the electrode, in order to identify the exact moment of the drop-off. Moreover, the voltage supply can be set with a cut-off current, below which the bias is put to zero. In fact, when the drop-off occurs the resistance at the tip-solution interface increases steeply, causing an abrupt drop of the current. By setting the right value for the cut-off current, the chemical reaction can be promptly stopped. Tungsten is widely employed for the fabrication of STM tips: the apex left after the drop-off is very sharp and a mild chemical as a 2 molar solution of NaOH is enough for the etching. The main drawback is its poor resistance to oxidation so it gets quickly contaminated. In the STM set-up described in section 2.3.2, a system for flashing the tip is installed in the preparation chamber. A thin Ta plate can be approached and put in electrical contact to the tip, once this has been inserted in the UHV chamber. A current in the range 3-6 A heats up the tip; at a temperature of 1000 °C the oxide layer (WO_3) is desorbed according to the following reaction [99]:

$$2WO_3 + W \rightarrow 3WO_2 \uparrow \tag{2–18}$$

Another advantage of the annealing process is that it can heal defects in the crystallographic structure of the tip [99]. Nonetheless, we have remarked that heating for too long can result in a blunting of the tip, hindering the success of the experiment. Usually, three flashes at 6 A of few seconds with pressure in the range of 10^{-9} mbar are enough to get rid of the oxide layer.

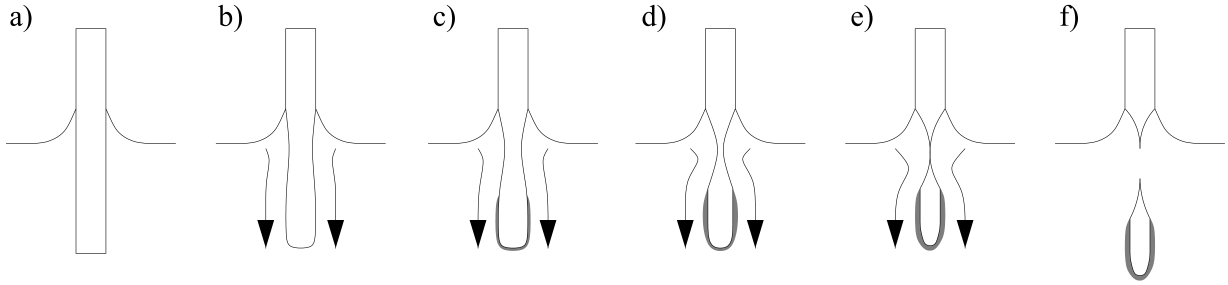

FIGURE 2.10: Illustration of the *drop-off process*. (a) Formation of the meniscus, (b)-(e) appearance of the necking phenomenon at the meniscus, (f) the drop-off. Reproduced from ref. [99].

2.4 X-ray diffraction

In this section I summarize the basic principle of X-ray diffraction, underlying the advantages with respect to other techniques and its implementation in the grazing configuration to enhance surface sensitivity. I will also describe the procedures for the analysis of grazing incidence X-ray diffraction (GIXD) data acquired with a point or 2D detector.

2.4.1 Basic principles of X-ray diffraction (XRD)

When an X-ray beam hits a material either it is scattered, which is the case of *elastic* and *incoherent scattering* respectively, or it is absorbed exciting an atom which can decay in the ground-state through several processes. The primary beam is an electromagnetic wave, the electric field component of which exerts a force on the electrons of the target atom accelerating them. It is known that an accelerated (or decelerated) charge produces an electromagnetic radiation. In the case of a crystalline sample the radiation is re-emitted by the electrons of each atom gives rise to a non-zero interference only along certain directions. This phenomenon is known as *diffraction*. Due to the weak cross section of X radiation, it is usually possible to adopt the *kinematic approximation*: the intensity of the diffracted beam is negligible with respect to the one of the incident beam. Consequently, the eventual *multiple scattering* can be neglected.

I will now introduce, in sequence, the amplitude diffracted by an electron, by an atom and by a crystal [100]. This amplitude is linked to the intensity of the diffraction peak usually measured in XRD. Eventually, a description for the case of diffraction from surfaces is given, along with a description of the related advantages of grazing incidence geometry.

2.4.1.1 Scattering amplitude and structure factors

The scattering of an electromagnetic wave by a free electron is given by the well-known *Thompson formula*. In the reference system employed, the position of the observer and of the electron are identified by $\boldsymbol{R}$ and $\boldsymbol{r}$, respectively. If E_0 is the amplitude of the incoming wave $E_0 e^{-i\boldsymbol{k}_i\boldsymbol{r}}$, with wavevector $\boldsymbol{k}_i$, the observed scattered field $E_e e^{-i\boldsymbol{k}_f\boldsymbol{r}}$ with wavevector $\boldsymbol{k}_f$, has an amplitude equal to:

$$E_e = E_0 \frac{e^2}{mc^2|\boldsymbol{R}|} P^{1/2} \tag{2–19}$$

where c is the speed of light in vacuum, m and e are the electron mass and charge, respectively. P is called the *polarization* and it accounts for the dependence of E_e from the polarization of the incoming wave:

$$P = \begin{cases} 1 & \text{if } E_0 \text{ is normal to the scattering plane} \\ cos^2 2\theta & \text{if } E_0 \text{ belongs to the scattering plane} \end{cases} \tag{2–20}$$

The scattering plane is defined by the $\boldsymbol{k}_i$ and $\boldsymbol{k}_f$ vectors; 2θ is the angle between them. Eq. 2–19 can be easily generalized to the case of an atom with Z scattering electrons. These are distributed around the nucleus with a density $\rho_a(\boldsymbol{r})$, thus:

$$E_a = \int \boldsymbol{E}_e \rho_a(\boldsymbol{r}) d\boldsymbol{r}' = E_0 \frac{e^2}{mc^2|\boldsymbol{R}|} P^{1/2} \int \rho_a(\boldsymbol{r}) e^{i\boldsymbol{q}\boldsymbol{r}} d\boldsymbol{r}' \tag{2–21}$$

in which $\boldsymbol{q} = \boldsymbol{k}_f - \boldsymbol{k}_i$ is the *momentum transfer* and I can define a new quantity, i.e. the *form factor* f_0:

$$f_0(\boldsymbol{q}) = \int \rho_a(\boldsymbol{r}) e^{i\boldsymbol{qr}} d\boldsymbol{r}' \tag{2–22}$$

If $\boldsymbol{q} = 0$ all the electrons scatter in phase and $f_0(\boldsymbol{q} = 0) = Z$; when the momentum transfer is finite, the value of the form factor decreases, due to the out-of-phase scattering of the electrons in the atom.

For energies close to the absorption edges of the atoms in the material, resonance effects must be taken into account. This is achieved by introducing dispersion corrections f' and f'' (imaginary) in the expression for the form factor:

$$f = f_0 + f' + f'' \tag{2–23}$$

As we have always worked far from the absorption edges of the atomic species probed by X-rays, there is no need to dwell into further details.

Let us consider eventually the case of atoms periodically arranged in 3D crystal lattice. The position of each atom is indicated as:

$$\boldsymbol{R}_{j,j_1,j_2,j_3} = j_1\boldsymbol{a}_1 + j_2\boldsymbol{a}_2 + j_3\boldsymbol{a}_3 + \boldsymbol{r}_j \tag{2–24}$$

$\boldsymbol{a}_1$, $\boldsymbol{a}_2$ and $\boldsymbol{a}_3$ are the lattice vectors and $\boldsymbol{r}_j$ represents the position of the atom inside the unit cell. The amplitude of the scattered wave now writes:

$$E_c = E_0 \frac{e^2}{mc^2|\boldsymbol{R}|} P^{1/2} \sum_{j,j_1,j_2,j_3} f_j(q) e^{i\boldsymbol{q}\boldsymbol{R}_{j,j_1,j_2,j_3}} = E_0 \frac{e^2}{mc^2|\boldsymbol{R}|} P^{1/2} F(\boldsymbol{q}) \sum_{j_{1,2,3}=0}^{N_{1,2,3}-1} e^{i\boldsymbol{q}(j_1\boldsymbol{a}_1 + j_2\boldsymbol{a}_2 + j_3\boldsymbol{a}_3)} \tag{2–25}$$

where $N_{1,2,3} - 1$ are the extensions of the crystal in the three directions of the unit-cell vectors and the new quantity $F(\boldsymbol{q})$ is defined as the *structure factor* of the crystal, obtained by summing the contribution to the scattered wave by each single atom within the unit cell of the lattice:

$$F(\boldsymbol{q}) = \sum_j f_j(q) e^{i\boldsymbol{q}\boldsymbol{r}_j} \tag{2–26}$$

The equations derived until now relies on the assumption that atoms are clamped in fixed positions. However, for finite temperature the atoms in a crystal vibrate due to thermal excitation around their equilibrium positions. Thus, the expression for the atomic positions at any instant should include a term indicating the instantaneous displacement due to thermal vibration, $\boldsymbol{R}'_{jj_1j_2j_3} = \boldsymbol{R}_{jj_1j_2j_3} + \boldsymbol{s}_{jj_1j_2j_3}$. Taking this into account leads to a correction for the structure factor (Eq. 2–26), known as *Debye-Waller factor* [101]:

$$F(\boldsymbol{q}) = \sum_j f_j(q) e^{-B_j(q/4\pi)^2} e^{i\boldsymbol{q}\boldsymbol{r}_j} \tag{2–27}$$

where B_j is called the *B-factor* and it is proportional to the 3D mean square displacement of atom j in the case of isotropic vibrations. For the systems studied in the present work, I have used two Debye-Weller factors for a surface, accounting for in-plane (xy) and out-of-plane (z) displacements. Due to the hexagonal symmetry of systems, there is no need of a third factor as $B_x = B_y$.

Indeed, in experiments one measures the diffracted intensity, an expression of which can be obtained by squaring the amplitude given in Eq. 2–25:

$$I(\boldsymbol{q}) = |E_0|^2 \left(\frac{e^2}{mc^2|\boldsymbol{R}|}\right)^2 P|F(\boldsymbol{q})|^2 \frac{\sin^2\left(\frac{1}{2}N_1\boldsymbol{q}\ \boldsymbol{a_1}\right)}{\sin^2\left(\frac{1}{2}\boldsymbol{q}\ \boldsymbol{a_1}\right)} \frac{\sin^2\left(\frac{1}{2}N_2\boldsymbol{q}\ \boldsymbol{a_2}\right)}{\sin^2\left(\frac{1}{2}\boldsymbol{q}\ \boldsymbol{a_2}\right)} \frac{\sin^2\left(\frac{1}{2}N_3\boldsymbol{q}\ \boldsymbol{a_3}\right)}{\sin^2\left(\frac{1}{2}\boldsymbol{q}\ \boldsymbol{a_3}\right)} \tag{2–28}$$

where N_1, N_2 and N_3 are the number of unit cells in the crystal, along the three crystal axes. In Eq. 2–28 it is implicitly given a formulation of the *Laue conditions*. In fact, the intensity peaks if the following conditions are fulfilled:

$$\boldsymbol{q}\cdot\boldsymbol{a}_1 = 2\pi h \qquad \boldsymbol{q}\cdot\boldsymbol{a}_2 = 2\pi k \qquad \boldsymbol{q}\cdot\boldsymbol{a}_3 = 2\pi l \tag{2–29}$$

where the integer numbers h, k, l are known as *Miller indexes* and, consequently, $\boldsymbol{q}$ is a reciprocal lattice vector to which a *Bragg spot* is assigned. The expression for the intensity of the peak reduces to:

$$I_{hkl}^{peak} = |E_0|^2 \left(\frac{e^2}{mc^2|\boldsymbol{R}|}\right)^2 P|F_{hkl}|^2 N_1^2 N_2^2 N_3^2 \tag{2–30}$$

The diffraction pattern associated with a bulk crystal consists of diffraction spots reflecting the 3D symmetries of the crystal (Fig. 2.11.a).

In the case of a 2D lattice, the periodicity of the crystal in one direction is dropped, so that the atomic lattice is described by only two basis vectors: $\boldsymbol{R}_{jj_1j_2} = j_1\boldsymbol{a}_1 + j_2\boldsymbol{a}_2 + \boldsymbol{r}_j$, assumed to be for simplicity in the plane of the surface. Note that $\boldsymbol{r}_j$ refers to the atomic positions within the surface unit cell and can have indeed non-zero component normal to the surface. The third Laue condition is relaxed, so that q_z, the momentum transfer normal to the surface, becomes a continuous variable. Thus, the diffraction pattern consists now of a 2D lattice of *Bragg rods*. The intensity now writes as:

$$I_{hk}^{peak}(l) = |E_0|^2 \left(\frac{e^2}{mc^2|\boldsymbol{R}|}\right)^2 P|F_{hk}(l)|^2 N_1^2 N_2^2 \tag{2–31}$$

The information about the x, y, z positions are mixed unless l=0 or h=k=0, from which it is possible to obtain the in-plane (x, y) or out-of-plane (z) components.

Eventually, I discuss the case of a semi-infinite crystal, i.e. a truncated 3D crystal in which the surface has the same in-plane periodicity of the bulk. The diffraction rods are no more flats as in the previous case, but their intensity is modulated in proximity of the reciprocal space positions associated with Bragg diffraction spots from the bulk Fig. 2.11.c. In first approximation, the intensity writes:

$$I_{hk}^{peak}(l) = |E_0|^2 \left(\frac{e^2}{mc^2|\boldsymbol{R}|}\right)^2 P|F_{hk}(l)|^2 N_1^2 N_2^2 \frac{1}{2sin^2(\pi l)} \tag{2–32}$$

Eq. 2–32 reduces to Eq. 2–31 in the positions far from Bragg peaks.

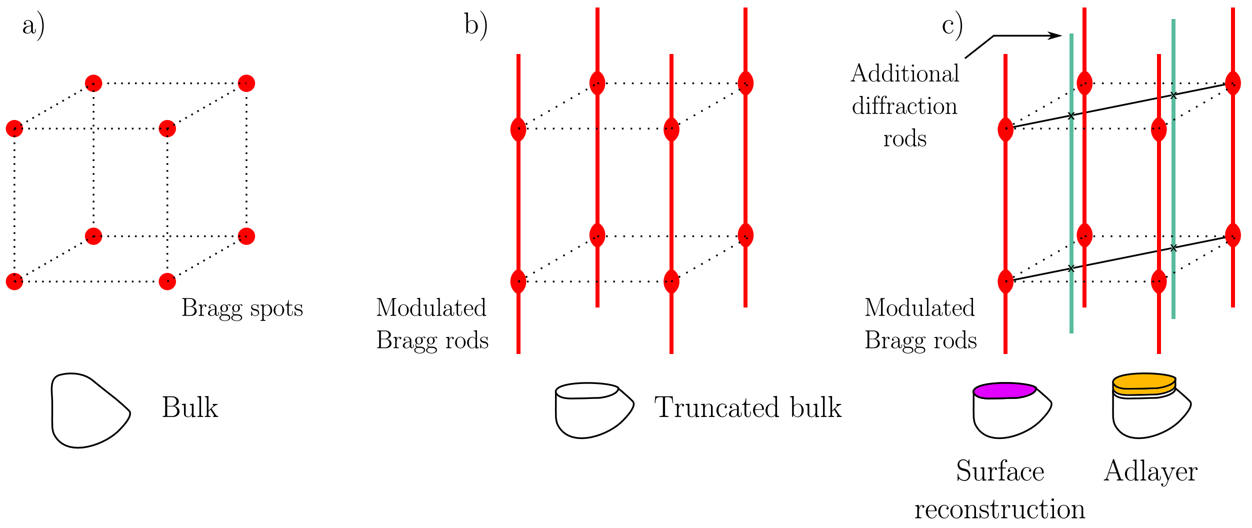

FIGURE 2.11: Diffraction pattern for a bulk cubic crystal (a), the relative truncated form in which we lack the periodicity along the direction normal to the surface (b), and the case, in which there is a surface reconstruction or adsorbed layer with different periodicity from that of the bulk (c).

In some case the surface of a sample reconstructs in order to minimize its surface energy, showing a periodicity different from that expected for the truncated bulk. This results in the appearance of diffraction rods in the reciprocal space associated with the new periodicity of the surface reconstruction (Fig. 2.11.c). The same thing applies to the case of an adsorbed layer with surface symmetry and/or periodicity not matching those of the substrate.

2.4.1.2 Grazing incidence X-ray diffraction

Grazing incidence X-ray diffraction is a powerful technique used to measure the intensities of the diffraction rods from a surface. In the last section I have shown that by measuring the intensity of diffracted spots and rods it is possible to obtain information about the atomic positions inside the unit cell of a crystal surface. This information is embedded in the expression of the structure factor directly related to the intensity of the diffraction rods (Eq. 2–31 adn2–32). Experimentally, it is possible to obtain surface sensitivity and high signal rate by:

- employing grazing incidence angles;
- using intense X-ray sources, such as the one supplied by synchrotron facilities;

The first point relies on the fact that when X-rays hit the interface between two media at an incidence angle smaller than a critical value α_c, the incoming beam is *totally reflected*. The *refractive index* of a material is defined as:

$$n = 1 - \delta - i\beta \tag{2–33}$$

where δ is the polarizability coefficient and β is the absorption coefficient; the former is of the order of 10^{-5}, while the latter 10^{-6}. As the real part of the optic index in the X-ray domain is smaller than one, total reflection can occur. This phenomenon is accompanied by an *evanescent wave* propagating along the interface between the two materials and is exponentially damped in the low refractive index material.

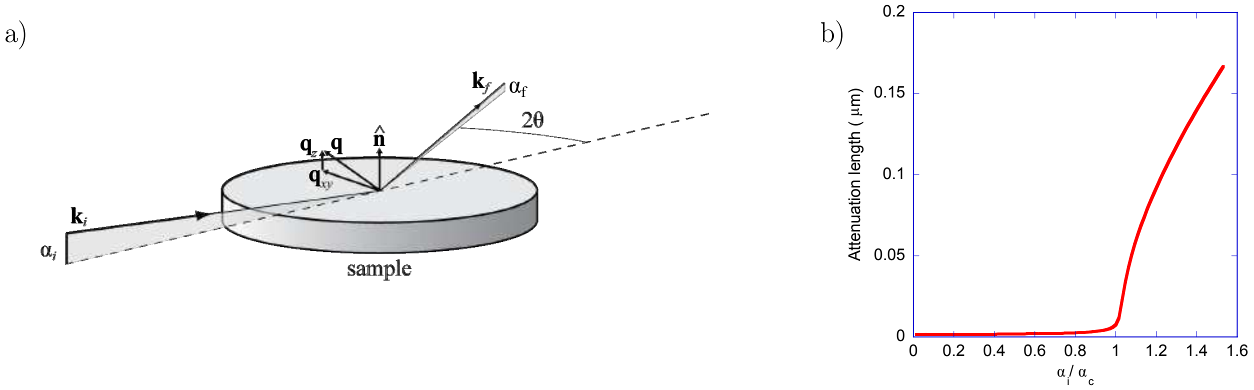

FIGURE 2.12: a) Grazing incidence geometry: if $\alpha_i < \alpha_c$, total reflection of the incident beam occurs, enhancing surface sensitivity and reducing penetration depth of the X-rays (b).

Consequently, the signal from the surface is enhanced and the penetration of X-Rays is decreased. A standard grazing incidence geometry is shown in Fig. 2.12.a. The X-ray beam enters (exits) the surface at angle α_i (α_f); $\boldsymbol{q}$ is the momentum transfer and $\boldsymbol{k}_i$ ($\boldsymbol{k}_f$) are the wavevectors of the incident (reflected) beam. In Fig. 2.12.b, I show the variation of the attenuation length of X-rays with energy equal to 18.46 keV in Ag, as a function of the incident angle of the beam. Below the critical angle the attenuation length is small and it rapidly increases just above $\alpha_i = \alpha_c$.

2.4.2 Data analysis

The determination of a crystal structure consists in the identification of both the size and shape of the unit cell and the exact atomic positions within. The structure factors contain information on the atomic positions inside the crystal unit-cell (section 2.4.1.1). These quantities can be accurately determined from the measured integrated intensities of diffracted spots and rods, obtained by grazing incidence X-ray diffraction (GIXD). During my PhD I performed GIXD experiments employing a point detector or a 2D detector.

Fig. 2.13 shows the Z-axis geometry of the diffractometer used for the experiments: α is the incidence angle, δ and γ define the detector position and ω represents the rotation of the sample around the normal to its surface.

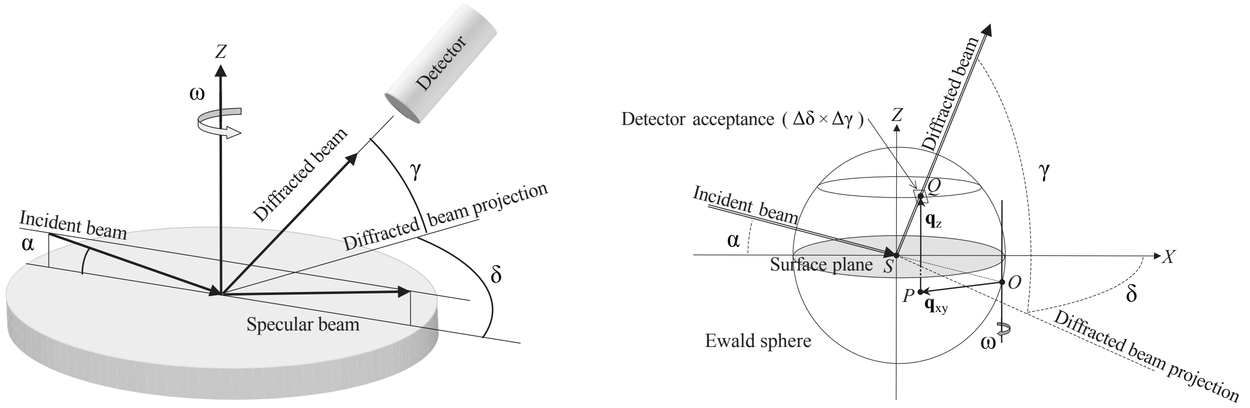

FIGURE 2.13: Schematic representation of the Z-axis diffractometer geometry and relative Ewald sphere construction [102].

2.4.2.1 Point detector

A point detector is characterized by the *acceptance*, i.e. the solid angle $\Delta\delta\Delta\gamma$ in which photons are collected at a certain time. The intensity is measured by rotating the sample around the normal to its surface, keeping the detector at fixed position. This measurement is known as *angular rocking scan* (ARS) or simply *ω-scan*. The detector acceptance $\Delta\delta$ must be larger than the width of the diffraction rod in order to collect all the diffracted photons. During the ω-scan the points of a certain rod or spot are progressively brought into diffraction condition. The measurement of diffraction rod consists in our case in a series of ω-scans at different values of q_z, increasing the exit angle γ (out-of-plane angle), while keeping fixed the values of q_{xy} and α.

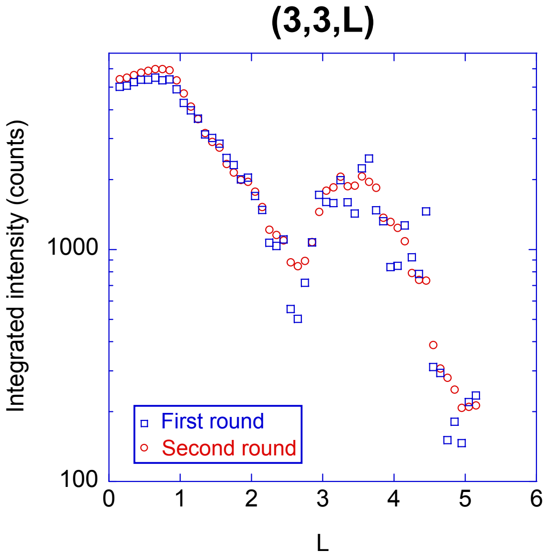

FIGURE 2.14: Integrated intensities along the (3,3,L) reconstruction rod of the (4 × 4) reconstruction of silicene/Ag(111). The log scale helps underline the better accuracy obtained in the second step of the fit (red circles), compared to the results of the first one (blue squares).

I present, for example, the analysis of the (4 × 4) reconstruction of Si on Ag(111), the results of which are thoroughly discussed in chapter 4. In this experiment, a monolayer of Si is deposited onto the Ag(111) with a substrate temperature of 570 K. The diffracted intensity have been measured along diffraction rods associated with the (4 × 4) reconstruction: several ω-scans have been performed at consecutive values of L, at the same in-plane (H,K) position. In order to accurately evaluate the integrated intensity along the rod for each ω-scan I have performed a *two-step fitting process*. The scans are fitted with a homemade software written by Geoffroy Prévot. In a first step the peaks are fitted with a pseudo-Voigt function, which is a sum of a Lorentzian and Gaussian profile, without imposing any constraint. The resulting integrated intensities are shown in Fig. 2.14 as blue squares.

Besides integrated intensities, the software provides also the peak positions and the full width at half maximum (FWHM). From the first fitting round it is possible to deduce the trend for these quantity which can then be imposed in the second round, obtaining more accurate values for the integrated intensities of the ω-scan. Firstly, the position of the fitted peaks are plotted as a function of the central value of the ω-scan, Fig. 2.15.a. A new linear fit of the curve is performed so to extract the value of the position for the second step of the fit. In fact, the peaks are expected to lie on a straight line which represents the diffraction rod. The curve of the FWHMs at low values of L, i.e. small exit angle, is interpolated with a quadratic function, Fig. 2.15.b, while after $L = 0.6$ a simple linear function is used, Fig. 2.15.c. Eventually, the position of the peaks and the FWHM extracted by the first step are imposed on the second one, the results of which are represented by red dots in Fig. 2.14. This fitting procedure reduces the uncertainty associated with the measurements. From the intensities obtained in this way, the experimental structure factors are calculated, see Sec. 2.4.2.3. These values are then compared to the theoretical structure factors obtained for a certain model. The χ^2-test is used to validate or reject the proposed model.

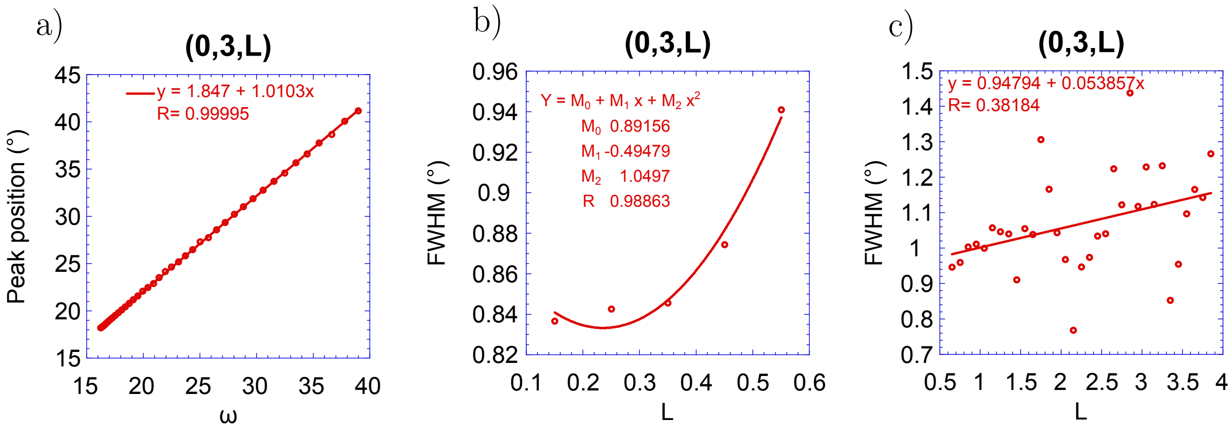

FIGURE 2.15: a) Position of the peaks as a function of the center of the ω-scans along the rod (0,3,L). b-c) Evolution of the FWHM of the fitted peaks as a function of L for the rod (0,3,L). The equations for the fit and the resulting fitting parameters are shown in each figure.

2.4.2.2 2D detector

The main difference between a 2D detector and a point detector is the extent of spatial information obtained in a single acquisition. This is of course greater for the 2D detector and it is a direct consequence of its larger acceptance.

By employing the 2D detector it is possible, in principle, to measure the intensity around a particular reflection in a single acquisition, with no need of performing an ω-scan. Indeed, this greatly shortens the acquisition time. However, these *stationary scans* can be performed only under certain conditions [103]:

- the in-plane projection of the acceptance of the detector must be sufficiently large to fully include the cross section of the rod and some area around it, which is fundamental for a correct estimation of the background contribution;
- the value of the structure factor $|F_{hkl}|$ must be constant over the intersected Δl range;

This two conditions are unlikely satisfied during a scan at small l values (i.e. small exit angles): in fact in this case the detector plane is almost perpendicular to the surface plane (hk-plane in the reciprocal space), i.e. parallel to the diffraction rod. Thus, the section of the rod is not entirely projected on the detector and at the same time a large Δl range is acquired, in which $|F_{hkl}|$ usually cannot be considered constant. Thus, in this situation an ω-scan is needed.

Another consequence of the large acceptance of the 2D detector is that, most likely, some areas of the reciprocal space are measured several times for different positions of the detector. This is particularly relevant when performing *reciprocal space integration*, which is a method used to integrate images obtained with a 2D detector, based on the projection of measured data onto the reciprocal space. In fact, in this case the results of different scans can be merged together, so it is possible to average data taken for the same volume of reciprocal space, improving the statistical error. This method is implemented in the *BINoculars* [104] software used for data analysis. The only requirement is the knowledge of the matrix converting the diffractometer angles in h, k, l values, which is used for the process of *voxelization* [1], i.e. to convert the intensity acquired by each pixel of the 2D detector into a reciprocal space 3D intensity map.

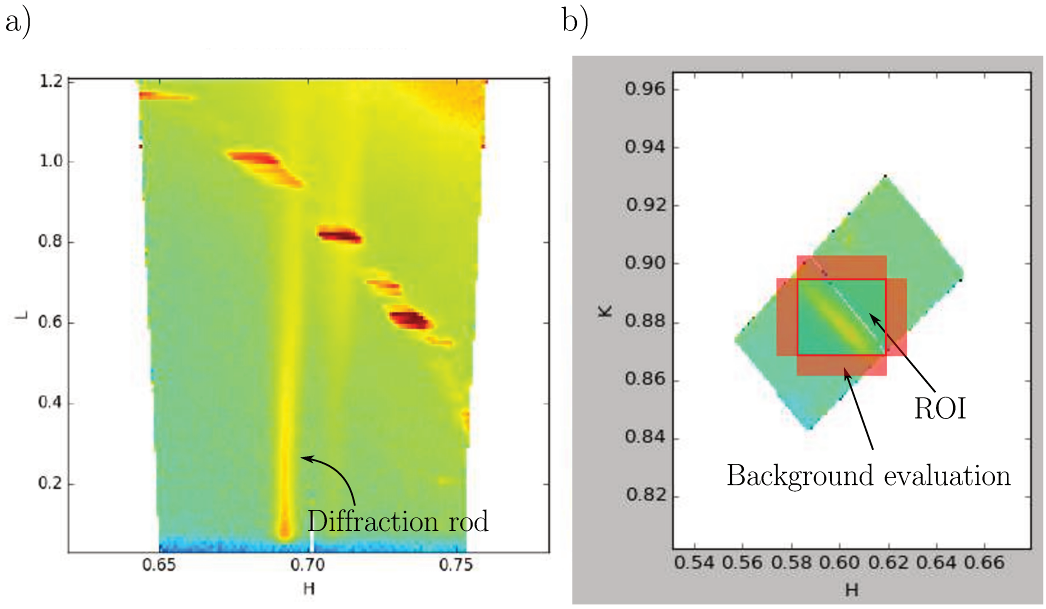

FIGURE 2.16: a) Example of diffraction rod associated to the $(2\sqrt{3} \times 2\sqrt{3})$ reconstruction of Si on Ag(111). b) Slice of a diffraction rod integrated with *BINoculars*.

BINoculars provide also built-in tools for data visualization, curve fitting and diffraction rod integration. Let us go through an example of data processing. It is possible to choose in which coordinates of the reciprocal space we want to perform the projection of the data: Q_x, Q_y, Q_z (coordinates of the momentum) or H, K, L (Miller indexes associated with the crystal used as a substrate). The resolution of the reciprocal space used in the conversion is set by the user; this defines the edges of the single voxel in terms of ΔH, ΔK, ΔL. It is then possible to visualize the rod: *BINoculars* allows the user to project the image on one (or two) reciprocal space axis, as in Fig. 2.16.a, and select the HKL range to show. An interesting feature of the software is the *integration tool*: the data of a certain rod-scan are imported and they are grouped in user-defined number of slices in the L direction. Each slice can be fitted with a 2D Lorentzian curve: it is possible to fit all the rod automatically or manually. In the latter case, the region of interest (ROI), i.e. the region we would like to integrate, is drawn for each slice. Also the area around the ROI used to evaluate the background contribution has to has defined (see Fig. 2.16.b). Once the fit and the integration of each slice in the rod are performed, the structure factors calculated by *BINoculars* can be plotted.

2.4.2.3 Corrections for the integrated intensities

The measured intensities need a series of correction factors [102, 105], due to the geometry of the experiment. Note that the following corrections are directly included in reciprocal space integration performed by *BINoculars*.

- **Lorentz factor**: it accounts for the geometry of the Ewald sphere, Fig. 2.13, crossing by the reciprocal node. In fact, the amount of integrated rod intercepted during an ω-scan, which collects photons in the $\Delta\delta\Delta\gamma\Delta\omega$ volume, depends upon the value of q_z at which scan is performed and upon the incidence angle:

---

[1] voxel: 3D pixel of the image in reciprocal space

$$\text{Lorentz} = \frac{2\pi}{\lambda}\cos(\alpha)\sin(\delta)\cos(\gamma) \tag{2–34}$$

- **Polarization factor**: in synchrotron experiments, the polarization of the incident beam is almost completely horizontal; this leads to a correction equal to:

$$\text{Polarization} = 1 - [\sin(\alpha)\cos(\delta)\cos(\gamma) + \cos(\alpha)\sin(\gamma)]^2 \tag{2–35}$$

- **Active diffracting area**: the incident beam is limited by slits, $s_{\|}$ and $s_{\perp}$, while the diffracted beam is limited by the *detector aperture*, s_{δ} and s_{γ}. By projecting the area selected by the two pairs of slits onto the sample surface, two rectangles of dimensions $[s_{\|} \times s_{\perp}/\sin(\alpha)]$ and $[s_{\delta} \times s_{\gamma}/\sin(\gamma)]$ are obtained. Their intersection defines the "active" area for diffraction, i.e. the portion of sample surface actually contributing to the detected signal, Fig. 2.17. Note that for grazing incidence angles the diffracting area is independent from $s_{\perp}$, as the incident beam casts light all across the sample, unless $s_{\perp}$ is very narrow. In this case the diffracting area is sensitive to the macroscopic shape of the sample and the direction of the incoming beam with respect to the sample can play a non-negligible role. In the present case the detector aperture was large enough to collect all of the sample portion irradiated by the incident beam, so no correction for the area was needed.

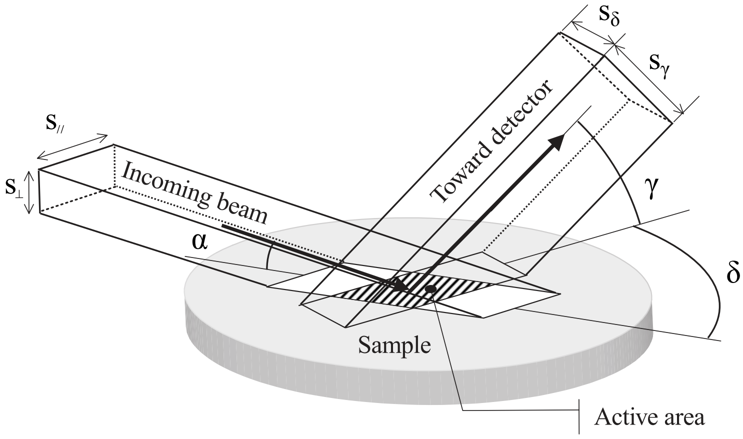

FIGURE 2.17: Schematic representation of the "active" area for diffraction (hatched area), defined as the interception between the projections of the incident beam slits and of the detector aperture on the sample surface (hatched area). [102].

- **Rod interception**: the non-zero detector acceptance results in the integration over a finite rod height during an ω-scan:

$$\text{Rod-height} = \Delta q_{\perp} = \frac{2\pi}{\lambda}\delta\gamma\cos(\gamma) \tag{2–36}$$

  Note that moving along a rod towards increasing values of $q_{\perp}$ at small exit angle means increasing γ; for higher values of the exit angle, the value of δ should be adjusted, too.

Finally, I can write the total correction for the integrated intensity of an ω-scan as:

$$\frac{\text{Lorentz}}{\text{Polarization} \times \text{Area}^{diff} \times \text{Rod-height}} \tag{2–37}$$

It is practical to remark that the angular coordinates can be translated in (H, K, L) positions in the reciprocal space, referring to some crystal coordinates, in the present case those of the Ag(111) substrate.

2.4.2.4 X-ray reflectivity (XRR) measurements

XRR can be used to analyze the reflection intensity curves from grazing incident X-ray beam to determine thin films parameters and in particular thickness in the range $\sim$ 1 nm - 1000 nm. The technique exploits the interference occuring between the X-rays reflected from the surface of the deposited film and the interface between the film and the substrate. By measuring the diffracted intensity as a function of the incidence angle μ we observe oscillations due to this interference [106]. The period of the oscillations gives information about the film thickness. In order extract the film thickness from our results, we employed the software available at the site of the Center for X-ray optics (cxro.lbl.gov). An example of XRR measurements and estimation of the thickness of Si film on Ag(111) is given in Fig. 2.18. The best agreement between simulated curve and data is obtained for a mean film thickness of 10.2 ML and a roughness of 1 ML.

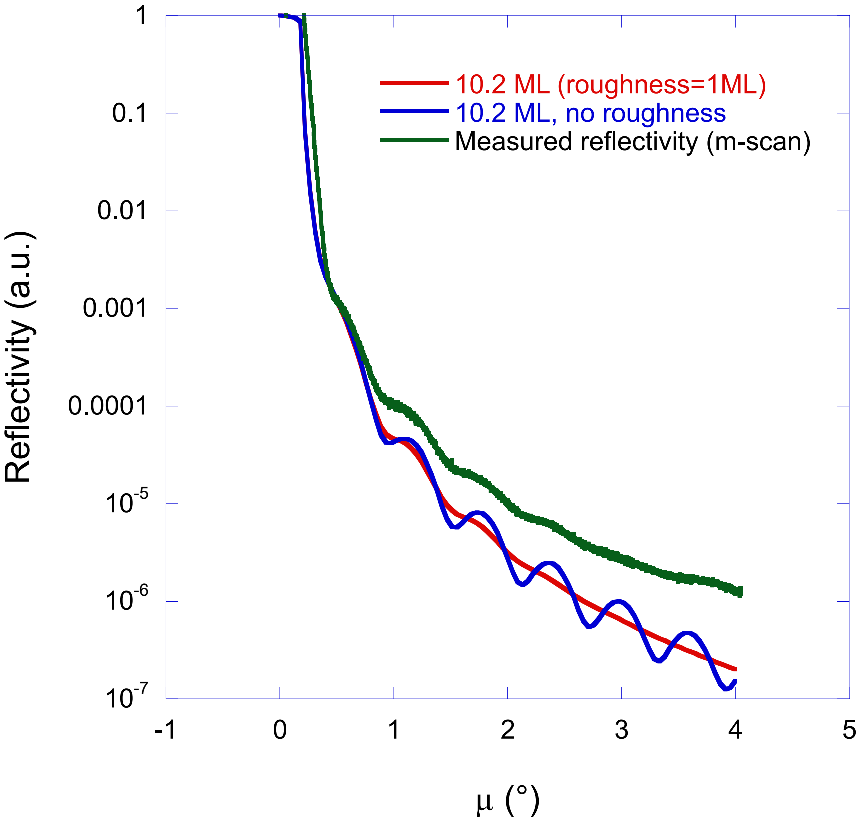

FIGURE 2.18: Reflectivity measurements (green line) compared to the simulated ones, which have same predicted thickness but different roughness.

2.5 Real-time surface differential reflectance spectroscopy (SDRS)

This technique is used to study the optical response of the surface of the studied systems in real-time, during Si deposition. In the present case, I mainly used SDRS to calibrate the Si evaporation rate on Ag(111) during our experiments. SDRS exploits linearly polarized light, with a wavelength ranging from the near-UV to the near-infrared wavelengths. The experimental apparatus is rather simple: it consists in a light source, an optical fiber, focusing lenses, a polarizer and a light analyzer. The data acquisition is controlled by a LABview software written by the engineer Sébastien Royer. In practice, the incident beam passes through the optical fiber and is focused on the sample. The reflected light is collected so that its can be compared with the bare Ag(111) reference spectrum.

The surface differential reflectance signal is given by:

$$\frac{\Delta R}{R} = \frac{R(d) - R_{sub}}{R_{sub}} \tag{2–38}$$

where R_{sub} and $R(d)$ are the optical reflectances of the bare substrate and after the evaporation of a film of thickness d [107], respectively. In the near-infrared region, Ag has a reflectance of almost one, but it suddenly drops at 3.8 eV due to plasmonic resonance [108]. The presence of the thin Si film on the Ag substarte leads to a redshift of this sharp negative feature of Ag and to the apparition of an additional negative feature located at at 3.3 eV, which is related to the 3.4 eV peak in the Si reflectance spectrum [109].

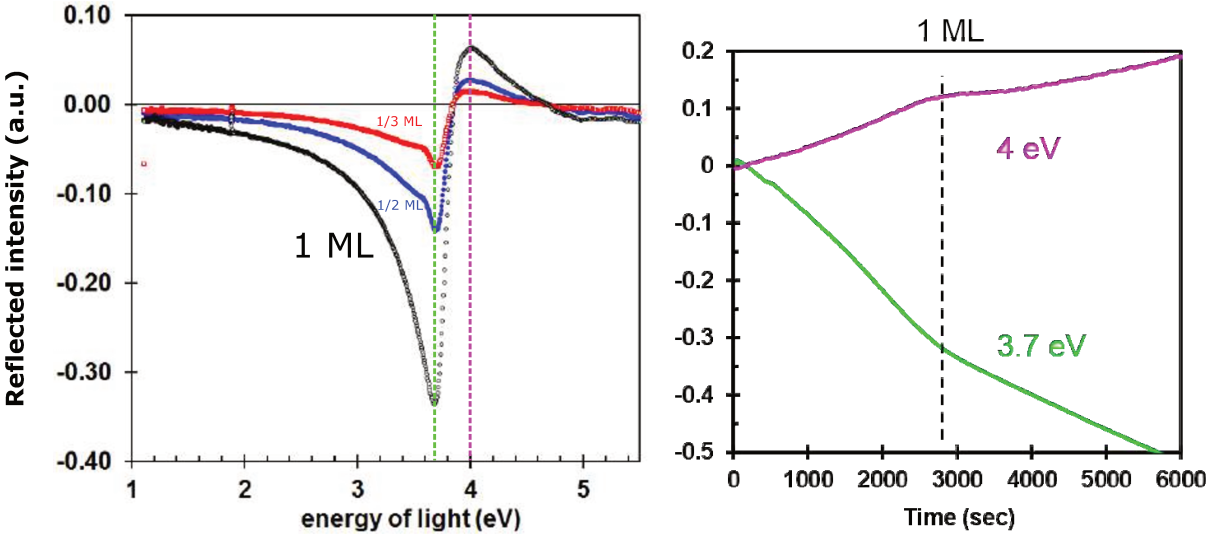

(a) (b)

FIGURE 2.19: a) SDRS spectra at different time of the evaporation: red and blue curves are obtained for sub-monolayer deposition, while the black curve corresponds to the ML completion. This information is deduced from the slope discontinuity observed in (b). b) Evolution of the SDR signal measured at 3.7 eV and at 4.0 eV as a function of the evaporation time. The discontinuity in the slope is the signature of Si ML completion.

SDRS spectra are reported in Fig. 2.19.a; they are measured at different time of the Si evaporation (black: 2700 s, pink: 1300 s, blue: 900 s) for T_{growth}=479 K.

Fig. 2.19.b shows the SDR signal at 3.7 eV (4 eV), thus near the plasmon-related negative feature, as a function of the Si evaporation time at 479 K. The decrease (increase) in the signal is due to the shift of the plasmonic resonance frequency due to the presence of evaporated silicon. The most striking feature is the presence of a discontinuity in the slope at ∼2700 s: this feature identifies the completion of the first monolayer of silicene [9]. The ratio between the total time of evaporation and the time corresponding to the ML completion gives the number of deposited Si monolayers, granted that the experiments are performed on the same substrate with the same evaporator flux and T_{growth}. Indeed, the number of the deposited

monolayer is just a measure of the "quantity" of Si on the surface: it does not give any information of the type of growth of Si.

Chapter 3

Density functional theory

3.1 Introduction

Numerical simulations provide a valuable help in the understanding and description of the physical phenomena laying behind experimental evidences. Not only they can unveil the basic mechanisms of the interaction among atoms, but they can also provide a numerical solution for equations which cannot be solved analytically, giving benchmarks for approximated theories. In principle, the physical properties of materials can be obtained solving the Schrödinger equation for a system of charged nuclei and electrons. The methods aimed to describe a system starting from the basic laws of quantum mechanics are called *ab-initio* or *first-principles* methods. These approaches do not make use of experimental input and, because of this, are expected to be *transferable*, meaning reliable regardless of the chemical environnement to which they are applied. Even for simple systems, the exact solution of the Schrödinger equation is actually not feasible, due to its complexity. In order to tackle this issue several theoretical approaches have been developed, such as post-Hartree-Fock or Monte Carlo simulations. Among *ab-initio* methods, those based on *density functional theory* (DFT) have become one of the most popular in the field of solid state physics. The main drawback is the presence of non-controlled approximations, but beacause of their simplicity they can be applied to relatively large systems. Moreover, DFT is considered predictive in several context, meaning that properties of real materials can be inferred from the results of the calculations, without previous experimental knowledge of the system under study. In this chapter I provide a basic description of the theory, focusing on the aspects relevant for the comprehension of the results presented in the next chapters. DFT has been implemented in several codes, some of which are Open Source, as for example the PW code of the QUANTUM ESPRESSO package [110, 111], which is the one I used to perform the calculations discussed in this Thesis.

3.2 Born-Oppenheimer approximation

Any material can be considered as a system in which N electrons and M nuclei interact through Coulomb forces. In absence of external magnetic fields, denoting by $\boldsymbol{r}_{el} = (\boldsymbol{r_1}, ..., \boldsymbol{r_N})$ and $\boldsymbol{R} = (\boldsymbol{R}_1, ..., \boldsymbol{R}_M)$ the electronic and nuclear positions, the non-relativistic Hamiltonian for a spin compensated system can be written (in atomic units) as:

$$\hat{\mathcal{H}}_{tot}(\boldsymbol{r}_{el}, \boldsymbol{R}) = -\frac{1}{2}\sum_i^N \nabla_i^2 - \sum_\alpha^M \frac{1}{2M_\alpha}\nabla_\alpha^2 - \sum_i^N\sum_\alpha^M \frac{Z_\alpha}{r_{i\alpha}} + \sum_i^N\sum_{j>i}^N \frac{1}{r_{ij}} + \sum_\alpha^M\sum_{\beta>\alpha}^M \frac{Z_\beta Z_\alpha}{R_{\alpha\beta}} \tag{3–1}$$

M_α and Z_α are the mass and the atomic number of the nucleus α, $r_{ij} = |\boldsymbol{r}_i - \boldsymbol{r}_j|$ and $R_{\alpha\beta} = |\boldsymbol{R}_\alpha - \boldsymbol{R}_\beta|$ represent the distances among electrons and among nuclei, respectively, while $r_{i\alpha} = |\boldsymbol{r}_i - \boldsymbol{R}_\alpha|$ denotes the distance between the ith electron and αth nucleus. The first two terms of Eq. 3–1 are the kinetic energies of electrons and nuclei. The other terms represent the Coulomb interaction, which is repulsive between charges of the same sign (4th and 5th terms), and attractive between charge of opposite sign (3rd term). The Hamiltonian can be simplified by exploiting the large difference between the masses of electrons and nuclei: the latter ones are much heavier than the former ones (10^3-10^5) and consequently move more slowly. It is possible to disentangle the electronic degrees of freedom from the nuclear ones, by assuming that nuclei are substantially clamped in fixed positions. They simply generate a potential field acting on electrons, the behavior of which is described within quantum mechanics by the resulting electronic ground-state. On the other hand, the electronic ground-state energy acts as a potential energy for the nuclear dynamics. This simplification takes the name of *Born-Oppenheimer* (BO) approximation. The total wavefunction can be split into two components:

$$\Psi_{tot}(\boldsymbol{r}_{el}, \boldsymbol{R}) = \Psi_{el}(\boldsymbol{r}_{el}, \boldsymbol{R})\Psi_{nucl}(\boldsymbol{R}) \tag{3–2}$$

Let us first consider only the electronic part. The Schrödinger equation for the N interacting electrons in an external nuclear potential writes:

$$\hat{H}_{el}(\boldsymbol{R})\ \psi(\boldsymbol{r}_1, ..., \boldsymbol{r}_N; \boldsymbol{R}) = E_G(\boldsymbol{R})\ \psi(\boldsymbol{r}_1, ..., \boldsymbol{r}_N; \boldsymbol{R}) \tag{3–3}$$

in which, for simplicity, $\psi = \Psi_{el}$; E_G is the energy of the ground-state. Note that in Eq. 3–3, $\boldsymbol{R}$ is now an external parameter and not a quantum mechanical variable as $\boldsymbol{r}_{el}$. Thus, the electronic Hamiltonian can be written as:

$$\begin{gathered}
\hat{H}_{el} = -\frac{1}{2}\sum_i^N \nabla_i^2 - \sum_i^N V_{ext}(\boldsymbol{r}_i, \boldsymbol{R}) + \sum_i^N \sum_{j>i}^N \frac{1}{r_{ij}} \\
V_{ext}(\boldsymbol{r}_i, \boldsymbol{R}) = \sum_\alpha^M \frac{Z_\alpha}{r_{i\alpha}} + \sum_\alpha^M \sum_{\beta>\alpha}^M \frac{Z_\beta Z_\alpha}{R_{\alpha\beta}}
\end{gathered} \tag{3–4}$$

in which the potential V_{ext} depends parametrically on the nuclear positions $\boldsymbol{R}$. By solving this Hamiltonian, one can determine the energy potential $E(\boldsymbol{R})$. This is the first step of the BO approach.

In a second step one can find the minimum of with respect to the atomic positions $\{\boldsymbol{R}\}$. This procedure, further discussed in section 3.8, leads to the determination of the zero-temperature equilibrium structure of the considered system. More in general, $E(\boldsymbol{R})$ can be used as a potential to compute a nuclear dynamics following the Newtonian equations of motion (*molecular dynamics*) or it can be expanded in Taylor's series with respect to the equilibrium positions $\boldsymbol{R}_0$ of a crystal obtaining the *phonon dynamics*. While in the first case the nuclear coordinates are treated as classical variables, in the second one they can be treated as quantum variables.

3.3 Density functional theory

Despite the BO approximation, the problem is still complicated, as the equations of quantum mechanics for a wavefunction $\psi(\boldsymbol{r}_1, ..., \boldsymbol{r}_N)$ depend on $3N$ variables. Density functional theory shifts the attention from the many-body wavefunctions of equation 3–3 to the *ground-state electronic charge density* $n(\boldsymbol{r})$, where $\boldsymbol{r}$ is the 3D spatial coordinate.

Let us now consider a system of N interacting electrons described by the many-body wavefunction $\Psi(\boldsymbol{r}_1, ..., \boldsymbol{r}_n)$, coupled to an external potential $\sum_i^N v(\boldsymbol{r}_i)$. The Hamiltonian can be written as $H = H_0 + V$, where V is the external potential, representing in this case the interaction with the nuclei. Obviously, $v(\boldsymbol{r})$ determines the ground-state energy E_G of the system, the many-body ground state wavefunction $|\Psi_G\rangle$ and the associated charge density $n_G(\boldsymbol{r}) = \langle\Psi_G| \sum_i^N \delta(\boldsymbol{r} - \boldsymbol{r}_i)|\Psi_G\rangle$. The two theorems given by Hohenberg and Khon (HK) in 1964 [112] set the base for *density functional theory*:

***Theorem* 1** *V, E_G and $|\Psi_G\rangle$ are determined unambiguously by $n(\boldsymbol{r})$; thus, they can be considered as functionals of $n(\boldsymbol{r})$.*

Theorem 2 *Variational principle. Given a certain* v*, one can define the functional* $E_v[\tilde{n}] = \langle \Psi_G[\tilde{n}] | H_0 + V | \Psi_G[\tilde{n}] \rangle$*, in which* $|\Psi_G[\tilde{n}]\rangle$ *is the ground state associated to* $\tilde{n}(\boldsymbol{r})$*. If* E_G *and* $n(\boldsymbol{r})$ *are the ground-state energy and density determined by* v*, then:*

$$E_G = E_v[n] < E_v[\tilde{n}] \qquad \textit{for } \tilde{n} \neq n \tag{3–5}$$

In other terms, the two theorems state that n can be obtained as the electron density minimizing the functional $E_v[\tilde{n}]$. The HK theorems do not provide any insight in the actual relation between energy and density. It is important to remark that the HK theorems are valid for the derivation of the ground-state only and in the case of a closed system of N electrons. This last condition can be formally written as:

$$\int d\boldsymbol{r}\; n(\boldsymbol{r}) = N \tag{3–6}$$

Assuming that an explicit expression for $E_v[n]$ is given, then it can be minimized employing the method of Lagrange multipliers with the constraint expressed in Eq. 3–6.

First of all a new functional is defined, including the constraint in density:

$$E_v[n] - \mu \int d\boldsymbol{r}\; n(\boldsymbol{r}) \tag{3–7}$$

This expression is than derived with respect to the $n(\boldsymbol{r})$. Note that for doing this, it is imperative to have an explicit expression for the energy. The zeroes of the derivative are found, keeping μ as a free parameter:

$$0 = \frac{\delta}{\delta n(\boldsymbol{r})} \left[E[n] - \mu \int d\boldsymbol{r}\; n(\boldsymbol{r}) \right] = \frac{\delta E[n]}{\delta n(\boldsymbol{r})} - \mu \tag{3–8}$$

A family of solution $n(\boldsymbol{r}, \mu)$ is obtained, as a function of the position and of the Lagrange multiplier. Eventually, μ is determined by imposing the constraint of equation 3–6 on the last expression calculated for the electron density:

$$\int d\boldsymbol{r}\; n(\boldsymbol{r}, \mu) = N \tag{3–9}$$

It can be easily demonstrated that μ is not just a mathematical expedient, but it represents in fact the chemical potential of the electron system, which coincides at $T = 0$ with the Fermi energy. The chemical potential of a system is defined as the derivative of the total energy with respect to the number of particles of the ensemble:

$$\frac{\partial E}{\partial N} = \int d\boldsymbol{r}\; \frac{\delta E[n]}{\delta n(\boldsymbol{r})} \frac{\partial n(\boldsymbol{r})}{\partial N} = \int d\boldsymbol{r}\; \mu \frac{\partial n(\boldsymbol{r})}{\partial N} = \mu \frac{\partial}{\partial N} \int d\boldsymbol{r}\; n(\boldsymbol{r}) = \mu \tag{3–10}$$

in which I have used Eq. 3–8 and Eq. 3–6.

As already stressed out, this procedure can be used only if an expression for the functional $E[n]$ is given. In the next paragraph I present how Kohn and Sham tackled the problem with a new intuition for describing the many-electron system.

3.4 Kohn-Sham equations

Thanks to the *variational principle* it is possible to derive simple one-particle equations, known as *Kohn-Sham equations* [113]. The idea is to divide the energy into two parts: the first consisting in the kinetic energy of a fictitious non-interacting N-electron system with the same density of the real one, and the second one accounting for meany-body effects. Let us define $|\psi_i\rangle$ as the wavefunction of a single electron in the non-interacting system. Its kinetic energy $T[n]$ is a functional of the electron density, which in turn can be written as:

$$n(\boldsymbol{r}) = \sum_i^N |\psi_i(\boldsymbol{r})|^2 \tag{3–11}$$

which coincides with the one of the interacting system, according to the starting hypothesis. I now introduce a term for the Coulomb interaction between electrons, which is known as the *Hartree term*:

$$E_H[n] = \frac{1}{2}\int\int d\boldsymbol{r}'\, d\boldsymbol{r}\, \frac{n(\boldsymbol{r}')n(\boldsymbol{r})}{|\boldsymbol{r}' - \boldsymbol{r}|} \tag{3–12}$$

The interaction of the electronic system with the external nuclear potential is included as:

$$E_{ext}[n] = \int d\boldsymbol{r}\, V_{ext}(\boldsymbol{r})n(\boldsymbol{r}) \tag{3–13}$$

All the contributions to the electron energy which are not described by $E_H[n]$ and $E_{ext}[n]$ have to be accounted for. For this purpose, I introduce the *exchange and correlation functional* E_{xc}, which describes:

1. the Pauli repulsion between electrons with the same spin (*exchange effect*)
2. a correction compensating for the spurious self-interaction term appearing in $E_H[n]$
3. *correlation effects*, i.e. how each electron influences all the others in terms of occupation of the orbitals and trajectory

Thus:

$$E_v[n] = T[n] + E_{ext}[n] + E_H[n] + E_{xc}[n] \tag{3–14}$$

Note that $E_{xc}[n]$ is defined without introducing any new approximation or assumption. Applying the variational principle to the $E_v[n]$ as written in the previous equation, the KS equations are obtained. First of all, let us write:

$$\frac{\delta E[n]}{\delta n(\boldsymbol{r})} = \frac{\delta T}{\delta n(\boldsymbol{r})} + V_{ext} + \frac{1}{2}\int d\boldsymbol{r}'\, \frac{n(\boldsymbol{r}')}{|\boldsymbol{r}' - \boldsymbol{r}|} + \frac{\delta E_{xc}[n]}{\delta n(\boldsymbol{r})} = \mu \tag{3–15}$$

from which the ground-state energy is calculated. Eq. 3–15 defines an effective potential $V_{KS}(\boldsymbol{r})$, which acts on the single particle of the virtual non-interacting system. Of course the information about the nuclear potential, Coulomb interaction, exchange and correlation is comprised inside this term:

$$V_{KS}(\boldsymbol{r}) = V_{ext}(\boldsymbol{r}) + \int d\boldsymbol{r}'\, \frac{n(\boldsymbol{r}')}{|\boldsymbol{r}' - \boldsymbol{r}|} + V_{xc}[n](\boldsymbol{r}) \tag{3–16}$$

in which the last term is known as *exchange and correlation potential*. The N Schrödinger equations for the one-particle orbitals ψ_i $(i = 1, N)$ of the non-interacting N-electron system subject to the potential $V_{KS}(\boldsymbol{r})$ and the expression of the electron density as a function of the one-particle orbitals are known as the *Kohn-Sham (KS) equations*:

$$h^{KS}[n]\psi_i(\boldsymbol{r}) = \left[-\frac{\nabla^2}{2} + V_{KS}(\boldsymbol{r})\right]\psi_i(\boldsymbol{r}) = \epsilon_i\psi_i(\boldsymbol{r}) \tag{3–17a}$$

$$n(\boldsymbol{r}) = \sum_i^N |\psi_i(\boldsymbol{r})|^2 \tag{3–17b}$$

$$N = \int d\boldsymbol{r}\, n(\boldsymbol{r}) \tag{3–17c}$$

It is worth now making few considerations:

- Eq. 3–17a is not an ordinary Schrödinger equation. In fact, the Hartree potential $V_H[n]$ and $V_{xc}(\boldsymbol{r}, [n])$ depend on $n(\boldsymbol{r})$, which is calculated from the KS orbitals ψ_i, which in turn depend upon the effective potential $V_{KS}(\boldsymbol{r})$. Thus, the problem is not linear and must be solved *self-consistently*. A simple way to do this is to implement an iterative approach. A *trial density* $n^{(0)}(\boldsymbol{r})$ is introduced, which can be alternatively obtained from *trial orbitals*. Then the KS Hamiltonian $h^{KS}[n^{(0)}]$ is solved and new single-particle wavefunctions $\psi_i^{(1)}(\boldsymbol{r})$ are obtained. From the new orbitals it is possible to construct a new electron density $n^{(1)}(\boldsymbol{r})$ through Eq. 3–17b, and then start a new cycle. When practically implemented, this procedure is iterated until $n(\boldsymbol{r})$ reaches *convergence*.
- The KS electronic bands ϵ_i, although being well-defined objects, can be misleading when used to interpret qualitatively electronic excitation energies which are not ground-state properties.
- Although μ should represent another physical quantity, i.e. the chemical potential, the approximations introduced for E_{xc} hinder the theoretical-experimental agreement on such a quantity.

3.5 Approximations to the exchange-correlation energy functional

The theory presented in the previous paragraphs is exact. However, it is probably clear to the reader at this point that DFT as described by Kohn and Sham relies on a trick: all complex contributions due to the interaction between electrons have been "hidden" inside the exchange-correlation term. Up to now, an exact formal expression for such a quantity is not available. However, some simple approximations for $E_{xc}[n]$ have proven to be quite accurate for reproducing and explaining a relevant number of phenomena observed experimentally.

3.5.1 Local density approximation (LDA)

This approximation, firstly introduced by Kohn and Sham [113], results from a generalization of the case of an homogeneous electron gas (HEG) with a uniform charge density, already discussed by Hohenberg and Khon [112]. For this system one can write:

$$\begin{aligned} E_{xc}^{HEG}(\bar{n}) &= V\,\bar{n}\,e_{xc}^{HEG}(\bar{n}) \\ \bar{n} &= \frac{N}{V} \end{aligned} \tag{3–18}$$

where V is the volume of the system and $e_{xc}^{HEG}(\bar{n})$ is the average XC energy of one electron of the uniform gas. The LDA approximation consists in generalizing Eq. 3–18 to the cases of electron densities non-uniform in space as :

$$E_{xc}^{LDA}[n] = \int d\boldsymbol{r}\ n(\boldsymbol{r}) e_{xc}^{HEG}(n(\boldsymbol{r})) \tag{3–19}$$

In this case the assuption is that inside the volume defined by $d\boldsymbol{r}$ the system behaves like an homogeneous electron gas. Note that $e_{xc}^{HEG}(n(\boldsymbol{r}))$ is now **function** of the density n evaluated in the position $\boldsymbol{r}$. The functional dependance on $n(\boldsymbol{r})$ is thus extremely simplified. $e_{xc}^{HEG}(n)$ has been accurately determined in 1980 through Monte Carlo simulation [114] and, within LDA, these results are used to construct the XC potential for a generic system. In the LDA calculations presented in the next chapters, the implementation proposed by Perdew and Zunger [115] has been used. LDA has proven to reproduce a large number of ground-state properties, especially for covalent or metallic systems. Nevertheless, one should keep in mind that LDA tends to underestimate cohesive and ionization energies, and overestimate binding energies, so that theoretical bond lengths are usually shorter than the experimental ones by a few percents. Moreover, LDA can present more serious problems in simulating systems where hydrogen bonds and van der Waals bonds play a relevant role.

3.5.2 Generalized gradient approximation (GGA)

A common attempt to improve LDA consists in simply assuming that XC energy is a function of the electron density **and** its gradient:

$$E_{xc}^{GGA}[n] = \int d\boldsymbol{r}\ n(\boldsymbol{r}) e_{xc}^{GGA}(n(\boldsymbol{r}), \nabla n(\boldsymbol{r})) \tag{3–20}$$

This is a very simple artifact, but it has been proven to be satisfying in many relevant cases. For example, it improves LDA in the simulation of hydrogen bonds. Nevertheless, GGA doesn't have to be considered an absolute improvement, as some systems are better reproduced by LDA. One last remark is that GGA tends to overcorrect LDA: cohesive energies are usually underestimated in the former approximation and, consequently, bond lengths are found to be larger in GGA than in the LDA case.

3.5.3 Semiempirical corrections to GGA

A general drawback of the GGA functionals is that thay fail to accurately account for long-range electron correlations, which are responsible for van der Waals forces. Stefan Grimme proposed in 2006 [116] a modification of the GGA approach, by including a damped atom-pairwise dispersion correction. Thus, the total energy is given by the standard self-consistent KS energy of Eq. 3–5 plus an empirical dispersion correction E_{disp}:

$$\begin{aligned} E_{grimme} &= E_G + E_{disp} \\ E_{disp} &= -s \sum_{\alpha=1}^{M-1} \sum_{\beta=i+1}^{m} \frac{C_{\alpha\beta}}{R_{\alpha\beta}^6} f_{dmp}(R_{\alpha\beta}) \end{aligned} \tag{3–21}$$

M is the number of atoms in the system, s is a global scaling factor, $R_{\alpha\beta}$ are the interatomic distances. f_{dmp} is a damping function, used to avoid near-singularities for small R values. $C_{\alpha\beta}$ denotes the dispersion coefficient for atom pair $\alpha\beta$ and depends on the ionization potentials I_p and static dipolar polarizabilities μ_{pol}:

$$C = 0.05\kappa I_p \mu_{pol} \tag{3–22}$$

where κ is a proportionality constant adjusted to reproduce results previously obtained.

3.6 Pseudo-potentials and plane-wave expansion

Among the different kinds of systems which can be simulated by DFT, I am especially interested in crystals. Ideal crystals contain an infinite number of atoms and electrons. However, thanks to their periodicity one can limit the description to the unit cell and apply *periodic boundary conditions* (PBC). Within PBC a particularly convenient basis set for expanding KS orbitals are the *plane waves* (PWs).

3.6.1 PW-solution of the KS equation

Let us consider a crystal. The potential defined in Eq. 3–16 has the same periodicity of the Bravais lattice of the crystal:

$$V_{KS}(\boldsymbol{r} + \boldsymbol{R}_l) = V_{KS}(\boldsymbol{r}) \tag{3–23}$$

where $\{\boldsymbol{R}_l\}$ are the Bravais vectors. In this case *Bloch's theorem* can be applied, meaning that the solutions of the KS equation 3–17a have the following form:

$$\begin{aligned} \psi_{\boldsymbol{k},\nu}(\boldsymbol{r}) &= e^{i\boldsymbol{k}\boldsymbol{r}} u_{\boldsymbol{k},\nu}(\boldsymbol{r}) \\ u_{\boldsymbol{k},\nu}(\boldsymbol{r} + \boldsymbol{R}_l) &= u_{\boldsymbol{k},\nu}(\boldsymbol{r}) \end{aligned} \tag{3–24}$$

where $\boldsymbol{k}$ is a reciprocal-space vector of the Brillouin zone (BZ) and ν is the band index. At this point, I make use of the PW expansion for the periodic functions $u_{\boldsymbol{k},\nu}(\boldsymbol{r})$:

$$u_{\boldsymbol{k},\nu}(\boldsymbol{r}) = \sum_{\boldsymbol{G}} c_{\boldsymbol{k},\nu}(\boldsymbol{G}) e^{i\boldsymbol{G}\boldsymbol{r}} \tag{3–25}$$

where the sum is done on the ensemble of the reciprocal lattice vectors $\boldsymbol{G}$. Substituting Eq. 3–25 and Eq. 3–24 in Eq. 3–17a, a linear eigenvalue problem is obtained and its eigenvectors are the coefficients $c_{\boldsymbol{k},\nu}(\boldsymbol{G})$. Eventually, the electron density is obtained from:

$$n(\boldsymbol{r}) = \frac{1}{V_{BZ}} \sum_{\nu}^{V} \int_{BZ} d\boldsymbol{k} \; |\psi_{\boldsymbol{k},\nu}(\boldsymbol{r})|^2 \tag{3–26}$$

where V_{BZ} is the volume of the Brillouin zone and the summation ν is done on valence (V) electrons only. In a practical implementation, the integral over the BZ can be calculated by evaluating $|\psi_{\boldsymbol{k},\nu}(\boldsymbol{r})|^2$ over a finite k-point grid, reduced by the crystal symmetry to a set of N_k nonequivalent points $\{\boldsymbol{k}_j\}$. Finally, each point is weighted with $\omega_{\boldsymbol{k}_j}$ according to the lattice symmetry:

$$n(\boldsymbol{r}) = \frac{1}{N_k} \sum_{v}^{V} \sum_{\{k_j\}} \omega_{\boldsymbol{k}_j} \left|\psi_{\boldsymbol{k}_j,v}(\boldsymbol{r})\right|^2 \tag{3–27}$$

Also the sum over the k-points in Eq. 3–27 needs in practice to be done over a finite number of $\boldsymbol{G}$ vectors, which are customarily chosen to be those with a **kinetic energy smaller than a given cut-off energy** E_{cut}; that is:

$$\frac{1}{2}\left|\boldsymbol{k}_j + \boldsymbol{G}\right|^2 < E_{cut} \tag{3–28}$$

The smaller the E_{cut}, the smoother in $\boldsymbol{r}$ will result the corresponding $\psi_{\boldsymbol{k},v}(\boldsymbol{r})$. The choice of the number of points of the k-point grid and the cut-off value must be a compromise between accuracy and computational feasibility. In general, an efficient numerical approach to solve KS equations consists in calculating the kinetic energy of the $\psi_{\boldsymbol{k},v}(\boldsymbol{r})$ (the term $\nabla^2/2$ in Eq. 3–17a) in reciprocal space, i.e. from the coefficients $c_{\boldsymbol{k},v}$ of Eq. 3–25. The application of $V_{xc}[n](\boldsymbol{r})$ is more convenient if performed in real space. Along with E_{cut}, which defines the number of PWs used in the expansion, it is necessary to introduce a grid in real space for the unit cell of our system. The passage between the $c_{\boldsymbol{k},v}$ to the $\psi_{\boldsymbol{k},v}(\boldsymbol{r})$, defined on this grid, is realized by Fast Fourier transforms. Note that, the cut-off for the real space grid where $n(\boldsymbol{r})$ is defined, labeled as E_{rho}, is at least four times the one used for the wavefunctions, E_{cut}.

However, PWs cannot be implemented efficiently in the KS equations. In fact, the potential experienced by an electron in proximity of the nuclei is very attractive, resulting in a strong *localization* of the core electrons. On the contrary, in the regions in-between the nuclei Coulomb varies smoothly. As a direct consequence, the wavefunctions of the electrons are smooth in the interstitial regions and oscillates rapidly when close to the nuclei, as they have to be orthogonal to the wavefunctions of core electrons. In order to accurately reproduce the behavior of these functions which drastically change on a small length scale, a very large number of PWs are needed, which means a long computational time. A possible workaround to this issue is the pseudo-potential approach.

3.6.2 Pseudo-potential approach

The basic idea of pseudo-potential relies on few considerations:

- bonds between atoms, which are responsible for the chemical behavior of a material, are mainly formed by valence electrons in regions quite far from the nuclei , where they are characterized by slowly varying wavefunctions, as previously said;
- core electrons are localized in proximity of the nuclei and behave very similarly, whether the atom is bonded or isolated;
- the energy of core electrons are much smaller than those associated to valence electrons.

For these reasons, it is possible to neglect all the degrees of freedom associated to the core electrons, which can be considered as frozen in their isolated-atom state. Their action on the valence electrons is described by the *pseudo-potential operators*. They are built in such a way that their solutions will be smooth near the core. The computational load is alleviated in two regards: the number of electrons to be actually simulated is smaller; the number of PWs to describe valence electrons is considerably reduced as the valence wavefunctions are smooth everywhere, aslo near the core. Formally, the all-electron valence orbital can be written as:

$$|\Psi_v\rangle = |\phi_v\rangle + \sum_{N_c} \alpha_{cv} |\Psi_c\rangle \tag{3–29}$$

where $|\phi_v\rangle$ is a smooth wavefunction, $|\Psi_c\rangle$ are the core electron orbitals and α_{cv} are the coefficients ensuring orthogonality. Designing by ϵ_v and ϵ_c the eigenvalues of the corresponding valence and core electron wavefunction, the Schrödinger equation can be easily rewritten as:

$$\left[\hat{H} + \hat{V}^{PS}\right] |\phi_v\rangle = \left[\hat{H} + \sum_c (\epsilon_c - \epsilon_v) |\Psi_c\rangle \langle\Psi_c|\right] |\phi_v\rangle = \epsilon_v |\phi_v\rangle \tag{3–30}$$

This a new problem in which the smooth valence wavefunction $|\phi_v\rangle$ is the solution of a new Hamiltonian with the same eigenenergies of the all-electron wavefunction $|\Psi_v\rangle$. The main drawbacks are: $|\phi_v\rangle$ is not normalized and not unique; $\hat{V}^{PS}$ is not unique either and is *non-local*.

In the construction of a pseudopotential, one usually defines a *core radius* R_c. The idea is that for distances bigger than the core radius, the valence band exactly reproduces the all-electron wavefunction, while for distances smaller than R_c the resulting valence wavefunctions are smooth by construction. This is meaningful because, as already said, electronic properties of a solid are mainly determined by the behavior of valence electrons in the interstitial regions. If R_c is diminished, the approximation can be improved, at expenses of increasing computational time. In the opposite case, a very smooth pseudopotential can result in a bad approximation.

Historically, one of the first type of pseudopotentials to be used are the so-called *norm-conserving*. This class of pseudopotential perfectly puts into practice the concepts introduced in this section. In the case of an isolated atom, the solutions of the KS equations have an angular and a radial component:

$$\psi_{nlm}(\boldsymbol{r}) = Y_{lm}(\theta, \phi)\chi_{nl}(r) \tag{3–31}$$

in which n, l, m are the principal, angular and azimuthal quantum numbers, respectively; θ and ϕ are the angular coordinates and r is the radial coordinate. As an example, let us consider a Si atom, which has this electronic configuration $(1s)^2(2s)^2(2p)^6(3s)^2(3p)^2$. Now I choose $(1s)^2(2s)^2(2p)^6$ as core electrons, leaving $(3s)^2(3p)^2$ as valence electrons. In Fig. 3.1 it can be seen that χ_{3s} and χ_{3p} all-electron wavefunctions have two and three nodes, respectively. For $r < r_c$ they have been replaced by a nodeless, smooth pseudo-wavefunction, which instead coincides with the all-electron one for $r > r_c$. Thus, the equation for the pseudo-wavefunctions writes:

$$\hat{H}^{PS}_{3s}\chi^{PS}_{3s} = \epsilon_{3s}\chi^{PS}_{3s} \tag{3–32}$$

in which ϵ_{3s} is the all-electron energy. Thus, given χ^{PS}_{3s}, one has to build the V^{PS} satisfying Eq. 3–32. Note that χ^{PS}_{3s} is normalized as the original all-electron wavefunction χ_{3s}, which is why these pseudopotentials are called *norm-conserving*. The same procedure applies also to χ_{3p}. Thus, the pseudopotential operator can be written as:

$$\hat{V}^{PS}(\boldsymbol{r}, \boldsymbol{r}') = \sum_{lm} V^{PS}_l(r) Y_{lm}(\hat{\boldsymbol{r}}) Y_{lm}(\hat{\boldsymbol{r}}') \tag{3–33}$$

The previous equation is said to be *semi-local*, i.e. it is local in the radial coordinate r, but not in the angular ones $\hat{\mathbf{r}}$, $\hat{\mathbf{r}}'$. Note also that each different value of l corresponds to a different pseudopotential. For a crystal it is convenient to apply the local component of the pseudopotential in real space and the non-local component in the reciprocal one. The non-local components have to be applied to each wavefunction at each step of the self-consistent cycle. The way this operation is performed is thus crucial for the computational efficiency of the code.

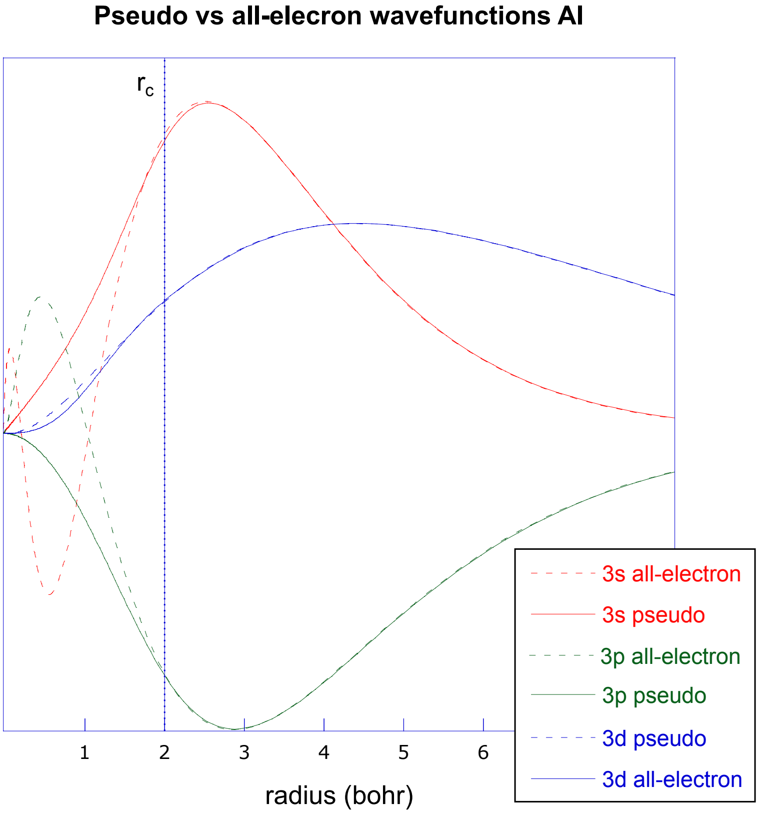

FIGURE 3.1: Radial part of $3s$, $3p$, $3d$ all-electron orbitals (dashed line) and the corresponding nodeless pseudo-wavefunction (full line) for Si. Note that even if the core radius is the same for the three cases, a different value could have been chosen for each of them.

Kleinman and Bylander [117] found out that it was computationally much more efficient to recast norm-conserving pseudopotentials into a *separable, fully non-local* form:

$$\hat{V}_{KB}^{PS} = V_{loc}(r) + \sum_{l} |\beta_l\rangle \langle\beta_l| \tag{3–34}$$

where V_{loc} is the local component.

The *ultrasoft (US) pseudopotentials*, introduced by Vanderbilt in the 90's[118], are also widely used. In fact, despite the improvement introduced by Kleinman and Bylander (KB), the norm-conserving condition still requires a relatively high cut-off energy (> 70 Ry) because of the norm-conserving condition. Vanderbilt realized that this condition could be lifted by generalizing the requirement for orthogonality of KS wavefunctions. A slightly different expression for the non-local part of the pseudopotential is used:

$$\hat{V}_{US}^{PS} = \sum_{lm} D_{lm} |\beta_l\rangle \langle\beta_m| \tag{3–35}$$

which requires a cut-off smaller than the one demanded for norm-conserving pseudopotential. On the other hand the local part of the pseudopotential (applied in real space) still requires a high cut-off E_ρ, but this affects the calculation efficiency in a less crucial way.

In practice, E_{cut} must be defined according to KB; E_{rho} can be fixed at $E_\rho = 4E_{cut}$. For US pseudopotentials, a smaller E_{cut} than for KB can be used, while E_ρ is a second independent convergence parameter (typically of the order of 12 E_{cut}), which however affects the efficiency of the calculation in a much less stringent way than E_{cut}.

3.6.3 Projector augmented-wave (PAW) method

This method has been introduced by Blöchl in 1994 [119] as a unification of the all-electron and pseudopotential approaches. The problem to be tackled is the same: wavefunctions are smooth in the interstitial bonding regions, while they oscillates rapidly near the nuclei. In PAW method a linear transformation is introduced which maps an *auxiliary smooth wavefunction* $|\tilde{\psi}_n\rangle$ to the true all-electron KS single particle wavefunction $|\psi_n\rangle$:

$$|\psi_n\rangle = \hat{T}|\tilde{\psi}_n\rangle \tag{3–36}$$

By inserting this expression in the KS equations, it is possible to calculate the auxiliary wavefunctions, which are smooth if $\hat{T}$ is properly defined. Since the all-electron wavefunctions are already smooth far from the nuclei, $\hat{T}$ acts only in regions close to the cores. Thus:

$$\hat{T} = 1 + \sum_{\alpha} \hat{T}^{\alpha} \tag{3–37}$$

where α is an atom index and $\hat{T}^{\alpha}$ has no effect outside a certain atom-specific *augmentation* region r_c^{α}. Inside these augmentation spheres the all-electron wavefunction is expanded in partial waves ϕ_i^{a}, for which the corresponding auxiliary smooth partial waves $\tilde{\phi}_i^{\alpha}$ is defined; they behave as the original ones outside r_c^{α}. Further considerations on the linearity of the operator $\hat{T}$ and the orthogonality of the implicated wavefunctions lead to a formal expression for the operator $\hat{T}$:

$$\hat{T} = 1 + \sum_{i,\alpha} (|\phi_i^{\alpha}\rangle - |\tilde{\phi}_i^{\alpha}\rangle) \langle \tilde{p}_i^{\alpha}| \tag{3–38}$$

where $\tilde{p}_i^{\alpha}$ are smooth *local* projector function, orthonormal to the smooth partial waves within the augmentation sphere. Thanks to Eq. 3–38, it is possible to give an expression for the all-electron wavefunction:

$$|\psi_n\rangle = |\tilde{\psi}_n\rangle + \sum_{i,\alpha} (|\phi_i^{\alpha}\rangle - |\tilde{\phi}_i^{\alpha}\rangle) \langle \tilde{p}_i^{\alpha}|\tilde{\psi}_n\rangle \tag{3–39}$$

The original KS wavefunctions are separated into smooth auxiliary wavefunctions and a rapidly-oscillating term, which contributes only in the small area of space (*augmentation regions*). Thanks to this separation, the two terms can be treated independently: the localized part is efficiently calculated in real space, to which the cut-off E_ρ, previously defined, corresponds; the smooth term instead is evaluated in reciprocal space with the cut-off E_{cut}. The same considerations on E_{cut} and E_ρ explained at the end of last section apply to this case.

3.6.4 Brillouin-zone integration in metals

In the case of insulators and semiconductors an accurate evaluation of Eq. 3–27 does not demand an extremely dense *k*-point grid, due to the separation between occupied and empty bands. The situation is more problematic in the case of metals, in which the integrand function is discontinuous over the BZ due to the partial filling of the bands. in this case a very fine reciprocal space sampling can be required, resulting in a heavy computational burden. A first approach to tackle the problem is to approximate the occupation step-function near the Fermi level with a Fermi-Dirac function. However it can be shown that this leads to a difference in the total charge with respect to the original case, Fig. 3.2.a, unless the integrated function is constant near E_F. The sampling method proposed for metals by M. Methfessel and A. T. Paxton solves the problem.

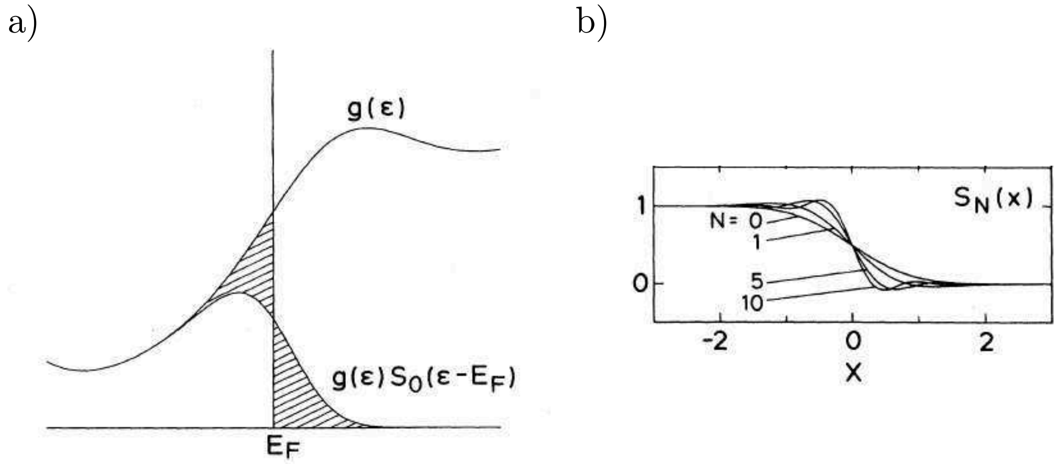

FIGURE 3.2: a) The density of state $g(\epsilon)$ is multiplied by the Fermi-Dirac function. This results in different total charge in the two case; in fact the two hatched areas are not equal. b) Succesive approximations for the step function S_N[120].

The proposed approach introduces a term $S_N(x_j)$ in Eq. 3–27, which is a smooth function meant to approximate the step function:

$$n(\boldsymbol{r}) = \frac{1}{V_{BZ}} \sum_i \sum_{\{\boldsymbol{k}_j\}} \omega_{\boldsymbol{k}_j} \left|\psi_{i,\boldsymbol{k}_j}(\boldsymbol{r})\right|^2 S_N \left(\frac{E(\boldsymbol{k}_j) - E_F}{W} \right) \tag{3–40}$$

N represents the degree of the approximation as illustrated in Fig. 3.2.b, *W* is the *width of the broadening*. The value of the latter parameter can be decided by the user: the smaller the value, the more accurate the simulation, but the denser the *k*-point mesh to be used. This stratagem leads to negligible error and it guarantees exponential convergence with the number of *k*-points.

3.7 Slab configuration and dipole correction

Up to now, I have only discussed the case of systems periodically arranged in all the three dimensions. Indeed, material physics deals also with materials in which the periodicity in one or more dimensions is missing. This is the case of isolated molecules and *low-dimensional materials*, such as quantum dots, monolayers, interfaces, but also simple surfaces. In the last case it is clear that the periodicity along *z*, the direction normal to the surface, is broken due to the presence of the surface. To simulate this kind of systems using PBC, some simple expedients can be introduced.

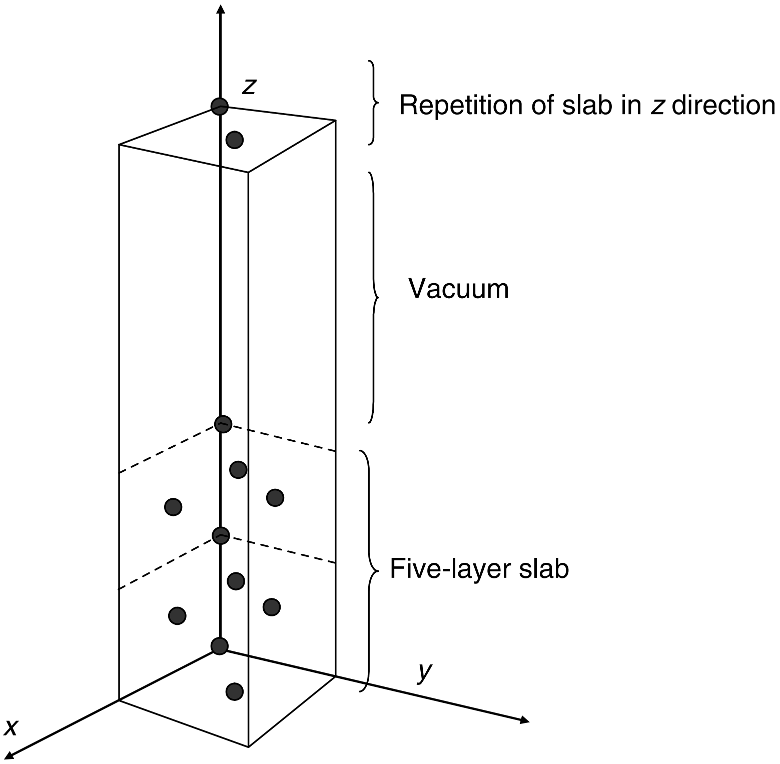

FIGURE 3.3: *Slab* configuration which defines a material with a solid surface when PBC are implemented [121].

In the case of surfaces, the so-called *slab configuration* is used: the classic PBC are applied to our system, but in the input cell a layer of several Å is left empty, i.e. no atoms are present in this volume. This layer corresponds to *vacuum*, which is meant to separate one surface from the other as depicted in Fig. 3.3. Two new parameters are implicitly introduced: the thickness of the vacuum region and the number of layers of the simulated material. Vacuum has to be thick enough to prevent the bottom surface from interacting with the top surface of the adjacent slab through the vacuum, i.e. the electron density of the material tails off to zero in this region. A way to test the separation is to find the thickness which does not change the value of the total energy of the simulated system if further increased. Similarly, also the number of layers in the slab needs to be chosen so that the surface-surface interaction is small. When performing calculations of surfaces using slab configuration, if the two surfaces are not equivalent you can have a *net dipole moment*. Because of this, in order to decouple the surfaces, one should use a very large vacuum region. The "dipole correction" approach [122] is an efficient alternative which introduces a compensating ramp-shaped potential in the vacuum region. The main idea can be understood by looking at Fig. 3.4 which represents the electrostatic potential of a two layer (2×2) slab of fcc. Al(110) with a Na tom adsorbed on side of the surface. Fig. 3.4.a is obtained as usual by applying PBC. Because of this the potential is periodic along z. Since the two surfaces of the slab are not equivalent, the potential in the vacuum region, which is linear, is not flat. Fig. 3.4.b represents a potential which is not periodic along z and it is flat in the vacuum region (zero electric field) as as it should be in a realistic situation. Fig. 3.4.c the potential is periodic along z, but thanks to the introduction of a discontinuity ("dipole correction") in the middle of the vacuum region, the potential on the two sides of the slab is now flat.

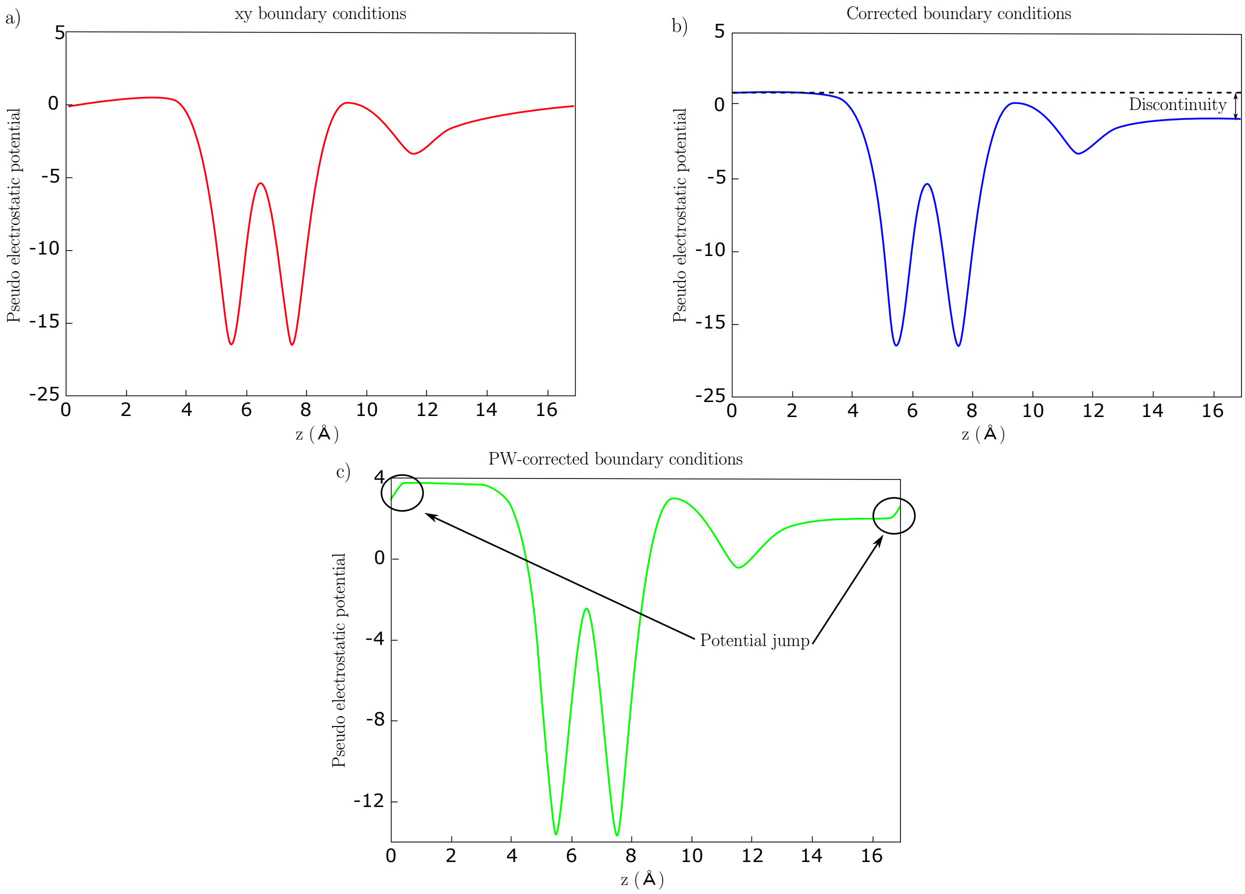

FIGURE 3.4: Different steps leading to the dipole moment correction in an asymmetric slab. z is the direction perpendicular to the surface of the slab. The two surfaces of the slab are roughly situated at $z\ \sim$4 and $z\ \sim$11 Å and the figure reports the electrostatic potential averaged along the x-y directions. The size of the z axis is the periodicity of the cell. a) potential periodic along z; b) potential non-periodic along z associated to zero electric field in the vacuum region; c) the potential is periodic along z and a discontinuity ("dipole correction") has been introduced in the vacuum to maintain a flat potential near the surfaces. Figure adapted from https://wiki.fysik.dtu.dk/gpaw/index.html

3.8 Relaxation of structures

The DFT approach allows the calculation of the total energy $E_G(\boldsymbol{R})$, as a function of the atomic coordinates. All the structures discussed in this work have been obtained after structural optimization, that is after finding the set of positions $\{\boldsymbol{R}_0\}$ which minimize $E_G(\boldsymbol{R})$. In practice, temperature effects are neglected and the atomic configurations stable at zero temperature are determined. This is possibly a major approximation but, given the complexity of the problem it has not been possible to go beyond.

To have an efficient structural optimization algorithm it is useful to determine the forces acting on the atoms. I would like to remind that this kind of calculation does not add a major computational burden because of the so called *Hellman-Feynman theorem* [123, 124], which states that:

$$\frac{dE_G(\boldsymbol{R})}{d\boldsymbol{R}_\alpha} = \frac{\partial E_v[n_0]}{\partial \boldsymbol{R}_\alpha}. \tag{3–41}$$

Here, the left-hand term is the force acting on the atom α. In the right-hand, the partial derivative on $E_v[n]$ ($E_v[n]$ is defined in Eq. 3–14) is done only by considering the explicit dependence of v on the $\boldsymbol{R}_\alpha$ coordinates and NOT the implicit dependence of n_0 on $\boldsymbol{R}_\alpha$. Thus, once n_0 has been calculated by solving self-consistently KS equation (this is the computationally heavy task), the forces acting the atoms can be obtained almost for free with a minimal computational effort (a new self-consistent cycle is not required).

3.9 DFT and grand-canonical ensemble

In the present work DFT calculations have been used to study the equilibrium structure and the energetics of different atomic models. These models consist of silicene or thin Si films deposited on a Ag(111) substrates. The slab associated with different structures do not contain the same number of atoms, thus the direct comparison of DFT energies of the equilibrium structures is meaningless. In such a situation, a possible solution is the introduction of the grand canonical surface energy. As an example, let us consider a slab containing N_{Si} and N_{Ag} atoms of Si and Ag, with energy $E_{slab}(N_{Si}, N_{sub}$. Let us, then, consider a second slab, representing the bare substrate, with N_{Ag} Ag atoms and energy $\tilde{E}(N_{Ag})$. The grand canonical surface energy can be defined as:

$$\gamma_{GC} = \frac{1}{2A}\left[(E_{slab}(N_{Si}, N_{sub}) - \tilde{E}(N_{Ag}) - N_{Si}\mu_{Si}\right], \tag{3–42}$$

where A is the surface of the slab unit-cell and, for simplicity, I consider the two surfaces (of each slab) to be equivalent. μ_{Si} is a new variable which, at the thermodynimical equilibrium, represents the Si chemical potential. The stability of different structures can then be done by comparing their grand canonical surface energy as a function of μ_{Si}. In practice, a given structure might result most stable in certain range of μ_{Si}, but not in another one.

It is clear that in the experiments described in this Thesis, the system is never at the thermodynamic equilibrium. Keeping this in mind, the comparison of the various surface energies γ_{GC} associated with different structures is the only meaningful energetics comparison which can be made.

Note that it is possible to convert the range of chemical potential in which one structure is more stable than the others into corresponding temperature-pressure ranges, obtaining surface phase diagrams. It is important to remark that the reliability of this kind of approach is restricted to the number of considered configurations, i.e. this approach cannot suggest the existence of unanticipated surface geometries or stoichiometries. The only way to overcome this limitation could be to sample large area of the configurational space, which can be done by implementing methods like Monte Carlo simulations.

3.10 Calculation of STM images

DFT simulations have been used to simulate STM images and the comparison between these simulated images and the experimental ones has been useful in validating or rejecting proposed models. The *post-processing* code included in QUANTUM ESPRESSO enables the calculation of constant-current STM images by applying the Tersoff-Hamann model, introduced in Sec. 2.3.4. From Eq. 2–16 it follows that tunneling current for a voltage V between the tip and the sample is, basically:

$$I(\boldsymbol{R}_T, V) \propto \int_0^{eV} n^s(\boldsymbol{R}_T, E_F + \epsilon)d\epsilon \approx \sum_{\epsilon_i \in [E_F, E_F+eV]} |\psi_i|^2 \tag{3–43}$$

Thus, the sum is made on the electron wavefunctions ψ_i in the eigenenergy range $\epsilon_i \in [E_F, E_F + eV]$, above or below the Fermi energy E_F depending on the sign of the bias voltage V. This is basically the local density of state (LDOS) for each (x, y, z) point in our slab. A practical way to represent the results is to define a density ρ_0 and to search for all the points in which LDOS=ρ_0 (*isodensity surface*). Thus, a 2D map (x, y, h_{STM}) is obtained, in which x and y are the in-plane spatial coordinates, while h_{STM} represents the height at which the LDOS is equal to ρ_0.

Although, several relevant details are neglected, e.g. the exact atomic termination of the tip, the comparison between experimental and theoretical images can tells us if a model is reasonable or not. In the present case, the agreement between an experimental and a theoretical image is judged by looking for example,

In the present case I have observed if the simulated STM images could reproduce the experimental surface features, e.g. bright protrusion and dark areas, with the same periodicity and orientation.

In general it is not possible to make precise considerations by comparing the apparent STM heights of simulated and experimental structures. However, in the present work I will show few cases in which the different heights of the structure is large enough (∼Å) to ensure that a discrimination among the model base on the apparent height can be meaningful (see Chap. 5).

Chapter 4

Atomic structure of the silicene layer on Ag(111)

In this chapter I will present the results of combined grazing-incidence X-ray diffraction measurements and first-principle calculations based on density functional theory, aimed to determine the atomic structure of the surface reconstructions of silicene single-layers grown on Ag(111). The remarkably good agreement between present simulations and experiments confirms the honeycomb structures previously proposed in the literature [3, 25, 59, 78, 125]. Moreover, it has also been possible to determine the exact atomic structure of the silicene phases on Ag(111), being sensitive also to substrate relaxations, and make energetics considerations about relative stability of the different surface reconstructions observed.

4.1 Introduction

Since the first experimental attempts of silicene synthesis [3, 52], Ag(111) has been the most studied and promising substrate. Whereas succesful synthesis of 2D Si sheet has been demonstrated, several papers have shown that there is a non-negligible interaction between the silicon sheet and silver [4, 65, 75, 76, 78, 87] , which results in the loss of the interesting electronic properties predicted for free-standing silicene, described in Chapter 1. Depending on both deposition rate and temperature [24, 25, 56, 65, 66, 125], different ordered superstructures form after one monolayer Si deposition on Ag(111). A coexistence of mainly (4×4) and $(\sqrt{13} \times \sqrt{13})R13.9^\circ$ is observed at low temperature ($T_{growth} \sim 500$ K), while at high temperature ($T_{growth} > 540$ K), the layer is mainly composed by $(2\sqrt{3} \times 2\sqrt{3})R30^\circ$ domains [25, 59, 125]. All the models proposed in the literature describe these structures in terms of hexagonal low-buckled single silicon layer, i.e. as a silicene plane. Here the notation refers to the silver substrate: in $(n_{rec} \times n_{rec})R\gamma_{rec}$ reconstruction, the cell parameters of the silicene reconstructions are n_{rec} times those of the Ag(111) unit cell and they are reciprocally rotated of γ_{rec}. The several reconstructions correspond to different orientation of the Si layer with respect to the Ag(111) substrate, as depicted in Fig. 4.1.

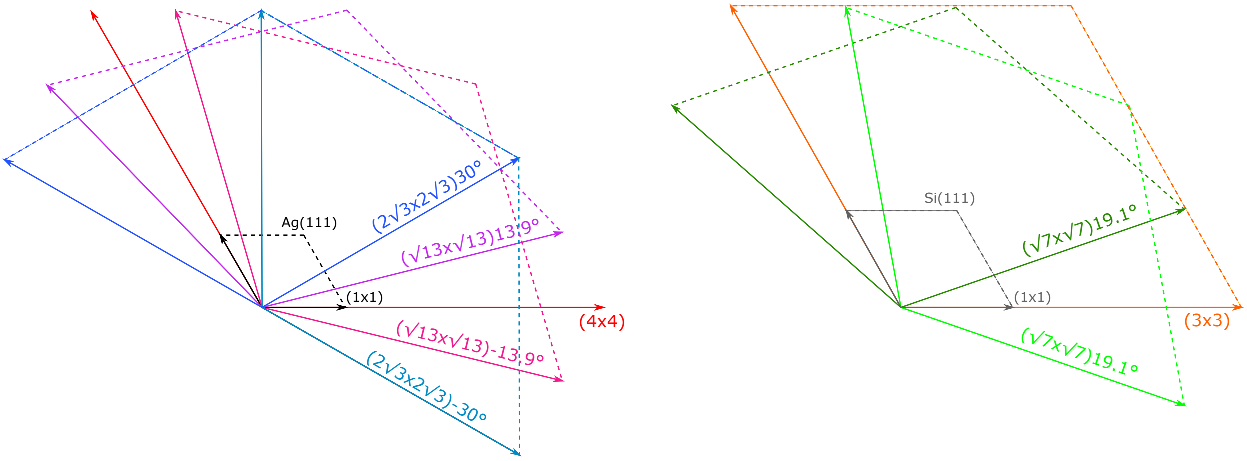

FIGURE 4.1: Unit cells of the different reconstructions represented with respect to the unit cell of Ag(111) (left) or Si(111) (right).

- The (4×4) reconstruction is the most studied silicene phase [3–5, 19, 21, 23–25, 52–60] and it corresponds to a (3×3) cell of Si(111) on top of a (4×4) cell of the Ag(111). The ratio between the lattice parameters of Si and Ag is $a_{Ag}/a_{Si} = 0.752$, meaning that the silicene reconstruction must be slightly dilated with respect to an ideal Si(111) (3×3) cell to have a perfect 3/4 match. The unit cell of the reconstruction is aligned with the one of the Ag substrate.
- The $(\sqrt{13} \times \sqrt{13})R13.9^\circ$ reconstruction is obtained by superimposing a $(\sqrt{7} \times \sqrt{7})$ cell of Si(111) onto a $(\sqrt{13} \times \sqrt{13})R13.9^\circ$ cell of Ag(111). The ratio between the lattice parameter of the Si-$(\sqrt{7} \times \sqrt{7})$ and

reconstruction/Ag(111)		reconstruction/silicene			
Size	Angle	Size	Angle	Silicene/Ag angle	Deformation
4	0°	3	0°	0°	+0.30%
$\sqrt{13}$	13.9°	$\sqrt{7}$	19.1°	5.2°, 27.0°	+2.51%
$2\sqrt{3}$	30°	$\sqrt{7}$	19.1°	10.9°	-1.51%

TABLE 4.1: Characteristic quantities of the various reconstructions with respect to the unit cells of Ag(111) or silicene lattice. The "deformation" column indicates the percentage of increase (+) or decrease (-) of the lattice parameter of the silicene lattice with respect to Si(111).

Ag-($\sqrt{13} \times \sqrt{13}$)$R$13.9° is $L_{\sqrt{7}-Si}/L_{\sqrt{13}-Ag}$ = 0.975 [71]. The (1 × 1) unit cell of the Si layer can be rotated by η=5.2° or 27.0° with respect to the [1$\bar{1}$0] direction of the Ag substrate. From now on I label as ($\sqrt{13} \times \sqrt{13}$)$R$13.9° $-$ *type I* and *type II* the reconstruction with the first and second orientation, respectively [60–62]. It should be noted that, while *type II* reconstruction is found to grow in large crystalline domains [63–65], *type I* configuration, also referred to as "dotted phase", is not always completely ordered and oriented along the same axis [25, 61, 66] and it has a metastable character [65]; it is occasionally identified as a (3.5 × 3.5)R26° reconstruction.

- Concerning the ($2\sqrt{3} \times 2\sqrt{3}$)$R$30° reconstruction, a contracted ($\sqrt{7} \times \sqrt{7}$) is superimposed to a ($2\sqrt{3} \times 2\sqrt{3}$)$R$30° cell of Ag(111), being $L_{\sqrt{7}-Si}/L_{2\sqrt{3}-Ag}$ = 1.015. The angle between the (1 × 1) unit cell of Si and the [1$\bar{1}$0] direction of the Ag substrate is in this case 10.9°. Some groups argued whether this reconstruction is due or not to Ag-Si sub-surface alloy, but Qiu *et al.* [126] have shown its pure Si nature by means of hydrogenation of the surface.
- The presence of long-range ordered structures, namely ($\sqrt{133} \times \sqrt{133}$)$R$4.3° and ($\sqrt{427} \times \sqrt{427}$)$R$7.2° reconstructions, has been reported concurrently with ($\sqrt{13} \times \sqrt{13}$)$R$13.9° and ($2\sqrt{3} \times 2\sqrt{3}$)$R$30° structures, respectively [71, 72, 127]. They have been interpreted as periodic relaxation of the strain or compression accumulated in large ($\sqrt{13} \times \sqrt{13}$)$R$13.9 and ($2\sqrt{3} \times 2\sqrt{3}$)$R$30° domains [71, 72].

Tab. 4.1 reports the characteristics of each reconstruction with respect to Ag(111) or to Si(111).

The electronic properties of silicene are intimately connected to its structural characteristics and, in particular, to the value of the buckling. Indeed, eventual relaxations from the surface can reveal an eventual interaction between the silicene layer and the Ag substrate. In the following I will discuss the models proposed in the literature, which I have simulated by DFT. From the equilibrium positions it is possible to derive the theoretical structure factors, which are then compared to the experimental ones obtained by GIXD measurements. From the comparison between theory and experiments, I identify the models which, after relaxation, give the theoretical structure factors reproducing the experimental ones.

4.2 Experimental and computational details

GIXD experiments have been performed on the SIXS beamline at SOLEIL sychtron facility. A monochromatic X-ray beam of 18.46 keV energy and an angle of the incident X-ray beam α=0.145° (close to the critical value) have been used. This grazing incidence geometry results in the reduction of the penetration depth of the incoming X-rays and the bulk diffuse scattering, as explained in Sec. 2.4. The diffracted intensity has been acquired by a point (1D) detector. The Ag(111) sample, prepared with the standard procedure described in section 2.2 and the rate of Si evaporation has been estimated to be equal to 1 ML/2700 s by surface differential reflectance spectroscopy, see Sec. 2.5. Hereafter, 1 ML correspond to one complete silicene sheet and it will be used to express the Si coverage θ_{Si} of the Ag substrate.

Concerning the diffraction results, the unit cell of the different reconstructions are taken as reference for indexing the reciprocal space. The corresponding vectors expressed in the hexagonal basis (Fig. 4.2) of the Ag(111) surface are:

$$\begin{aligned} a = b = n_{rec}\frac{a_{Ag}}{\sqrt{2}}, \qquad & c = \sqrt{3}a_{Ag} \\ \alpha = \beta = 90^\circ, \qquad & \gamma = 120^\circ \end{aligned} \tag{4–1}$$

where a_{Ag} is the lattice parameter of silver, equal to 4.085 Å and n_{rec} is defined in Sec. 4.1. The lattice parameters (a, b, c), and the angles among them (α, β, γ) for the hexagonal basis are represented in Fig. 4.2.

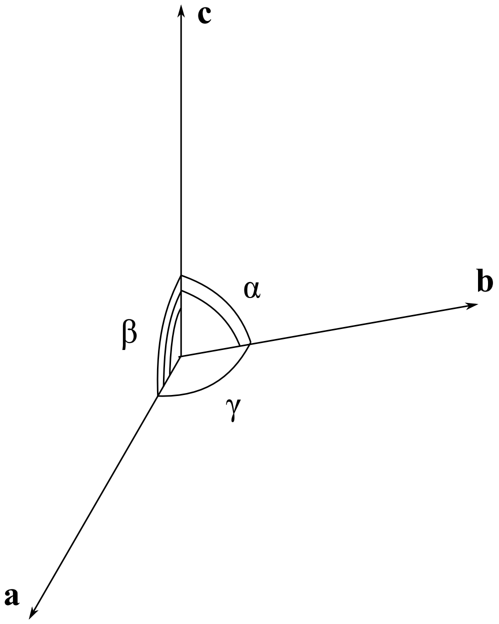

FIGURE 4.2: Representation of the lattice parameters and the angles among them for the hexagonal basis.

The reciprocal lattice of a simple hexagonal Bravais lattice with lattice constants a and c is another simple hexagonal lattice with lattice constants $|\boldsymbol{a}^*| = |\boldsymbol{b}^*| = 4\pi/\sqrt{3}|\boldsymbol{a}|$ and $|\boldsymbol{c}^*| = 2\pi/|\boldsymbol{c}|$. In real space I consider an angle of 120° between $\boldsymbol{a}$ and $\boldsymbol{b}$, so that the angle between the respective reciprocal lattice parameters is 60°. Note that in reciprocal space the distances are inverted with respect to real space: e.g. the Brillouin zone associated with the (4 × 4) reconstruction is sixteen times smaller than the one associated with Ag(111).

Let us now focus on the details of the DFT calculations. Concerning the simulations of the (4 × 4) structure, I have tested three different approximations for the Kohn-Sham potential: local density approximation (LDA) [115], generalized gradient approximation (GGA) [128] and GGA including eventually phenomenological van der Waals corrections (GGA+vdW) [116, 129]. The action of core electrons on valence band electrons is described by the pseudo-potentials, according to the Bloch's projector-augmented wave method [130]. Instead, the valence electron orbitals are expanded in plane waves, for which a cut-off E_{cut}=30

Ry is used; the cut-off for the charge is set to E_ρ=240 Ry. The broadening of the density of states at the Fermi level improves the sampling accuracy of a certain set of k points. This is taken into account according to the cold-smearing broadening, invented by Marzari and Vanderbilt [131], set in our calculations at a value of 0.025 Ry. The system is simulated by a slab consisting of the (4×4) silicene reconstruction on top of either six or four Ag(111) layers. A volume of vacuum as thick as six Ag layers terminates the structure. It was tested to be sufficient to prevent the bottom Ag layer and the (4×4) reconstruction to interact with each other. In fact, I recall that due to the periodic boundary conditions implemented in the code, the same 3D cell is repeated in space in all the three directions: the vacuum stands between two consecutive slabs in the z direction. The electronic density is evaluated on a $6 \times 6 \times 1$ k-point grid, chosen considering both accurate sampling of the reciprocal space and affordable computational burden. The QUANTUM ESPRESSO code finds by default the symmetries of the system and during relaxation atoms are moved preserving these symmetries. Positioning the atoms slightly out of their ideal positions ensure that no symmetry is imposed, so that, during relaxation, atoms can span a larger zone of the phase space. The atomic positions are relaxed until atomic forces were less than 10^{-3} Ry/Bohr. The input atomic positions of the bottom Ag layer are kept fixed. The lattice parameters for silver bulk structure have been tested for convergence for both the approximations used in the pseudopotentials: an equilibrium value of 2.837 Å and 2.935 Å was found for LDA and GGA, respectively, while the experimental reference is 2.899 Å. Accounting for the vdW corrections does not change the value of the equilibrium lattice constant.

I remark that the relaxed surface structure is not substantially altered by changing from four to six substrate layers. The theoretical structure factors calculated for the (4×4) reconstruction and presented in Sec. 4.5, refer to the results of simulations obtained for six Ag layers. The results are qualitatively the same by considering less demanding parameters for the calculations, i.e. 25/20 Ry for the cutoff, 0.05 Ry for the smearing and a $3 \times 3 \times 1$ k-point grid has been performed, with no major influence on the structure of the slab.

Concerning the $(\sqrt{13} \times \sqrt{13})R13.9°$ and $(2\sqrt{3} \times 2\sqrt{3})R30°$ reconstructions, they have been simulated using the GGA, which gives the best agreement between theoretical and experimental structure factors in the case of the (4×4) reconstruction (see Sec. 4.5). The substrate is simulated by four Ag layers (the last one is fixed) and I have used the same parameter as for the (4×4) structure (cut-off of 30/240 Ry, smearing set to 0.025 Ry and $6 \times 6 \times 1$ k-point grid).

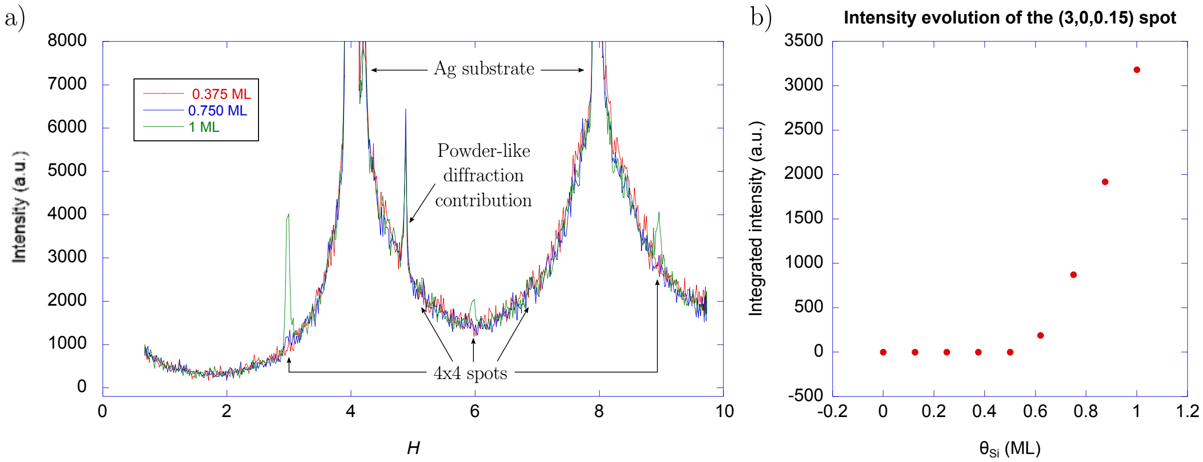

FIGURE 4.3: a) Diffracted intensity along the reciprocal space axis H at different Si coverage, with the silver substrate at a temperature of 520 K. For θ_{Si} ~0.625 ML spots of the (4×4) reconstruction appear. The most intense is at (3,0,0.15) but other three are visible at H = 5, H = 6 and H = 9. The constant peak at H = 4.88 is due to Ag powder-like areas. b) Evolution of the integrated intensity of the (3,0,0.15) peak.

4.3 GIXD measurements: experimental structure factors

The formation of the silicene sheet has been followed by real-time GIXD measurements. Moras *et al.* [59] have shown that the intensities of the diffraction spots associated to the various reconstructions follow a peculiar evolution depending on the temperature. According to what this group reported, I expect to see the appearance of the (4 × 4) spots and then a growth of their intensity. Evaporation must stop before they lose brilliance, as this would be the signature of the growth of the second silicon layer [59]. The study by Moras *et al.* reports also the percentage of surface covered by each reconstruction at θ_{Si} = 1 ML Si deposition for several growth temperatures. This information will particularly useful in Chapter 5 to determine the exact growth regime, which is intimately connected with T_{growth}.

In Fig. 4.3.a one can see the intensity evolution of an H-scan, i.e. the diffracted intensity between the reciprocal points $(0.8, 0, 0.15)$ and $(10, 0, 0.15)$, for the measurements performed at 520 K; the H-axis refers to the (4 × 4) reconstruction. At the very beginning of the evaporation and until a coverage of ∼0.625 ML, the only visible peaks are the ones related to the substrate. They are very intense and can be easily recognized in Fig. 4.3.a at H = 4 and H = 8. The peak at H = 4.88 correspond to a diffraction sphere due to the scattering from Ag powder-like areas, which usually form in proximity of the sample edges. This scattering sphere is associated with the {200} family plane of Ag.

Starting from a coverage of θ_{Si} ∼0.625 ML, diffracted intensity appears at (3,0,0.15), associated with (4 × 4) structure. The intensity increases until the completion of the monolayer. This can be easily explained: in the first stages Si domains are still too small to give rise to ordered structures. After a critical size of these domains, Si atoms can rearrange and crystallize, as shown in ref. [65]. Diffracted intensity from the reconstruction can also be seen at H = 5, H = 6 and H = 9.

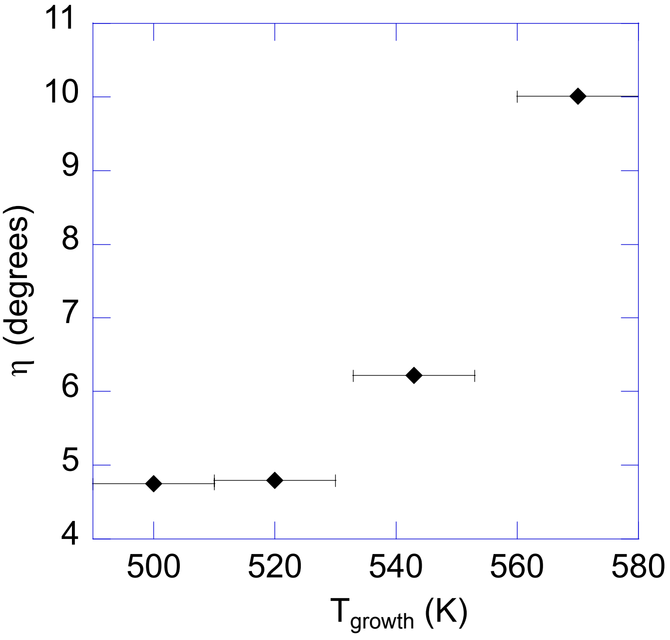

FIGURE 4.4: Evolution of η, which is the angle between the unit cells of silicene and Ag(111), with the growth temperature T_{growth}.

From present measurements, I could determine the structure of the silicene monolayers formed for various substrate temperatures in the 500 K - 570 K temperature range. The (4 × 4) structure is always present in this temperature range, with a silicene lattice constant of 3.852 Å, equal to 4/3 of the Ag(111) surface lattice constant. In addition to this superstructure, other diffraction spots are visible, for example for a value of the in-plane transferred wave-vector $q_{\|} \approx 1.87$ Å or $q_{\|} \approx 3.24$ Å. All these spots correspond to silicene lattices rotated with respect to the Ag substrate with an angle $\eta \in [4.8°, 10°]$ which depends on the growth temperature T_{growth}, as shown in Fig. 4.4. At low temperature, η is close to the relative angle of 5.2° between the Ag lattice and the Si lattice in the $(\sqrt{13} \times \sqrt{13})R13.9° - type\ II$ reconstruction, whereas at high temperature, η is nearly equal to the relative angle (10.1°) between the Ag lattice and the Si lattice in the $(2\sqrt{3} \times 2\sqrt{3})R30°$ reconstruction. For these structures, the lattice constant of the silicene lattice, measured at room temperature after growth, does not depend on the growth temperature; it is equal to $a_{Si}^{exp} = 3.884 \pm 0.04$ Å. This indicates that all these structures are not exactly in registry with the Ag substrate, since the expected lattice constants for the $(\sqrt{13} \times \sqrt{13})R13.9°$ and $(2\sqrt{3} \times 2\sqrt{3})R30°$ reconstructions are 3.937 Å and 3.783 Å, respectively.

Such an angle variation with respect to the ideal structures have already been reported in the literature [71, 72] from STM measurements. However, the size of the superstructures reported, 10.8 ± 0.2 Å for the $(\sqrt{13} \times \sqrt{13})R13.9°$ [55–57, 61, 71] and 9.6 ± 0.2 Å for the $(2\sqrt{3} \times 2\sqrt{3})R30°$ [63, 72] are not in agreement with the value of a_{Si}^{exp} found in the present study, if one assumes that these structures corresponds to $(\sqrt{7} \times \sqrt{7})$ silicene reconstructions.

Any of the observed diffraction spot could be associated with a $(\sqrt{13} \times \sqrt{13})R13.9° - type\ I$ reconstruction, i.e. with a silicene lattice turned by $\eta \approx 27°$ from the Ag lattice.

In Fig. 4.5.b, I report the GIXD map of the diffracted intensity for in-plane conditions ($L = 0.05$) for 1 ML of Si evaporated at 570 K; these measurements correspond to the last point on the right in Fig. 4.4. At this temperature the most intense spots are associated with a $(1.338 \times 1.338)R \pm 10.02°$ reconstruction, which corresponds to a small distortion of the $(2\sqrt{3} \times 2\sqrt{3})R30°$ superstructure usually observed at high temperature [72, 127]. Spots of the (4×4) are visible, too, but they have a lower intensity. On the other hand, for deposition at 520 K (second point in Fig. 4.4), the most intense signal comes from the (4×4) structure, whereas a $(\sqrt{13} \times \sqrt{13})R13.9°$ is also visible. I have measured for both temperatures the intensity of the in-plane (4×4) reflections by performing 35 angular rocking scans (ARSs) in the (H, K) positions indicated by yellow dots in Fig. 4.5.a. Employing ARSs, one can explore small regions of the reciprocal space at a constant value of the transferred wave-vector. By performing these measurements I can measure the integrated intensity of the spots and rods and then derive the experimental structure factors, see Sec. 2.4. The Fig. 4.5.c shows the comparison between two in-plane ARSs performed on the $(3, 3, 0.05)$ spot in the two experiments at 520 K and 570 K. The integrated intensity of a (4×4) spot is also proportional to the portion of sample covered by this reconstruction; its full width at half maximum (FWHM) is inversely proportional to the size of its domains. At the lower temperature, the peak is 2.5 times broader and its integral is 2.4 times higher, with respect to the results obtained at higher temperature. Thus, I can state that in the experiment at 520 K the domains of the (4×4) are smaller, but cover a higher percentage of the surface.

I have performed ARSs at consecutive values of of L, in order to collect the diffracted intensity along several superstructure rods (SRs) associated with the (4×4) and $(2\sqrt{3} \times 2\sqrt{3})R30°$ reconstructions for the experiments at 570 K, and for the (4×4) and $(\sqrt{13} \times \sqrt{13})R13.9°$ structures for the experiment at 520 K. As already explained in Chapter 2, the diffraction pattern consists of diffraction rods reflecting the symmetry of the surface I am probing, e.g. truncated bulk, surface reconstructions, adsorbed layers. The (H, K) positions of the measured SRs are indicated as black and violet circles in Fig. 4.5.a, for the experiment at 570 K. An important remark has to be done. Whereas the crystal truncation rods associated with the Ag(111) carry also the contributions of each silicene phase due to the superposition of their diffracted intensities in these reciprocal space positions, the analyzed SRs are exclusively associated to one reconstruction. This situation is ensured at 570 K by the distortion of the $(2\sqrt{3} \times 2\sqrt{3})R30°$ phase: some of its diffraction spots would superimpose to those of the (4×4) reconstruction, but here it is not the case thanks to the aforesaid deformation. At 520 K, none of the diffraction spots associated to the two coexistent reconstructions, i.e. (4×4) and $(\sqrt{13} \times \sqrt{13})R13.9°$, share the same (H, K) position, except at the nodes of the Ag(111) surface lattice.

The details of the fitting process are described in Sec 2.4.2. Through this procedure I have obtained the integrated intensities for each in-plane spot and each SR. The associated structure factors are than given by $F = C\sqrt{I}$, where I is the integrated intensity and C is a standard geometrical correction [132], Sec. 2.4.1.1. The analyzed spots and rods of the (4×4) are found to be nearly the same at 570 K and 520 K; the comparison between the experimental structure factors are shown in Fig. 4.6. This similarity in the results means that the atomic structure of the (4×4) reconstruction and the relaxations of the underlying Ag(111) substrate are not markedly affected by the temperature difference between the two experiments.

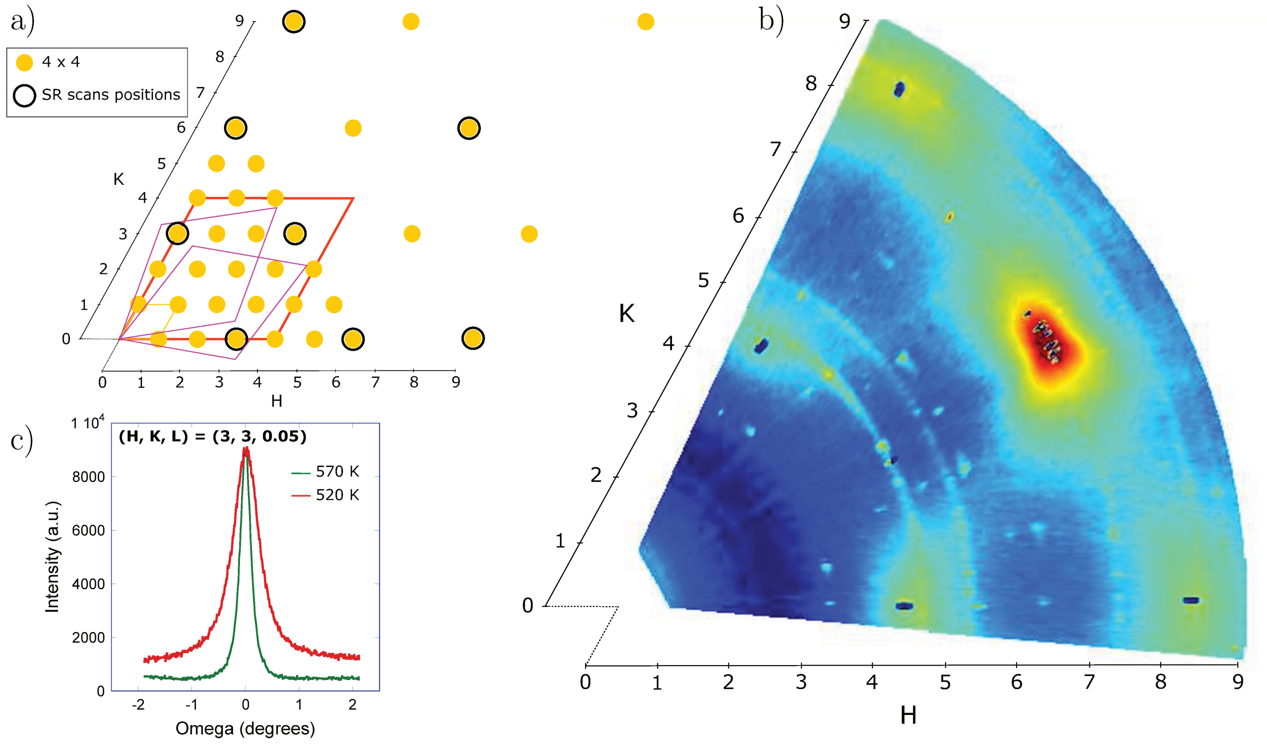

FIGURE 4.5: a) Schematic representation of the diffraction spots and rods measured and 570 K after the evaporation of ~1 ML of silicon on Ag(111). The indexing of the axis refers to the (4×4) silicene reconstruction. The unit cells of the structures are indicated by parallelograms: yellow for the (4×4), pink for the two domains of the $(1.338 \times 1.338)R \pm 10.02°$ (i.e. the distorted $(2\sqrt{3} \times 2\sqrt{3})R30°$) and finally red for the Ag(111) unit cell. Yellow dots indicate the (H, K) positions of the in-plane angular rocking scans, whereas the black circles indicate the (H,K) positions in which I have measured the superstructure rods of the (4×4) reconstruction. The same measurements on the (4×4) spots and rods have been performed also at 520 K. b) In-plane diffraction map of the reciprocal space obtained by GIXD measurements performed at 570 K. Diffraction spots are clearly visible in the positions of angular rocking scans. c) Rocking scan performed around $(H, K, L) = (3, 3, 0.05)$ at 520 K (red line) and 570 K (blue line). The almost identical intensity at ω=0 is fortuitous.

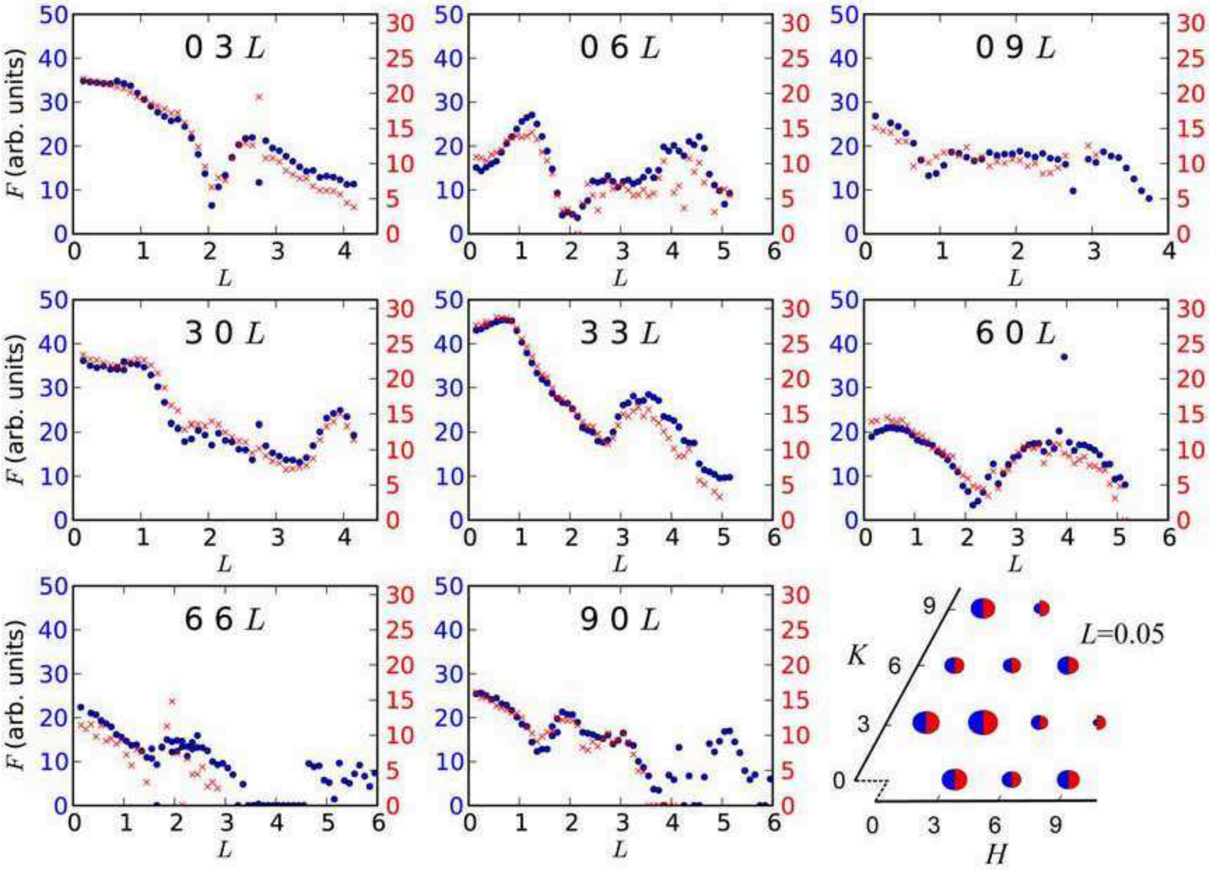

FIGURE 4.6: Experimental structure factors along nine SRs and in-plane spots corresponding to the Si/Ag(111) (4 × 4) reconstruction. Red and blue colors correspond to the results obtained for the experiments performed at 570 K and 520 K, respectively. The structure factors measured in the two cases are found to be nearly the same within a scale factor of 1.6.

4.4 DFT calculations: foreseen theoretical structure

In the models describing the various surface reconstructions, I want to make sure that the system obtained from the superposition of the silicene layer and the Ag(111) substrate possesses the $p3$ symmetry. In order to ensure that, the high symmetry points labeled by the Wyckoff indexes a, b, c (Fig. 4.7.a) must correspond to symmetric positions of the silicene cell. Thus, the three Wyckoff positions are always occupied by an Ag atom of the 1st, 2nd or 3rd layer (Fig. 4.7.b); on top of them there can be either an atom of the hexagonal Si lattice or the center of an hexagonal Si ring (Fig. 4.7.c). In this way each reconstruction can be labeled also with three indexes corresponding to the kind of occupation of the Wyckoff positions a, b, c, respectively. Each index specifies the position of the Si lattice with respect to the particular Wyckoff position (t=Si atom on top, h center of the hexagonal Si ring). The subscript indicates the layer number the Ag atom, in that position, belongs to. Finally, a reconstruction can be written as:

$$(n_{rec} \times n_{rec})R\gamma_{rec}\ s_i r_j t_l, \qquad \text{with } s,r,t \in \{h,t\};\ i,j,l \in \{1,2,3\} \tag{4–2}$$

For example, a reconstruction labeled with $h_2t_3h_1$ would have hexagonal Si rings around the Wyckoff positions a and c, and a Si atom on top of c; concerning the substrate a Ag atom from the first layer is in c, one of the second layer in a and one of the third in b.

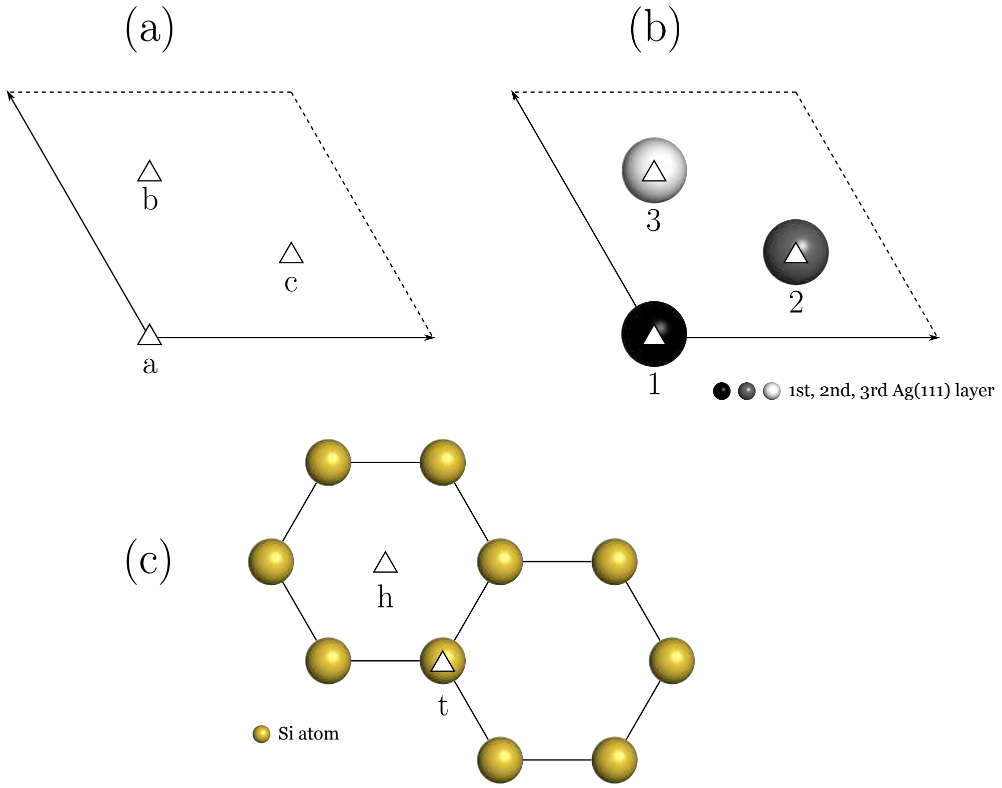

FIGURE 4.7: a) Representation of the Wyckoff indexes for $p3$-symmetry structure. b) Example of occupation of the Wyckoff positions by the atoms of the Ag substrate. c) t and h occupation of the Wyckoff sites by the silicene lattice.

4.4.1 (4×4) structure

In the model independently proposed by Vogt *et al.* [3] and Lin *et al.* [55], the (4×4) structure consists of 18 Si atoms arranged in a honeycomb lattice (Fig.4.8.a): six of them are displaced vertically giving a buckling of 0.7/0.75 Å, according to the two research groups [3, 55]. The model has been put forward on the basis of STM and LEED experiments, along with DFT calculations. A good agreement is found between the experimental and the simulated STM images, in which six protrusions are clearly visible and correspond to the high-lying Si atoms, represented by red spheres in Fig. 4.8. Vogt *et al.* report more details about the structure: the average Si-Si distance is 2.2 Å and the distance between the bottom silicon atoms and the first Ag layer is 2.92 Å. The side of the triangular structures formed by protruding Si atoms is equal to 0.38 Å, in agreement with what reported by Lin *et al.*.

In the present case, I have simulated the (4×4) structure using three different approximations for the calculations: LDA, GGA and GGA+vdW. Fig.4.8 reports the equilibrium structure obtained for GGA simulations. Using the notation introduced in Sec. 4.4, the simulated configuration can be exactly identified as (4×4) $h_1h_3h_2$. Two other inequivalent configurations could be obtained by changing the Ag atom in the Wyckoff position a. The results obtained for LDA, GGA and GGA+vdW are very similar. Table 4.2 reports the buckling of the silicene layer, the range of Si-Si bond length and the bond angles given by our simulations results, as well as the results of previous experimental and theoretical works.

Depending on the approximation of the pseudopotential employed in the calculation, Ag(111) substrate has slightly different equilibrium lattice parameters (LDA: 2.837 Å, GGA: 2.935 Å). In order to make a direct comparison all theoretical distances have been scaled to the experimental Ag lattice constant, 2.889 Å. Among the various values computed, the buckling of the Si layer is the more sensitive to the choice of the DFT approximation. In fact, whereas a value of $\varDelta_{Si}$ = 0.76 Å is obtained within GGA, which is quite close to the value of the buckling of a bulk Si(111) biplane (0.78 Å), a significantly higher value is obtained within the LDA. A reasonable explanation can be given considering the different mismatch between Si and Ag bulk lattice constants $f = a_{Si}/a_{Ag}$ computed in the two approximations. Whereas $f_{GGA} = 1.3171$ is close to the experimental value $f_{exp} = 1.3295$, $f_{LDA} = 1.3467$ is larger. The associated compression stress

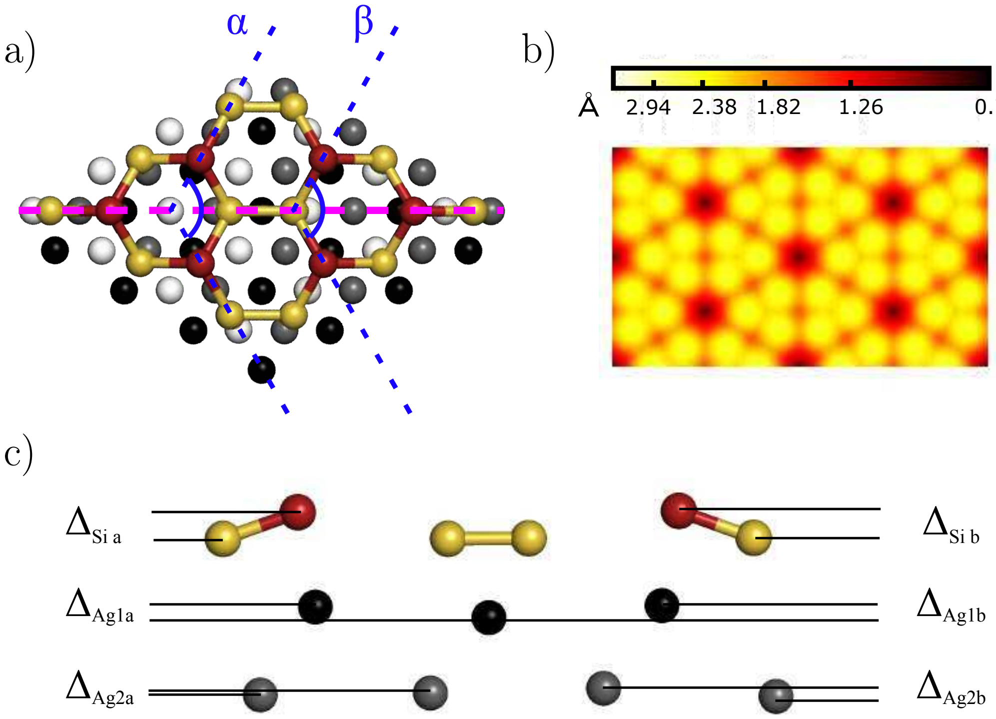

FIGURE 4.8: Top (a) and lateral (c) view of the relaxed (4 × 4) structure on Ag(111). The two Ag bottom layers have been omitted. α and β are the angles indicated by dotted blue lines. The lateral view is a cut along the pink dotted line drawn in (a). b) Simulated STM image of (4 × 4) reconstruction (U=2 V).

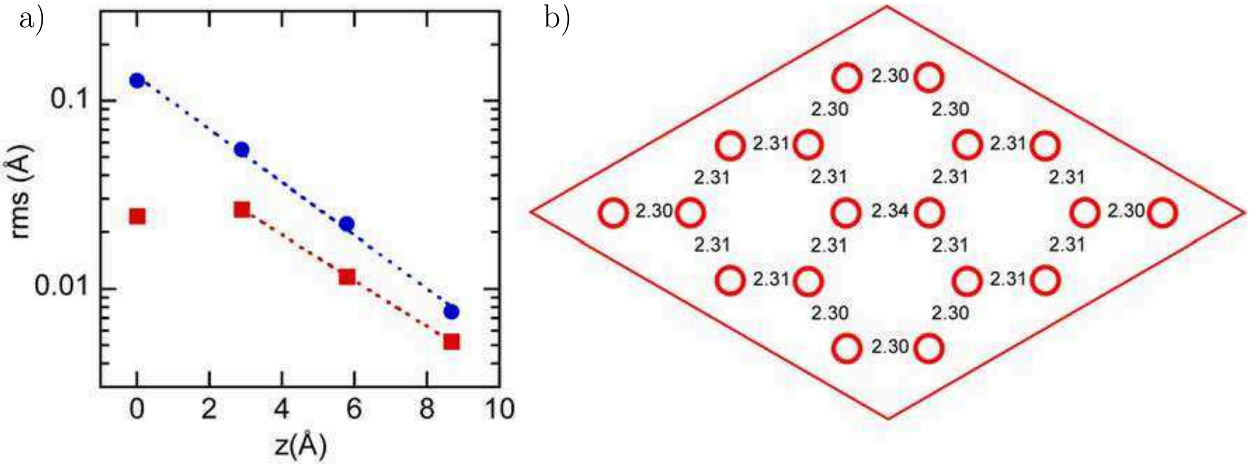

FIGURE 4.9: a) Root-mean-square displacements from the truncated bulk equilibrium positions for Ag atoms as a function of depth (z=0 corresponds to the surface) in semi-logarithmic scale. Red squares: in-plane displacements; blue dots: out-of-plane displacements. Dotted lines correspond to exponential fits and the associated attenuation lengths are $\lambda_{\parallel}$ = 3.58 Å and $\lambda_{\perp}$ = 3.07 Å for the in-plane and out-of-plane set of values, respectively. b) Si-Si bond lengths in the (4 × 4) silicene layer.

		d (Å)	$\Delta_{Si\ a/b}$ (Å)	$\Delta_{Ag1a/b}$ (Å)	$\Delta_{Ag2a/b}$ (Å)	α	β
Free standing silicene	DFT-LDA [1]	2.25	0.44				
(4 × 4) Si/Ag(111)	DFT-GGA [2]	2.35	0.8	0.4			
	DFT-GGA [3]	2.32	0.75			110°	118°
	LEED [4]	2.29-2.31	0.77/0.74	0.29/0.31	0.10/0.21		
	RHEPD [5]		0.83			112°	119°
	DFT-GGA/GIXD	2.30-2.33	0.76	0.25/0.27	0.05/0.24	108.6°	111.1°
	DFT-GGA+vdW	2.30-2.34	0.78/0.79	0.23/0.25	0.04/0.17	108.0°	110.5°
	DFT-LDA	2.33-2.37	0.90/0.91	0.29/0.32	0.07/0.27	105.6°	109.3°

TABLE 4.2: Comparison between the relevant structure parameters obtained in this work and those available in literature, from DFT calculations or experiments. The present DFT-GGA calculations produces the values in better agreement with GIXD results.

induces thus a more pronounced rippling in the Si layer. Nevertheless, in both cases the value is much higher than the one predicted for free-standing silicene, 0.44 Å. Within GGA, the silicon bond lengths obtained are in the 2.30-2.34Å range, which is in between the expected Si-Si length in free-standing silicene (2.25 Å) and the Si-Si nearest-neighbor distance in bulk Si (2.35 Å). The whole set of bond lengths is shown in Fig. 4.9.b. The bond angles can be compared to the ideal angles for sp_2 and sp_3 hybridization. A complete sp_2-hybridization is characteristic of graphene, which has a completely planar structure, i.e. with no buckling of C atoms. Three σ-bonds are formed in-plane, separated by 120°. They result from the superposition of s, p_x and p_y orbitals. In the z direction the π-bands are formed by the coupling of p_z-orbitals between nearest-neighboring atoms. On the contrary, sp_3-hybridization, which is characteristic of bulk Si(111), leads to the formation of a 3D tetrahedral structure. The bonds have an out-of-plane component due to the hybridization of the s-orbital with all three π-orbitals. The angle between each bond is 109.5°. The calculated (4 × 4) structure is an intermediate case, as already reported in the literature [53]. The angles α and β are those used as reference in other papers [3, 5]. The angle α = 108.6° is slightly smaller of the ideal value for a sp_3-hybridization, whereas β=111.1° is somewhat larger. They are both far from the value expected for sp_2-hybridization. Related to the higher buckling of the Si layer, α and β are even lower for the calculations in LDA. The presence of the Si layer clearly affects the structure of the topmost Ag layers. The Ag atoms undergo an out-of-plane relaxation as important as Δ_{Ag1a} = 0.25 Å and Δ_{Ag1b} = 0.27 Å in the first layer, for the left and right half of the reconstruction, respectively, in the GGA results. The most affected Ag atoms are those approximately laying below red Si atoms, i.e. the most protruding ones. The deformation is non-negligible also for the second layer (Δ_{Ag2a} = 0.05 Å and Δ_{Ag2b} = 0.27 Å) and becomes less and less important in the deeper layers. From Table 4.2 it can be noted that these values are not very sensitive to the kind of approximation used. In-plane relaxations occur too, but with an amplitude smaller than for out-of-plane relaxations. They are larger in the second Ag plane than in the first one. The evolution with depth of the root-mean-square displacements is shown in Fig. 4.9a: they decay exponentially in the bulk. By fitting the curves, the associated decay lengths can be extracted: $\lambda_\perp$ = 3.07 Å for out-of-plane relaxations and $\lambda_{\|}$ = 3.58 Å for the in-plane ones. These values are two times lower than the value of $1/k$ = 1.59 Å expected for isotropic crystals, where k is the wave-vector associated with the reconstruction. Such difference is due to the high crystalline anisotropy of Ag [133]. These results as well as the comparison with previous works are reported in Table 4.2.

4.4.2 $(\sqrt{13} \times \sqrt{13})R13.9^\circ$ and $(2\sqrt{3} \times 2\sqrt{3})R30^\circ$ structures

In the case of the $(\sqrt{13} \times \sqrt{13})R13.9^\circ$, a total of six inequivalent configurations have been found, three of *type I* and three of *type II*. For each type, one configuration differs from the other by a translation of the silicene plane equal to $\sqrt{3/2}\, a_{Ag}$ along the [11$\bar{2}$] Ag direction. These configurations have been obtained by changing the occupation of the Wyckoff positions (see Sec.4.4): two of them are always occupied by Si atoms ("t"), while the third is surrounded by an hexagonal Si ring ("h"). In each Wyckoff position there is an Ag atom from a different layer. Depending on which layer has an Ag atom in the same position of the h site, a different configuration is obtained for each type: $t_1t_2h_3$, $t_1h_2t_3$, $h_1t_2t_3$.

Concerning the $(2\sqrt{3} \times 2\sqrt{3})R30^\circ$ reconstruction, also in this case two Wyckoff positions occupied by Si atoms ("t"), with the third is in correspondence of a hexagonal Si ring (h). Indeed, this is not fortuitous: both $(\sqrt{13} \times \sqrt{13})R13.9^\circ$ and $(2\sqrt{3} \times 2\sqrt{3})R30^\circ$ correspond to a $(\sqrt{7} \times \sqrt{7})$ Si cell, which presents this characteristic. All the three high-symmetry points have Ag atoms of the layer in their positions. Depending on whether they belong to the 1st, 2nd or 3rd Ag layer, a different configuration is obtained. In the present work I only have simulated the $h_1t_1t_1$ structure.

The totality of the simulated equilibrium structures and relative STM images obtained by DFT calculations are shown in Fig. 4.10, while the associated structural parameters and energies are reported in Tab. 4.4, which can be compared with the results found in the literature, Tab. 4.3. I report also the results already described for the (4 × 4) reconstruction in order to ease the comparison.

	$2\sqrt{3}$	$\sqrt{13} - type\ I$	$\sqrt{13} - type\ II$
Pflugradt *et al.*	1.12	1.14	0.78
Tchalala *et al.*		1.32	0.78
Enriquez *et al.*	1.0	1.2	0.8
Gao *et al.*	1.19	1.39	
Wang *et al.*	1.19		

TABLE 4.3: Value of the buckling expressed in Å for the $(2\sqrt{3} \times 2\sqrt{3})R30^\circ$ and $(\sqrt{13} \times \sqrt{13})R13.9^\circ - type\ I/II$ reconstructions reported in the literature.

	(4 × 4)	$\sqrt{13} - type\ I$			$\sqrt{13} - type\ II$			$2\sqrt{3}$
	$h_1h_3h_2$	$t_1t_2h_3$	$t_1h_2t_3$	$h_1t_2t_3$	$t_1t_2h_3$	$t_1h_2t_3$	$h_1t_2t_3$	$h_1t_1t_1$
NN-distance (Å)	2.30-2.33	2.32-2.37	2.30-2.39	2.31-2.39	2.31-2.39	2.30	2.32	2.25-2.33
Δ (Å)	0.76	0.78	1.29	0.30	0.71	0.74	0.52	1.10
ϵ_{elas} (eV/Ag(111) unit cell)	0.0205	0.0207	0.0192	0.0054	0.0238	0.0246	0.0030	0.0242
ϵ_{rec} (eV/Si atom)	0.1435	0.1661	0.1661	0.2161	0.1518	0.1496	0.2011	0.1532

TABLE 4.4: Equilibrium structural parameters and energetics information for the DFT-simulated reconstructions. NN-distance is the nearest neighbor distance between Si atoms in the reconstruction, Δ is the value of the buckling; ϵ_{elas} is the energy associated to the elastic deformation of the substrate, while ϵ_{rec} is the energy of the Si atoms in the silicene plane with respect to bulk Si atoms; they are defined in 4–4

Note that the $t_1h_2t_3$ configuration is the only *type I* structure which shows dotted shaped protrusions as those addressed to in the literature [71]. However, the orientations reported do not match with the angle

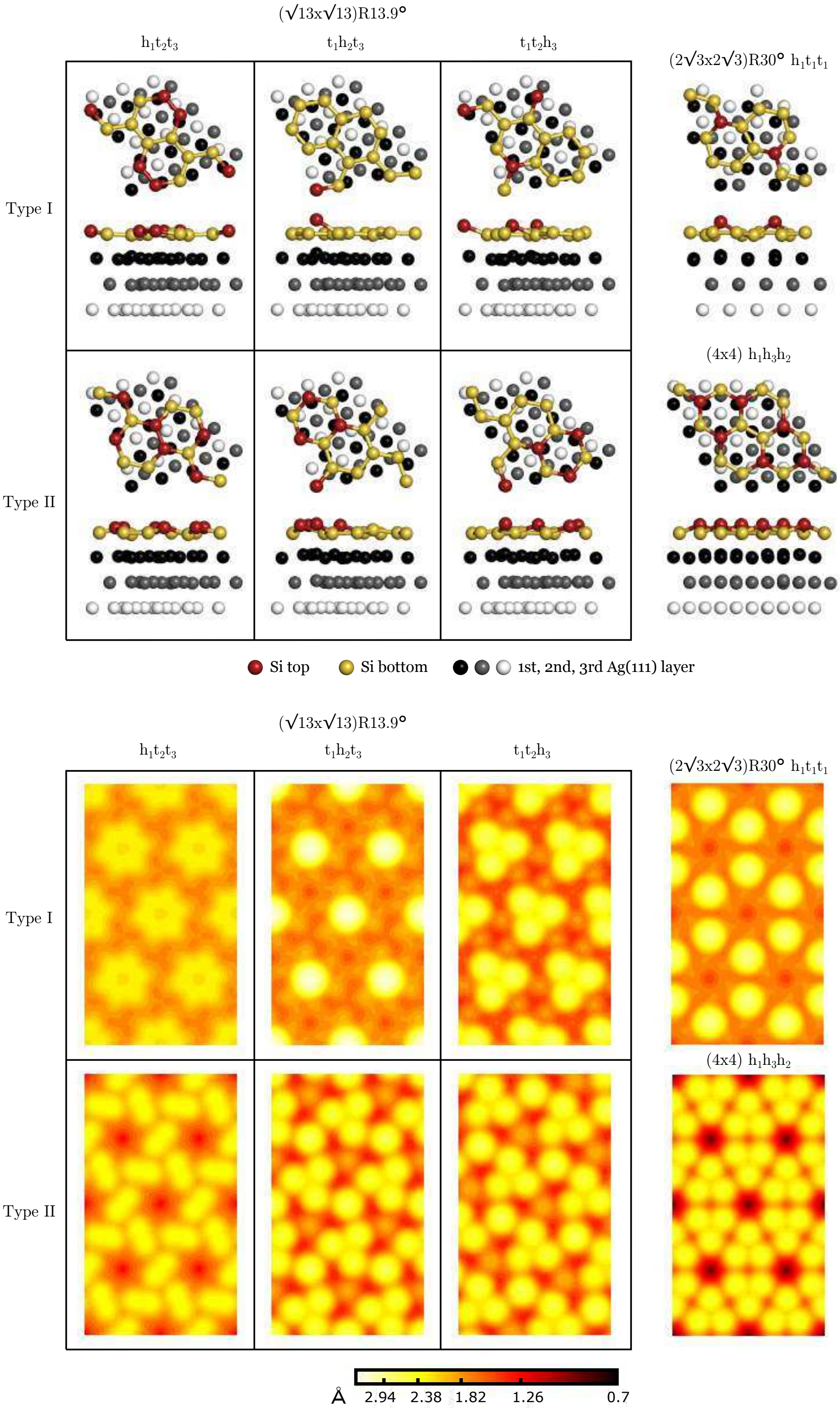

FIGURE 4.10: Top panel: schematics representation of the (4×4), $(2\sqrt{3}\times2\sqrt{3})R30°$ and $(\sqrt{13}\times\sqrt{13})R13.9°$ – *type I/II* equilibrium structures, obtained by DFT calculations. Bottom panel: corresponding simulated STM images.

of the $(\sqrt{13}\times\sqrt{13})R13.9°$ reconstruction. Concerning the *type II* structures, the $t_1h_2t_3$ and $t_1t_2h_3$ configurations correspond to those usually described in the literature: they both have very similar Δ compared to those previously reported (0.71 Å and 0.74 Å *vs.* 0.78 Å and 0.80 Å) and the corresponding simulated STM images are very similar to the experimental ones: trimers of protrusions plus one which links the trimers between them. The structural parameters for the $(2\sqrt{3} \times 2\sqrt{3})R30^\circ$ reconstruction are in good agreement with those previously reported and the same applies to the simulated STM image [72].

4.5 Experimental vs. theoretical structure factors of the simulated reconstructions

In this section I show the comparison between the experimental and theoretical structure factors for the simulated reconstructions. From the atomic positions determined by DFT, one can calculate the theoretical structure factors, by using Eq.2–27. In the present case, the only adjustable parameters are the in-plane and out-off-plane Debye-Weller (DW) factors, for Ag and Si atoms. A scale factor A_0 have been applied to the present measurements, in order to have matching intensities. It is possible to judge the agreement between experimental (F_{exp}) and theoretical (F_{th}) structure factors by invoking the χ^2 test, in which:

$$\chi^2 = \frac{1}{N_{pts} - N_{par}} \sum^{N_{pts}} \left(\frac{F_{th} - F_{exp}}{\sigma_{exp}} \right)^2 \tag{4–3}$$

where N_{pts} is the number of experimental structure factors, and N_{par} is the number of free parameters, σ_{exp} is the experimental uncertainty.

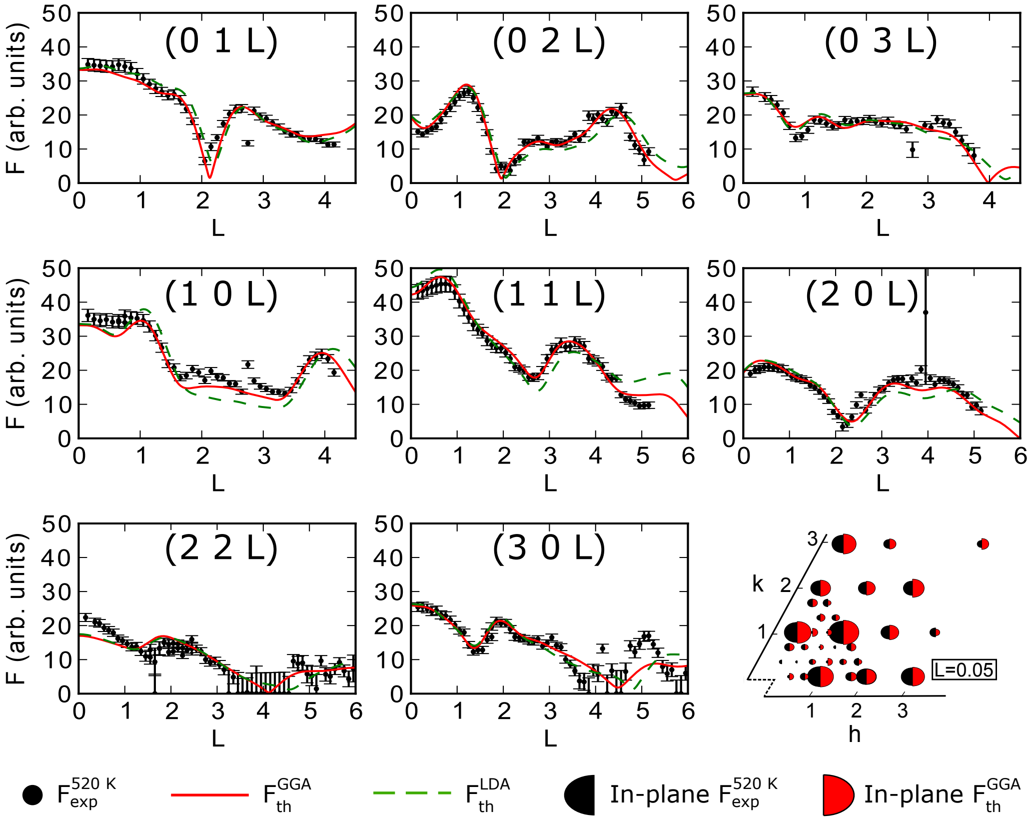

FIGURE 4.11: Comparison between experimental, ($F_{exp}^{520\ K}$, T_{growth} = 520 K), GGA-simulated (F_{th}^{GGA}) and LDA-simulated (F_{th}^{LDA}) structure factors of the (4 × 4) structure , along several superstructure rods and for in-plane diffraction conditions (L = 0.05).

In the sum the discrepancy between experimental value and the theoretical one is compared to the experimental deviation. In the case of a good agreement, the value of the sum is expected to be $\sim N_{pts} - N_{par}$. Thus, the better the agreement the more χ^2 will be close to the unity. The (*h*,*k*) indexes used in this section for labeling a reflection in the reciprocal space refer to the silicene basis of the diffracting reconstruction being taken into consideration. The third index *l* is set identical to the one associated with the Ag(111) surface basis (with *c* axis of norm 7.075 Å).

Let us first consider the (4 × 4) reconstruction. In Fig. 4.11 I show the comparison between the experimental structure factors, obtained for the measurements at 520 K, and the theoretical ones obtained employing GGA and LDA approximations. The theoretical rods look quite similar. Nonetheless, whenever there is a substantial difference with experimental data, GGA simulations (χ^2_{GGA}=5.3) are always qualitatively much better than the LDA ones (χ^2_{LDA}=9.9). In the evaluation of the χ^2_{GGA}, I have used N_{par} = 7, six DW and one scale factor. Accounting for the vdW corrections do not improve the situation (χ^2_{vdW}=7.5). Thus, GGA positions can be considered as the best fit to measurements. For this reason the other reconstructions have been simulated only within GGA, as anticipated in the last section. In conclusion, the comparison between GIXD measurements and DFT results clearly confirms the model proposed in the literature by Vogt *et al.*. Such a structure affects the substrate by inducing a relaxation of the Ag atoms. It is worth noting that even if the Si sheet has an almost perfect hexagonal symmetry, this property is not reflected in the intensity of the superstructure rods. For example, the rods (0 1 *L*) and (1 0 *L*) are separated by an angle of 60° and should be equivalent for symmetry, but instead are remarkably different. This is due to the contribution of the substrate to the diffracted intensity, which has in fact a trigonal symmetry.

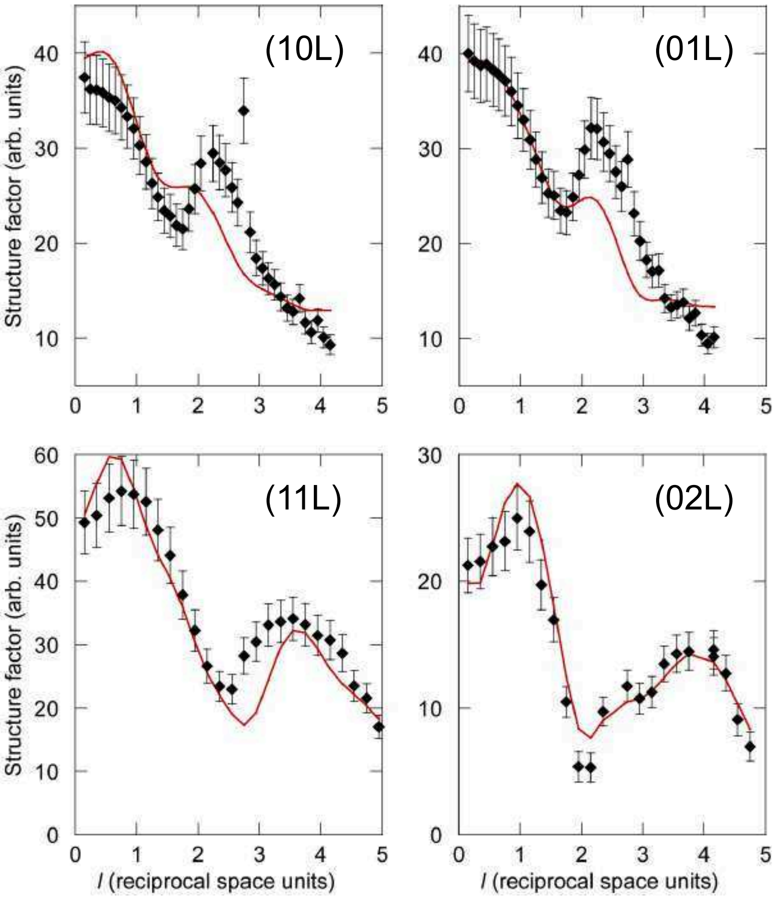

FIGURE 4.12: Comparison between experimental (black dots) and theoretical (red line) structure factors for various rods of the $(2\sqrt{3} \times 2\sqrt{3})R30^\circ$ structures grown at 570 K.

For what concerns the $(2\sqrt{3} \times 2\sqrt{3})R30^\circ$, beside the usual scale factor A_0, I have used only four different values of the Debye-Waller factors, corresponding to in-plane or out-of-plane components, for Si or for Ag atoms. The χ^2 written in Eq. 4–3 evaluates the agreement between experimental (F_{exp}) and theoretical (F_{th}) structure factors. In this case the number of experimental structure factors is N_{pts}=130. Fig. 4.12 shows the comparison between experimental and (black dots) and theoretical (red line) structure factors for the $(2\sqrt{3} \times 2\sqrt{3})R30^\circ$ reconstruction grown at 570 K. The value χ^2 = 2.5 indicates a good agreement. In particular the position of the dips observed in the curves are well reproduced. I have not tried to improve the fit by allowing further relaxation of the atomic positions, since it would involve a huge number of free parameters (14 for Si atoms and 35 for three Ag layer, taking into account the $p3$ symmetry of the structure) with respect to the number of experimental points measured.

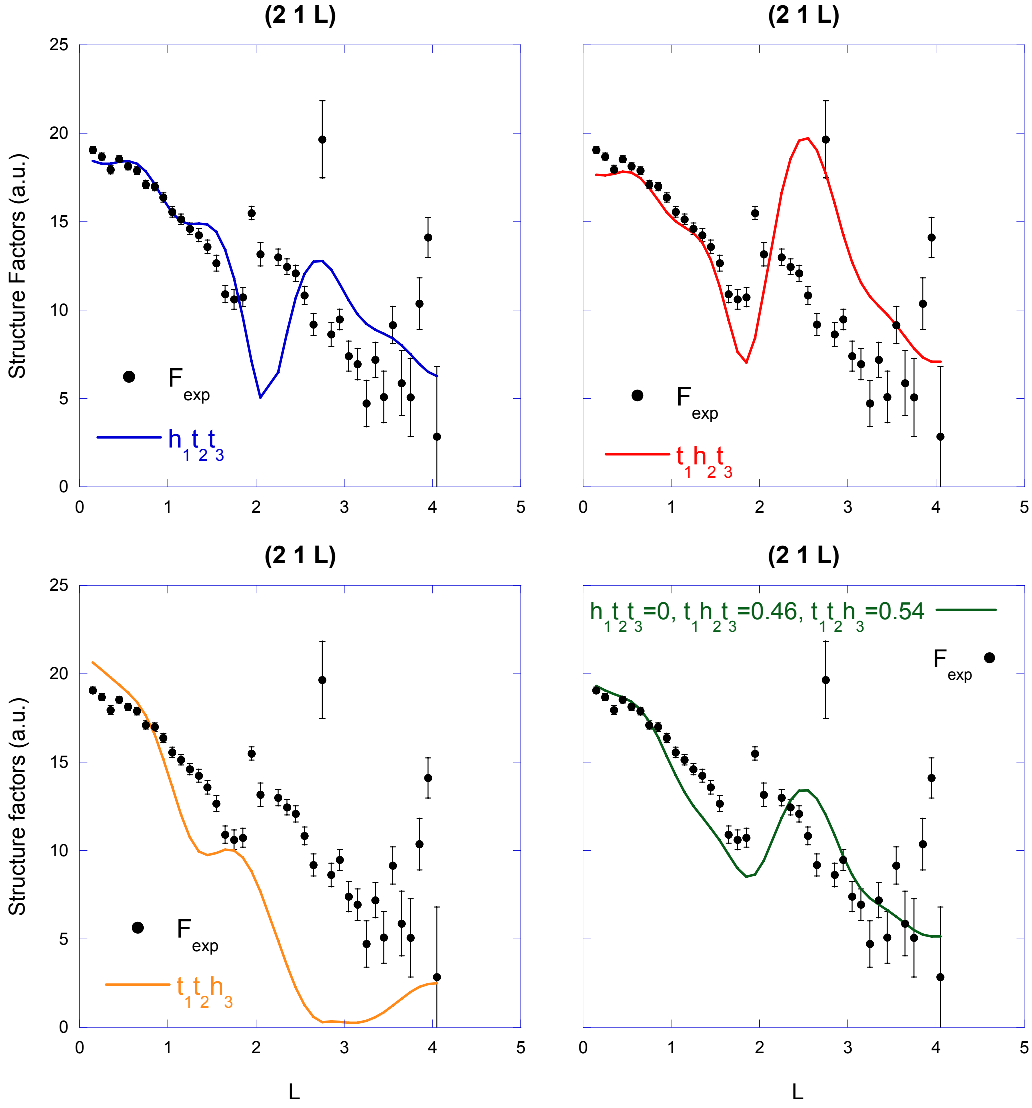

FIGURE 4.13: Comparison between experimental (black dots) and theoretical (solid lines) structure factors for the (2,1,L) rod of the $(\sqrt{13} \times \sqrt{13})R13.9^\circ$ reconstruction grown at 520 K. The theoretical results refers to the three inequivalent configurations of the *type II* structure and a mix of the $t_1h_2t_3$ and $t_1t_2h_3$ configurations.

Finally, I consider the $(\sqrt{13} \times \sqrt{13})R13.9^\circ$ reconstruction, for which one superstructure rod could be analyzed. The theoretical structure factors of the *type I* configurations completely failed to reproduce the experimental data. However, also the results of simulations for the *typeII* structures do not show a perfect agreement with measurements (Fig. 4.13). The best fit consists in a mix of the $t_1h_2t_3$ (54%) and $t_1t_2h_3$ (46%)

configurations. These two structures are also those for which the simulated STM images better reproduce the experimental ones [71].

4.6 Discussion

As already mentioned, the relaxations of surface Ag atoms propagates elastically into the bulk with an exponential decay. GIXD is sensitive to this kind of displacements that give specific contributions to the superstructure rods [134]. Signatures of this effect can be identified, for example, in the peaks near $L = 1$ on the rod $(1\ 0\ L)$ and $(0\ 2\ L)$ SRs of the (4×4) reconstruction on Fig. 4.11, but also in proximity of $L = 2$ on the $(3\ 0\ L)$ rod and in the dip at $L = 2$ on the $(02L)$ rod of the $(2\sqrt{3} \times 2\sqrt{3})R30°$ structure. DFT-GGA simulations set the basis for few considerations on the energetics relative to the relaxation of the substrate and to the silicene layer. The (4×4) structure in this case has been simulated with the same parameters (cut-off energies, smearing, k-point grid, number of Ag layers in the slab) used for the other reconstructions. In Tab. 4.4 I have reported the values of ϵ_{elas} and ϵ_{rec}. These two quantities have been introduced to evaluate the energy associated with the elastic deformation of the substrate of the single Ag(111) unit cell (ϵ_{el}) and the energy of one atom in the Si layer with respect to bulk Si atom (ϵ_{rec}). These two quantities have been calculated thanks to the determination of three energies:

- the energy of the equilibrium slab of a certain reconstruction, E_{slab};
- the energy of the Ag surface when it is stripped of the Si atoms, $E_{slab-Si}$;
- the energy of the clean Ag(111) relaxed surface, $E_{bare\ Ag}$.

Thus, I can calculate ϵ_{elas} and ϵ_{rec}:

$$\begin{aligned} \epsilon_{elas} &= \frac{E_{slab-Si} - E_{bare\ Ag}}{N_{Ag\ cells}} \\ \epsilon_{rec} &= \frac{E_{slab} - E_{slab-Si}}{N_{Si\ rec}} - E_{Si}^{blk} \end{aligned} \tag{4–4}$$

in which $N_{Ag\ cells}$ is the number of the Ag(111) cells of the reconstruction, $N_{Si\ rec}$ is the number of Si atoms in the silicene layer in simulated slab and E_{Si}^{blk} is the cohesive energy of a Si atom in the diamond lattice. The systems associated to E_{slab}, $E_{slab-Si}$ and $E_{bare\ Ag}$ are depicted in Fig. 4.14.

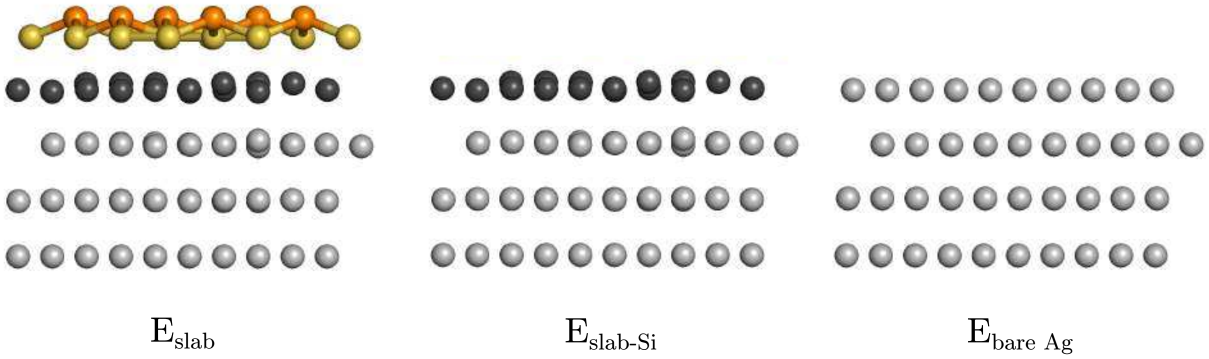

FIGURE 4.14: Schematics of the calculated structures and the relative energies, used to estimate the energy of the elastic deformation in the substrate.

From the structural parameters and the values of ϵ_{elas} and ϵ_{rec} reported in Tab. 4.4 I can make few considerations about the energetics of the different reconstructions. Firstly, it is interesting to note that the two $h_1t_2t_3$ configurations have the most similar buckling and and nearest-neighbor distance (NND) compared to free-standing silicene, which should posses a NND of 2.25 Å and a buckling of 0.44 Å [1]. For this reason, one could expect this arrangement to be quite stable. Instead, the value of ϵ_{rec} is the highest for this configuration compared to the other monolayer structures, indicating rather the opposite. At the same time, the two Si structure with $h_1t_2t_3$ configuration induce very little deformation in the substrate; the deformation energy is estimated to be ϵ_{elas}=0.0054 eV/Ag(111) unit cell and 0.0030 eV/ Ag(111) unit cell for *type I* and *type II*, respectively. The four most stable structures according to the value of ϵ_{rec} are the (4 × 4), the $(\sqrt{13} \times \sqrt{13})R13.9° - type\ II$ in $t_1h_2t_3$ and $t_1t_2h_3$ configuration and the $(2\sqrt{3} \times 2\sqrt{3})R30°$ structures. Their values of ϵ_{elas} are much higher than the previously discussed $h_1t_2t_3$ structures.

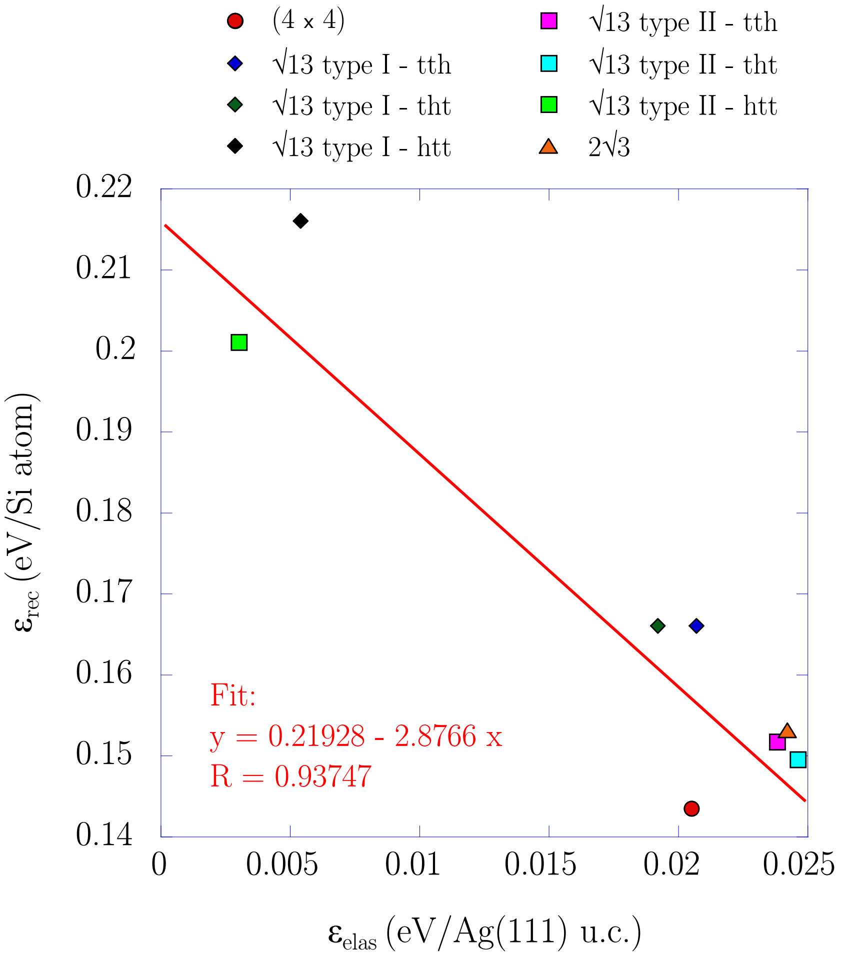

FIGURE 4.15: Plot of the energy associated with the elastic deformation of the substrate of the single Ag(111) unit cell (ϵ_{el}) as a function of the energy of one atom in the silicene layer with respect to bulk Si atom (ϵ_{rec}) for different surface reconstruction.

The $t_1t_2h_3$ and $t_1h_2t_3$ configurations of the *type II* reconstruction have very similar atomic configurations: the buckling of the silicene layer is 0.71 Å and 0.74 Å, respectively, while they both show NNDs in the 2.31-2.39 Å range. This value is very close to the one observed for the (4 × 4) reconstruction, for which Δ=0.76 Å. Moreover, also the simulated STM images of the *type II* $t_1t_2h_3$ and $t_1h_2t_3$ structures, reported in Fig. 4.10, show the same features. This similarity is not surprising: the structure of these two configuration is almost the same, except for the fact that the h site corresponds with a Ag of the second layer for the $t_1h_2t_3$ configuration and with one of the third layer in the case of the $t_1t_2h_3$ configuration. Both of them have been experimentally observed in ref. [71] by STM. Concerning *type I* models, $t_1t_2h_3$ and $t_1h_2t_3$ configurations have the same value of E_{rec}, but their structures and relative STM images are markedly different: the former presents three protruding Si atom and a buckling of 0.78 Å, while the latter has only one protruding atom and a much higher buckling value, namely 1.29 Å. By plotting the values of ϵ_{rec} as a function of ϵ_{elas}, Fig. 4.15, I find an interesting trend: the reconstructions with a higher elastic energy associated to the relaxation of the Ag substrate (ϵ_{elas}) are also those having a lower energy in silicene layer (ϵ_{rec}). Moreover, a higher ϵ_{elas} is associated to a larger buckling. Thus, the structural characteristics predicted for the FSS are not those energetically favored for a silicene layer on Ag(111), which prefers to be more corrugated inducing, eventually, a larger deformation in the first layers of Ag(111), with respect to the low-buckled $h_1t_2t_3$ configurations of the $(\sqrt{13} \times \sqrt{13})R13.9^\circ$ reconstruction, characterized by a small substrate deformation but an high energy of the Si layer.

4.7 Summary of the results of Chapter 4

By combined GIXD measurements and DFT calculations I have investigated the exact atomic structure of three silicene surface reconstructions, namely the (4×4), the $(\sqrt{13} \times \sqrt{13})R13.9^\circ$ and $(2\sqrt{3} \times 2\sqrt{3})R30^\circ$ phases, their stability and their interaction with the substrate.

- The (4×4) reconstruction (model proposed by Vogt *et al.* [3]) has been simulated within three approximations: LDA, GGA and GGA+vdW. The structure factors calculated from the GGA equilibrium positions give the best agreement with the experimental GIXD structure factors. The (4×4) silicene layer shows a buckling of 0.76 Å and an inter-atomic distance of 2.30-2.33 Å. The elastic deformations induced in the Ag(111) surface are exponentially damped in the first substrate layers.

- The $(2\sqrt{3} \times 2\sqrt{3})R30^\circ$ is observed in coexistence with the (4×4) reconstruction at T_{growth}=570 K, but it deviates from its ideal 30° orientation with respect to the Ag(111) substrate. Its equilibrium structure has a 1.10 Å buckling and 2.25-2.33 Å inter-atomic distances, according to present results.

- Concerning the $(\sqrt{13} \times \sqrt{13})R13.9^\circ$ reconstruction I have simulated all the inequivalent configurations for the so called *type I* and *type II* structures. Depending on the configuration, quite different buckling values have been obtained (see Tab. 4.4). The experimental structure factors could be reproduced only by taking into consideration a mix of $type\ II - t_1h_2t_3$ and $type\ II - t_1t_2h_3$ configurations. I could not obtain any evidence of the presence of the *type I* structure in the silicene layer.

- From DFT results I could draw some important conclusions concerning the stability of the reconstructions. In particular, I have observed that the surface structures inducing the higher deformation in the Ag(111) substrate (higher elastic deformation ϵ_{elas}) are also the most stable (lower energy of the silicene layer ϵ_{rec}). Thus, according to present results, **the interaction with the substrate is responsible for the stabilization of the silicene layer**.

Chapter 5

Atomic structure of Si thin films on Ag(111)

5.1 Introduction

In the previous chapter I have discussed the most common configurations of silicon monolayers on Ag(111). Despite the intriguing properties predicted for the free-standing form, silicene on Ag(111) is characterized by a strong layer-substrate interaction which strongly affects the electronic properties of the system compared to the free-standing silicene. It has been suggested that this drawback could be overcome by decoupling the silicene layer from the substrate [7, 135], either by transferring the silicon monolayer on a different substrate [136] or by growing a stacking of low-interacting silicene layers, forming a pseudo-layered material. In the latter case one could expect that the silicene layers on top of the stack weakly interact with the Ag substrate, recovering the free-standing-like properties, in analogy to bilayer graphene on SiC [137, 138]. This stacking of silicene layers, has been named *multi-layer silicene* or *silicite*, in analogy to *graphite*, the layered allotrope of carbon.

A possible way to synthesize this new material could be the deposition of thick Si films ($>$ 1 ML) on Ag(111), hoping this could lead to the realization of a "pile" of silicene layers, as those described in Chapter 4, connected by weak inter-planar forces.

This kind of experiment has been realized by several research groups, but the existence of the so-called *silicite* (or *multilayer silicene*) is highly controversial [6, 7, 9, 67, 81, 83, 139–142].

The first striking observation, which resulted from these experiments, was the one announced by Wu's group [24, 54], which reported the formation of a new unexpected reconstruction, with an apparent $(4/\sqrt{3} \times 4/\sqrt{3})$ unit cell with respect to the Ag(111) substrate. This reconstruction, also called $(\sqrt{3} \times \sqrt{3})R30^\circ$ when referred to a silicene plane, arises at the surface of the Si film on Ag(111), for a Si coverage above θ_{Si}=1 monolayer (ML) [37, 56, 81, 83, 139], and it has never been observed neither for the silicene monolayer nor for pristine Si(111) [83, 143]. In the following, 1 ML corresponds to a complete (4×4) silicene layer, i.e. 18/16 of the atomic density of a Ag(111) plane. This is only 0.8% less than the atomic density of a Si(111) biplane in bulk silicon. The $(\sqrt{3} \times \sqrt{3})R30^\circ$ reconstruction, which remains visible even for 16 ML deposits [6], has been interpreted as a first experimental evidence of the realization of a new silicon allotrope, along with other proofs supporting this thesis. In particular, De Padova *at al.* have shown that:

- the Raman peak obtained for these thick Si films is at 523.26 cm^{-1}, i.e. 2.86 cm^{-1} higher than the reference value of Si(111) at 520.40 cm^{-1} [6];
- the Si inter-layer spacing measured from *ex-situ* XRD experiments is 1% smaller than (111) interplanar distance in bulk Si [6].

In another work, De Padova *et al.* have discussed the effect of the temperature in the growth of what they claim to be multi-layer silicene. More in detail, using *ex-situ* energy dispersive grazing incidence x-ray diffraction (ED-GIXD), they have measured the lattice constant of 10 ML thick Si films grown at either 473 K or 573 K. Diamond-like Si is observed after growth at T_{growth}=573 K. Instead, after growth at T_{growth}=473 K, the diffraction pattern shows that the in-plane lattice constant of the Si film is 3.740 Å, i.e. 2.7% lower than the value found for Si(111) (3.841 Å). In their measurements, the out-of-plane lattice constant displays also a weaker contraction, in the order of 1.5%. They have concluded that the crystal structure of the Si film differs from the one of diamond and that multilayer silicene forms for low temperature growth, whereas deposition at higher temperatures leads to the formation of 3D Si crystallites.

A first consideration about these two different temperature-dependant growth regimes can be done by looking at previously reported results. I have shown in Chapter 4, that the (4×4) and $(\sqrt{13} \times \sqrt{13})R13.9^\circ$ silicene phases preferentially form at low temperature, whereas the $(2\sqrt{3} \times 2\sqrt{3})R30^\circ$ phase is generally seen for growth at T_{growth} >540 K [3, 25, 59]. This temperature also corresponds to a transition observed during multilayer growth. In fact, above T_{growth}=540 K, the growth of the second silicon layer is accompanied by a dewetting of the first layer, leading to the recovery of bare Ag surface regions [59, 144–146]. On the contrary, the silicene monolayer does not dewet below T_{growth}=540 K, but is progressively replaced by the growing film [6, 9, 81, 83]. Thus, if one assumes, following De Padova and collaborators, that there exists a transition temperature for the structure of thick Si films grown on Ag(111), it is reasonable to assign this temperature to the *transition temperature* T_c=540 K above which silicene monolayer dewets right before reaching completion.

Despite their important claim, De Padova *et al.* do not put forward any structural model for silicite which could explain their findings.

However, Rubio's group has proposed an original model for *silicite* [135, 147]. According to their calculations, above 1 ML coverage Si atoms may form dumbbell geometries (DB) arranged in a $(\sqrt{3} \times \sqrt{3})$ honeycomb superlattice. They hve put forward a growth model in which the (4×4) reconstructed silicene layer formed on Ag(111) gradually transforms in this new superlattice by the adsorption of Si atoms, as depicted in Fig. 5.1. The trigonal dumbbell silicene (TDS) and hexagonal dumbbell silicene (HDS) configurations, proposed in Cahangirov's work, have 1/6 and 1/3 of a Si layer adsorbed in DB configuration, respectively. The HDS structure is found to be energetically more favorable. However, during the growth of successive planes, the HDS is forced to change to TDS to enable the formation of a Si-Si bond with the second grown layer. Thus, the silicite models proposed consist of a staking of TDS Si planes. Note that, because of the perpendicular Si-Si chemical bonds in each unit cell which connect the adjacent TDS layers, the interaction is not van der Waals-like, as is in graphite or MoS_2 [148], but still the inter-layer interaction is predicted to be weaker than in Si(111). Yet the inter-planar distance does not match with the value determined by De Padova *et al.* (4.29 Å *vs.* 3.09 Å, respectively).

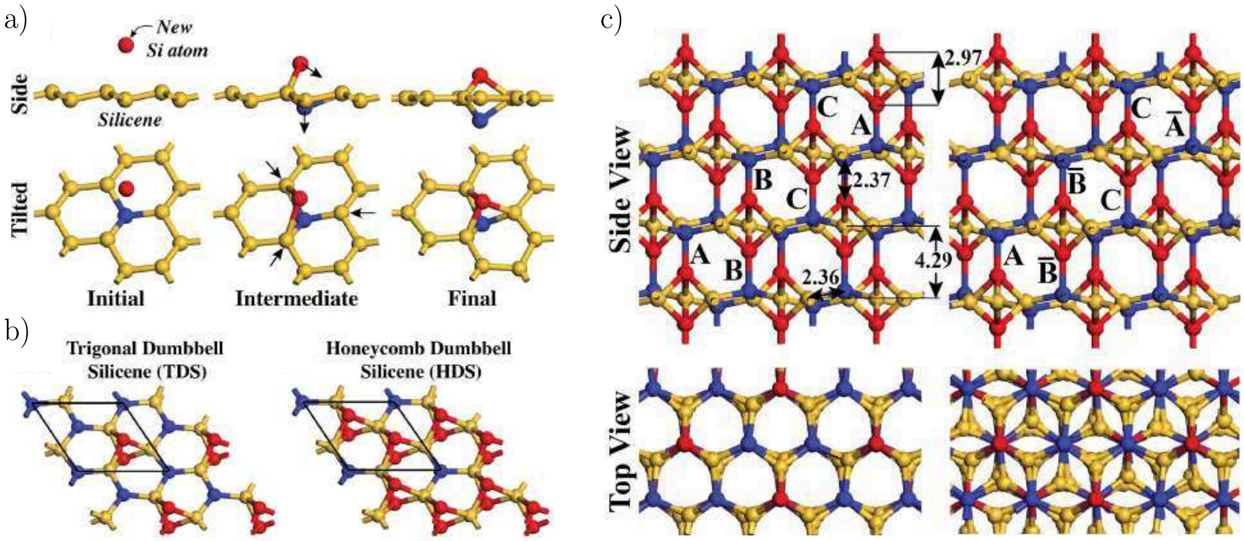

FIGURE 5.1: Models and growth mode proposed by Cahangirov *et al.* [135, 147]. a) Transition from a perfect silicene (4×4) layer to the DB building block unit. b) Atomic structure of $(\sqrt{3} \times \sqrt{3})$ trigonal DB silicene (TDS), in which 1/6 of a Si plane is adsorbed in DB configuration, and honeycomb DB silicene (HDS) in which 1/3 of the atoms are adsorbed in DB configuration. c) Side and top view of the silicite model obtained stacking together TDS Si layer. Two different ways of stacking are possible.

Successful multilayer silicene synthesis has been put into questions by other experimental studies performed by independent groups, e.g. by low-energy electron diffraction (LEED) experiments on Si thick films grown at T_{growth}=500 K.

These data have been interpreted in the following way. The $(\sqrt{3} \times \sqrt{3})R30^\circ$ reconstruction at the surface of Si islands (thick $\geq$ 2 ML) is explained by the presence of Ag atoms adsorbed on the top of the Si surface. Moreover, the structure of the Si film is found to be compatible with that of a thin film of bulk-like diamond Si film. The $(\sqrt{3} \times \sqrt{3})R30^\circ$ surface structure is similar to the well-known $(\sqrt{3} \times \sqrt{3})R30^\circ$ reconstruction observed when Ag atoms are adsorbed on the (111) surface of diamond Si [10, 149]. The same conclusion has been put forward on the basis of a comparison between STM measurements performed on Si/Ag(111) and on Ag/Si(111) films in the 473 K-623 K temperature range [8], and by some experimental results I obtained during my internship, before the beginning of the PhD. From Auger electron spectroscopy (AES) and optical reflectance measurements, I have shown that the optical response of thick (>10 layers) Si/Ag(111) films grown at T_{growth}=473 K or 503 K is similar to the one of diamond-like bulk Si, and that Ag atoms were segregated at the surface during growth [9]. The ABC stacking of Si biplanes, similar to the one of diamond-like Si has been also evidenced by STM [150], whereas the Ag termination of the surface has been confirmed by core-level photoemission spectroscopy (XPS) measurements (T_{growth}=503 K) [151, 152], angle-resolved photoemission spectroscopy (ARPES) measurements (473 K $\leqslant T_{growth} \leqslant$ 543 K) [152], metastable atom electron spectroscopy (T_{growth}=500 K), and by deuterium exposure of the surface leading to the formation of Ag 3D islands (450 K $\leqslant T_{growth} \leqslant$ 550 K) [144].

Despite these last experimental evidences, the controversy on multi-layer silicene growth is far from being over. In fact, the origin of the differences observed by Raman and X-ray diffraction (XRD) between Si/Ag films and bulk Si is not fully understood, and no structural model has been validated up to date.

In this chapter I tackle the question of the atomic structure of the Si film by means of grazing incidence X-ray diffraction (GIXD), which is, as already stressed out, a powerful technique for the *in-situ* crystal structure determination of epitaxial films. I will present the measurement performed in the low-temperature regime T_{growth}=510-520 K, for which De Padova *et al.* have claimed the formation of multilayer silicene, on a 8 ML thick Si film on Ag(111). The present measurements show that all the diffraction spots associated with the Si film can be labeled according to a defective bulklike diamond Si (symmetry group $Fd\bar{3}m$) possibly with stacking faults along the direction perpendicular to the surface, ruling out the hypothesis of multilayer silicene or silicite .

5.2 Atomic structure of the Si film

In Chapter 4, I by means of GIXD experiments that for 1 ML Si evaporation on Ag(111) at T_{growth}=520 K, the silicene layer is preferentially formed by a (4×4) silicene structure with a small fraction of $(\sqrt{13} \times \sqrt{13})R13.9^\circ$ [64]. Here I present a study conducted in the same temperature range on a thicker Si deposit, namely 8 MLs, as estimated from surface differential reflectance spectroscopy (see Sec. 2.5). After growth, a good agreement for the film thickness is found with X-ray reflectivity (XRR) measurements; the comparison between experimental and simulated XRR has already been shown in Sec. 2.4.2.4.

De Padova *et al.* have stressed the important role of the temperature. As mentioned before, the low-temperature regime, for which multi-layer silicene growth is claimed, coincides with that range of temperatures in which the silicene layer is mainly composed by (4×4) and $(\sqrt{13} \times \sqrt{13})R13.9^\circ$ reconstructions. Using the same kind of real-time measurements described in section 4.3, I have verified that these two reconstructions were actually the only visible below 1 ML coverage, confirming that the experiments were conducted in the low-temperature regime, i.e. below T_c.

5.2.1 Diamond structure and epitaxy relations

Fig. 5.2 shows various maps of the diffracted intensity after Si deposition. They correspond to the intensity measured for reciprocal space planes perpendicular to the sample surface. Crystal truncation rods (CTRs) at integer values for *h* and *k* correspond to the diffraction from the Ag interface, and the intense spots at (101), (202), (110), (113), to the Bragg diffraction conditions for the Ag crystal, in the surface unit cell coordinates. Other spots are visible which were not present for the ML deposit. They correspond to the diffraction from the silicon thin film.

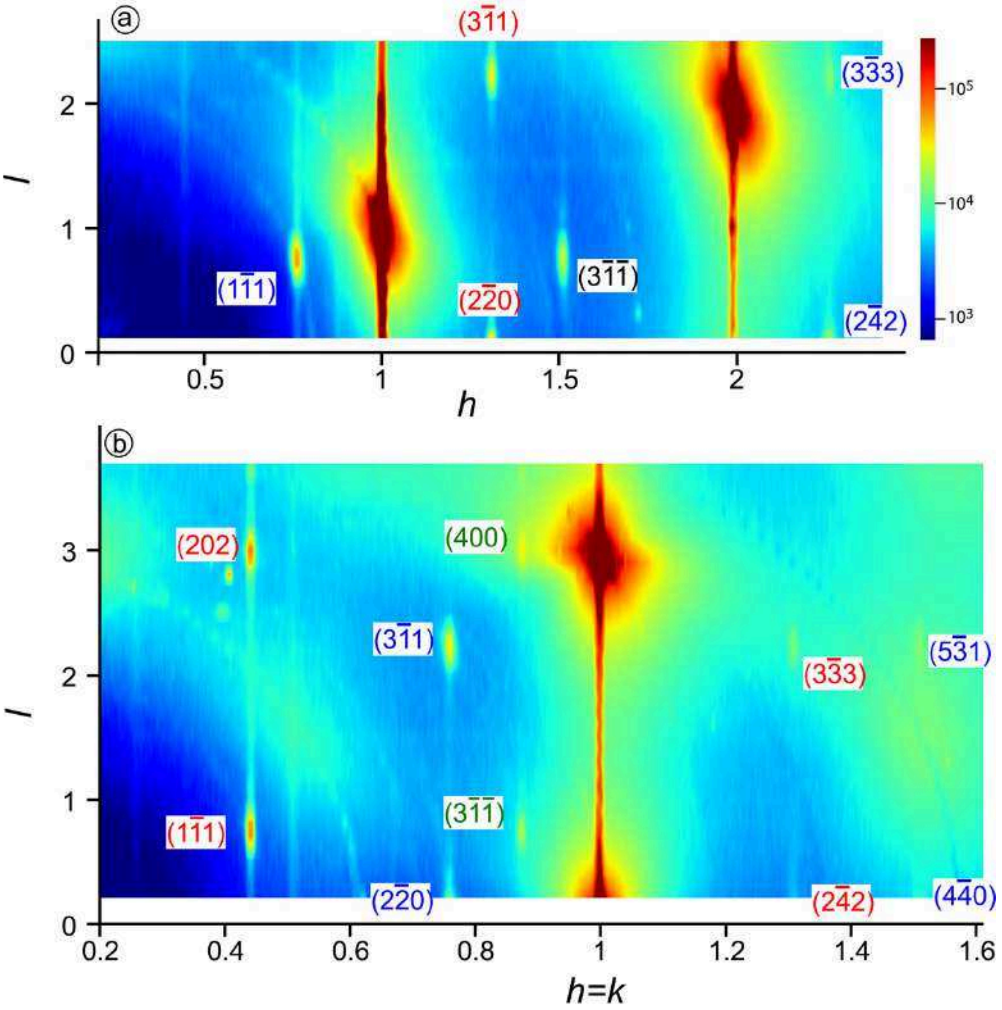

FIGURE 5.2: Maps of the intensity diffracted by 8 ML Si evaporated on Ag(111) at T_{growth}=520 K. Measurements are performed at the same temperature. a) for $k = 0$, b) for $h = k$. The color scale is the same for both maps. The indexed spots belong to diamond-like silicon with four orientations (corresponding to blue, red, green and black labels). The indexing refers to the Ag(111) substrate.

First of all, I extract from the data the measured value of the momentum transfer q_{exp}, associated with a certain diffraction spot (Tab. 5.1). A rather small number of different values are found for q_{exp}. Thus, I expect a simple structure for the Si thin film and so, as a first try, I have labeled its diffraction spots according to a diamond structure.

Bragg's law states states that the measured value of q_{exp} associated with a certain spot must be equal to a reciprocal space vector of Si. This conditions writes:

$$q_{exp} = \frac{2\pi}{a_{Si}}\sqrt{H_{Si}^2 + K_{Si}^2 + L_{Si}^2} \tag{5–1}$$

where a_{Si}=5.431 Å is the lattice parameter of bulk silicon and H_{Si}, K_{Si}, L_{Si} are the Miller indexes of Si in the cubic lattice. The distance between two spots, Δq, is associated with a distance d:

$$d = \frac{2\pi}{\Delta q} \tag{5–2}$$

This condition is used in the next section to calculate the lattice parameters of the Si film.

h	k	l	$\{H_{Si}K_{Si}L_{Si}\}$	q_{th}	q_{exp}
0.43	0.43	0.75	{1 1 1}	2.00	2.00
0.75	0.00	0.75	{1 1 1}	2.00	2.01
0.75	0.76	0.15	{2 2 0}	3.27	3.28
1.31	0.00	0.15	{2 2 0}	3.27	3.28
0.43	0.43	3.05	{2 2 0}	3.27	3.30
0.87	0.87	0.75	{3 1 1}	3.84	3.84
1.50	0.00	0.75	{3 1 1}	3.84	3.85
0.75	0.75	2.25	{3 1 1}	3.84	3.84
1.31	0.00	2.25	{3 1 1}	3.84	3.84
0.87	0.87	3.05	{4 0 0}	4.63	4.66
1.31	1.31	0.15	{2 4 2}	5.67	5.70
2.27	0.00	0.15	{2 4 2}	5.67	5.69
2.27	0.00	2.25	{3 3 3}	6.01	6.03
1.31	1.31	2.25	{3 3 3}	6.01	6.02
1.51	1.51	0.15	{4 4 0}	6.54	6.57
1.51	1.51	2.25	{5 3 1}	6.84	6.87

TABLE 5.1: Comparison between q_{exp} of several diffraction spots and q_{th} calculated starting by the guess values H_{Si}, K_{Si} and L_{Si}. These same values identify the diffraction planes for a diamond structure associated with the Si film. Note that the in-plane spots cannot be measured below l=0.15.

Here, I want to determine the value of the momentum transfer q_{th} which satisfies the diffraction condition in Eq. 5–1 for a certain spot. To achieve this goal, an ansatz is put forward for the values of H_{Si}, K_{Si} and L_{Si} so I can calculate the expected value of the momentum transfer q_{th}. If its value matches with the measured value q_{exp}, the spot is associated with the family plane identified by (H_{Si},K_{Si},L_{Si}). All the measured diffraction spots are associated with a bulk diamond-like silicon film with (111) epitaxy and they identify the {111}, {220}, {311}, {400}, {242}, {333}, {440}, {531} families of lattice planes of Si. The values are reported in Tab. 5.1.

Most importantly, the identified families of diffraction planes satisfy the *non-extinction conditions* for the diamond structure: (H_{Si}, K_{Si}, L_{Si}) have the same parity and $H_{Si} + K_{Si} + L_{Si} \neq 4n + 2$, see Annex B.

The labeling of the diffraction spots according to the diamond structure of Si and the fulfillment of the relative extinction conditions unambiguously demonstrates the diamond structure of the Si film, rejecting the interpretation of multilayer silicene or silicite having structural cheractristincs different from diamond

Si. The diamond structure is depicted in Fig. 5.3. It can be described by a cubic Bravais lattice with a 8-atoms basis. This configuration forms a tetrahedrical structure where each green atom is surrounded by four equal-distanced neighbors (red spheres).

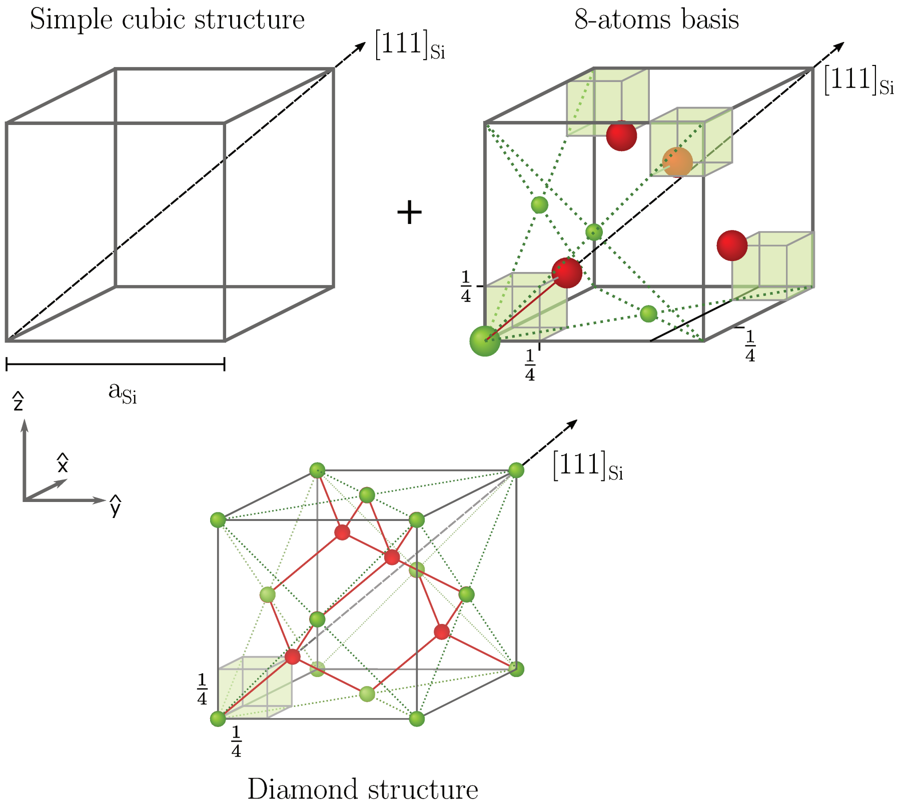

FIGURE 5.3: Unit cell of the monoatomic diamond lattice (bottom), depicted as an simple cubic Bravais lattice with 8-atoms basis (top).

Other important information obtained obtain from Fig. 5.2, is that no signal can be seen in the positions expected for the (4×4) and $(\sqrt{13} \times \sqrt{13})R13.9°$ reconstructions. That is, for this Si coverage the two reconstructions that characterize the presence of the silicene monolayer have disappeared. This is in good agreement with STM and LEED observations for thick Si/Ag(111) films prepared under similar conditions [6, 9].

In order to determine the sign of H_{Si}, K_{Si} and L_{Si} for a certain diffraction spot, I compare the experimental value of $cos(\alpha_{exp})$, i.e. the angle between the crystallographic direction identified by the spot and the direction [111] of Si perpendicular to the surface, with the theoretical one $cos(\alpha_{th})$, in the expression of which I specify the sign of H_{Si}, K_{Si}, L_{Si}:

$$cos(\alpha_{exp}) = \frac{q_{\perp,exp}}{|\boldsymbol{q}_{exp}|}; \qquad cos(\alpha_{th}) = \frac{(H_{Si}K_{Si}L_{Si}) \cdot (111)}{|(H_{Si}K_{Si}L_{Si})||(111)|} \tag{5–3}$$

$q_{\perp,exp}$ is the component of transferred wavevector $\boldsymbol{q}_{exp}$ perpendicular to the surface. Note that one can always find a permutation of $\pm H_{Si}, \pm K_{Si}, \pm L_{Si}$ so that, for a certain spot, the angle between (h, k, l) and (001) corresponds to the one between (H_{Si}, K_{Si}, L_{Si}) and (111): this show that that the Si film has a (111) epitaxy. However, in order to determine the exact crystallographic direction identified by a certain spot, I need to find the right order of the Miller indexes associated with this spot, which is done by comparing the angle between (h_1, k_1, l_1) and (h_2, k_2, l_2) with the angle between $(H_{Si,1}, K_{Si,1}, L_{Si,1})$ and $(H_{Si,2}, K_{Si,2}, L_{Si,2})$ ("1" labels the first spot and "2" the second one) in order to find a match. With this procedure I can also find spots belonging to different rotational domains.

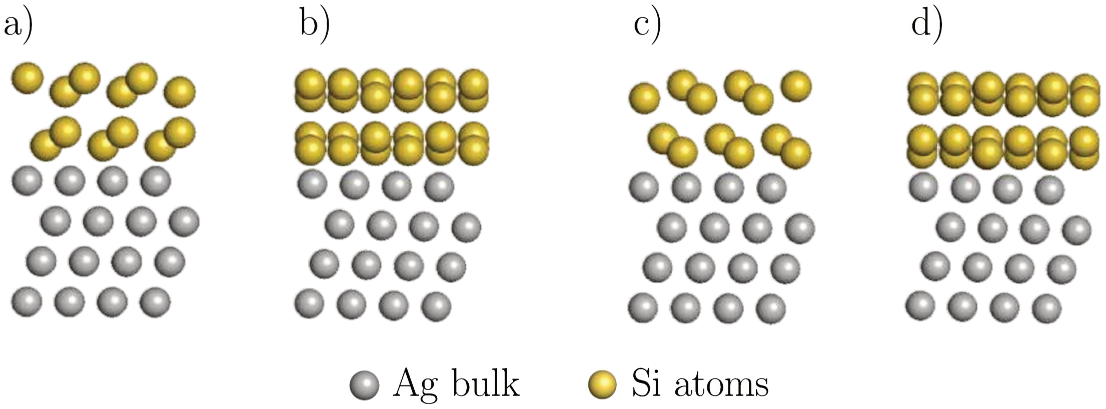

FIGURE 5.4: Schematics of the four rotational domains found for the bulklike diamond Si film grown onto Ag(111), seen along $[1\bar{1}0]_{Ag}$ direction. a-c) $[1\bar{1}0]_{Si} \parallel [1\bar{1}0]_{Ag}$ and ABC or ACB stacking for Si planes respectively; b-d) $[1\bar{1}0]_{Si} \parallel [1\bar{2}1]_{Ag}$ and ABC or ACB stacking in the Si film.

From the diffraction maps in Fig. 5.2, I can identify four rotational domains for the Si film, corresponding to $[1\bar{1}0]_{Si} \parallel [1\bar{1}0]_{Ag}$ or $[1\bar{1}0]_{Si} \parallel [1\bar{2}1]_{Ag}$ and ABC or ACB stacking for the successive Si double planes. These rotational domains are depicted in Fig. 5.4. Diffraction rods passing through the Si film spots can be associated with the truncation of the Si film, whereas other rods faintly visible at $(h,k) \approx (0.25, 0.25)$ and $(h,k) \approx (0.5, 0.5)$ for the $[1\bar{1}0]_{Si} \parallel [1\bar{1}0]_{Ag}$ epitaxy and at $(h,k) \approx (0.433, 0)$ and $(h,k) \approx (0.866, 0)$ for the $[1\bar{1}0]_{Si} \parallel [1\bar{2}1]_{Ag}$ epitaxy can be associated with the $(\sqrt{3} \times \sqrt{3})R30^\circ$ reconstruction of the Si surface; they are discussed in the next chapter.

A wide azimuthal angle scan corresponding to $(3\bar{1}1)$-oriented Si planes is shown in Fig. 5.5. Various peaks are visible. I have fitted the signal with a combination of Voigt curves. From this scan I see that there are more orientations of the Si film than the four ones identified in Fig. 5.2. Orientations 0°, 1.08°, 10.91°, 25.32°, 36.54°, 30° and their symmetry with respect to 30° are obtained from the fits. This result is similar to that found by LEED [81], which reported angles of 3°, 24.8° and 30° after growth at 510 K.

Similar observations can be made around the other diffraction conditions, and confirm that *all orientations can be associated with diamond-like silicon.*

5.2.2 Lattice parameters and stacking faults

From the positions of the various diffraction spots, I have precisely determined the lattice constants of the Si diamond-like film by using Eq. 5–2. From these measurements I find out that the Si diamond-like film is not commensurate with the Ag surface. Whereas the ratio of the lattice constants for the Ag surface and the (4 × 4) silicene layer is exactly 3/4 at this temperature (520 K), the ratio measured for the film is 0.759 ± 0.007. This indicates a relaxation towards a smaller Si in-plane lattice constant ($a^{Si}_{in-plane} = a_{Si}/\sqrt{2}$) when silicene transforms into bulk Si. The Ag in-plane lattice ($a^{Ag}_{in-plane} = a_{Ag}/\sqrt{2}$) parameter at 520 K is 2.901 Å [153]; the measured value for Si at 520 K is 3.823 ± 0.005 Å. At this temperature, bulk silicon should have an in-plane lattice constant of 3.843 Å [154], and the measured constant corresponds thus to a 0.5% contraction. Once the sample is cooled down at room temperature, an identical small contraction is observed. The in-plane lattice constant of 3.818 ± 0.004 Å measured at 300 K is associated with a contraction of 0.6% with respect to the expected value of bulk silicon (3.840 Å). I have measured the same quantity for

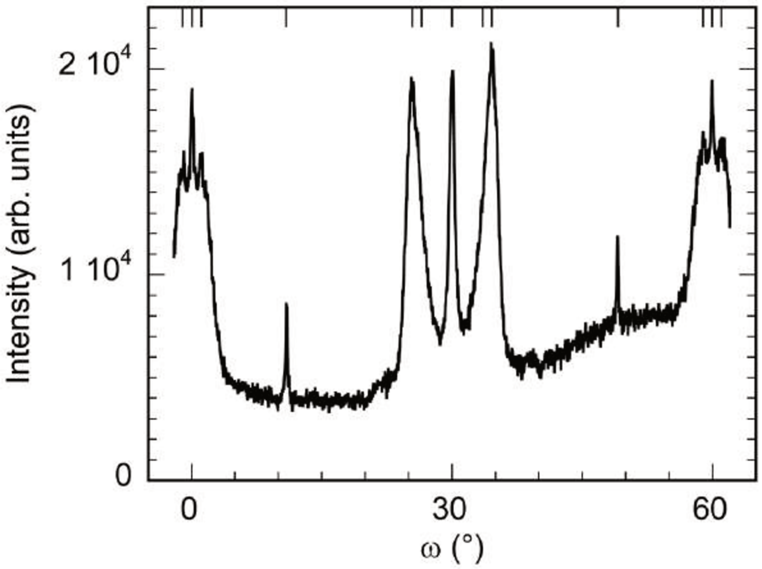

FIGURE 5.5: Schematics of the four rotational domains identified in Fig. 5.2 for the bulklike diamond Si film grown onto Ag(111), seen along $[1\bar{1}0]_{Ag}$ direction. a-c) $[1\bar{1}0]_{Si} \parallel [1\bar{1}0]_{Ag}$ and ABC or ACB stacking for Si planes respectively; b-d) $[1\bar{1}0]_{Si} \parallel [1\bar{2}1]_{Ag}$ and ABC or ACB stacking in the Si film.

all the orientations. This contraction is similar, although three times smaller, to the one observed by De Padova *et al.* for deposition at a lower temperature (470 K).

I have also obtained, at the deposition temperature, the (111) interplanar distance for the Si film ($d_{111}^{Si} = a_{Si}/\sqrt{3}$). This quantity is calculated by converting in real space the distance along l of two consecutive Bragg spots on the same diffraction rod.

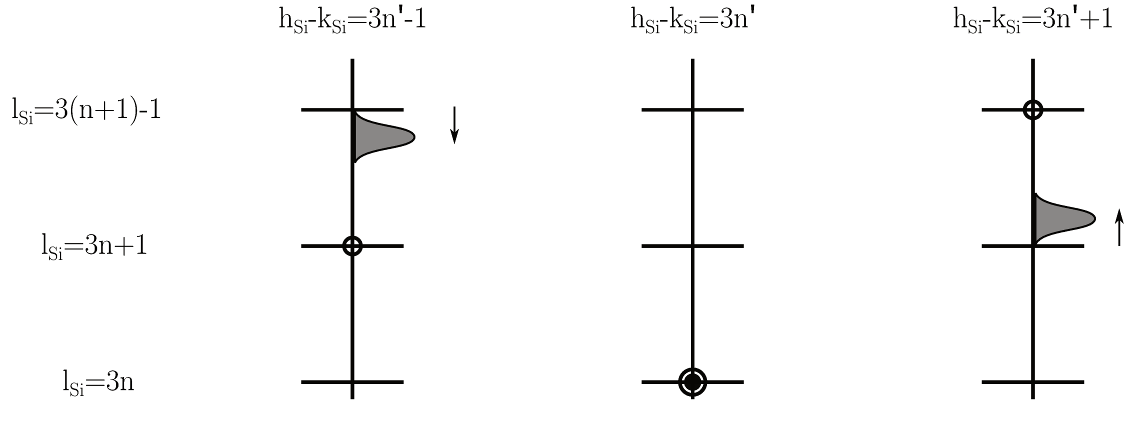

FIGURE 5.6: Reciprocal lattice representation of the influence of stacking faults on the X-ray reflections of the Si(111) film. The shaded areas indicate the intensity of a shifting peak. Reproduced from [155]

Let us take, for example, the distance between $(1\bar{1}1)$ and (202) which are expected to be, for a perfect fcc crystal, at $l = \frac{1}{3} l_{Si(111)}$ and $l = \frac{4}{3} l_{Si(111)}$, respectively. However, these spots, and $(3\bar{1}\bar{1})$ and (404) spots as well, are not observed exactly at the theoretical positions. Taking as a reference the value $l_{Si(111)} = 2.241$ between two consecutive spots along the same rod, I have obtained that these spots display a shift $\delta l = 0.035$. Such shift can be associated with the presence of *stacking faults* in the films. Stacking faults have been shown to move the positions of some diffraction peaks [155]. If $h_{Si}k_{Si}l_{Si}$ are the Miller indexes expressed in the hexagonal coordinates, then, according to the *Paterson model*, the diffraction rods associated to Si(111) thin film belong to three classes depending on the values of h_{Si}, k_{Si}, which can satisfy one of the three conditions

$h_{Si} - k_{Si} = 3n', 3n' \pm 1$. Moreover, each spot in the rod corresponds to $l_{Si} = 3n, 3n+1, 3n+2$. As depicted in Fig.5.6, in the presence of stacking faults in the film, the reflections with $h_{Si} - k_{Si} = 3n'$ and $l_{Si} = 3n$ remain sharp, but other reflections have their maxima shifted from the expected value. In the present case, the spots at $l = ml_{Si}$ ($l_{Si} = 3n$ in the Si hexagonal base) are not shifted, spots at $l = (m+1/3)l_{Si(111)}$ ($l_{Si} = 3n+1$) are shifted towards higher values, and spots at $l = (m-1/3)l_{Si(111)}$ ($l_{Si} = 3n+2$) are shifted towards lower values. Within the Paterson model, in which correlation between faults are neglected, it is possible to obtain an expression of the peak shift δl as function of *stacking fault probability* p [156]:

$$\frac{\delta l}{Si(111)} = \frac{1}{6} - \frac{1}{2\pi} arctan(\sqrt{3}(1-2p)) \tag{5–4}$$

From this equation I can estimate the quantity p, as δ can be measured and is equal to 0.035. A value of $p = 1$ is found, which corresponds to an average number of one stacking fault in the film, considering the mean film thickness of 8 ML.

From the position of the non-shifted $(3\bar{1}1)$ and $(3\bar{3}3)$ spots at $l = l_{Si} = 2.255$, a value of 3.104 ± 0.005 Å is measured for the Silicon (111) interplanar distance d_{111}. Indeed, this corresponds to the expected value for Si at this temperature. On the contrary a different value of $d_{111} = 3.157$ Å corresponding to $l_{Si} = 2.241$, is obtained from the distance along l between the $(1\bar{1}1)$ and (202) spots and between the $(3\bar{1}\bar{1})$ and (400) spots, see Fig. 5.2. This is due to the fact that the (200) and (400) spots are shifted, according to the aforementioned model and thus this latter value of the inter-planar distance could be altered by the presence of stacking faults in the Si film

Even though this interpretation is in good agreement with present results, I cannot exclude that the measured shift may be due, instead, to a non-negligible contribution of the surface reconstruction to the diffracted signal.

5.3 Discussion

The GIXD measurements, that I have reported, determine the nature of a 8 ML-thick Si film deposited on Ag(111) at 520 K. Whereas De Padova *et al.* have hypothesized the existence of a low-temperature and a high-temperature growth regime to explain the inconsistency between their results and and those of other groups, my observations demonstrate that, also for low temperature deposition conditions, i.e. for T_{growth} <540 K, the so-called multilayer-silicene is in fact a thin diamond-like Si film. The precision of current measurements can provide explanations for the different experimental evidences observed between high- and low-temperature Si growth. The Si crystal quality obviously depends on the growth temperature. Perfect Si nanocrystals are obtained for 573 K deposition [7], with a lattice constant equal to that of bulk Si. At 510-520 K, I also observe the formation of diamond-like Si, but with a lattice constant smaller than that of bulk Si. At 470 K, the lattice constant measured by De Padova *et al.* is even smaller. Instead of being related to the formation of a new crystal structure, these lattice constant variations could be related to an increasing number defects in the film structure as the growth temperature is lowered. At 510-520 K, from the shift of the Bragg reflections at $l = (n+1/3)l_{Si(111)}$ and $l = (n-1/3)l_{Si(111)}$, I have established the presence of one stacking fault on average in the film. It has been theoretically shown that the in-plane lattice constant of a Si film depends on the stacking sequence of the successive planes [157]. In particular, 10 ML thick Si films with wurtzite structure (ABAB) have a lattice constant 6% smaller than similar films with diamond structure (ABC) [157]. Thus, the presence of a stacking fault could explain the smaller in-plane lattice constant measured. Finally, these results can give an alternative explanation to the Raman signal measured by De Padova *et al.* [6, 7]. Lattice contractions are expected to shift phonons to higher frequencies [158], therefore the +0.6% shift observed in the G band with respect to the 520 cm^{-1} bulk silicon can be attributed to the contracted Si lattice foud in the sample. The broad bands between 430 cm^{-1} and 500 cm^{-1} observed by De Padova *et al.* resemble that of amorphous Si [159]. Moreover, a similar Raman line shape is expected for diamond Si presenting stacking faults along the [111] direction (Pandolfi S. *et al.*, submitted).

5.4 Summary of the results of Chapter 5

From new experimental data based on GIXD measurements, there is no evidence for the novel atomic organization of Si named silicite in the Si/Ag epitaxial films. I show instead that, in the same temperature regime for which silicite growth was claimed, **Si films grown onto Ag(111) have a defective diamond-like structure with stacking faults**, which could account for controversial experimental evidences reported in the literature.

However, few perplexities remain still unanswered and they will be addressed in the next chapter. In particular, despite the determination of the diamond structure for Si films on Ag(111):

- the origin and nature of the $(\sqrt{3} \times \sqrt{3})R30^\circ$ termination of such a film is still debated, as certain authors claim that this reconstruction is due to the presence of adsorbed Ag atoms over the Si film [8–10, 149, 151, 152], while others claim a pure silicon Ag-free structure [6, 7];
- I have not described the mechanism of the transition between the silicene monolayer and the diamond bulk-like Si film;
- it is not clear how Ag atoms segregate at the surface of the Si film, as reported by several groups [8–10, 149, 151, 152];

Chapter 6

Surface structure and growth mechanism of Si thin films on Ag(111)

6.1 Introduction

In the last chapter I have shown that the multilayer Si film on Ag(111) has a defective diamond-like structure which cannot be distinguished from that of diamond bulk Si. In this chapter I will address the open questions with which I have concluded Chapter 5. I remind that the silicene monolayer on Ag(111) is characterized by several surface reconstructions, as the (4×4) and the $(\sqrt{13} \times \sqrt{13})R13.9^{\circ}$ ones. These structures are well understood and described in literature, although a precise description of the atomic structure has been possible thanks to the present work, Chap. 4. The present Chapter focuses on two new reconstructions, which will be named $(\sqrt{3} \times \sqrt{3})R30^{\circ} - \alpha$ and $(\sqrt{3} \times \sqrt{3})R30^{\circ} - \beta$ or simply α and β phases. These two new structures are not observed in the presence of the monolayer, but are observed only when the second silicene layer starts growing. Their atomic structure is still debated.

Concerning the open questions, from literature it is not evident that there are two distinct α and β $(\sqrt{3} \times \sqrt{3})R30^{\circ}$ reconstructions. With the notable exception of Sone *et al.*, authors usually describe only one $(\sqrt{3} \times \sqrt{3})R30^{\circ}$ phase.

Moreover, as already mentioned, according to spectroscopic and microscopic measurements [144, 151, 152] the $(\sqrt{3} \times \sqrt{3})R30^{\circ}$ reconstruction shows the segregation of Ag atoms at the surface. This hypothesis is also supported by energetics studies, showing that Si islands covered by Ag atoms is a very stable configuration with respect to the other tested [7, 160]. However, other authors claim that the Si film is terminated by a $(\sqrt{3} \times \sqrt{3})R30^{\circ}$ Si reconstruction (Ag free) [7, 135].

The mechanism of the growth is very obscure. In fact, It is known, theoretically and experimentally, that the silicene monolayer is not energetically favored with respect to bulk silicon. As a matter of fact, above a certain temperature, silicene dewets and forms 3D silicon islands. In spite of this, during the growth on the Ag surface the silicene monolayer appears as an extremely stable structure, even in the presence of bulk nucleation centers. Indeed, the silicene monolayer can easily cover a quite wide area of the bare Ag surface before a second silicene layer appears. Only at this point dewetting can occur. Why does the silicene monolayer appear so anomalously stable?

This point has already been partially discussed in the energetic considerations reported in Chapter 4; here I will give a wider picture including the multilayer growth in the discussion.

In Chapter 1, I have stressed out how silicene is a paradigmatic case of a 2D material which cannot be obtained by exfoliation, differently from graphene or 2D transition metal dichalcogenides. Thus, understanding the Si growth on Ag(111) could have a relevance more general than the specific case of Si, in view of the synthesis of new phases, potentially thermodynamically unfavored, which could keep a weak interaction with the substrate.

The present chapter is organized as follows. In the first part I describe the formation and evolution of the $(\sqrt{3} \times \sqrt{3})R30^{\circ}$ islands, which appear after the completion of the silicene monolayer. Then, employing GIXD measurements, I give the exact atomic structure of the $(\sqrt{3} \times \sqrt{3})R30^{\circ}$ termination of the Si islands. In the last part, I present the results of combined real-time STM measurements and DFT calculations, aimed to understand and describe the growth mechanism of Si thin films on Ag(111).

6.2 Formation and evolution of the $(\sqrt{3} \times \sqrt{3})$ Si islands

In this section I report real-time STM measurements during Si growth on Ag(111), in the stages right after the completion of the silicene monolayer. At this moment, the second Si layer appears, on top of which the $(\sqrt{3}\times\sqrt{3})R30^\circ$ is observed.

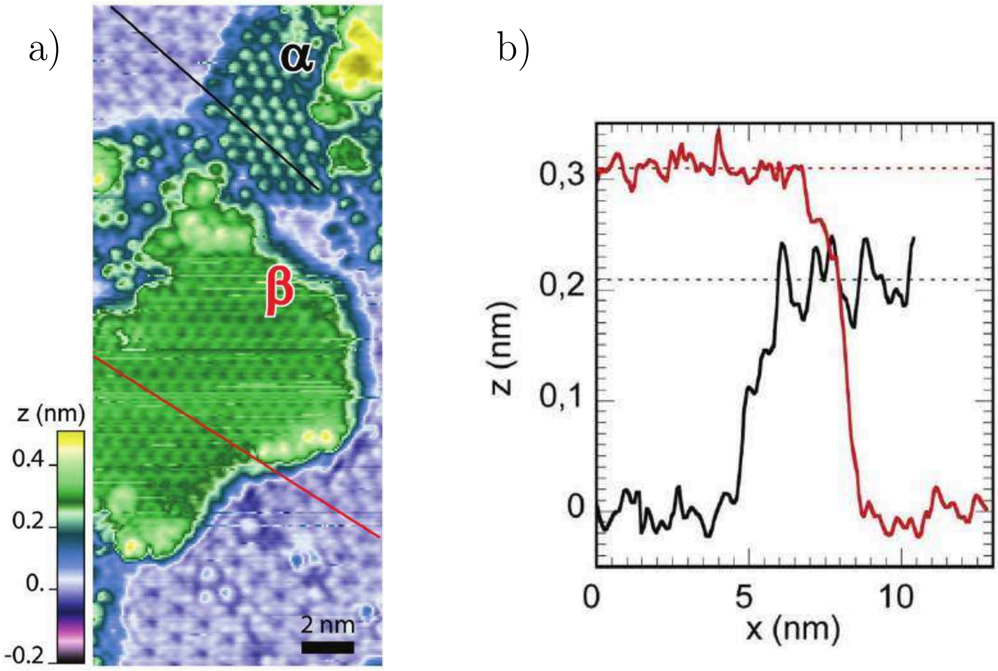

FIGURE 6.1: a) A STM image after Si evaporation at 500 K above 1 silicene monolayer. The $(\sqrt{3}\times\sqrt{3})-\alpha$ and $(\sqrt{3}\times\sqrt{3})-\beta$ islands display a different STM contrast. b) Profiles along the lines shown in (a). The size of the image: 11×25 nm^2. Tunneling conditions: U = 1.6 V; I = 50 pA.

6.2.1 $(\sqrt{3}\times\sqrt{3})-\alpha$ and $(\sqrt{3}\times\sqrt{3})-\beta$ islands

In Fig.6.1.a I report a STM image acquired right after the completion of the silicene monolayer evaporated at 500 K. In this image, Si islands corresponding to growth of the second Si layer (green) can be identified, surrounded by different phases of the silicene monolayer (blue), with (4×4) (lower right) and $(\sqrt{13}\times\sqrt{13})$ (upper left) reconstructions. The Si islands show two different surface reconstructions, which share in turn the same $(\sqrt{3}\times\sqrt{3})$ periodicity and 30° degree rotation with respect to the (4×4) structure (and thus also with respect to the Ag(111) lattice). These two reconstructions correspond to the $(\sqrt{3}\times\sqrt{3})-\alpha$ and $(\sqrt{3}\times\sqrt{3})-\beta$ phases, as labeled in Fig.6.1.a. The only other work to have ever reported this two different phases for the $(\sqrt{3}\times\sqrt{3})$ reconstruction, is the one by Sone *et al.* [80]. The $\sqrt{3}$-unit cells of the two phases α and β have the same size 0.66 ± 0.03 nm. However, the two structures display a completely different surface appearance:

1. their contrast is opposite, as the $(\sqrt{3}\times\sqrt{3})$ triangular pattern of the α islands corresponds to bright dots, while the β one corresponds to dark spots surrounded by a brighter uniform region. The bright dots of the α structure are outward protrusions while the dark spots of the β phase are intrusions, topographically speaking.

2. Their surface corrugations are different, being $\sim$0.06 nm for the α islands and $\sim$0.02 nm for the β ones, Fig.6.1.b. The fact that the α phase appears smoother suggests a more metallic character of this phase with respect to the β one.

3. Finally, contrary to previous observations [80], the apparent heights of the islands, measured with respect to the surrounding silicene layer, are markedly different. In particular, while the α islands are

observed at 0.21 ± 0.01 nm above the surrounding silicene monolayer, the β ones are at 0.31 ± 0.01 nm, Fig.6.1.

Thus, without making assumptions on the exact structure of the α and β islands, Fig.6.1 clearly indicates that their atomic and electronic structures are different.

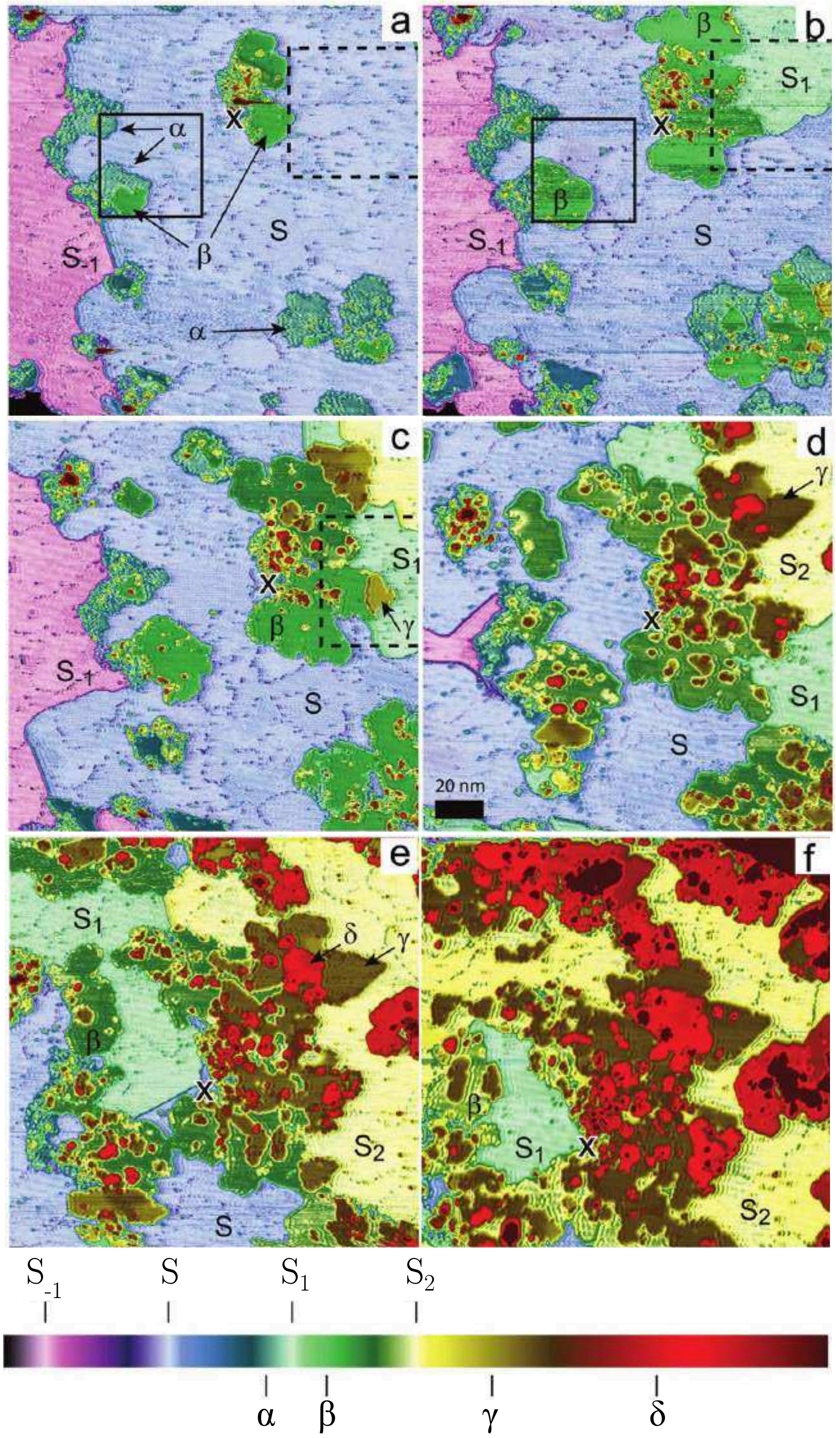

FIGURE 6.2: a-f) STM images of the same area during continuous Si evaporation at 500 K. Corresponding estimated Si coverages are 1.1, 1.4, 1.6, 1.9, 2.2, and 2.5 ML. The black cross indicates a reference position and the squares correspond to the detailed views in Fig. 6.3 and Fig. 6.14. The colourscale spans a 1.58 nm range. S_{-1}, S, S_1 and S_2 label areas of silicene monolayers lying on different Ag terraces. α, β, γ and δ correspond to Si islands of increasing height that have grown on the terrace S. The size of the images: 168 × 168 nm^2. Tunneling conditions: U=1.8 V; I=50 pA.

6.2.2 Evolution of the $(\sqrt{3} \times \sqrt{3})$ islands with increasing Si deposition

Let us take a look on how the sample surface evolve after the silicene monolayer completion during Si evaporation. Fig. 6.2 is one of the most meaningful results presented in this Thesis and it should be studied with particular care. It displays the evolution of the same region during Si growth above the silicene monolayer at 500 K at large scale. The set of images correspond to detailed views of a 700 × 700 nm^2 area that is also periodically fully scanned with lower resolution. Let us consider the regions labeled as S_{-1} (magenta), S (lavander), S_1 (seafoam/light-green) and S_2 (light-yellow). These regions are staggered in height by multiples of 0.235 nm, which is the height of a Ag(111) step. Within each of these regions, the surface displays domains with different reconstructions, mainly identified as (4×4) and $(\sqrt{13} \times \sqrt{13})$, which indeed are the reconstructions of the silicene monolayer expected for this growth temperature (see Chapters 4 and 5). The darker dotted lines are defects present at the boundaries between the different domains of the monolayer reconstructions (see also Fig. 6.3). Thus, the regions labeled as S_{-1} (magenta), S (lavander), S_1 (seafoam/light-green) and S_2 (light-yellow) correspond to silicene monolayers lying on different Ag terraces.

After completion of the first Si layer, islands with a $(\sqrt{3} \times \sqrt{3}) - \alpha$ reconstruction starts growing. They correspond, for example, to the small light green islands visible in Fig. 6.2.a (labeled as α). For increasing Si coverage, they are progressively replaced by the $(\sqrt{3} \times \sqrt{3}) - \beta$ islands (green areas in Fig. 6.2.c, labeled as β, then brown and red areas in Fig. 6.2.c-e). This process can be seen more clearly in the zoom-in in Fig. 6.3.

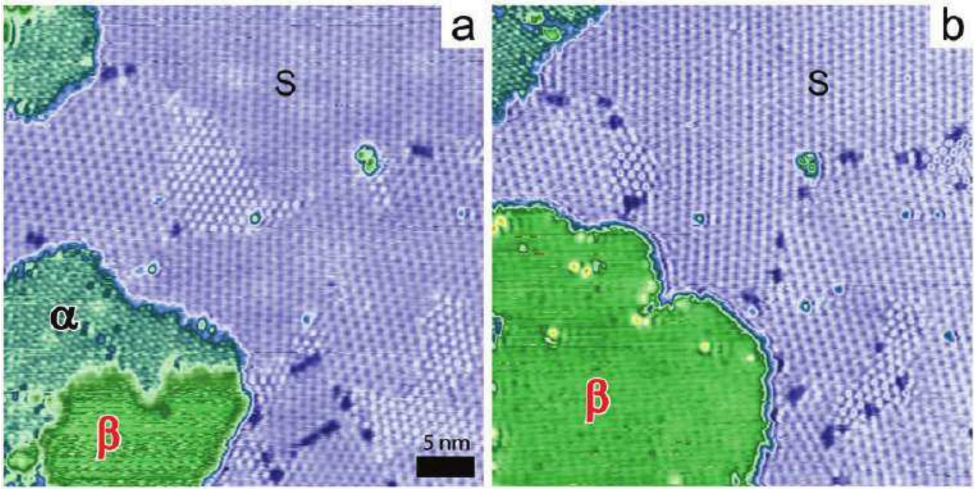

FIGURE 6.3: A detailed view of Fig. 6.2a and b (42 × 42 nm^2) corresponding to the position of the continuous black squares drawn in Fig. 6.2

In Fig. 6.3, different domains of the silicene monolayers (lavander areas) are clearly visible. Two islands at a higher level can also be seen. In Fig. 6.3a, the bottom-left one partly consists of $(\sqrt{3} \times \sqrt{3}) - \alpha$ (turquoise), where the reconstruction is visible, and partly of $(\sqrt{3} \times \sqrt{3}) - \beta$ (green). For a larger amount of deposited silicon (Fig. 6.3b), the α domain of the lower islands is completely replaced by the β structure. Upon further Si evaporation, the β domains continue growing laterally while the α ones progressively disappear, as it is visible in Fig. 6.2b and c. In Fig. 6.2, note that by 2 ML Si deposition only silicene areas and β islands are present at the sample surface. β islands also grow vertically in a layer-by-layer way. In Fig. 6.2, β (green), γ (brown), and δ (red) correspond to areas of increasing heights with the same apparent topographical contrast. The interlayer spacing, 0.30 ± 0.01 nm, is similar to what observed by others [8, 83, 144] and could correspond to the distance between two silicene layers as well as to the height of the (111) step of bulk silicon.

Another important aspect of Si growth on Ag(111) is the inhomogeneity of the thickness of the Si film, which can be inferred with some effort from Fig. 6.2. The evolution of the surface area covered by the silicene monolayer as a function of Si coverage is shown in Fig. 6.4.a. In particular, the "monolayer fraction" (the ratio between the surface covered by the silicene monolayer and the total surface) is obtained after direct inspection of the STM images. The "ML coverage" corresponds to the quantity of silicon adsorbed on the surface which is not necessarily distributed uniformly on the surface. Thus, in Fig. 6.4.a, one can observe that part of the monolayer is still visible after 2 ML silicon coverage. This means that the third layer starts growing before the completion of the second, causing the inhomogeneity in the thickness of the Si film. This is in good agreement with STM observations performed on 2.5 ML thick films grown at 490 K, where Si islands with various heights coexist with the silicene layer at the surface of the Ag(111) sample [83]. However, I stress out that eventually all the ML will be covered by a thicker Si film (see ref. [142] for further details), as also confirmed by the disappearance of the ML reconstructions spots mentioned in Chapter 5. The growth mechanism is completely different from that observed at 540 K, see Fig. 6.4.b. Indeed, for this growth temperature, thick Si islands appear: the one in Fig. 6.4.b has an height of 11 nm, corresponding to 35 Si layers, roughly. Note that the silicene layer has not completely dewetted at this temperature and that a large part of the surface is covered by it. At even higher temperature the silicene layer completely dewets.

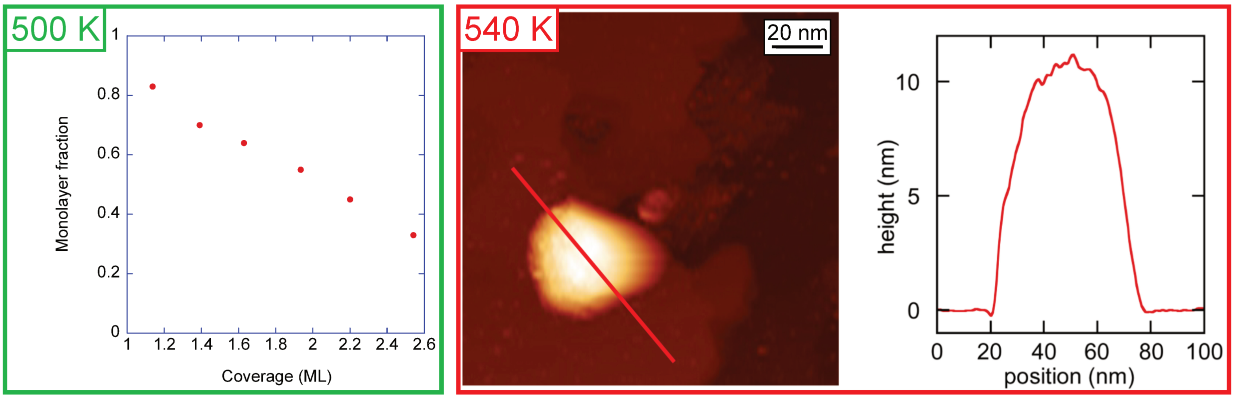

(a) (b) (c)

FIGURE 6.4: a) Evolution of the surface fraction covered by the monolayer after silicene monolayer completion at 500 K derived by the STM measurements shown in Fig. 6.2. b) STM image of the Ag(111) surface after the evaporation of ≈3 ML Si at 540 K. c) Height profile along the line shown in (b).

6.3 Atomic structure of the $(\sqrt{3} \times \sqrt{3})R30^\circ$ reconstruction

In this section I present the results of GIXD experiments aimed to determine the atomic structure of the $(\sqrt{3} \times \sqrt{3}) - \beta$ reconstruction. The measurements shown here have been conducted on a Si film evaporated on Ag(111) at T_{growth} = 510 K and corresponding to a coverage of 2 ML (see previous paragraph). Note that, as shown in Fig. 6.2, in these conditions the β phase has already completely replaced the α one.

I have followed the evolution of the diffracted signal during the growth. Fig. 6.5 shows the evolution as a function of Si coverage θ_{Si} of the diffracted intensity near the (0.75,0.75,0.15) position; the indexing is with respect to the Ag(111) unit cell. This peak is associated with a (4 × 4) reconstruction and, thus, corresponds to the silicene monolayer. From figure Fig. 6.5, one can see that, starting from a bare Ag surface, the (4 × 4) silicene monolayer appears for coverage larger than 0.5 ML. The same behaviour has already been described in Chapter 4, Fig. 4.3, and by previous STM observations [65, 87].

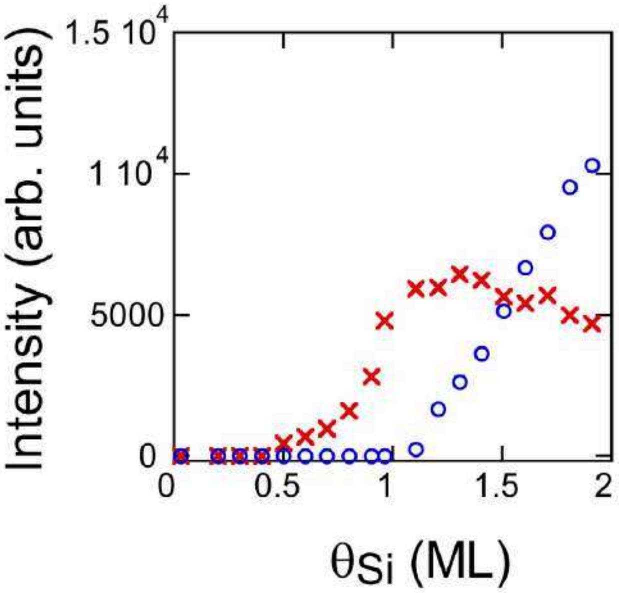

FIGURE 6.5: Evolution of the diffracted intensity for the (0.75,0.75,0.15) position (red-crosses) and the (0.76,0.76,0.15) position (blue circles), during Si evaporation at T_{growth}=510 K.

Above 1 ML, a second peak appears near (0.76,0.76,0.15). I associate this second peak to the presence of the thicker Si film. The peak intensity grows linearly with the coverage, while the intensity of the spots associated with the (4 × 4) silicene monolayer slowly decays. This decreasing trend has also been observed with low energy electron microscopy (LEEM) measurements at 491 K [59] and our STM observations. I also recall that, for the thick 8 ML deposit, no signal could be seen for the (0.75,0.75,0.15) position ((4 × 4) reconstruction spot). This indicates that the structure of the interface silicene-monolayer/Ag-surface is not preserved underneath the thicker film. Thus, I deduce that the signal observed in the early stages of growth is related to parts of the surface which remain covered by the silicene layer. Fig. 6.6 shows the in-plane diffracted signal around the (0.75,0.75,0.15) diffraction condition for 2 ML deposition. The spots corresponding to the (4 × 4) and $(\sqrt{13} \times \sqrt{13})R13.9°$ reconstructions remain visible, which confirms that in this low-temperature regime, there is no dewetting of silicene occurring above 1 ML Si deposition. The most intense spots correspond to the thin Si(111) film, with a main epitaxy relationship of 30° between the Si and Ag lattice, while the other less intense spots correspond to other domains at ±4.3° from the main orientation. Wider less intense peaks are also present at ±2.7°, which are faintly visible in the figure. More generally, nearly the same orientations as those founds for the 8 ML film are recovered, except the orientations previously observed at 10.91°.

From Fig. 6.6, note that the Si(111) film has a lattice constant smaller than that of silicene: the spots of the Si film are identified by a reciprocal vector with a higher absolute value. At room temperature, I have measured for the thin film a Si in-plane lattice constant of 3.786 ± 0.005 Å, a value 1.4% smaller than Si bulk lattice constant (3.840 Å). This reduction is twice the value found for the 8 ML film, which indicates that the in-plane lattice constant of the film depends on the thickness and/or the small growth temperature difference (510 K versus 520 K). From the width of the Bragg spots of the Si film in the l direction, I obtain that the diffracting domains have an average thickness of 4 atomic diamond double planes. As the average coverage is 2 ML, this indicates that the Si film in inhomogeneous, having regions covered by 1 Si ML and regions with multiple Si layers. This is confirmed by the observed small decay of the intensity in the

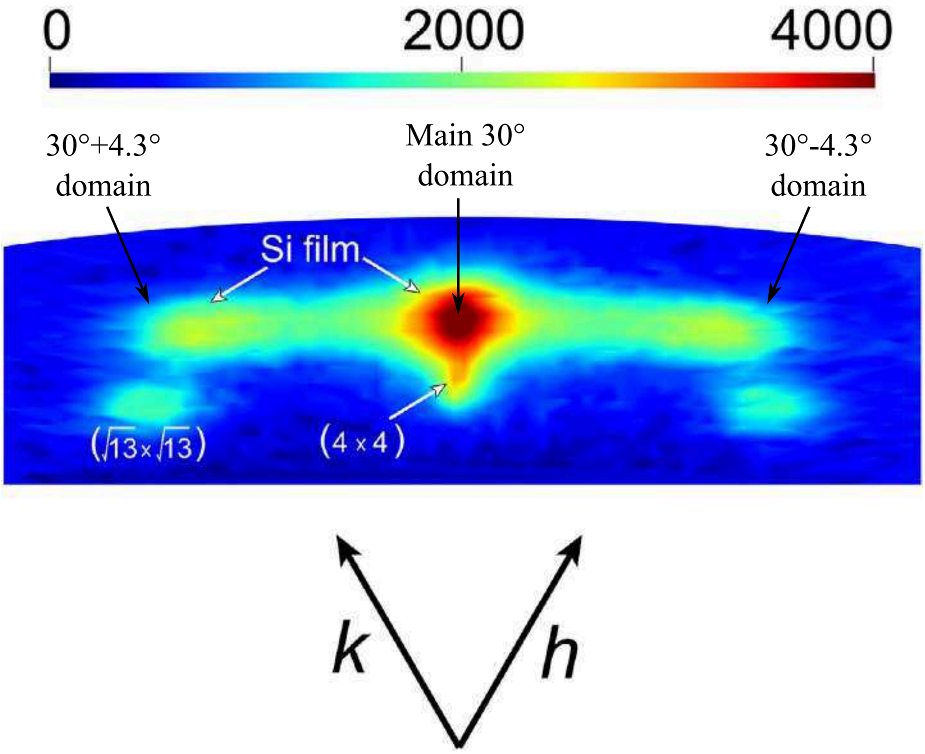

FIGURE 6.6: In-plane map of the diffracted intensity near the (3/4,3/4) spot at l=0.05, for 2 ML of Si deposited at 510 K.

diffracted by the (4 × 4) domains. Only a small fraction of the silicene monolayer has been converted to thicker islands, with a height distribution that is not directly accessible with GIXD.

On this thin Si film, I have measured the structure factors associated with the $(\sqrt{3} \times \sqrt{3})R30^\circ$ reconstruction of the Si islands. For this purpose I have performed, for in-plane conditions, standard rocking scans at l=0.05 along several spots corresponding to the $(\sqrt{3} \times \sqrt{3})R30^\circ$ superstructure, and for out-of-plane conditions, standard rocking scans along four superstructure rods (SRs), corresponding, in the Ag(111) basis, to $(h,k) \approx (0.254, 0.254)$, $(h,k) \approx (0.509, 0.509)$, $(h,k) \approx (1.27, 1.27)$, and also along two Si CTRs at $(h,k) \approx (0.763, 0.763)$ and $(h,k) \approx (1.53, 1.53)$. In the Si $(\sqrt{3} \times \sqrt{3})R30^\circ$ basis, these rods are labeled as $(10L_{Si})$, $(20L_{Si})$, $(30L_{Si})$, $(50L_{Si})$ and $(60L_{Si})$ with $L_{Si} = \frac{4}{3}l$. The standard instrumental corrections were applied to the structure factors to take into account the geometry of the diffractometer and the sample dimensions [102], the details of which have been discussed in Section 2.4.2.3. In the next section I will present the models used to simulate the theoretical structure factors, employed in the fitting of the experimental results.

6.3.1 Structural models

Here I present possible structural models for the $(\sqrt{3} \times \sqrt{3})R30^\circ - \beta$ reconstruction observed on silicon thin films. These models will be used to fit our experimental GIXD data. Given the lack of consensus, I will consider structures in which Ag atoms are added over the top of the silicon film surface and also Ag-free reconstructed silicon surfaces. Silicon is assumed to be a three layers thick bulk-like film.

The first model I am going to discuss is the *honeycomb chain triangle (HCT) model*, which is the same structure describing the well-known Ag termination of the $(\sqrt{3} \times \sqrt{3})R30^\circ$ reconstruction, as proposed by several groups [8–10, 140, 149]. The other models I have considered are all “Ag-free" reconstructions. The

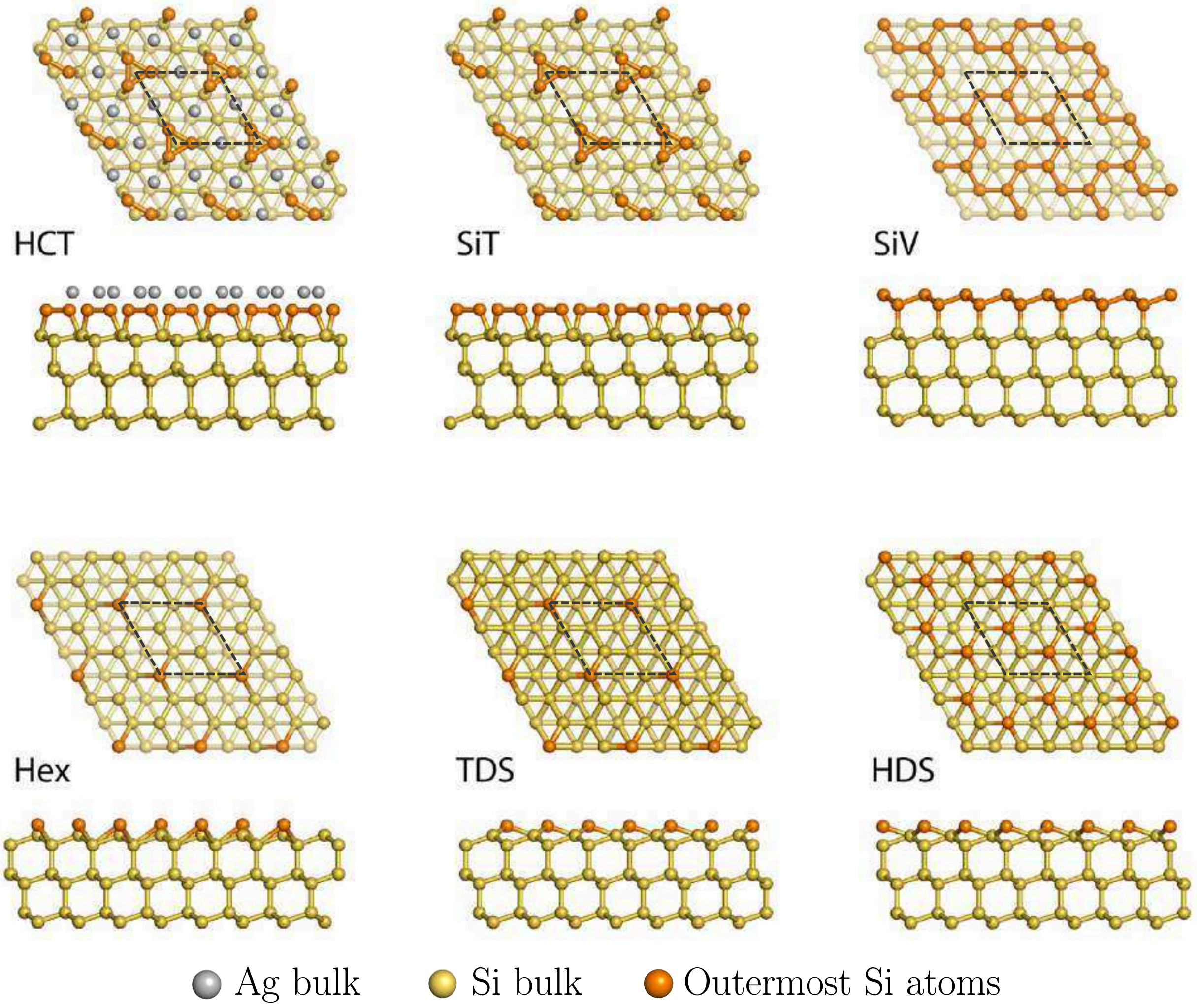

FIGURE 6.7: Schematic views (top and lateral) of the different atomistic models used for fitting the GIXD data (honeycomb chain triangle model, Si trimers, Si vacancies, buckled hexgonal, trigonal dumbbell structure and hexagonal dumbbell structure) and of their unit cell (black dotted rhombuses). For the HCT model, the atomic positions correspond to the best fit of the data, while the others correspond to the starting positions for the fit.

trigonal dumbbell silicene (TDS) and hexagonal dumbbell silicene (HDS) models proposed by Cahangirov *et al.* [147] have been initially proposed as a reconstruction of the single silicene layer, and they represented the 2D building block of silicite [135]. As I have ruled out in the last chapter the hypothesis of silicite growth, these two reconstructions have been used as simple $(\sqrt{3}\times\sqrt{3})$ termination of a bulk-like Si film. All the models are represented in Fig. 6.7.

Ag/Si(111) structure: the honeycomb chain triangle (HCT) model and the inequivalent triangle (IET) model

Silver atoms adsorbed onto Si(111) give rise to a $(\sqrt{3}\times\sqrt{3})R30^\circ$ reconstruction [161–163], which exists in two slightly different atomic configurations. Both of them consist of a Si half-layer, the atoms of which relax in trimers, and a termination with Ag atoms with the same density of a Si half-layer.

IET forms preferentially at low temperature below 150 K, while HCT is more stable at higher temperature. The Ag adsorbates form chained triangles that are arranged in a honeycomb network, Fig. 6.8. The

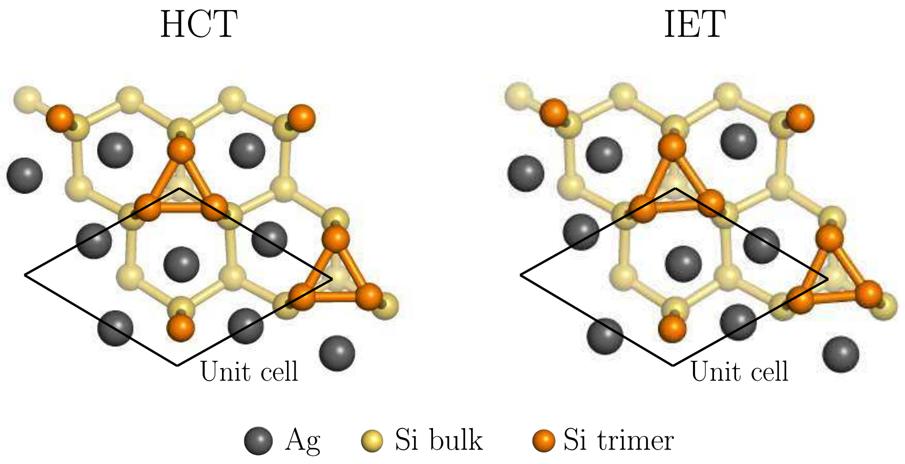

FIGURE 6.8: Atomic configuration of the HCT and IET models. The triangles of Ag atoms in the HCT model are all the same. In the IET model one of the triangles in the unit cell is smaller than the other. The half silicon layer below the Ag adsorbates is arranged in trimers for both models.

same thing happens in the IET model with the difference that one of the two Ag-triangles in the unit cell is bigger than the other.

Silicon trimer (SiT) model

It is basically the same atomic arrangement described for HCT model, but stripped of the Ag adsorbates on top. Thus, the reconstruction consists in a half Si layer, in which atoms are arranged in trimers, with the expected periodicity, i.e. $(\sqrt{3} \times \sqrt{3})R30^\circ$ with respect to a Si(111) plane. It is proposed as a new Ag-free surface termination of a Si thin film [149]; this kind of trimer reconstruction has never been observed for bulk Si(111), which is usually terminated by the well-known (7×7) structure [143].

Si vacancies (SiV) model

This vacancy model has been originally proposed for a clean Si(111) surface which reconstructs in a $(\sqrt{3} \times \sqrt{3})R30^\circ$ after 1 keV Ar ion bombardment and successive annealing at 1000° [164]. Indeed, it has been proven to be less stable than the (7×7) reconstruction at high temperature, but is quite stable for several days at room temperature[164]. It has been considered as a possible explanation for multi-layer silicene growth in the wotk of Kawahara et al. [149].

Highly-buckled hexagonal surface (Hex) model

This model has been proposed by Guo and Oshiyama [165] in a work reporting a systematic investigation of $(\sqrt{3} \times \sqrt{3})R30^\circ$ and other reconstructions of the Si thin films on Ag(111) as a function of the thickness of the Si overlayer. In the model, 1/6 of the atoms in the last layer are more protruding with respect to the others. Also this reconstruction has never been observed experimentally for bulk Si(111).

Trigonal dumbbell (TDS) model and honeycomb dumbbell (HDS) model

Initially, these two configurations have been proposed by Cahangirov et al. [147] as a reconstruction of the silicene monolayer. 1/6 or 1/3 of Si(111) layer is adsorbed on top of silicene in a "dumbbell" configuration, resulting in the formation of the TDS or HDS structure respectively. In the dumbbell configuration a Si atom sits on top of another Si atom of the silicon (or silicene) layer at the sample surface, as depicted in Fig. 6.7. Cahangirov *et al;* found out that free-standing HDS (coehesive energy E_c=4.018 eV/atom) should be energetically favored with respect to free-standing TDS (E_c=4.013 eV/atom), but both of them should be more stable than free-standing silicene (E_c=3.958 eV/atom). When considering the Ag substrate instead, the TDS model has a larger cohesive energy (E_c=4.663 eV/atom) than the HDS (E_c=3.471 eV/atom). In the dumbbell structure the Si adatoms are in the same configuration as the Si adatoms found on top of the well-known and stable (7 × 7)-Si(111) reconstruction.

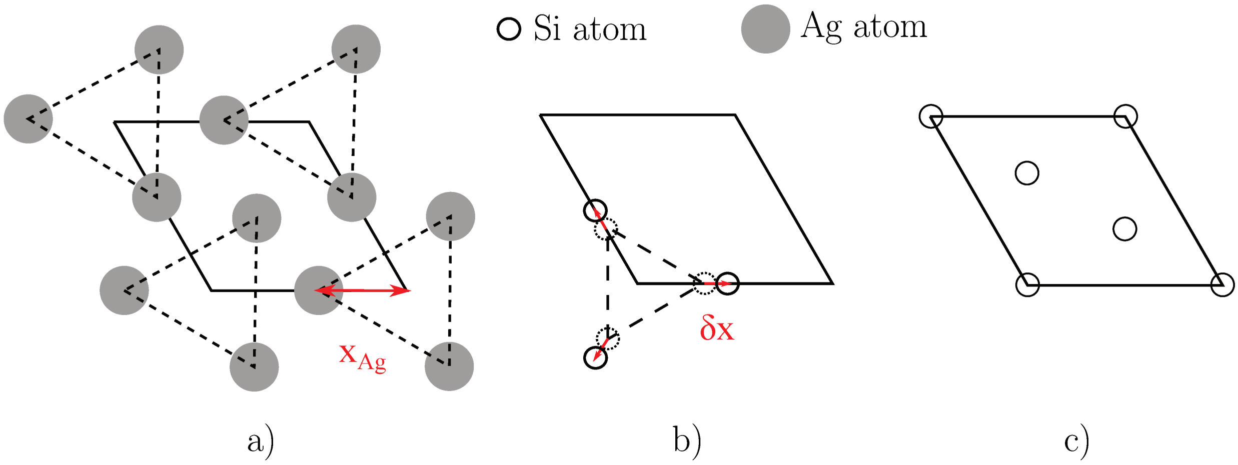

FIGURE 6.9: a) Illustration of the arrangement of the surface Ag atoms in the $Ag - (\sqrt{3} \times \sqrt{3})R30^\circ/Si(111)$ unit cell (solid lines). The size of the Ag-triangles, defined by the parameter x_{Ag}, is relaxed during the structural optimization. b) Atoms in the first and second Si layer and relative in-plane relaxations (red lines). c) Atoms in the third Si layer, in which no in-plane relaxation is allowed because of symmetry constraints.

6.3.2 Comparison between experimental and theoretical structure factors

Here I compare the experimental structure factors of the β reconstructed Si thin film with the ones simulated from the models described in Sec. 6.3.1 (Fig. 6.7). For the calculation of the structure factors, the ROD program has been used with Levenberg-Marquard and simulated annealing procedures [166]. Two scale factors are used as free parameters (for crystal truncation rods (CTRs) and superstructure rods (SRs), respectively), Debye-Waller factors for the different layers, and in-plane and out-of plane relaxations of all the atoms in three silicon layers near the surface, taking into account the symmetry of each model. In the case of the HCT model, the possible relaxations are described in the paper by Takahashi and Nakatani [162]. The total structure factor ($F_{th}(l)$) is the sum of the one associated with the Si surface (F_{Si}^{surf}) and the one coming from Ag atoms on top F_{Ag}:

$$F_{th}(l) = F_{Si}^{surf} + F_{Ag} \tag{6–1}$$

The expression of the two terms is given by Eq. 2–27. The in-plane relaxations in the Ag plane and in the first three Si planes are depicted in Fig. 6.9. Concerning the Ag plane on top of the Si film, the

Model	N_{par}	χ^2
HCT [162]	12	3.7
SiT [149]	12	16.3
SiV [164]	9	25.4
Hex [165]	9	20.4
TDS [147]	9	18.0
HDS [147]	9	13.8

TABLE 6.1: Optimized χ^2 for the various models of the $(\sqrt{3} \times \sqrt{3})R30^\circ$ reconstruction and values of N_{par} used for each model. N_{par} takes into consideration Debye-Weller and scale factors.

allowed relaxation changes the dimension of the triangle formed by the atoms, which is determined by the parameter x_{Ag}. The first and second Si layers contain two Si atoms which can move along the sides of the $(\sqrt{3} \times \sqrt{3})R30^\circ$ unit cell. Finally, in the third layer the atoms have no in-plane relaxations allowed, due to symmetry constraints.

The agreement between experimental (F_{exp}) and theoretical (F_{th}) structure factors is estimated by the value of χ^2, the expression of which has already been given in Eq. 4–3. In this case the number of experimental structure factors is N_{pt} = 171, and the number of free parameters N_{par} depends on the models taken into consideration. The χ^2 values of the fits and N_{par} are given in Table 6.1

A good agreement (χ^2=3.7) is obtained with the HCT model, i.e. with a film surface similar to the $(\sqrt{3} \times \sqrt{3})R30^\circ$ reconstruction of Ag/Si(111), while a very poor agreement is obtained with all other models ($13.8 < \chi^2 < 25.4$), for which quite unrealistic relaxations of the atoms in the structure are obtained. The comparison between experimental and simulated structure factors along different rods is shown in Fig. 6.10 and 6.11; the spots are indexed according to the $(\sqrt{3} \times \sqrt{3})R30^\circ$ unit cell (see Ann. A). While the intensity variations of the SRs are well reproduced with the HCT model, the fits based on the Ag-free models give a poor agreement. For example, the TDS and HDS models display strong oscillations that are not observed experimentally.

Note that the $(03l_{\sqrt{3}})$ rod is always more or less well reproduced by the theoretical results: being a CTR, this rod is sensible to the volume and not to the surface. The width of the Bragg peak at (033) defines the thickness of 3 ML for the Si film.

The spurious oscillations visible at $l_{\sqrt{3}}$=1.5 on the fit of the HCT model are due to the interference pattern occurring between the interface and the surface of the Si film. These interference contributions depend on the film thickness distribution, which has been considered constant in the simulations, equal to 3 ML as defined by the width of the (033) Bragg peak. By accounting for a different film distribution, one could get rid of these spurious oscillations. Finally, none of the Ag-free models is able to reproduce the high intensity of the of the $(20l_{\sqrt{3}})$rod at $l_{\sqrt{3}}$=0. This is easily explained by the fact that the atomic scattering factor f depends strongly on the atomic number, as already explained in Section 2.4.1. In the present case, for the (200) diffraction condition, f_{Ag}=39.8 and f_{Si}=10.2. *Thus, it is unrealistic to fit the experimental structure factors along the reconstruction rods with models that do not take into consideration the presence of Ag atoms at the surface of the grown Si film.*

Thus, thanks to GIXD measurements I have shown that the $(\sqrt{3} \times \sqrt{3})R30^\circ - \beta$ reconstruction observed on Ag(111) after the evaporation of $\theta_{Si} > 1$ ML of Si, can only be described by the model commonly used for the Ag-termination of Si(111), i.e. HCT model [9, 10, 142, 151, 152]. Indeed, in the previous chapter I have shown that thick (>1 ML) Si layers on Ag(111) has a diamond-like structure similar to Si(111). It is

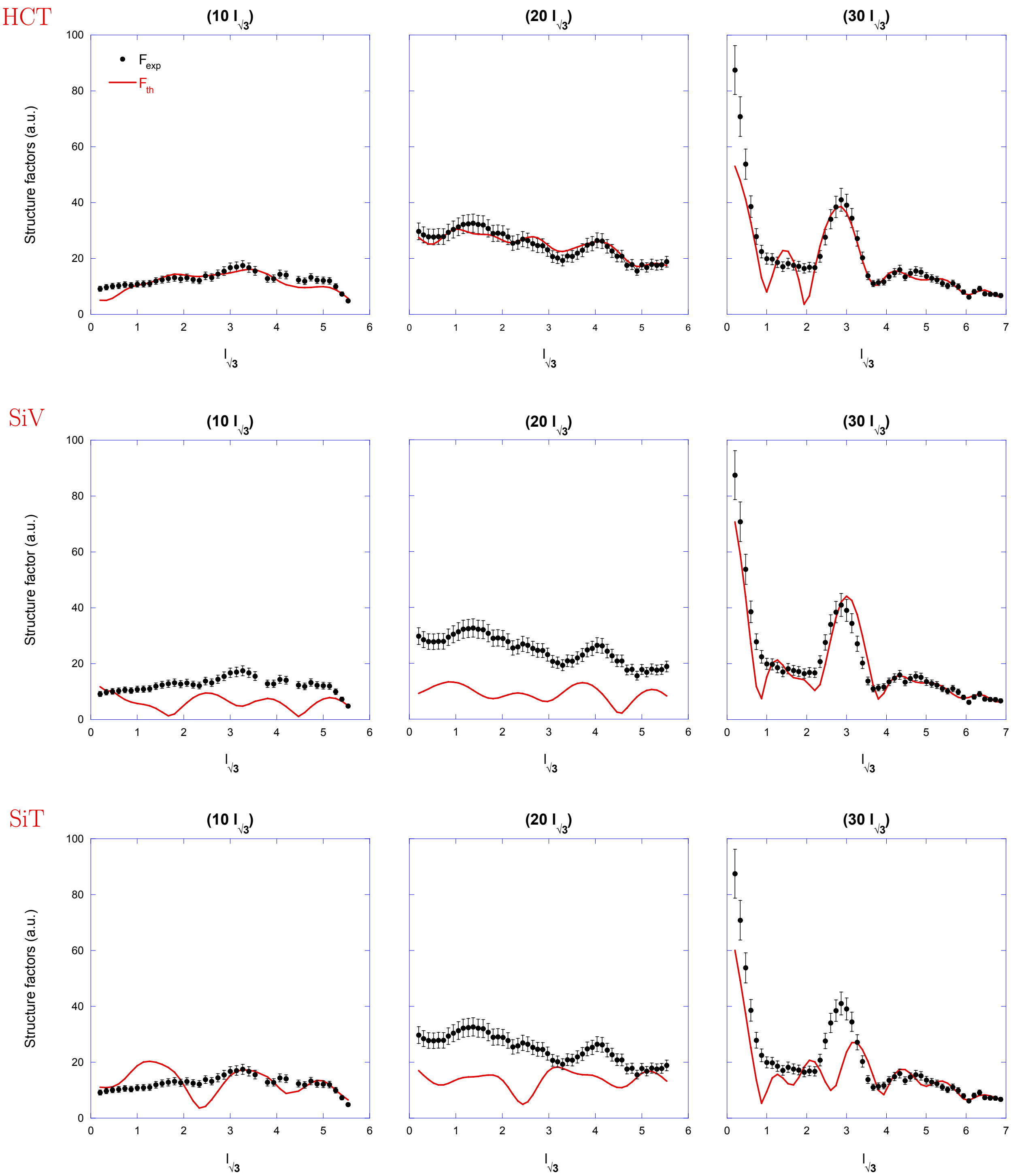

FIGURE 6.10: Comparison between the experimental structure factors of the β reconstructed Si thin film (black dots) with the ones simulated from the HCT, SiT and SiV models, along three diffraction rods.

thus not surprising that the surface of this bulk-like thin film has the same termination found on bulk Si in the presence of Ag atoms.

However, GIXD measurements cannot identify the metastable phase α, for which I will have to combine real-time STM measurements and a consisting load of DFT calculations, which are discussed in the next sessions.

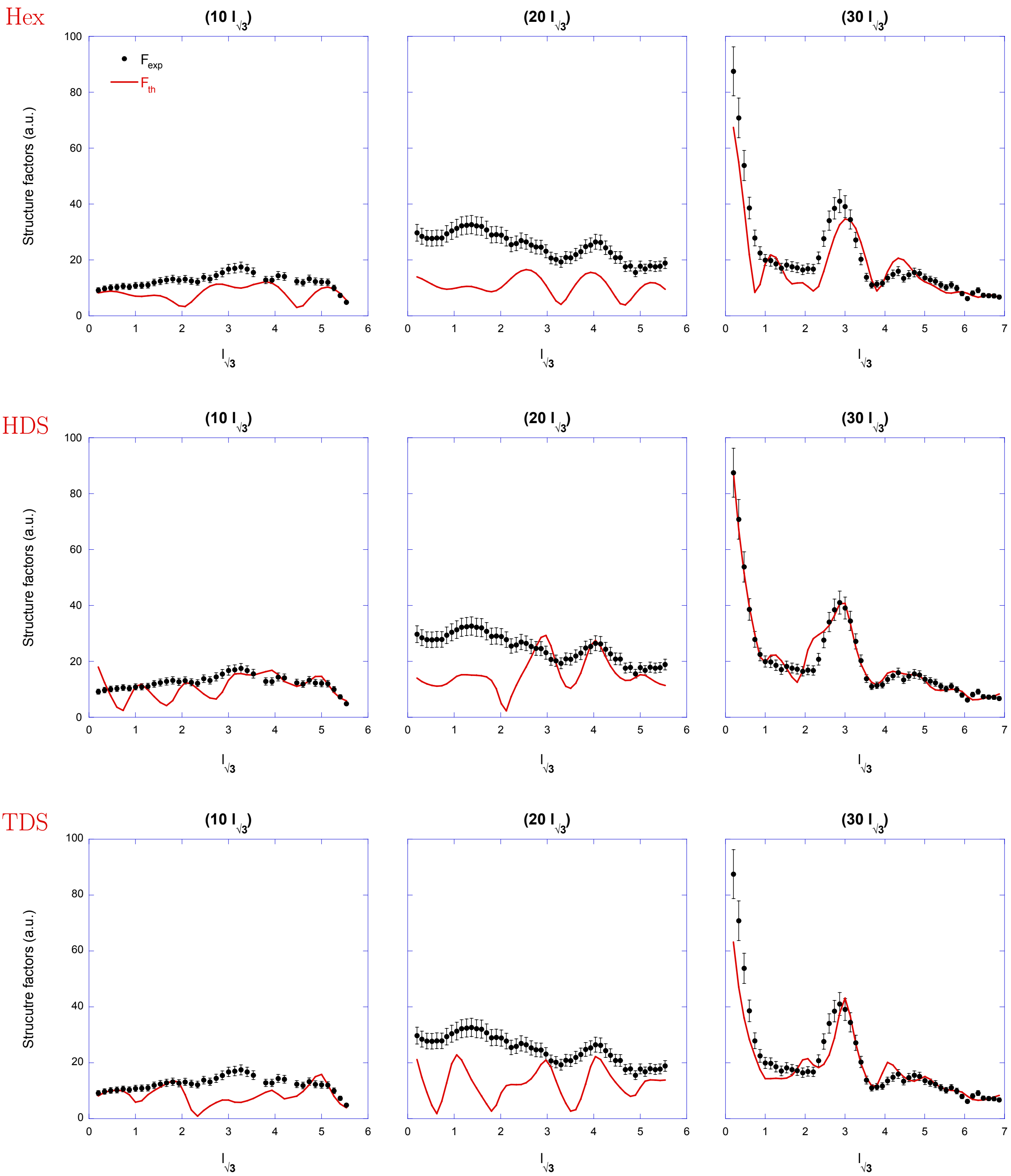

FIGURE 6.11: Comparison between experimental and simulated structure factors of Hex, TDS and HDS models along three rods.

6.4 DFT models for the α and β phase

In the previous section, I have described possible terminations for bulk silicon to explain the β reconstruction observed on top of Si thin films grown on Ag(111). Now I will describe possible structures obtained by adding atoms over the silicene monolayer to explain the α and β phases observed in the first stages of growth the second Si layer. The structures described in the present section have been simulated by density functional theory (DFT) calculations. This will allow us to conduct a study of the energetic stability of the different simulated structures.

The results presented in the follwing are obtained using generalized gradient approximation (GGA) [167] which gives the best agreements with X-ray diffraction measurements for the silicene monolayer structures, see Chapter 4. Results were tested against the inclusion of dispersive corrections as in refs. [116, 129]. Unless otherwise stated, I consider silicene-based supercells with $(\sqrt{3} \times \sqrt{3})$ periodicity lying on a (4×4)-Ag(111) surface supercell. Atomic positions were always relaxed by energy minimization (only the Ag-slab bottom-layer positions were fixed) setting the in-plane lattice spacing to the theoretical Ag bulk one (0.2935 nm). STM simulations were performed as described in Section 3.9.

Consistently with the results obtained in the previous section, I assume that the β phase appearing in the first stages of growth after the silicene monolayer completion, is a single Si layer, terminated by Si and Ag adatoms in the HCT structure. This system will be referred to as "ML+Si/Ag".

I remind that the α phase structure is substantially different from the β one, see Sec. 6.2, Fig. 6.1. Thus, I assume that the α phase corresponds to a Ag-free structure. In particular, I consider a Si bilayer with AB or AA stacking, as proposed in refs. [168–170], and a Si monolayer with adsorbed Si atoms on top, as in the TDS model proposed by Cahangirov *et al.* and already described. I ruled out some of the models used in the structure factors simulation, Sec. 6.3.1. The calculations I have perfored showed that the "Hex" model proposed by Guo *et al.* [165] is not stable and relax into a Si bilayer with AB-stacking. This last type of bilayer instead has been taken into account in the simulations of the theoretical structure factors; it has been labeled as "BL-AB".

According to ref. [147] the simulated STM image of the HDS model has a different periodicity with respect to the protrusions of the α-phase reconstruction (Fig. 6.1), so it can be excluded *a priori*. Thus, I consider only the case of a TDS plane on top of the Ag(111) substrate, and I label it as "ML+Si".

Also the models with Si vacancies (SiV) [164] and Si trimers (SiT) have not been considered, as one would expect intrusions in correspondence of the vacancies and triangular-shaped features for the trimers in the respective STM images.

I have also considered the calculations of the bilayer model proposed by Pflugradt *et al.* [170]. This Si bilayer with AA-stacking has a true periodicity of $(2\sqrt{3} \times 2\sqrt{3})$, and lies on a $(\sqrt{19} \times \sqrt{19})$ Ag-supercell. However, its simulated STM image shows a $(\sqrt{3} \times \sqrt{3})$ periodicity. I will refer to this model as "BL-AA".

Thus, the structures I have simulated in this first stage are:

- ML+Si/Ag: the HCT termination of a single Si layer, to describe the β phase;
- ML+Si: a single TDS Si layer [147];
- BL-AB: simple Si bilayer with Ab-stacking;
- BL-AA: bilayer model proposed by Pflugradt *et al.* [170].

The equilibrium structures obtained by DFT calculations and the simulated STM images are reported in Fig. 6.12. All the structural parameters for the relaxed structures are reported in Annex C. By looking at the simulated STM images shown in Fig. 6.12, one can observe that for ML+Si and BL-AA models the $(\sqrt{3} \times \sqrt{3})$ periodicity is given by an array of bright protrusions, similar to those observed in Fig. 6.1 for the α phase. However, BL-AA has a slight different orientation which does not stick to the usual one observed for α-domains. Concerning the ML+Si/Ag model, its STM simulation shows $(\sqrt{3} \times \sqrt{3})$ periodicity given by dark areas (intrusions) and it quite well reproduces the surface appearance of the β phase (Fig. 6.1). The simulates STM image of the BL-AB does not resemble to any of the structures observed experimentally. Concluding only the ML+Si is a reasonable candidate for the α phase.

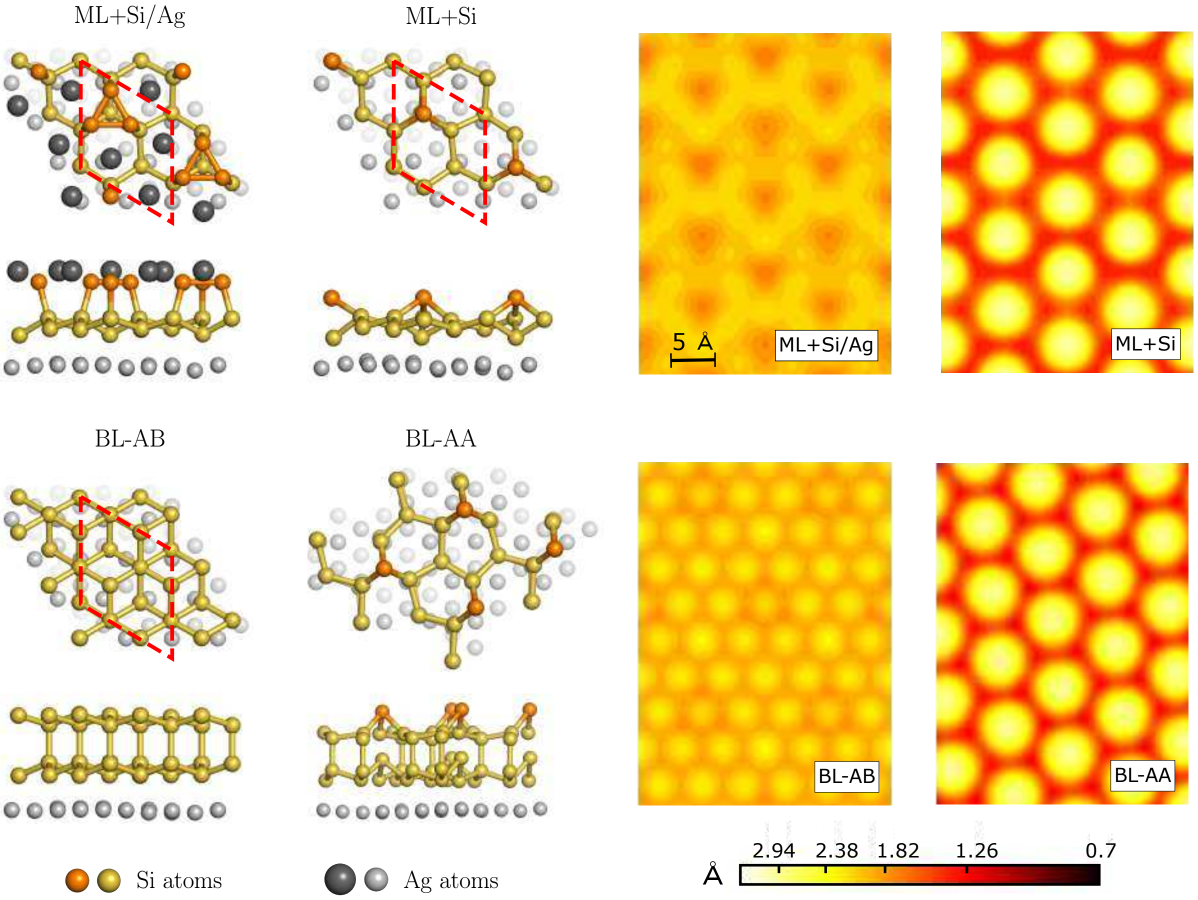

FIGURE 6.12: Schematic representation of the various computed structures after relaxation and corresponding simulated STM images. The unit cell of the $(\sqrt{3} \times \sqrt{3})$ reconstruction is represented by a red rhombus. For BL-AA, the structure correspond to a $(\sqrt{19} \times \sqrt{19})$ unit cell, referred to Ag(111). The three bottom Ag layers have been omitted from the lateral views. STM images are simulated for U=0.5 V. The ML+Si and BL-AA reproduces quite well the protrusion characteristic of the α phase surface appearance, while ML+Si/Ag is in agreement with the STM topography of the β phase. The BL-AB model does not reproduce any structure observed experimentally.

Let us now compare the stability of the simulated models in order to understand whether their formation is thermodyinamically favorable or not. For this purpose, I make use of the grand-canonical surface energy γ_{GC} (here γ for simplicity), introduced in Section 3.9. In the case of the "ML+Si/Ag" model, i.e. the HCT reconstruction, there are also Ag atoms involved in the reconstruction, thus γ is a function of the Si (μ_{Si}) and Ag (μ_{Ag}) chemical potentials:

$$\gamma(\mu_{Si}, \mu_{Ag}) = \frac{1}{A}[E_{slab}(N_{Si}, N_{Ag}) - \tilde{E} - N_{Si}\mu_{Si} - N_{Ag}\mu_{Ag}] \qquad (6\text{–}2)$$

E_{slab} is the energy of the simulated slab containing N_{Si} Si atoms and N_{Ag} Ag atoms. A is the surface of the slab and $\tilde{E}/A$ is the surface energy of the bare Ag surface at the bottom of the slab (kept fixed during relaxation), which is calculated independently.

Fig. 6.13 shows the calculated surface energies of the structures previously described and compares them with calculations done for the clean silicene monolayer (4×4) and $(\sqrt{13} \times \sqrt{13})$ reconstructions (on top of Ag(111)), named "ML (4×4)" and "ML $(\sqrt{13} \times \sqrt{13})$", respectively. μ_{Ag} is fixed to E_{Ag}^{bulk}, the cohesive

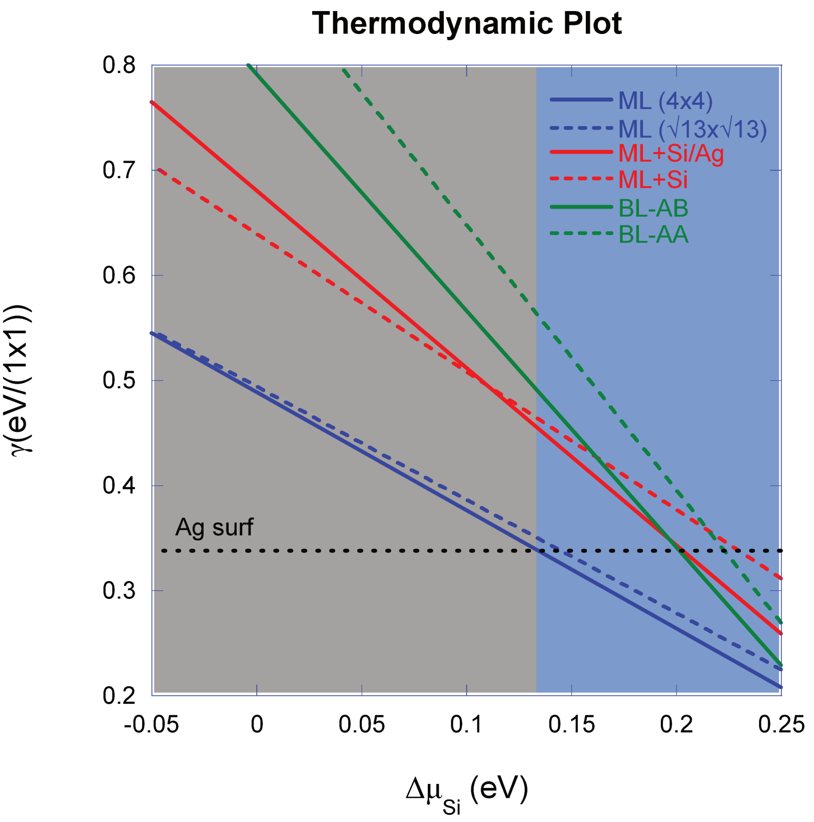

FIGURE 6.13: Surface energies of the different phases as a function of $\varDelta\mu_{Si} = \mu_{Si} - E_{Si}^{bulk}$. $\gamma_{1\times1} = \gamma \times A_{1\times1}$, where γ is defined in Eq. 6–2 and $A_{1\times1}$ is the area of the Ag(111) surface unit-cell. The silicene monolayer (ML) is calculated in the two (4×4) and $(\sqrt{13} \times \sqrt{13})$-type II reconstructions ("ML (4×4)" and "ML $(\sqrt{13} \times \sqrt{13})$", respectively), thoroughly described in Chapter 4. "Ag bare" corresponds to the relaxed Ag(111) surface. Other labels are defined in the text.

energy in the fcc Ag lattice. This is justified by the presence of bulk Ag and that at the temperature of the experiments the atomic mobility of Ag is large enough to ensure that the thermodynamic potential is the same for all Ag atoms. The energies are plotted as a function of $\varDelta\mu_{Si} = \mu_{Si} - E_{Si}^{bulk}$, where E_{Si}^{bulk} is the Si cohesive energy in the diamond Si lattice. I can make now a few simple considerations by looking at Fig. 6.13. Two "thermodynamic regions" can be identified, indicated by the grey-shaded and blue-shaded areas. In the first one, i.e. for $\mu_{Si} \approx \mu_{Si}^{blk}$, the most stable surface is the one relative to the bare Ag substrate, which appears to be even more favorable than the clean silicene monolayer ("ML (4×4)" and "ML $(\sqrt{13} \times \sqrt{13})$). Indeed, this is not surprising: silicene is known to be a metastable configuration of Si, as also evidenced by the dewetting of the silicene layer for T_{growth} >540 K. In the blue-shaded area, the silicene monolayer becomes energetically favorable (blue lines lower than the black one). Thus, the formation of silicene can be associated with those values of μ_{Si} near the transition between one region to the other, i.e. $\varDelta\mu_{Si}$=0.13 eV. The most remarkable evidence is that, in the entire range of μ_{Si} shown in Fig. 6.13 the proposed models for the Si islands are energetically unfavored: the BL-AB and BL-AA are way higher than the other values, but also ML+Si/Ag and ML+Si are not stable. Thus, according to DFT, the silicene monolayer is stable and it is not stabilized by the added-atom reconstructions, which instead are known for lowering the energy of bulk Si surfaces [143].

This result is in strong opposition to the pictures proposed so far for the Si growth on Ag(111) [6, 7, 135, 147]. However, in the following sections I will propose a new, alternative, explanation.

6.5 New evidences concerning the Si growth mechanism beyond monolayer deposition

According to the previous section, the clean monolayer is a stable structure which is not stabilized by added-atom reconstructions. Thus, the occurrence of the α and β phases is still a mystery.

To gain further insight, I report in Fig. 6.14 real-time STM images on the same area of the images in Fig. 6.2, but at a finer scale; the scanned surface corresponds to the area identified by the dotted square. Note that the amounts of deposited Si (Fig. 6.14) do not exactly correspond to the ones in Fig. 6.2, as Si was continuously deposited during the scanning of the STM. The sequence of images in Fig. 6.14 allows us to unveil a subtle mechanism.

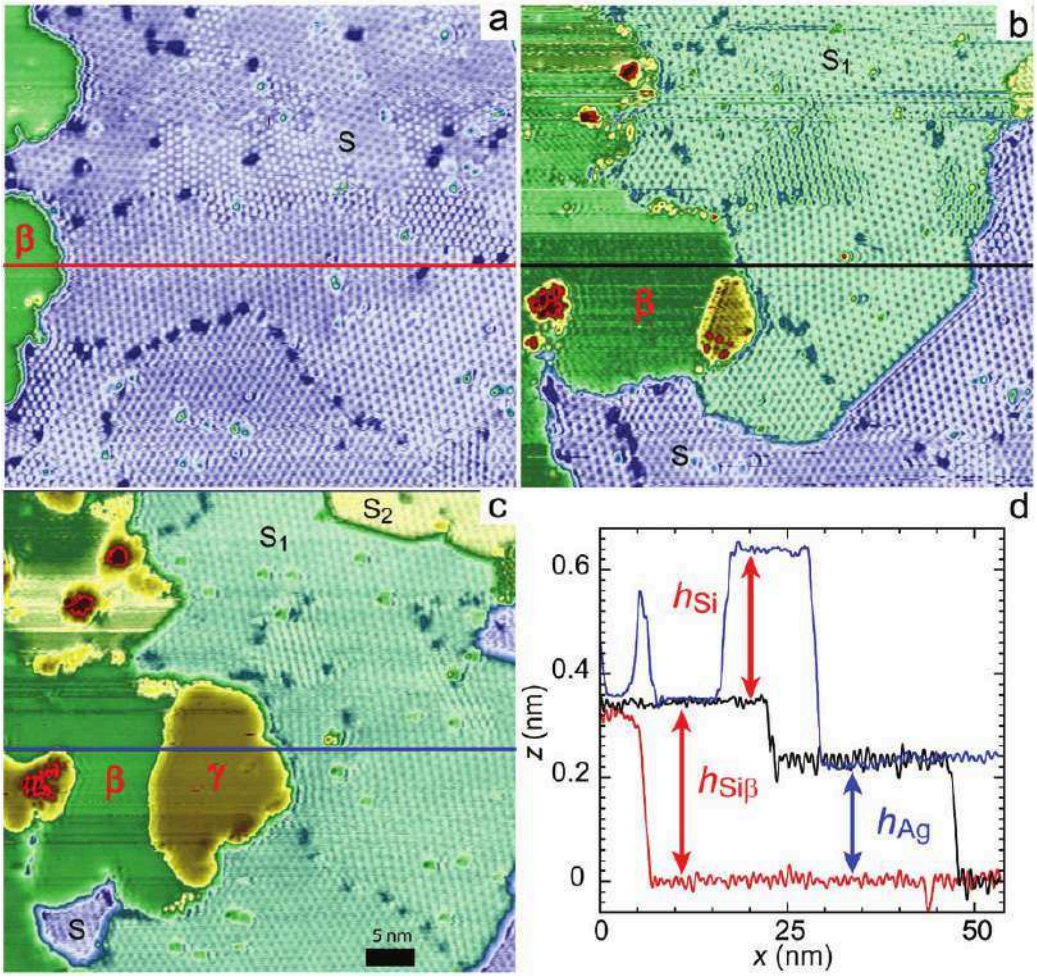

FIGURE 6.14: a-c) A detailed view of the evolution of the silicene layer during Si evaporation at 500 K corresponding to the dotted squares drawn in Fig. 6.2. The region is exactly the same for images a-c. The size of the image 53 × 52 nm^2. d) Evolution of the STM height profile: the red, black, and blues profiles correspond to the horizontal lines drawn in panels a, b, and c, respectively.

On the left side of Fig. 6.14.a, two parts of a β island (colored in green) are present. They are identified by their surface appearance and by their height (h_{Si_β} = 0.32 ± 0.01 nm) with respect to the silicene layer (S) as it is shown by the profile along the red line, Fig. 6.14.d. With increasing amount of deposited Si, several modifications can be observed in Fig. 6.14.c:

	ML	ML	α	ML+Si	β	ML+Si/Ag
h (nm)	**0**	0	**0.21**	0.11	**0.32**	0.25
Δh (nm)	**0.05**	0.08	**0.06**	0.08	**0.02**	0.04

TABLE 6.2: Characteristics of the simulated STM images of the structures described in the text. h is the apparent height with respect to the silicene monolayer and Δh is the corrugation. The quantities in boldface are from measurements. α and β refer to the two $(\sqrt{3} \times \sqrt{3})$ phases; ML refers to the monolayer (4×4) reconstruction.

- the β island is spreading out on the surface and covers a larger part of the silicene layer (left part of the figures, in green);
- the majority of the silicene layer (S_1 in seafoam color in Fig 6.14.b,c is now 0.235 ± 0.01 nm above the initial silicene layer (S in lavander color in Fig. 6.14.a), as shown by the height profiles along the black line;
- a new level of the silicene layer appears at the upper right part of Fig. 6.14.c (S_2, yellow), 0.235 ± 0.01 nm above the S_1 silicene layer;
- a new flat island colored in brown (γ) develops upon in Fig. 6.14.c, corresponding to a height increase h_{Si} = 0.30 ± 0.01 nm.

The most striking feature is that the height increase of the silicene regions, when changing from S to S_1 and from S_1 to S_2, coincides with h_{Ag} = 0.235 nm, which is the *height of a single Ag(111) step*. It is also very remarkable that the different domains and their orientations observed on *the initial silicene layer* (S region, lavender in Fig. 6.14.a) *is generally preserved* in the corresponding higher silicene terrace. (S_1, seafoam in Fig. 6.14.b). This is clearly seen at the bottom of Fig. 6.14.b, where the growth front separates upper (S_1) and lower terraces (S) with the same (4×4) reconstruction. These observations indicate that the growth (from from S to S_1 and from S_1 to S_2) corresponds to the *insertion of an additional Ag layer* (located at h_{Ag} above the initial (111) Ag surface) *below the silicene layer* and not to the second silicene layer, which would grow above the first one at $h_{Si} \sim \frac{4}{3} h_{Ag}$. This is the signature of an unexpected intercalation of an Ag layer below the silicene plane, which preserves its structure during the process.

At this point one question is natural:

where do these Ag atoms come from?

Indeed, the only possible explanation is that these Ag atoms come from the substrate as there is not any other source or reservoir of Ag. As a consequence of this, I propose, as only possible explanation, that *the Si islands showing* $(\sqrt{3} \times \sqrt{3}) - \alpha$ *and* $(\sqrt{3} \times \sqrt{3}) - \beta$ *reconstruction grow by digging into the substrate, ejecting in this way Ag atoms*. This scenario is not entirely surprising. Indeed, in the works by Prévot and collaborators [33, 65, 85, 87]. it has been shown that the Si insertion within the atoms of the outermost layer of Ag(111) is the fundamental mechanism behind the formation of the silicene monolayer, see Sec. 1.4.4. Fig. 6.14 indicates that a similar mechanism could explain also the formation of the bilayer. I will support this picture also by means of theoretical considerations based on DFT calculations, in the next section.

Important complementary information can be deduced from Tab. 6.2, which reports the apparent heights h with respect to the silicene monolayer in the STM images. By comparing the theoretical values with the experimental ones, I ascertain that the height h for ML+Si and ML+Si/Ag do not match the experimental values obtained for $(\sqrt{3} \times \sqrt{3}) - \alpha$ and $(\sqrt{3} \times \sqrt{3}) - \beta$ islands, respectively, confirming the conclusions drawn in the last paragraph.

	ML	ML	α	BL+Si	β	BL+Si/Ag
h (nm)	**0**	0	**0.21**	0.22(0.46)	**0.32**	0.30(0.53)
Δh (nm)	**0.05**	0.08	**0.06**	0.09	**0.02**	0.05

TABLE 6.3: Characteristic of the simulated STM images of the for BL+Si/Ag and BL+Si structures described in the text. h is the apparent height with respect to the silicene monolayer and Δh is the corrugation. The quantities in boldface correspond to STM measurements. α and β refer to the two $(\sqrt{3} \times \sqrt{3})$ phases; ML refers to the monolayer (4×4) reconstruction. For BL+Si/Ag and BL+Si, h has been reduced by 0.235 nm (the Ag-Ag interlayer distance) assuming that the atoms of the outermost Ag layer are expelled during the growth (this choice is clarified in the discussion). The values in parenthesis are obtained without applying this correction.

6.6 Si islands observed beyond silicene monolayer completion are reconstructed Si bilayers

In the previous section I have uncovered two important pieces of the puzzle:

- the α and β Si islands (appearing at the beginning of the second-layer formation) grow by digging into the Ag substrate. The consequent ejection of the Ag atoms is associated with a macroscopic movement of the Ag terraces.
- the calculated height of ML+Si and ML+Si/Ag are smaller than those of the Si islands measured experimentally.

These findings can be explained by assuming that silicene, after the ML completion, directly transforms into a Si bilayer. This new bilayer does not simply develop above the monolayer, but grows by digging into the substrate ejecting Ag atoms.

In the previous discussion (Sec. 6.4), I had hypothesized that the α and β phases are possibly due to the adsorption of Si and Ag atoms forming, respectively, the TDS and the HCT reconstructions on a silicene layer. These structures have been labeled as ML+Si and ML+Si/Ag. Accordingly I now consider the same two added-atoms reconstructions to terminate a silicon bilayer (BL) and I will call them BL+Si and BL+Si/Ag. The two structures will be used to interpret, respectively, the experimentally observed α and β phases and have been simulated by DFT calculations. The equilibrium configurations along with the corresponding simulated STM images are represented in Fig. 6.15. The equilibrium structural parameters are reported in Annex C.

Firs of all, notice that, just as for ML+Si/Ag and ML+Si, the simulated STM topographies of BL+Si/Ag and BL+Si are in good agreement with the surface appearance (corrugation and structure orientation) observed for the β and α domains (Fig. 6.1), respectively. Nevertheless, their apparent height with respect to the silicene monolayer is very high (numbers within parenthesis in Tab. 6.3) when compared with the experimental apparent height of the α and β phases. However, I still have to subtract the height of Ag(111) plane (i.e. 0.235 nm, the Ag-Ag interlayer distance), since I am assuming that the bilayer grows by digging into the Ag surface. The results are reported in Tab. 6.3 in which I observe a quite good agreement between predictions and experimental observations.

This argument, based on considerations about the experimental and theoretical STM heights, is however not conclusive (see Sec. 3.10) due to the high uncertainties associated with DFT calculations, which rely on the Tersoff-Haman model.

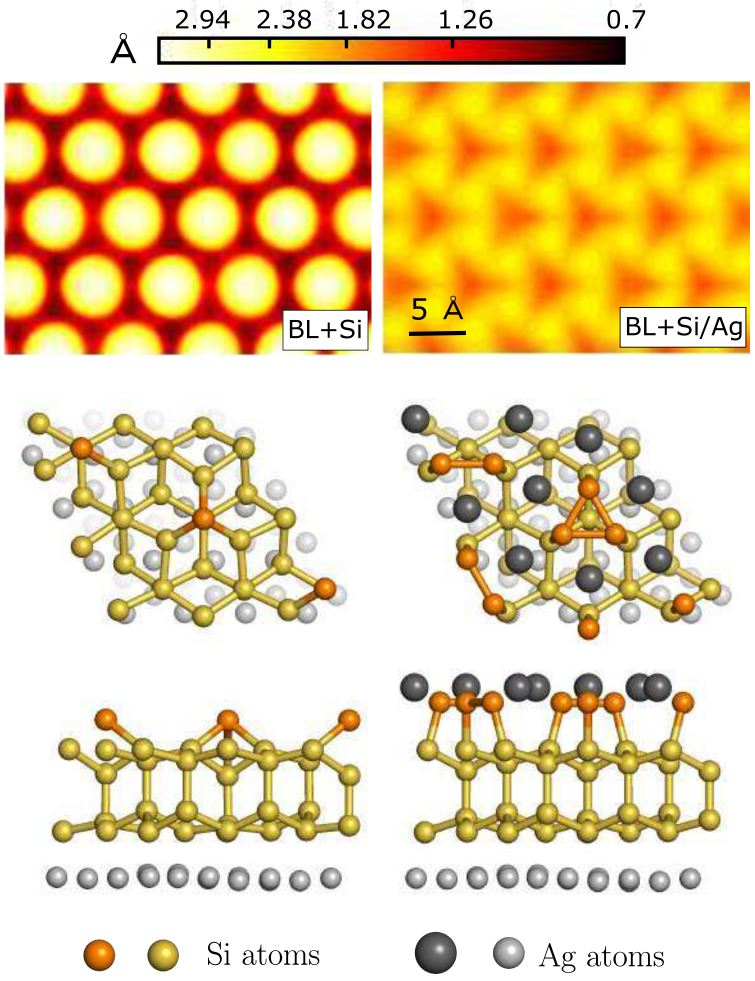

FIGURE 6.15: Schematic representation of the equilibrium structure for BL+Si/Ag and BL+Si along with the corresponding simulated STM images (U=0.5 V). The three bottom Ag layers have been omitted from the lateral views of the structures. The simulated STM topographies of BL+Si/Ag and BL+Si well reproduce the experimental surface appearance (Fig. 6.1) of the β and α islands, respectively, in compliance with the results of the simulations for their monolayer counterparts.

Let us now look at the stability of the new bilayer structures. Fig. 6.16 compares the grand canonical surface potential γ for the new BL+Si/Ag and BL+Si structures in the same $\Delta\mu_{Si}$ range as in Fig. 6.13. In panel (a), I compare, again, the two added-atom reconstructions ML+Si and ML+Si/Ag to the silicene monolayer. In panel (b) (the bilayer counterpart) the same added-atom reconstructions (BL+Si and BL+Si/Ag) are compared to the silicon bilayer. Information of great importance can be deduced from these two figures. Indeed, as already said, the added atom reconstructions do not stabilize the silicene monolayer (in Fig. 6.16.a, the ML+Si and ML+Si/Ag lines are above the ML $(4 \times 4)/(\sqrt{3} \times \sqrt{3})$ lines). On the contrary, the same reconstructions stabilize the bilayer structure (in Fig. 6.16.b, the BL+Si and BL+Si/Ag lines are below the BL-AB line). This is true in a very wide range of the Si chemical potential. The meaning of this finding is straightforward. It is well known that the (111) surface of bulk Si needs to be stabilized by added atom reconstructions resembling those presently considered (e.g. dumbbell configuration in the (7×7) reconstruction and HCT model, see discussion in Sec. 6.3.1). On the contrary, the silicene monolayer is a relatively stable structure (in a wide range of condition) which does not need to be stabilized by added atoms. Fig. 6.16.b shows that, according to DFT, the silicon bilayer is substantially different from the monolayer and needs to be stabilized in an analogous way to the bulk. These consideration strongly corroborate our hypothesis that the α and β reconstructions correspond to a bilayer structure terminated by added-atoms reconstructions.

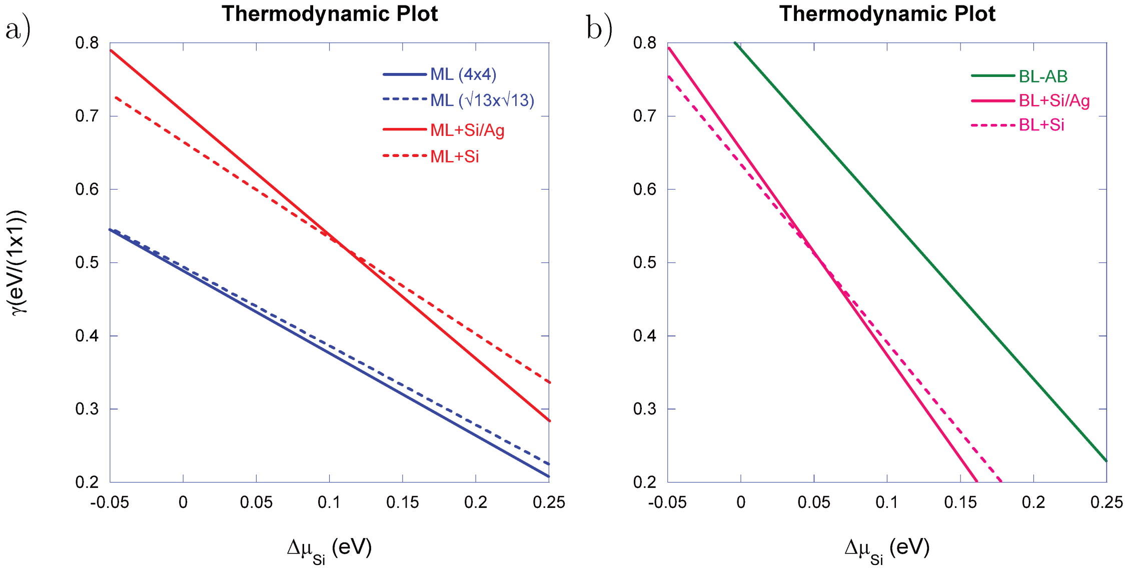

FIGURE 6.16: a) Comparison between the surface energies of the silicene monolayer reconstructions (ML (4×4) and ML $(\sqrt{13} \times \sqrt{13})$) and the silicon monolayer terminated by added-atoms reconstructions (ML+Si and ML+Si/Ag). b) Comparison between the surface energies of the non-reconstructed Si bilayer (BL-AB) and the silicon bilayer terminated by added-atoms reconstructions (BL+Si and BL+Si/Ag).

Let us now compare the bilayer structures with the monolayer and the bare silver structure, as shown in Fig. 6.17. The grey shaded region represents the $\Delta\mu_{Si}$ range in which the bare Ag surface is the most stable surface (as in Fig. 6.13), i.e. one wouldn't expect the formation of silicene or other Si 2D structures in this range of $\Delta\mu_{Si}$. As in Fig. 6.13, silicene (blue lines) starts to be energetically favorable for $\Delta\mu_{Si}$=0.13 eV.

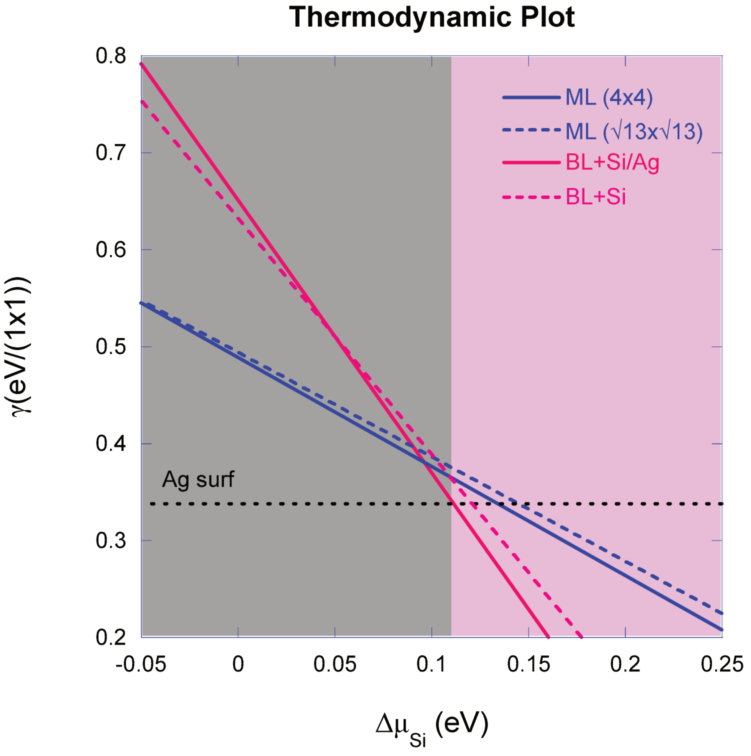

FIGURE 6.17: Surface energies for BL+Si/Ag and BL+Si compared to ML reconstructions and bare Ag. The $\Delta\mu_{Si} = \mu_{Si} - E_{Si}^{bulk}$ range reported is the same as in Fig. 6.13.

I stress out again that, experimentally, I expect to be close to this value, because the bare substrate surface and the silicene monolayer coexist during growth. Nonetheless, starting from $\Delta\mu_{Si}$=0.13 eV (pink shaded area) the bilayers structures are more favorable with respect to both silicene and Ag s urface. This means that in the $\Delta\mu_{Si}$ range predicted for our experiments, the formation of these bilayer structures is thermodynamically possible and favored, corroborating our hypothesis of direct transition from silicene monolayer to Si bilayer structure. Observe, also, that the BL+Si/Ag, i.e. the Ag-terminated Si bilayer (HCT model) describing the β phase, is slightly more favorable with respect to the BL+Si structure, i.e. the TDS-terminated bilayer associated with the α phase. This is in compliance with the process described in Sec. 6.2.2, by which the α phase observed in the first stages of growth of the second Si layer is progressively replaced by the β phase, until it completely disappears (metastable character of the α phase with respect to the β phase).

6.7 Si adsorption and substitution sites on Ag(111)-supported (4 × 4) silicene layer

Up to now, I have given theoretical and experimental evidences showing that the silicene monolayer transforms directly directly (upon further Si deposition) into a Si bilayer terminated by added-atom reconstructions. In this section I study the adsorption and substitution sites for a Si atom arriving on a complete (4 × 4) silicene layer on Ag(111) by DFT calculations. The aim is to confirm the last part of the general growth picture; i.e. that the Si bilayers (α and β phases) grow digging into the Ag substrate.

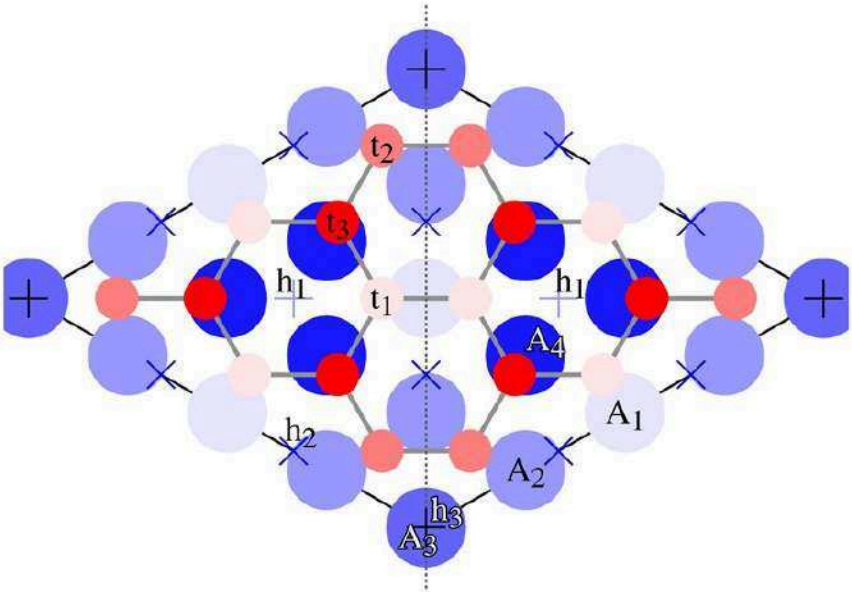

FIGURE 6.18: Adsorption sites for Si atoms on the (4 × 4) reconstruction (top view). Labels are defined in the text. Bluish disks are Ag atoms of the outermost layer, while reddish ones are Si atoms of the surface reconstruction. The black line represents the (4 × 4) unit cell. The system has C_3 symmetry around the sites labeled as h_1 and h_3. To simplify the notation I assume a mirror symmetry for the plane vertical to the surface and passing through the dotted line. There are four inequivalent Ag sites labeled as A_1, A_2, A_3, A_4. Using the same notation, there are three inequivalent Si sites: t_1, t_2 and t_3. The crosses indicate the centers of the Si hexagons formed in the reconstruction and they are labeled as h_1, h_2, and h_3.

The (4 × 4) reconstruction is simulated on top of a four layers Ag(111) slab (16×4+18=82 atoms per unit cell) and has energy $E_{(4\times4)}$. If I add one Si atom to the silicene structure and perform full relaxation of the atomic positions, I obtain the energy E_{+Si}. Various adsorption sites were tested and I report only the most stable here: a Si atom can be added on the top of a Si atom of silicene (sites labeled as "t" in Fig. 6.18 and grouped in three inequivalent possible positions) or on top of one center of the silicene hexagons ("h" sites in Fig. 6.18. I then consider a Si atom inserted below the silicene layer, substituting one Ag atom ("A" sites in Fig. 6.18); the corresponding energy is E_{+Si-Ag}. As a comparison, I compute the energy E_{+Ag} corresponding to one Ag atom on top of "h" sites.

ϵ_{+Si}		ϵ_{+Si-Ag}		ϵ_{+Ag}	
$6t_1$	0.65	$3A_1$	0.49		
$6t_2$	1.02	$6A_2$	0.68		
$6t_3$	1.21	$1A_3$	0.79		
$2h_1$	0.62	$6A_4$	0.87	$2h_1$	0.40
$6h_2$	1.22			$6h_2$	0.64
$1h_3$	1.52			$1h_3$	0.51
Ag(111)	1.27		0.50		0.67
Ag_{blk}	0.67	$Si_{(4\times4)}$	0.14		

TABLE 6.4: Adsorption energies in eV associated with the different adsorption sites with respect to the energy of bulk Si atoms E_{Si}^{blk}. The same labels used in Fig. 6.18 appear here preceded by an integer number indicating the number of equivalent sites (e.g. $3A_1$ means that there are three equivalent A_1 sites), which could be identified through the color code of Fig. 6.18. I have highlighted the most favorable adsorption sites.

Also in this case various adsorption sites above and below the silicene layer were tested. The "h" sites are the most stable. Tab. 6.4 reports the atomic adsorption energies (on various adsorption sites) defined as:

$$\begin{aligned}
\epsilon_{+Si} &= E_{+Si} - E_{(4\times4)} - E_{Si}^{blk} \\
\epsilon_{+Si-Ag} &= E_{+Si-Ag} - E_{(4\times4)} - E_{Si}^{blk} + E_{Ag}^{blk} \\
\epsilon_{+Ag} &= E_{+Ag} - E_{(4\times4)} - E_{Ag}^{blk}
\end{aligned} \tag{6–3}$$

Tab. 6.4 reports in the row labeled as "Ag(111)", the three analogous energies obtained after adsorption on the clean Ag surface (these quantities are those already calculated in Ref. [65] and in the last row ("Ag_{blk}"), the energy of a substitutional Si atom in a Ag bulk supercell (48 atoms). Note that in Fig. 6.18 I assume the equivalence of the two C_3 symmetric centers (both labeled as "h_1"). In the actual (4×4) reconstruction the two centers are not exactly equivalent because of the presence of deeper layers (not shown in Fig. 6.18) below the Ag surface plane, and the number of strictly inequivalent sites is roughly double with respect to those reported in the table. For the present purpose, this asymmetry is however slight: the adsorption energies of two slightly inequivalent sites differ by no more than 0.01 eV.

Finally, I have also calculated the energy of ϵ_{-Ag} to subtract one of the outer most Ag atoms (on top of silicene) from the two considered Ag-rich reconstructions labeled as "ML+Si/Ag" and "BL+Si/Ag", i.e. the energy to create an advacancy at the surface of the film. Let us call $E^{BL+Si/Ag}$ the energy of the slab simulating the BL+Si/Ag reconstruction ($4\times16+9$ Ag atoms + $2\times18+9$ Si atoms) and $E_{-Ag}^{BL+Si/Ag}$ the energy (determined after atomic relaxation) of the same slab in which one of the outermost Ag atoms has been subtracted. Analogous quantities can be defined for the ML+Si/Ag structure. Thus:

$$\begin{aligned}
\epsilon_{-Ag}^{BL+Si/Ag} &= E_{-Ag}^{BL+Si/Ag} - E^{BL+Si/Ag} + E_{Ag}^{blk} = +0.49\ eV \\
\epsilon_{-Ag}^{ML+Si/Ag} &= E_{-Ag}^{ML+Si/Ag} - E^{ML+Si/Ag} + E_{Ag}^{blk} = +0.24\ eV
\end{aligned} \tag{6–4}$$

These values can be compared with the energy (present calculations) to create an advacancy on the clean Ag(111) surface, $\epsilon_{-Ag}^{Ag(111)}$=0.59 eV, and to create a vacancy in the Ag bulk ϵ_{-Ag}^{blk}=0.78 eV. The energy to create a Ag vacancy immediately below the silicene (4 × 4) reconstruction, ϵ_{-Ag}^{ML} is defined in analogous way and depends on the Ag site considered. Using the labels of Fig. 6.18, I have obtained:

	A1	A2	A3	A4
ϵ_{-Ag}^{ML} (eV)	0.51	0.52	0.084	0.71

6.8 Energetics considerations and growth model

In previous sections I have concluded that α islands and β islands correspond to the BL+Si and BL+Si/Ag structures, respectively. The other structures considered, in particular ML+Si and ML+Si/Ag, are found to be less stable than the silicene monalyer structures in a large $\Delta\mu_{Si}$ range (Fig. 6.13). The fact that the ML+Si and ML+Si/Ag are less stable than the monolayer and that the BL+Si and BL+Si/Ag, on the contrary, are more stable than the bilayer is not entirely surprising. Indeed, while silicene (ML) is a relatively stable configuration with a hybridization different from that of diamond, the bilayer (BL) is more similar to diamonds and need to be stabilized by non-ideal reconstructions as it is the case for bulk-silicon surfaces.

One of the interesting observation, among the present ones, is that the formation of the $(\sqrt{3} \times \sqrt{3}) - \beta$ phase is accompanied by an increase in the adjacent silicene regions, which testifies the intercalation of Ag atoms under these layers (Fig. 6.14, 6.2). The emergence of these additional Ag atoms was, at first sight, very puzzling and raised the question of their origin. Knowing that the β phase is a bilayer (BL+Si/Ag), the most natural answer is that the bottom Si-layer of the bilayer is located below the original silicene monolayer and forms by dislodging the atoms of the outermost Ag layer. The expelled Ag atoms partially intercalate under neighboring silicene regions, increasing the height of the terraces, and partially go on top of the silicon (to form the $(\sqrt{3} \times \sqrt{3}) - \beta$ reconstruction). I have then argued that this dynamics has already started during the formation of the $(\sqrt{3} \times \sqrt{3}) - \alpha$ phase. This is not evident on the sole basis of Fig. 6.14, 6.2. However, I have concluded that the measured STM height of the α phase is a bilayer (BL+Si). Observing that the measured STM height of the α phase is smaller than that of the β one (0.21 nm and 0.30 nm, respectively), it is straightforward to deduce that the BL+Si structure has also formed by expelling the outermost Ag layer (otherwise the height would be much higher). Note also that the attribution of $(\sqrt{3} \times \sqrt{3}) - \alpha$ and $(\sqrt{3} \times \sqrt{3}) - \beta$ to bilayers (BL+Si and BL+Si/Ag) that are inserted below the outermost Ag layer is comparable with the calculated STM height reported in Tab. 6.3. This counterintuitive dynamics, which rules the growth of the Si bilayers, is represented in Fig. 6.19.

The presently described dynamics is compatible with the energetics for the adsorption of one Si atom on silicene/Ag(111), I have discussed in the previous section. According to these theoretical results, the substitution of a silicon atom with one Ag atom of the outermost Ag layer (which is below the silicene) is energetically favored with respect to the adsorption of one Si atom on top of the silicene layer. This dynamics contrast with a more intuitive and classical picture in which a Si atom would stick on the top of the surface and act as a nucleation centre for the growth of the second layer. This can be justified by looking at the energies reported in Tab. 6.4. ϵ_{+Si} quantifies how much a Si atom prefers to bind on a certain site on top of the silicene/Ag(111) system. All ϵ_{+Si} are > 0, meaning that Si atoms are more stable in the Si bulk. Consistently, ϵ_{+Si-Ag} quantifies how much a Si atom prefers to bind in a site below silicene after having displaced an Ag atom. Smaller values correspond to more stable configurations. The most relevant result from Tab. 6.4 is that, among the various values of ϵ_{+Si} and ϵ_{+Si-Ag}, the smallest one corresponds to ϵ_{+Si-Ag}

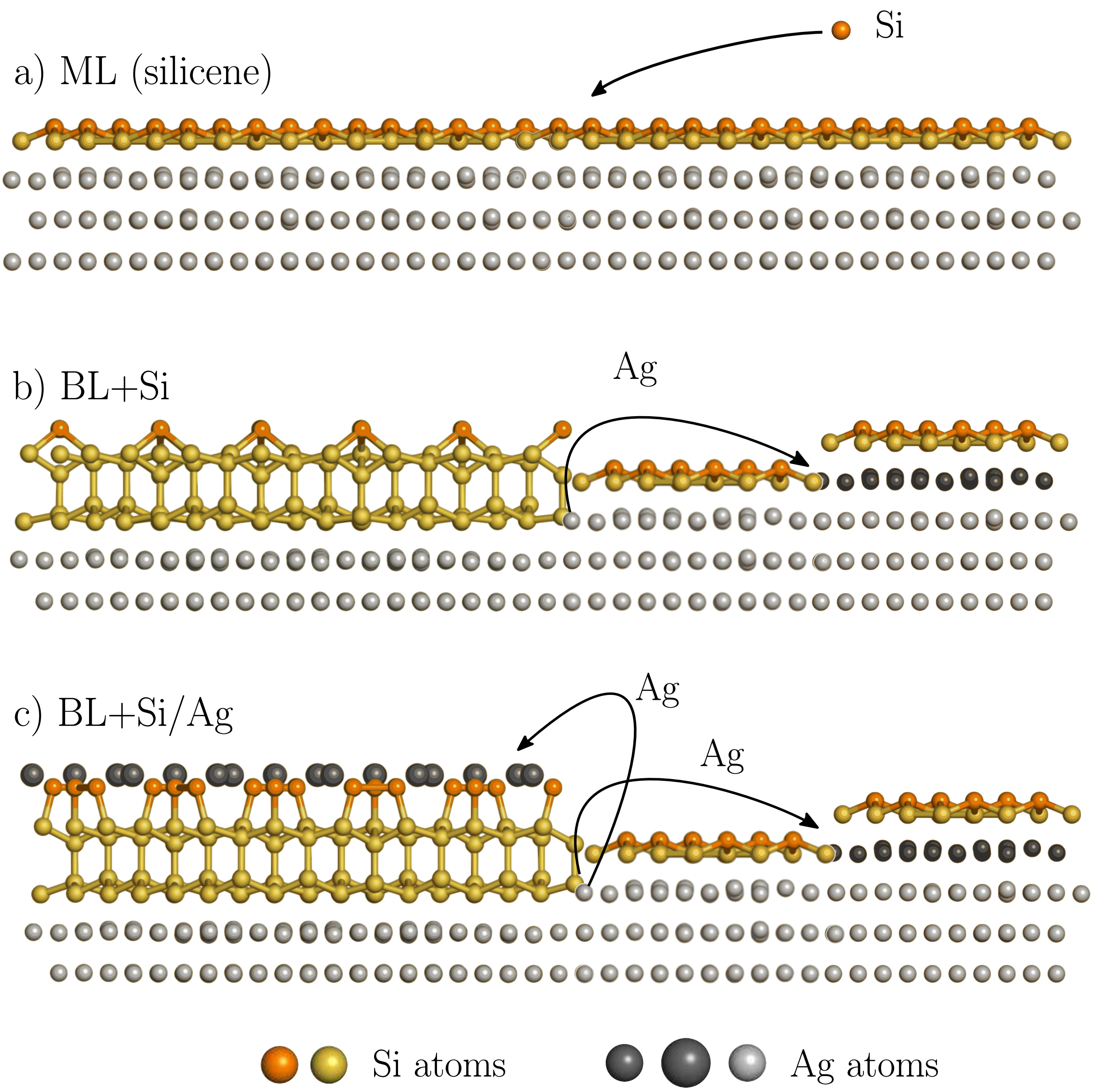

FIGURE 6.19: Complete silicene monolayer (ML) covering the Ag(111) substrate; b) formation of the Ag-free bilayer terminated by the TDS reconstruction (BL+Si); c) the initial bilayer is replaced with the HCT Ag-rich reconstruction (BL+Si/Ag). Note that in (b) and (c) the bilayer is inserted within the substrate, leading to the expulsion of the Ag atoms, which either reinsert below the silicene layer (b) or adsorb above the growing bilayer (c).

(in the A_1 configuration). This means that it is energetically more favorable for a Si atom to insert below the silicene layer (displacing one Ag atom) rather than to stick on the top of the silicene, as previously stated. Note also that these values are all higher than the energy of a Si atom bound in the ML-(4 × 4) ($Si_{(4\times4)}$=0.14 eV). This is not unexpected and, on the contrary, confirms the experimental evidences according to which an atom of Si prefers to bind to the silicene ML, before growing the successive layers. This is the result which corroborates the picture of silicene bilayers forming by dislodging the atoms of the outermost Ag layer, which is below the original silicene monolayer.

I now consider the energy to create a Ag vacancy below the silicene layer, ϵ^{ML}_{-Ag}. These energies can be used to quantify the strength of the Ag-Ag bonds, which is a relevant quantity to better understand the process of formation of the β phase, since this process is associated with the migration of the underlying Ag atoms. The vacancy formation energy of the clean Ag(111) surface, $\epsilon_{-Ag}^{Ag(111)}$=0.59 eV, is slightly smaller than the adsorption energy of an Ag atom over the Ag surface (0.67 eV). In principle, one should expect the presence of silicene to stabilize (increase) the energy of the outermost Ag atoms of the surface, because of additional bonding. Indeed, ϵ_{-Ag}^{ML}=0.71 eV for the site A_4 (corresponding to the clean Ag atoms almost below the t_3 Si atoms and, probably, more directly involved in the Si-Ag bonding). Unexpectedly, for the sites A_1 and A_2, ϵ_{-Ag}^{ML} (0.51 eV and 0.52 eV) is not substantially changed with respect to the clean surface value $\epsilon_{-Ag}^{Ag(111)}$=0.59. Even more surprisingly, the advacancies creation energies for the A_3 site (ϵ_{-Ag}^{ML}=0.084 eV) is smaller (the A_3 site corresponds to Ag atoms directly below the center of one of the Si hexagons and it is, thus, probably less involved in the Si-Ag bonding). I can thus conclude that the presence of a silicene layer on top of the Ag(111) surface does not stabilize the Ag atoms as much as one would expect, and, actually, diminishes the relative stability of certain Ag atoms, possibly favoring the Ag migration process.

The Ag/Si bond on the Ag-rich silicene reconstruction BL+Si/Ag, associated with the β phase, is relatively strong being ($E_{-Ag}^{BL+Si/Ag}$=0.49 eV) and only 0.1 eV smaller than $\epsilon_{-Ag}^{Ag(111)}$. The fact that $E_{-Ag}^{ML+Si/Ag}$=0.24 eV is smaller is consistent with the conclusion that the Ag-rich reconstruction stabilizes the β phase, but not the ML+Si and ML+Si/Ag structures. Exchange between Si and Ag atoms already occurs in the early stage of growth of the silicene monolayer: the insertion of a Si atom within the clean Ag(111) surface is a relatively fast process associate with an experimentally-determined small energy barrier of 0.43 eV [65]. Indeed, by comparing the adsorption of Si on the bare Ag(111) surface (next to last line of Tab. 6.4), it is evident that ϵ_{+Si-Ag} is smaller with respect to ϵ_{+Si} to such a degree that:

$$\epsilon_{+Si-Ag} + \epsilon_{+Ag} = 0.50\, eV + 0.67\, eV < 1.27\, eV = \epsilon_{+Si} \tag{6–5}$$

This means that the insertion of one Si atom can be accompanied by the expulsion of one Ag atom which adsorbs on top of the surface under an energetically favored process. In the present case, this relation does not hold (compare the smallest values available for each of the three quantities ϵ_{+Si-Ag}, ϵ_{+Ag} and ϵ_{+Si} from Tab. 6.4) and the expelled Ag atom (at least in the first stages of the bilayer growth) tends to remain trapped below the silicene layer within a process probably requiring a high activation barrier.

The insertion energy of a Si atom inside the Ag bulk (ϵ_{+Si} in the last line of Tab. 6.4) is higher than ϵ_{+Si-Ag} for both the Ag(111) surface and for the A_1 site below silicene. This means that, as expected, in both cases a Si atom that has inserted in the outermost layers of the surface does not have the tendency to migrate below.

Finally, although the process is energetically favored, it is not evident how a Si atom added on the top of the (4 × 4) silicene/Ag(111) surface can pass through silicene and insert within the Ag surface. The process should be associated with a relevant activation barrier since it implies the displacement of Ag atoms. Possible adsorption dynamics for the free-standing silicene are discussed in Ref. [147]. However, for the present silicene/Ag(111) case, the dynamics is expected to be substantially different. Indeed, by looking at the silicene from the top, one can distinguish between inward-buckled (t_1 and t_2 sites, Fig. 6.18) and outward-buckled (t_3) Si atoms. The adsorption of one Si atom on top of the inward-buckled atoms is favored. This is true for the (4 × 4) reconstruction, Fig. 6.18, and also for the free-standing silicene [147]. However, the relative position of the inward-buckled (IB) and outward buckled (OB) sites is different: in free-standing silicene, each IB site is surrounded by three OB sites; on the contrary, in (4 × 4) silicene/Ag(111) each IB site has at least one other IB site among the three neighbors (e.g. the two t_1 sites in the middle of Fig. 6.18 are adjacent). Once a Si atom has adsorbed on an IB site of the (4 × 4) silicene/Ag(111), it is possibly allowed to jump to neigboring sites with similar adsorption energy. Moreover, in the case of the (4 × 4) reconstruction, the adsorption on h_1 sites is particularly favored. This kind of adsorption is not expected to be relevant in the case of free-standing silicene (the small energy for the h_1 sites in Fig. 6.18 is a direct consequence of the presence of the Ag surface). The h_1 sites are adjacent to the t_1 sites suggesting that, because of the very similar energy, the adsorbed atom could be allowed to jump from the h_1 to the t_1 site and vice versa, creating a channel for the diffusion. Concluding, once a Si atom sticks on the top of thee surface on an energetically favored site (t_1, h_1, or t_2), it possibly could be allowed to diffuse by jumps from one site to the other still remaining on the top of the surface. Because of the presence of these diffusion channels on silicene/Ag(111) the adsorbed Si atom could finally reach a particularly favored location (possibly a step or a defect) to insert below the silicene layer. Note that a quite similar behavior also considering other ML structures.

This entire picture could explain why the bilayer starts growing only when the monolayer has completely covered the Ag surface, a fact observed experimentally.

Indications that a Si adatom diffusion is fast are given by DFT calculations on free-standing silicene [171], which provide an energy barrier of 0.75 eV for the diffusion of a dumbbell unit created by the addition of a Si adatom. This should result in high jump rate at T=500 K, of the order of 10^5 s^{-1}, considering the usual attempt frequency of 10^{13} s^{-1}. Note also that the reorganization of the silicene layer during growth (which involves Si-Si bond breaking) has been predicted [172] and experimentally observed [65]. Thus, energy barrier for Si diffusion and Si-Si bond reorganization are low-enough to enable 2D growth at 500 K.

Concerning the Ag kinetics, the expelled Ag atoms are expected to easily wet Si islands due to their fast diffusion. Indeed, an activation barrier of 0.25 eV has been measured for Ag atoms on the Si(111) (7×7) reconstruction of Si is also fast with a barrier of 0.33 eV [173]. The diffusion of Ag atoms on the Ag-$(\sqrt{3} \times \sqrt{3})$ reconstruction of Si is also fast, with a barrier of 0.33 eV [174]. Lower barriers should be obtained for Ag atomic jumps on the silicene surface, in analogy with graphene. Finally, further growth of the Si islands proceeds by exchange between incoming Si atom and surface Ag atoms forming the $(\sqrt{3} \times \sqrt{3})$ reconstruction. Such an effect has been already evidenced during Si homoepitaxy on Si(111)-$(\sqrt{3} \times \sqrt{3})$ Ag at 570 K [175]. Si diffusion through the Ag layer has already been evidenced during Co deposition on Si(111)-$(\sqrt{3} \times \sqrt{3})$ Ag where cobalt silicide formation on the $(\sqrt{3} \times \sqrt{3})$ reconstruction is observed above 400 K [176].

6.9 Summary of the results of Chapter 6

A joint experimental investigation, based on GIXD and real-time STM measurements, and theoretical study, based on DFT calculations, has given new and original results concerning the structure and growth of Si films on Ag(111).

- By GIXD measurements, I have determined that Si films on Ag(111) (2 ML Si coverage) are terminated by a $(\sqrt{3} \times \sqrt{3})R30^\circ$ reconstruction substantially identical to the $(\sqrt{3} \times \sqrt{3})R30^\circ$ Ag termination of Si(111), described by the so-called honeycomb chain triangles (HCT) model. Thus, Ag atoms segregate at the surface during the growth of the 2nd and successive Si layers.
- Real-time STM measurements show the presence of two $(\sqrt{3} \times \sqrt{3})R30^\circ$ phases in the first stages of growth of the 2nd Si layer. They have been labeled as α and β phases.
- The β phase grows at expenses of the α phase. At 2 ML (and higher) Si coverage only the β phase is visible. Thus, it is reasonable to believe that the β phase coincides with the structure previously determined by GIXD, i.e. the Ag-$(\sqrt{3} \times \sqrt{3})R30^\circ$ termination of the bulk-like Si film.

- To determine the structure of the α phase I have performed extensive DFT calculations taking into consideration several Ag-free models proposed in the literature, for which I have also simulated the theoretical STM images. The only model reproducing the experimental STM images of the α phase consists of a silicon monolayer with a $(\sqrt{3} \times \sqrt{3})R30^\circ$ added-atom reconstruction with Si atoms in dumbbell configuration (trigonal dumbbell silicene or TDS model), which I have labeled as ML+Si. To compare the stability, I have also simulated the β phase with the HCT Ag-$(\sqrt{3} \times \sqrt{3})R30^\circ$ reconstruction on top a single Si layer, labeled as ML+Si/Ag. Its simulated STM images are in good agreement with the surface appearance of the β islands.

- The thermodynamic plot for the simulated reconstructions have shown than neither the ML+Si nor the ML+Si/Ag models are more stable than the silicene layer (ML (4×4) and ML $(\sqrt{13} \times \sqrt{13})$, in a wide range of the Si chemical potential μ_{Si}. A new interpretation is needed.

- To escape this impasse, new real-time STM evidences have come to our help. During the growth of the 2nd and successive Si layers, STM images show that the step edges covered by the silicene monolayer evolve. In particular, in their proximity the silicene sheet on the lower terrace is pushed up of exactly the height of one Ag(111) step. This means that there must be Ag atoms diffusing on the surface and reinserting below the silicene layer near the step edges. These Ag atoms must come from the substrate.

- The only explanation to the previous point is that **the second Si layer (both α and β phases) do not grow on top of the silicene monolayer, but grow by digging into the Ag(111) substrate ejecting Ag atoms, which then diffuse toward step edges and reinsert below the silicene layer.**

- To confirm the previous picture I have performed again DFT calculations. Now the α phase is simulated by a Si bilayer terminated by the dumbbell added-atom Si reconstruction (BL+Si) and the β phase by the HCT Ag-$(\sqrt{3} \times \sqrt{3})R30^\circ$ reconstruction on top of a Si bilayer (BL+Si/Ag). Also in this case the simulated STM images are in good agreement with the experimental ones.

- The thermodynamic plot this time shows a different trend from the previous one. In a wide range of μ_{Si} both BL+Si and BL+Si/Ag are more stable than the silicene monolayer and than the bare Ag surface. This evidence corroborates the proposed picture of direct transition from silicene monolayer to Si bilayer terminated by added-atom reconstructions. Thus, α coincides with BL+Si (TDS model) and β with BL+Si/Ag (HCT model), in the first stages of growth of the second Si layer on Ag(111). Moreover, the two reconstructions are much more stable than a simple Si bilayer with AB stacking (BL-AB).

- The comparison between the two thermodynamic plots gives another important evidence: the silicene monolayer is not stabilized by added-atom reconstructions (ML+Si and ML+Si/Ag), while the energy of the Si bilayer (BL-AB) is lowered by the same added-atom reconstructions (BL+Si and BL+Si/Ag). I recall that surface reconstruction similar to the simulated ones usually terminate the Si bulk (see the (7×7) reconstruction and the HCT Ag-structure on Si(111)). Thus, **the silicene monolayer is a peculiar system substantially different from bulk Si. On the contrary, the Si bilayer already behaves similarly to Si(111)**, the surface of which needs to be stabilized by surface reconstructions.

- I have also presented energetics considerations on the adsorption of Si atoms on top of the silicene (4×4) layer and substitution in the underlying 1st Ag(111) layer. For certain sites, it is energetically favorable to have a Si atoms inserted in the Ag(111) substrate below the silicene layer instead of having it adsorbed on top. This further supports the interpretation according to which the α and β phases grow by digging into the Ag substrate.

Chapter 7

Si evaporation on layered materials

7.1 Introduction

From the discussions detailed in Chapter 4, 5 and 6, it is clear that the growth of silcene on Ag(111) is characterized by a strong coupling between the substrate and the silcene layer. In Chapter 4, I have shown that the interaction with the substrate is responsible for the stabilization of the 2D Si sheet. Also the properties of the silicene layer are strongly affected by this interaction and they result to be substantially different from those expected for free-standing silicene [1, 76, 79].

For this reason a new class of materials suitable for silicene synthesis is highly desired. A possible choice is represented by the layered materials, such as graphite or transition metal dichalcogenides (TMDCs). These materials have several characteristics which make them suitable *a priori* for silicene synthesis:

- many of them have an hexagonal surface symmetry, as the one expected for silicene;
- they are inert and they do not possess dangling bonds at the surface;
- defect-free surfaces can be easily obtained by cleaving with scotch tape.

Several experiments have been devoted to study the growth of Si and Ge on HOPG [30] and MoS_2 [31]. In particular on HOPG, it has been hypothesized that the weak interaction of Si an Ge with the substrate could be crucial in the formation of an hexagonal lattice [30, 177, 178].

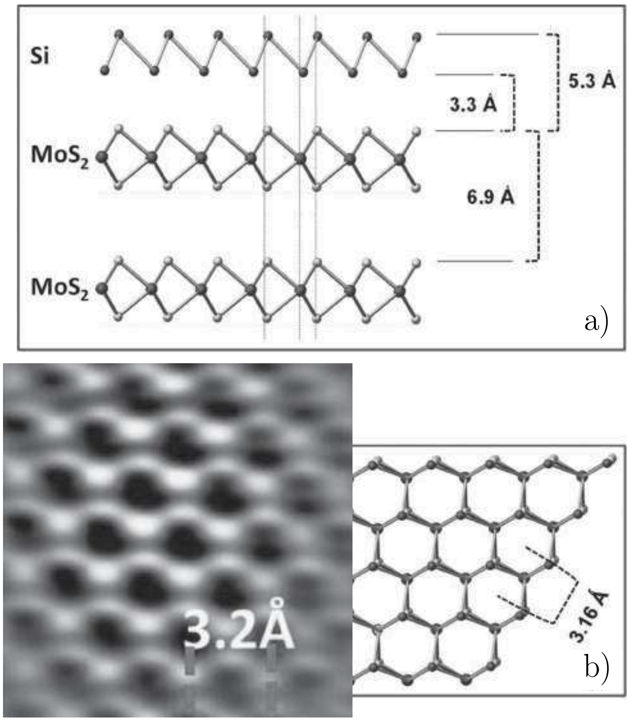

FIGURE 7.1: High-buckled silicene model proposed by Chiappe *et al.* [31] based on DFT calculations. The image reports the lateral (a) and top (b) view of the minimum energy configuration. In (b), an atomically-resolved STM image is partially superimposed to the structural model.

Chiappe *et al.* have concluded to the formation of a silicene layer covering the MoS_2 substrate, on the basis of STM and RHEED measurements, supported by DFT calculations. After the evaporation of 0.8 ML of Si at T_{growth}=473 K the surface appears partially covered by 2D islands associated with Si domains with the same surface periodicity as the underlying MoS_2 substrate (see Fig. 7.1). As a consequence of this (1×1) reconstruction, RHEED measurements do not show additional streaks after evaporation. The model proposed consists in a highly-buckled (Δ=2.0 Å) silicene layer with the same lattice parameter as the underlying MoS_2 substrate, (see Fig. 7.1.a). This result has been put into question by experimental evidences of Si intercalation in MoS_2, reported for small Si deposition (0.2 ML) at room temperature [179], a behavior confirmed also for Si deposition on another TMDC, namely WSe_2 [180].

Concerning Si/HOPG, some studies have reported an island (or Volmer-Weber) growth for Si/HOPG [181, 182]. More recently, De Crescenzi *et al.* have performed atomic force microscopy and STM measurements, supported by *ab-initio* molecular dynamics calculations. After the evaporation of Si at room temperature on HOPG, they have reported the formation of Si clusters and in-between these clusters they have observed a $(\sqrt{3} \times \sqrt{3})R30^\circ$ reconstruction (Fig. 7.2). This surface structure has been interpreted as a silicene layer.

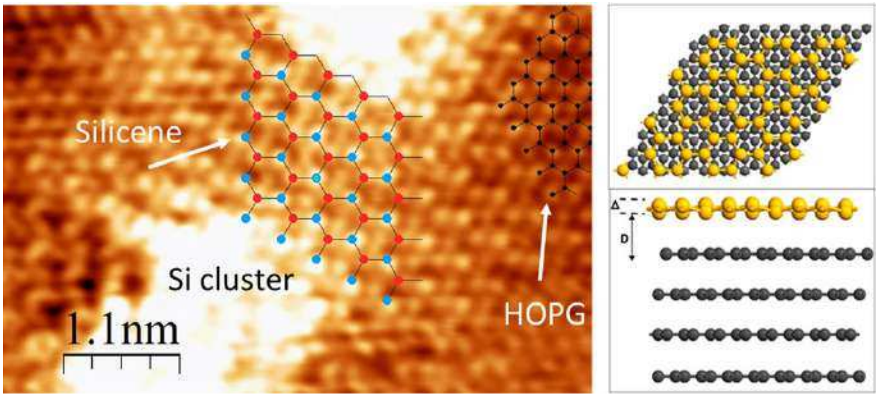

FIGURE 7.2: Images reproduced from ref. [30]. Left: STM image obtained at room temperature of 1 ML of Si deposited on HOPG at room temperature. The ball-and-stick models identify the silicene (blue and red circles) and HOPG (black lattice) structures. Right: top and lateral view of the proposed silicene model.

De Crescenzi *et al.* also report evidences of sp_2 behavior and the presence of a Dirac cone for the silicene layer, by means of scanning tunneling spectroscopy and DFT calculations.

In a more recent publication [183], this thesis is also supported by Raman measurements. In particular, a Raman mode is reported at 542.5 cm^{-1}, along with the Si nanocluster mode and the transverse optical peak of bulk Si. However, the Raman E_{2g} resonance is expected at 575 cm^{-1} for a buckling value of 0.44 Å [184]. This inconsistency is explained in terms of potentially different buckling of the synthesized silicene layer, as an increase of such a parameter should result in a downshift of the E_{2g} feature [185]. Despite these last findings, the nature of the $(\sqrt{3} \times \sqrt{3})R30^\circ$ reconstruction is still debated, as some studies have reported a similar reconstruction in the presence of nanoclusters of different atomic species [186–189].

In this chapter, I report the results of STM investigations of the Si growth on four different layered materials: HOPG, MoS_2, $TiTe_2$ and $ZrSe_2$. Note that, as shown in Tab. 7.1, HOPG and MoS_2 have a lattice parameter quite different from the one expected for silicene (36% and 18% lattice mismatch, respectively). On the contrary, the lattice parameters of $TiTe_2$ and $ZrSe_2$ are much more similar (lattice mismatch of 1.4%). Epitaxial growth of a Si layer on these two last materials could potentially lead to a (1×1) reconstruction, while in the case of HOPG and MoS_2, a surface structure with different periodicity is more likely to be obtained, or a highly buckled silicene layer as reported by Chiappe *et al.* [31],(even if its free-standing form should be unstable [1]).

	HOPG	MoS_2	$TiTe_2$	$ZrSe_2$
a_{1x1}	2.46 Å	3.15 Å	3.77 Å	3.77 Å
mismatch with silicene	36%	18%	1.4%	1.4%

TABLE 7.1: Lattice parameters of the studied materials and their matching with the silicene lattice parameter 3.83 Å [190, 191]. The lattice constant of $TiTe_2$ is the one given by the seller; in ref. [192], the lattice constant is found to be equal to 3.87 Å.

7.2 Si/HOPG

Fig. 7.3.a reports STM images taken at room temperature of the pristine HOPG surface. The sample has been peeled-off in air and then intriduced in the UHV chamber, where it has been annealed for one hour at 200 C°. The STM image reveals the triangular lattice of graphite, with a lattice constant of 2.46 Å, which corresponds to second-nearest-neighbor distance, as depicted in Fig. 7.3.b. The observed triangular lattice reflects the sublattice asymmetry expected for Bernal stacked graphite (stacking ABA), for which the "A" atoms, represented in Fig. 7.3.b, are stacked above the same type of atoms of the second layer, while "B" atoms of the surface layer are above the hollow sites of the second carbon layer [193, 194]. Local density of state near the Fermi level is much more important on "B" atoms. This can be explained by observing that at the K-point of the Brillouin zone of graphite, the electronic band is flat in k_z (out-of-plane component of the electronic momentum) for "B" atoms as they are not coupled with those of the underlying plane. On the contrary, the "A" atoms possess a dispersed electronic band because of the interaction with the atoms of the second HOPG layer.

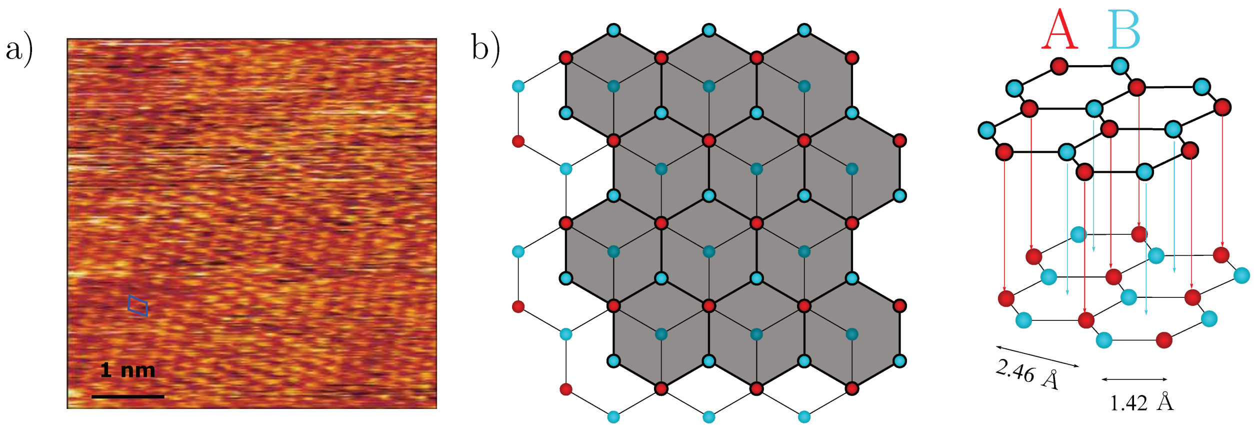

FIGURE 7.3: a) STM image of the bare HOPG substrate obtained at room temperature (U=0.2 V, I=50 pA), in which it is possible to identify the typical triangular lattice of pristine HOPG. The blue rhombus represents the unti cell of HOPG. b) Schematic representation of Bernal stacked graphite. "A" and "B" label the atoms which have or not a corresponding C atom in the second layer, respectively. Because of this configuration STM can image only the "B" atoms [193], as explained in the text.

It is known from the literature [195–197] that the surface appearance obtained in atomically resolved STM images near step edges can be quite different. In some cases the triangular lattice is no longer visible and instead a surface reconstruction, identified as a $(\sqrt{3} \times \sqrt{3})R30°$ structure, is observed. The measured lattice constant of this structure (4.3±0.1 Å) is consistent with the expected value $\sqrt{3} \times 2.46$ Å = 4.26 Å [195].

After evaporation of 0.2 ML of Si at room temperature on the HOPG surface (Fig. 7.4), bright protrusions appear, similar to those reported in ref. [30]. These features are attributed to small Si clusters, in agreement with ref. [182]. The apparent height of the clusters in the image is about 4 Å. The cluster in

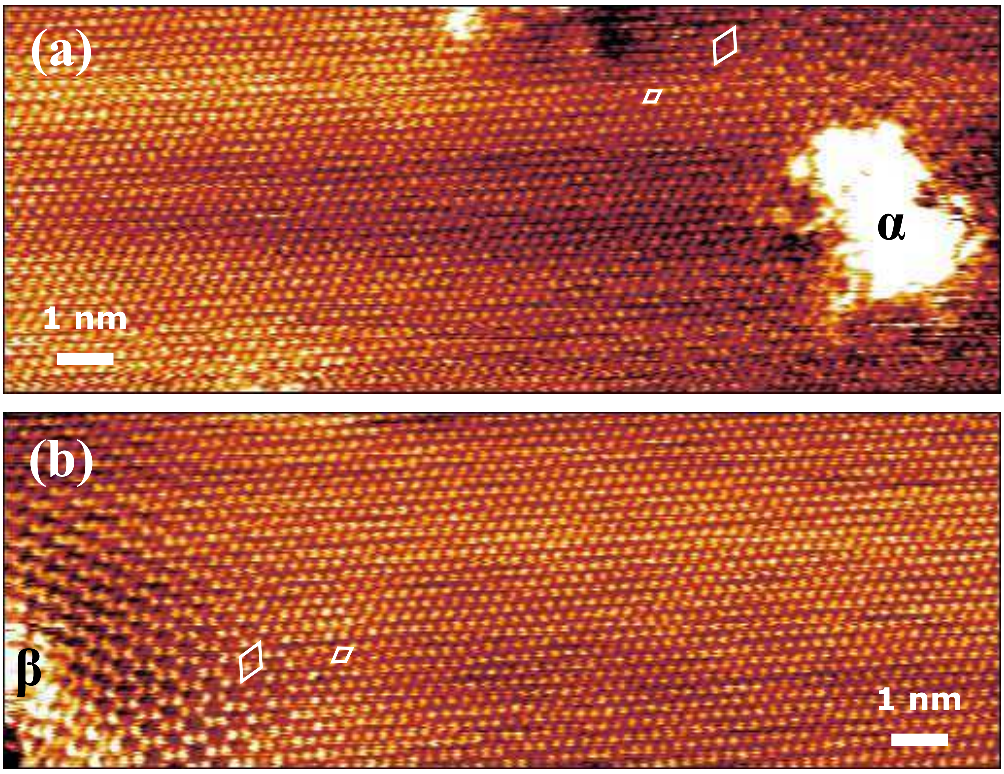

FIGURE 7.4: a-b)STM images acquired after the evaporation of 0.2 ML of Si at room temperature on HOPG. Two silicon clusters are labeled as α and β. In both images we report the unit cells of HOPG and $(\sqrt{3} \times \sqrt{3})R30^\circ$. Tunneling conditions: U=0.2 V, I=50 pA.

Fig. 7.4.b is found in proximity of a HOPG step edge. It is interesting to note, in these two images, that whereas the expected HOPG triangular lattice is observed on the majority of the atomically flat surface, in the vicinity of the Si clusters a different surface structure is observed. Fig. 7.5 is a magnification on the bottom left part of Fig. 7.4.b. The measured lattice constant of the honeycomb superstructure is 4.25±0.05 Å. Note that this value is identical to the lattice constant measured for the $(\sqrt{3} \times \sqrt{3})R30^\circ$ reconstruction reported on the bare HOPG substrate. This is also very similar to the value reported by De Crescenzi *et al.* [30](4.1±0.2 Å).

The first controversial point is that the value found for the $(\sqrt{3} \times \sqrt{3})R30^\circ$ reconstruction on HOPG (after and before Si evaporation) is different from the value expected for a silicene layer. For a 30° rotation between an hypothetical silicene sheet and the HOPG substrate, the *ab initio* simulations reported in ref. [30] have predicted a lattice constant equal to 3.79 Å(for the Si lattice), which is very close to what is expected for free-standing silicene (3.83 Å). This value is 11% smaller than the experimental value (experimental uncertainty <2%).

Another questioning point with the silicene picture proposed, is that Cai *et al.* [198] have predicted that, for the similar case of silicene/graphene, a coexistence of several phases of silicene should be observed at room temperature. In compliance with the case of silicene/Ag(111) (Chapter 4, the different phases are associated with different orientations of the silicene layer with respect to the HOPG substrate); a large number of simulated configurations have been found to have nearly the same free energy, the most stable one corresponding to the superposition of a $(\sqrt{21} \times \sqrt{21})R10.9^\circ$ silicene supercell over a $(2\sqrt{13} \times 2\sqrt{13})R13.9^\circ$ graphene supercell.

For these reasons, it is not clear if the observed reconstruction $(\sqrt{3} \times \sqrt{3})R30^\circ$ corresponds to the presence of a silicene layer.

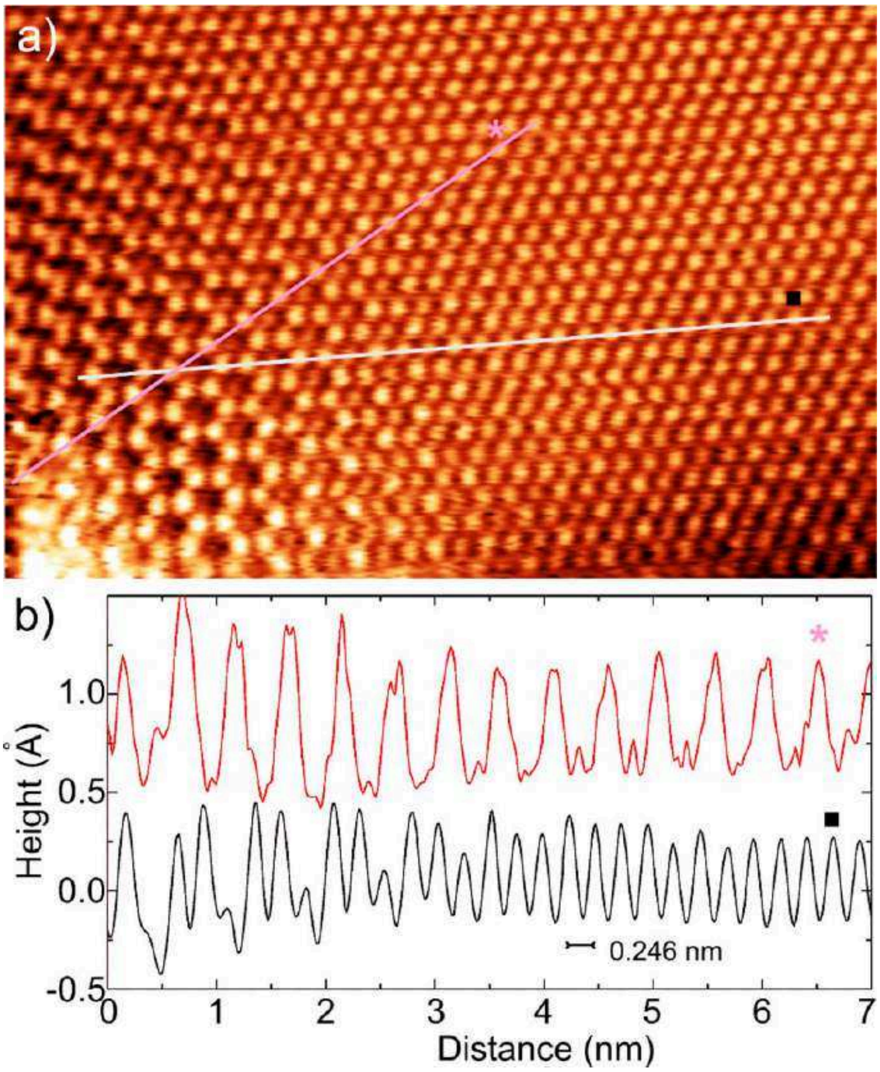

FIGURE 7.5: a) High-magnification STM view of the left-down part of Fig. 7.4.b. b) Height profiles along the white and pink segment shown in (a). Tunneling conditions: U=0.2 V, I=50 pA.

Additionally, Fig. 7.5 shows that there is a continuous transition from the unreconstructed areas, where HOPG triangular lattice is observed, to the $(\sqrt{3} \times \sqrt{3})R30^\circ$ hexagonal reconstructed areas in proximity of the defects. This transition occurs along with a slight increase of the corrugation, as one can see in the height profiles in Fig. 7.5.b, which can be compared to those reported by De Crescenzi *et al.* [30]. Indeed, in the presence of a silicene, it would be reasonable to expect a rather abrupt change from the $(\sqrt{3} \times \sqrt{3})R30^\circ$ hexagonal reconstructed areas to the triangular ones, and not this continuous transition which extends over 30 Å.

Let us now take a closer look at the change from one structure to the other. Interestingly, in the hollow sites of the hexagonal reconstruction associated with the $(\sqrt{3} \times \sqrt{3})R30^\circ$ superstructure, an atom progressively appears when moving toward the pristine HOPG surface. The intensity of the STM image changes until the apexes of the hexagon and the atom in the center have all the same intensity, recovering the triangular surface appearance of HOPG. Note that the atom appearing in the hollow site is not expected in the case of a silicene layer which should lie 3.3 Å above HOPG, as pointed out in the calculations reported in ref. [30].

For all the reasons discussed above, the association of the $(\sqrt{3} \times \sqrt{3})R30^\circ$ reconstruction with a weakly interacting silicene layer on HOPG is questionable. Instead, the observation of Si clusters is consistent with previous observations reported in the literature [182] and with the fact that Si adatoms can easily diffuse onto the HOPG surface. At this point the $(\sqrt{3} \times \sqrt{3})R30°$ reconstruction could result from a long-range perturbation of the charge density at HOPG surface due to interference phenomena between the surface electron waves and scattered waves from defects (step edges included) or clusters [189, 199, 200]. A similar pattern has already been observed after the adsorption of other chemichela elements (e.g. ozone [189] and hydrogen [188]), particles (e.g. Pt [186, 187], Mo [201], and/or the creation of defects induced by Ar$^+$ bombardment [202–204]. In particular the images reported for Pt adsorption on HOPG are very similar to those reported here and in refs. [30, 183]. In all the cited cases the charge density waves decay over distances in the 20-50 Å range, depending on the type of defects.

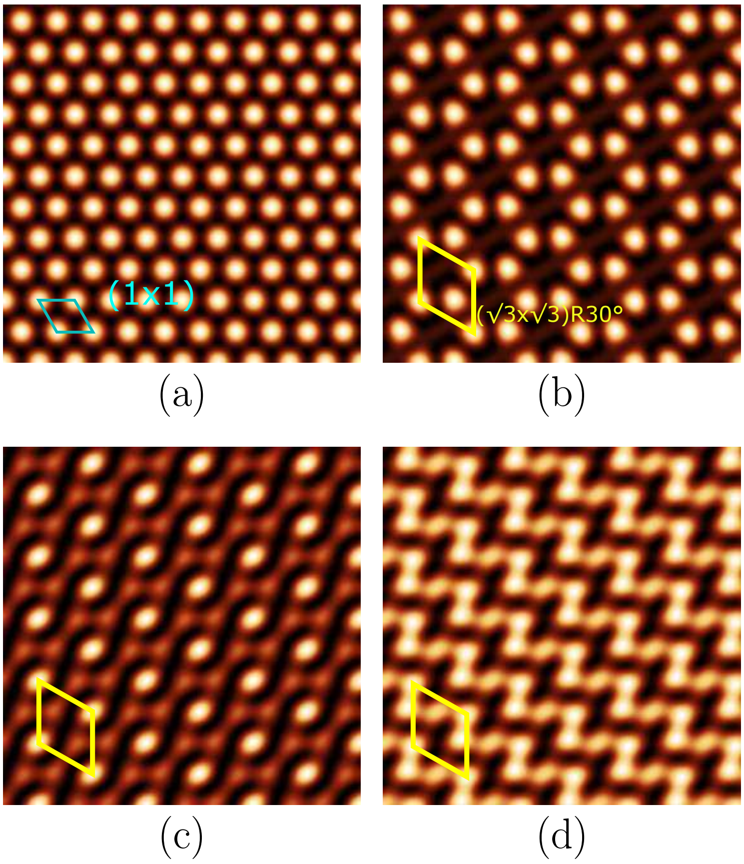

(a) (b)

(c) (d)

FIGURE 7.6: Simulated local density of states at the Fermi level, for various sets of a_i and b_i coefficients. a) a_i=b_i=1; b) a_1=a_2=0, a_3=b_i=1; c) a_1=a_2=b_2=b_3=1, a_3=2,b_1=0, d) a_1=b_2=1, a_2=b_1=0, a_3=b_3=2.

To support this interpretation, the charge density waves is simulated by employing the interference model proposed in the literature [189, 200], keeping in mind that at low bias voltages, the STM images reflect the wavefunctions of electron states near the Fermi surface. Therefore, let us take into considerations six plane waves corresponding to the different K and K' points of the Brillouin zone at the Fermi energy for HOPG. The electron density can be written as:

$$n(\boldsymbol{r}) = \Psi_s^2 + \Psi_a^2 = \left(\sum_{i=1}^{3} a_i cos(\boldsymbol{K}_i \boldsymbol{r})\right)^2 + \left(\sum_{i=1}^{3} b_i cos(\boldsymbol{K}_i \boldsymbol{r}_i)\right)^2 \tag{7–1}$$

where Ψ_s and Ψ_a are the symmetric and anti-symmetric linear combinations of the six plane waves, $\boldsymbol{r}$ is the spatial coordinates and a_i and b_i are coefficients. For an unperturbed surface, one expects all coefficients

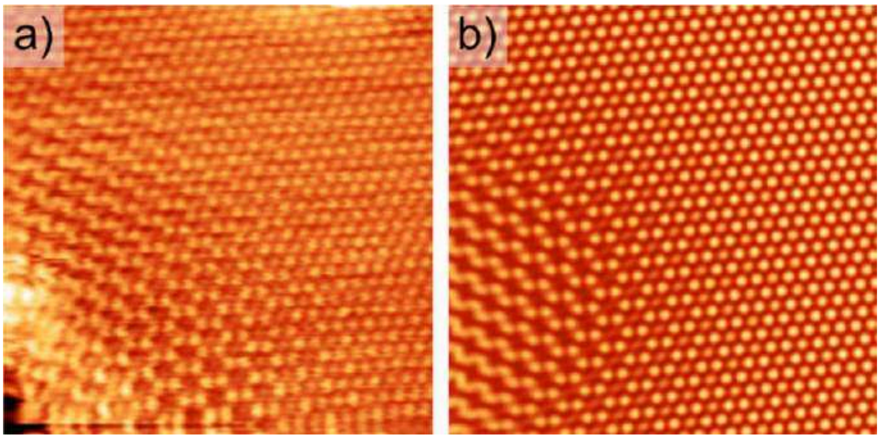

FIGURE 7.7: Comparison of (a) the experimental STM image of Fig. 7.4b with (b) a simulated STM image where the electronic interference is considered.

to be equal, giving rise to the trigonal pattern of Fig. 7.6.a, with a (1×1) periodicity. Whenever the coefficients do not have the same value, a $(\sqrt{3} \times \sqrt{3})R30^\circ$ reconstruction appears, as reported in Fig. 7.6.b,c,d. The interference pattern can display different features (always with the same periodicity), depending on the relative values of the coefficients a_i and b_i, which well reproduce the STM observations reported in the literature [30]. By simulating the combined effect of a linear step edge and a silicon island (see Fig. 7.7), it has been possible to reproduce the progressive decay of the $(\sqrt{3} \times \sqrt{3})R30^\circ$ structure into the trigonal pattern of the unperturbed HOPG surface. For this purpose, two perturbation waves have been introduced, exponentially attenuated from the positions of a linear defect, which simulates a step edge, and from the position of a circular defect, which mimics a Si island. d represents the distance from the defect/step and α is the damping coefficient, which is the same for both waves. Without attempting any fit of the experimental images, the simulated images nicely reproduce the features and behavior observed at the sample surface in proximity of the island grown near a step edge and, in particular, the transition between a hexagonal pattern and a zigzag chain, Fig. 7.4.b.

Although present results clearly associate the $(\sqrt{3} \times \sqrt{3})R30^\circ$ reconstruction to charge density waves, they still cannot explain the Raman peak observed for Si/HOPG [183]. Further measurements are necessary, but a first guess could be that Si atoms in part aggregate and form Si nanoclusters and in part intercalate beneath the HOPG surface, where they could possibly arrange in a 2D hexagonal pattern. This hypothesis would also explain the surprising stability of the Raman response of the material after prolonged air exposure [183].

7.3 Si evaporation on TMDCs

In this section I report some results regarding Si evaporation on TMDCs. First of all, I have studied the Si/MoS_2 system, to make a comparison with the results of silicene growth reported by Chiappe *et al.* [31]. This system could be of great interest in the field of van der Waals heterostructures [205], in which a stacking of several 2D materials leads to the formation of a new functional material [206]. The samples have been cleaved in air and then introduced in the UHV chamber.

For Si deposition at room temperature, I have experienced, since the first measurements, a strong instability of the tunneling conditions. This could be due to the low adhesion of Si on MoS_2. In any case, I couldn't obtain any clear evidence of the formation of a 2D Si layer. Contrary to that, the experimental evidences suggest a 3D island growth as it can be seen in Fig. 7.8, which reports an STM image acuired after a sub-monolayer Si evaporation on MoS_2. The surface appears staggered with 3D features several nanometers high; the strands parallel to the scanning direction (left to right) are probably due to Si aggregates dragged by the tip.

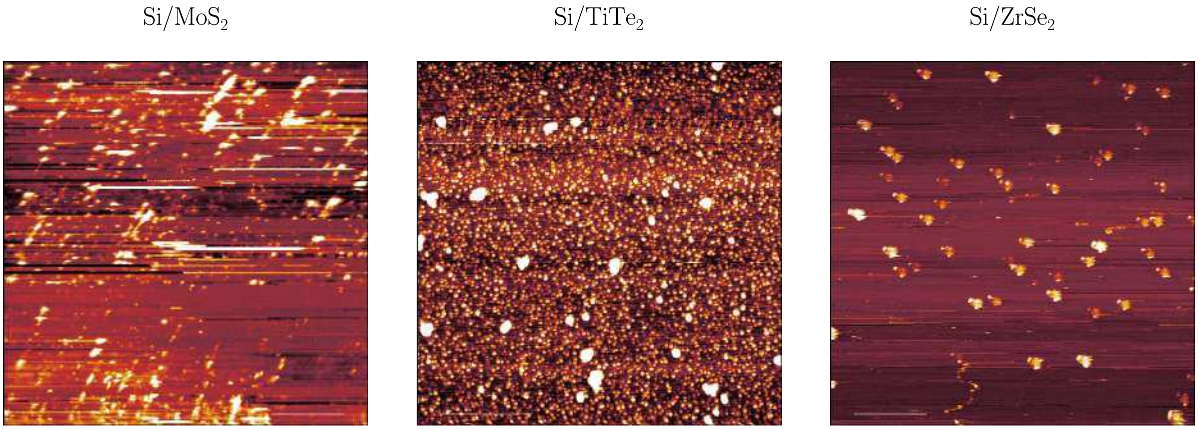

FIGURE 7.8: STM images of three different TMDC substrates after Si evaporation. MoS_2: 500×500 nm^2, U=-1.5 V, I=50 pA, sub-monolayer coverage; $TiTe_2$: 200×200 nm^2, U=2.0 V, I=20 pA, $\approx$2 Si MLs; $ZrSe_2$: 500×500 nm^2, U=1.5 V, I=30 pA, sub-monolayer coverage.

The same type of 3D growth has been observed also on $TiTe_2$ and $ZrSe_2$, despite the better lattice matching with respect to MoS_2, discussed in Sec. 7.1. In this case I have cleaved the samples inside the UHV chamber, employing the system described in Sec. 2.2. After the evaporation of $\approx$2 ML of Si at room temperature on $TiTe_2$ (Fig. 7.8), one can clearly see the appearance of 3D particles: the smaller ones have a height in the 0.1-0.5 nm range and a width of 1-4 nm. Also bigger islands can be observed, which are 1 nm high and $\sim$7 nm wide.

I report also the results of real-time STM measurements obtained at high temperature (T_{growth}=476 K) during Si evaporation on MoS_2. Whenever Si is evaporated during STM scanning, the tip induces a shadowing on the sample surface. On the same direction of evaporation, the presence of the tip prevents Si atoms from being deposited on the cone-shaped area right behind the tip (with respect to the position of the shutter). In order to minimize the shadowing of the tip, I have oriented the image along the axis of the evaporator and I have scanned (line-by-line) toward the shutter. In the STM image in Fig. 7.9, Si islands gradually appear along the scanning direction. They show increasing height and seem to saturate around 23-25 Å, see Tab.7.2. A similar behavior has also been reported by Sone *et al.* for Si evaporation on graphene. In this work they show a similar 3D growth at T_{growth}=520 K and a saturation in height of the Si island around 40 Å [207]. Note that in Fig. 7.9 there is a non-negligible contribution of the tip shape, so the density of Si islands observed could be different from the real one.

# of the island	1	2	3	4	5	6	7	8	9
height (Å)	1.51	7.48	10.31	11.40	15.11	23.12	23.90	25.26	24.48

TABLE 7.2: Height of the islands in Fig. 7.9.

Concerning $TiTe_2$, I have performed some STM measurements also after annealing of the sample at 360 C°. Consequent to this annealing procedure, I have observed the appearance of three kinds of features, Fig. 7.10.a:

- triangular shaped holes, with a depth of exactly one TiT_2 step height;

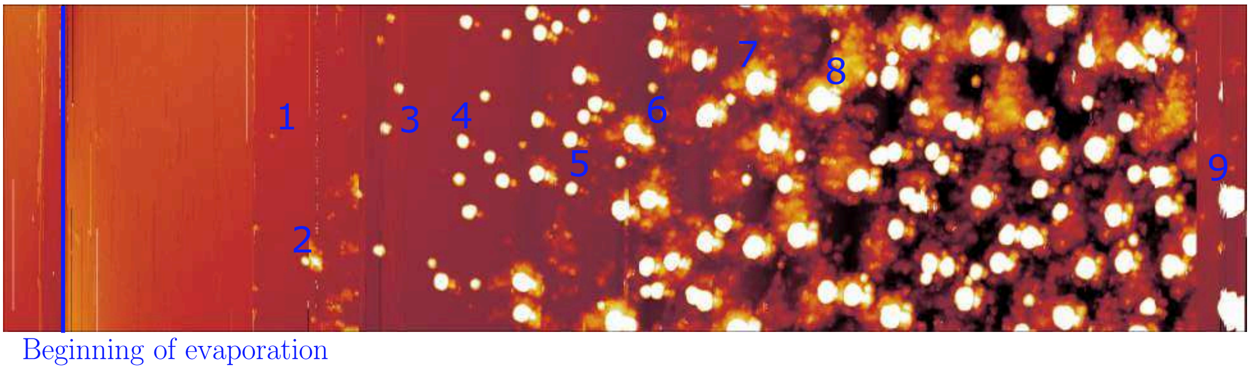

FIGURE 7.9: Real-time STM image (100×400 nm^2, U=2 V, I=100 pA) during Si evaporation on MoS_2 at T_{growth}=476 K. The blue line coincides with the opening of the shutter of the Si evaporator. The numbers labeling some Si islands refer to Tab.7.2.

- hexagonal structures with an apparent height of $\gtrsim 1$ Å;
- 3D islands with a height of several nanometers (≈ 10 nm).

The triangular shaped holes have been identified as missing flakes of the first $TiTe_2$ layer, induced by the high temperature annealing. The same kind of pits have been reported on MoS_2 after annealing at similar temperatures [208–210].

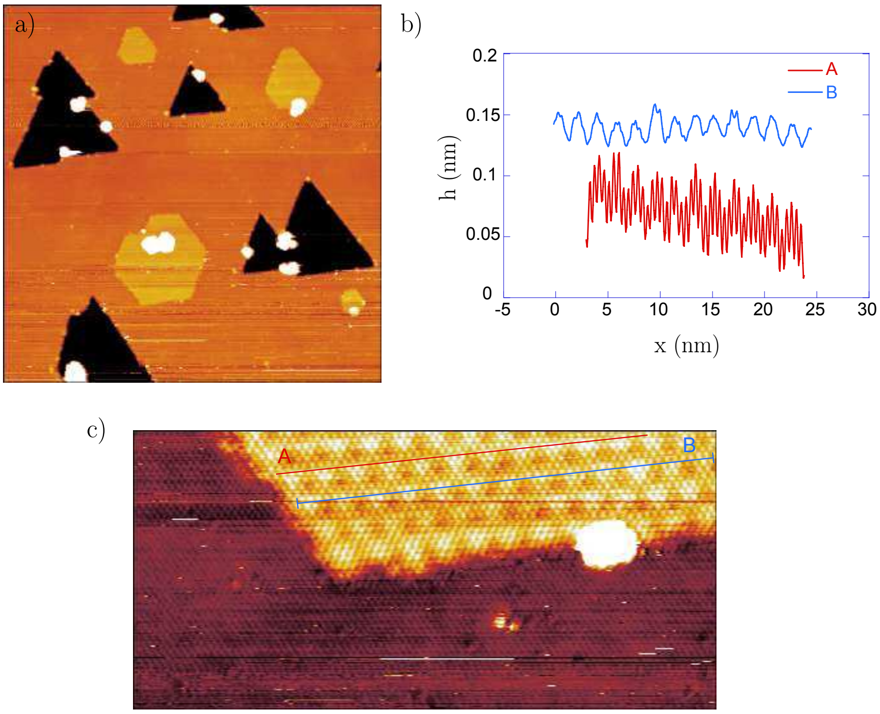

FIGURE 7.10: a) STM image (200×200 nm^2, U=2 V, I=20 pA) in which the triangular shaped defects, the hexagonal structures and the 3D features (white features) are clearly visible. c) High-resolution image of the hexagonal structures (40×19 nm^2, U=2 V, I=20 pA) showing the long-range and short-range periodicity, which can be identified in the two height profiles in (b).

The two other types of defects are probably due to a contamination by the Ag paste (which fixes the sample to the sample-holder), caused by annealing at high temperature. In fact, the same kind of experiments have been performed on a $TiTe_2$ sample fixed with a washer and few Ta plates to the sample-holder. No evidences of the hexagonal features have been found.

The hexagonal structures shows a moiré-like pattern with a periodicity of 19.2±0.3 Å (Fig. 7.10.b) and a much finer structure with periodicity of 4.60±0.03 Å. In the same image, it is possible to observe also the atomic resolution on the areas corresponding to the bare $TiTe_2$ substrate, for which I have measured a lattice constant equal to 3.8±0.1 Å in good agreement with the expected value of 3.77 Å.

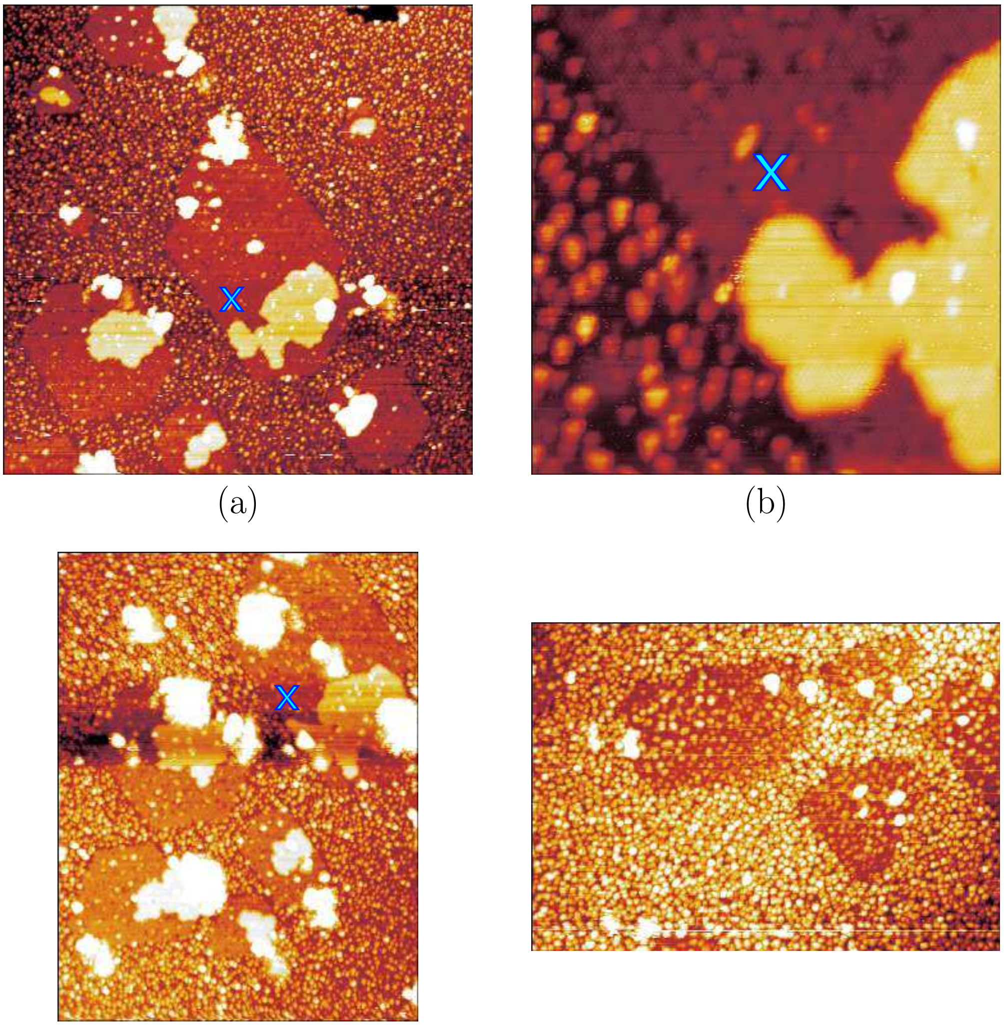

(a) (b)

(c) (d)

FIGURE 7.11: STM images obtained during Si evaporation. The blue cross indicates the same point of the sample surface. a) Flat islands appear on the hexagonal structures and 3D particles on the pristine $TiTe_2$ substrate (200×200 nm^2, U=2 V, I=20 pA). b) Magnification of (a) in which the short range periodicity of the hexagonal structure can be seen. Note that the same periodicity is also faintly visible on the flat islands in the right-upper part (40×40 nm^2, U=1.8 V, I=180 pA). c) STM image the evolution of the flat islands due to Si evaporation (200×153 nm^2, U=2 V, I=20 pA). d) Sample surface after annealing at 573 K. The hexagonal islands are faintly visible, but there is no sign of the flat islands previously observed (200×140 nm^2, U=2 V, I=20 pA).

I have performed a Si evaporation at 300 K on the $TiTe_2$ substrate with the hexagonal features, see Fig. 7.11.a. As expected, in the areas corresponding to pristine $TiTe_2$ deposited Si atoms form 3D islands; surprisingly, on the hexagonal structures almost no particles are present, but instead flat islands are visible. These islands have an height of $\sim$3 Å.

Finally, in order to be sure that these islands are actually due to deposited Si, I have performed real-time measurements during Si evaporation, Fig. 7.11.c. It is clear that the flat islands grow upon further Si evaporation, confirming Si involvement in the process of formation and growth of the flat islands. These islands are not stable with the temperature. In fact after an annealing at 573 K (Fig. 7.11d), on top of the faintly visible hexagonal structures there are only 3D Si cluster particles, while no flat Si islands are observed.

7.4 Summary of the results of Chapter 7

In this chapter I have presented some STM results concerning Si evaporation on several layered materials: HOPG, MoS_2, $TiTe_2$ and $ZrSe_2$.

- Si evaporation at room temperature on HOPG leads to the formation of 3D Si islands. In their proximity, the surface appears different from pristine HOPG. In particular, a $(\sqrt{3} \times \sqrt{3})R30^\circ$ reconstruction is observed.
- In the literature this reconstruction is associated with the presence of a silicene layer [30].
- STM measurements have shown that there is a continuous smooth transition from the areas with $(\sqrt{3} \times \sqrt{3})R30^\circ$ reconstruction to the areas characterized by the pristine HOPG surface appearance.
- It is known from the literature that the presence of adsorbed atoms on the HOPG surface can induce a charge density modulation with a $(\sqrt{3} \times \sqrt{3})R30^\circ$ periodicity due to the interference between the surface electron waves and the scattered waves from defects or clusters [186–189].
- By simulating the electron density at the HOPG surface as the sum of a symmetric and anti-symmetric linear combination of six plane waves, it has been possible (changing the coefficients of the linear combinations) to reproduce the different surface patterns observed experimentally in proximity of the Si nanoclusters, validating the hypothesis of charge density waves.
- Si evaporation on the other layered materials has resulted in the formation of 3D Si islands of different size and height.
- I have reported some preliminary interesting STM observation of Si evaporation on $TiTe_2$. After annealing at high temperature (360 C°), hexagonal features have appeared at the $TiTe_2$ surface. They are probably due to Ag contamination from the Ag paste.
- Si evaporation on the $TiTe_2$ samples showing the hexagonal features has led to the formation of 3D Si nanoclusters on the bare surface, while flat islands have appeared on top of the hexagonal structures.
- Real-time STM measurements have shown the evolution of these flat islands upon further Si evaporation.
- These islands are not stable: annealing at 573 K results in their dewetting.

Conclusions and perspectives

In this work I have summarized the studies conducted during my PhD, concerning the synthesis of silicene layers and thin Si films on Ag(111) and Si deposition on layered materials. I have presented original results which has unveiled interesting physical phenomena associated with the system under study.

Here I will give an account of the principal results, trying to illustrate once again the common thread of this work.

In the Introduction I have set the context of the research on bidimensional (2D) materials. I have showed how graphene, the 2D allotrope of carbon, triggered the interest toward other atomically-thin materials, motivated by the interesting properties observed for the carbon monolayer. Theoretical studies predicted that a metastable 2D arrangement of Si atoms could exist. This new material was later called *silicene* and it can be considered as the silicon counterpart of graphene. The very interesting properties predicted for the free-standing form of this new material gave the initial impetus for the quest for its experimental realization. Differently from graphene, this material cannot be exfoliated from its layered allotropic form, but it must be grown onto a substrate.

Among the many possible choices, an interesting one is Ag(111), which was investigated in the last years by many research groups. Several studies reported the synthesis of 2D Si arrangements on this material. However, the properties reported for silicene/Ag(111) differ from those predicted for the free-standing silicene, because of the interaction between the substrate and the layer.

In Chapter 4 I have investigated the structure of the silicene monolayers on Ag(111). I have put in evidence also the deformation induced by the Si sheet in the Ag substrate, which can be regarded as a signature of the interaction between the two materials. Silicene layers on Ag(111) (T_{growth}=500-570 K) are always composed by patches of different surface reconstructions. By combined grazing incidence X-ray diffraction (GIXD) and density functional theory (DFT) calculations I have determined the exact atomic arrangement of the (4×4) silicene reconstruction, characterized by a buckling of 0.76 Å and an inter-atomic distance of 2.30-2.33 Å. GIXD measurements have also allowed us to determine with great precision the relaxation of the Ag(111) substrate. The elastic deformation identified in the first surface Ag layers is exponentially damped inside the Ag bulk. The same joint theoretical and experimental approach has been applied also for the determination of two other silicene reconstructions, namely the $(2\sqrt{3} \times 2\sqrt{3})R30^\circ$ and the $(\sqrt{13} \times \sqrt{13})R13.9^\circ$ structures. The former, observed in coexistence with the (4×4) phase for T_{growth}=570 K, deviates from its ideal 30° orientation with respect to the Ag substrate. The theoretical structure factors obtained from the equilibrium atomic positions of the simulated $(2\sqrt{3} \times 2\sqrt{3})R30^\circ$ structure are in a good agreement with the experimental ones. The equilibrium structure has a buckling of 1.10 Å and interatomic distances in the range 2.25-2.33 Å. Concerning the $(\sqrt{13} \times \sqrt{13})R13.9^\circ$ reconstruction, observed at T_{growth}=500 K, I have simulated all its inequivalent configurations for the so-called $type\ I$ and $type\ II$ structures. The experimental structure factors could be reproduced only considering a mix of the $type\ II - t_1h_2t_3$ and $type\ II - t_1t_2h_3$ configurations (for the notation I send the reader back to Sec. 4.4). I could not find any evidence of the presence of the $type\ I$ structure in the silicene layer.

I have concluded Chapter 4 with energetic considerations about the stability of the different silicene monolayer configurations and on the deformation they induce in the Ag(111) substrate. I have show that the structures inducing the highest elastic deformation in the Ag substrate are also the ones with lowest energy associated with the silicene atoms. This evidence suggests that the interaction of the silicene with the Ag substrate is actually responsible for the stabilization of the system. A possible improvement to this chapter consists in the simulation of the other inequivalent configurations of the (4×4) and $(2\sqrt{3} \times 2\sqrt{3})R30^\circ$ reconstructions. Even though no major structural differences are expected with respect to the presented results, their energy could give complementary information concerning the trend of the energy of the silicene layer as a function of the substrate elastic deformation (Fig. 4.15).

As already mentioned, the strong interaction between the silicene layer and the Ag(111) substrate results in the loss by the 2D Si sheet of the interesting electronic properties predicted for its free-standing form. Researchers started to get interested in the growth of thick Si films on Ag(111) exploring the possibility that this procedure could lead to the formation of the layered allotrope of Si, called *silicite* or *multi-layer silicene*. For specific growth temperatures some works claimed successful silicite synthesis [6, 7]. However further studies put into question this interpretation [8–10]. In order to determine the nature of Si films on Ag(111), I have performed GIXD measurements on a Si film grown in the same temperature range in which silicite synthesis was claimed. All the diffraction spots belonging to the Si thin film have been associated with a diamond bulk-like Si structure, rejecting any interpretation of silicite or multi-layer silicene growth. However some of the observed diffraction spots appear shifted from their ideal theoretical positions. Using the Paterson model, I have attributed these shifts to the presence of stacking faults in the Si film.

The growth of the second and successive Si layers on Ag(111) is characterized by a $(\sqrt{3} \times \sqrt{3})R30^\circ$ surface termination. GIXD measurements after 2 ML Si deposition at 510 K showed that this phase is compatible with the $(\sqrt{3} \times \sqrt{3})R30^\circ$ termination of Ag on Si(111), described by the so-called honeycomb chain triangle (HCT) model. Thus, Ag atoms segregate at the surface starting from the growth of the second Si layer.

Performing STM measurements in the first stages of growth of the second Si layer, I have noticed the presence of two different phases of the $(\sqrt{3} \times \sqrt{3})R30^\circ$ reconstruction that I have labeled as α and β. Real-time STM measurements have shown that the α phase is progressively replaced by the β one upon further Si deposition. By 2 ML Si coverage, only the β phase can be seen at the sample surface. Consequently, it is reasonable to state that the $(\sqrt{3} \times \sqrt{3})R30^\circ$ structure previously determined by GIXD measurements and basically coinciding with the Ag-termination of Si(111) surfaces, is associated with this β phase. An interpretation for the α phase is still missing at this point.

I have then simulated by DFT several $(\sqrt{3} \times \sqrt{3})R30^\circ$ Ag-free models (differently from the HCT/β structure) proposed in the literature. The simulated STM images associated with the theoretical models have been compared to the experimental ones. Only one model could reproduce the experimental images: it consists of a single Si layer with on top a $(\sqrt{3} \times \sqrt{3})R30^\circ$ added-atom reconstruction with Si atoms in dumbbell configuration (trigonal dumbbell silicene or TDS model), that I have labeled as ML+Si. As the β phase is described by the HCT model, the Ag-$(\sqrt{3} \times \sqrt{3})R30^\circ$ reconstruction has been simulated on top of a single Si layer (labeled as ML+Si/Ag), similarly to the ML+Si model. As expected, its simulated STM image is in good agreement with the surface appearance of the β phase.

At this point I have introduced the grand canonical surface energy, used to compare the energy of models with different number of atoms. It is a function of μ_{Si}, which at the thermodynamical equilibrium coincides with the Si chemical potential. Thus, introducing this quantity I have compared the stability of the ML+Si and ML+Si/Ag models with the one of the silicene monolayer reconstructions, i.e. ML (4×4)

and ML ($\sqrt{13} \times \sqrt{13}$). I have shown that none of the new added-atom reconstructions was more stable than the silicene structures in a large μ_{Si} range.

In order to come up with a new alternative interpretation, I have presented other real-time STM evidences. I have shown that starting from the growth of the second Si layer, the areas of the sample near the step edges covered by the silicene monolayer are lifted up of exactly the height of one Ag(111) step height, preserving in the transition its surface structure. There is only one possible interpretation: there are some silver atoms at the surface, necessarily ejected from the substrate, which diffuse and reinsert below the silicene layer at the Ag(111) step edges. This increases the height of the silicene layer of one Ag(111) step. The natural question at this point is: where do these Ag atoms come from?

I have proposed that the α and β phases are actually Si bilayers terminated by the $(\sqrt{3} \times \sqrt{3})R30^\circ$ added-atom reconstructions previously proposed for the mononlayer, i.e. the TDS Ag-free and HCT Ag-rich structures (for α and β phases). These two models have been labeled as BL+Si and BL+Si/Ag. In this case the comparison among the grand canonical surface energies have shown that in a wide range of μ_{Si} the BL structures are more stable than the silicene monolayer reconstructions ML (4×4) and ML ($\sqrt{13} \times \sqrt{13}$). This corroborates the picture of direct transition from silicene monolayer to Si bilayer terminated by added-atom reconstructions. Moreover, BL+Si/Ag is slightly energetically favored with respect to BL+Si, which could explain why experimentally, the β phase (BL+Si/Ag) grows at expenses of the α phase (BL+Si). In addition to this, the BL+Si and BL+Si/Ag structures are always energetically favored with respect to a simple Si(111) bilayer with AB stacking. I can draw some conclusions at this point. While the Si bilayers need to be stabilized by surface reconstructions similar to those observed for Si(111) surface (see HCT model and TDS model), the silicene monolayer is a very stable structure which does not need an added-atom reconstruction to lower its energy. This shows that silicene behaves differently from bulk Si, while Si bilayers can be considered, strictly speaking, as two layers of Si(111).

In the last part of Chapter 6, I have presented some considerations on the energetics of adsorption of Si atom on top and below a silicene (4×4) layer, discussing the substitution with Ag atoms in the first layer of the substrate. I have found out that in some cases it is even energetically more convenient, for a Si atom, to insert below the silicene layer and eject a Ag atom from the substrate, taking its place. This supports the evidence according to which the reconstructed Si bilayers BL+Si and BL+Si/Ag (associated with the α and β phases) grow by digging into the Ag substrate.

Let us give once again the general picture for the growth of Si on Ag(111) after the silicene monolayer completion. The incoming Si atoms do not simply deposit on the silicene layer, but they prefer to insert below silicene ejecting Ag atoms from the substrate. Thus, the silicene monolayer directly transforms into Si bilayer inserted in Ag substrate, showing, in a first moment, a Ag-free added-atom $(\sqrt{3} \times \sqrt{3})R30^\circ$ reconstruction at its surface (BL+Si, α phase). The ejected Ag atoms diffuse on the surface and can either re-insert below the silicene layer as observed experimentally, or go on top of the surface and give rise to the β phase. This structure is interpreted as a Si bilayer inserted in Ag substrate terminated by a $(\sqrt{3} \times \sqrt{3})R30^\circ$ Ag-rich reconstruction (BL+Si/Ag). The β phase grows at expenses of the α one, being energetically more favorable. At 2 ML Si coverage only the β phase is observed.

In Chapter 7 I have presented an STM study concerning Si deposition on several layered materials: HOPG, MoS_2, $TiTe_2$ and $ZrSe_2$. I have shown that the Si evaporation at room temperature on HOPG leads to the formation of Si nanoclusters surrounded by a $(\sqrt{3} \times \sqrt{3})R30^\circ$ reconstruction. Interpreted in the literature as signature of the presence of a silicene layer, I have concluded that this alteration of the HOPG surface appearance is actually due to charge density waves.

Concerning Si evaporation on the three other materials, I have always observed the formation of 3D Si islands.

Some unexpected observations have been obtained for $TiTe_2$. After annealing at 360 °C of the bare substrate, hexagonal structures have appeared, different from the pristine $TiTe_2$ surface. These structures are probably due to Ag contamination from the Ag paste used to fix the samples to the sample-holder. Si evaporation on this "altered" substrate has resulted in the formation of 3D Si particles in the areas corresponding to the bare $TiTe_2$ surface and to the formation of flat islands on top of these hexagonal features. Real-time STM during Si evaporation has shown the evolution and growth of the flat islands, which thus are induced by Si evaporation. These flat islands are not stable: they have dewetted upon a 573 K annealing.

Several works can still be done on these layered materials. First of all, it would be interesting to find stable imaging conditions for STM at different temperatures. This could give some more precise information about Si growth on this class of materials. An hypothesis which has not been explored yet, is the eventuality of Si intercalation, which could explain the Raman spectrum recently reported by Castrucci *et al.*. Moreover, it could be interesting to perform other measurements aimed to obtain the hexagonal features observed on $TiTe_2$. An idea is to deposit a small quantity of Ag on this substrate at different temperatures and see if structures similar to those observed appear. Otherwise, it could be interesting to obtain the hexagonal features in the same way as the previous experiments and perform spectroscopy measurements (e.g. Auger electron spectroscopy, scanning tunneling spectroscopy) in order to determine the chemical composition of these structures and/or their electronic behavior.

Appendix A

Diffraction basis

Here I give a complete account of the basis used for labeling the GIXD measurements in Chapters 4, 5 and 6. The crystal basis is presented as

$$(a, b, c; \alpha, \beta, \gamma) \tag{A–1}$$

in which the quantities refer to Fig.A.1.

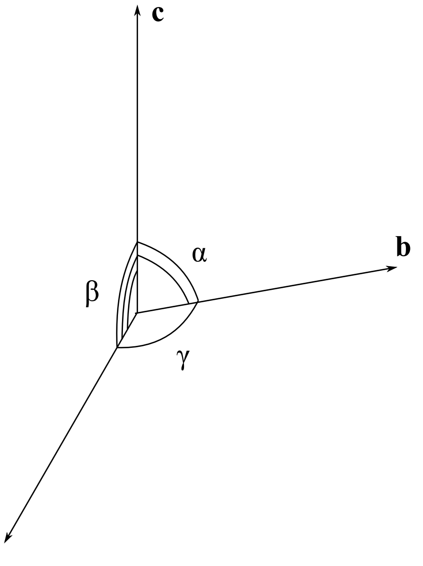

FIGURE A.1: Representation of the system of axis used in the labeling of the structures.

- **Ag(111)**:

  $a_{Ag(111)} = \frac{a_{Ag}}{\sqrt{2}}$, $c_{Ag(111)} = \sqrt{3}a_{Ag}$;

  $\left(a_{Ag(111)}, a_{Ag(111)}, c_{Ag(111)}; 90^\circ, 90^\circ, 120^\circ\right)$,

  in which a_{Ag} is the lattice parameter of Ag, equal to 4.0853 Å.

  Miller indexes: *hkl*.

The basis of the silicene ML reconstructions are referred to the aforementioned Ag(111) hexagonal basis.

- **ML-**(4×4):

  $\left(4a_{Ag(111)}, 4a_{Ag(111)}, c_{Ag(111)}; 90°, 90°, 120°\right)$

  Transformation matrix:

  $$M = \begin{pmatrix} 4 & 0 & 0 \\ 0 & 4 & 0 \\ 0 & 0 & 1 \end{pmatrix}$$

  Miller indexes: H, K, L

- **ML-**$(\sqrt{13} \times \sqrt{13})R13.9°$:

  $\left(\sqrt{13}a_{Ag(111)}, \sqrt{13}a_{Ag(111)}, c_{Ag(111)}; 90°, 90°, 120°\right)$

  Transformation matrix:

  $$M = \begin{pmatrix} 3 & 1 & 0 \\ -1 & 4 & 0 \\ 0 & 0 & 1 \end{pmatrix}$$

  Miller indexes: H, K, L

- **ML-**$(2\sqrt{3} \times 2\sqrt{3})R30°$:

  $\left(2\sqrt{3}a_{Si(111)}, 2\sqrt{3}a_{Ag(111)}, c_{Ag(111)}; 90°, 90°, 120°\right)$

  Transformation matrix:

  $$M = \begin{pmatrix} 2 & 2 & 0 \\ 4 & -2 & 0 \\ 0 & 0 & 1 \end{pmatrix}$$

  Miller indexes: H, K, L

  The structure of bulk diamond have been thoroughly described in Chapter 5 and in Annex B.

- **Si(111)**:

  $a_{Si(111)} = \frac{a_{Ag}}{\sqrt{2}}, c_{Si(111)} = \sqrt{3}a_{Si};$

  $\left(a_{Si(111)}, a_{Si(111)}, c_{Si(111)}; 90°, 90°, 120°\right),$

  in which a_{Si} is the lattice parameter of Si, equal to 5.4309 Å.

  Miller indexes: $h_{Si}k_{Si}l_{Si}$.

  Transformation basis (from Si cubic basis):

  $$M = \begin{pmatrix} \frac{1}{2} & -\frac{1}{2} & 0 \\ 0 & -\frac{1}{2} & \frac{1}{2} \\ 1 & 1 & 1 \end{pmatrix}$$

- $(\sqrt{3} \times \sqrt{3})R30^\circ$ with respect to Si(111):

  $a_{\sqrt{3}} = \dfrac{a_{Si(111)}}{\sqrt{2}}, c_{\sqrt{3}} = c_{Si(111)};$

  $\left(a_{\sqrt{3}}, a_{\sqrt{3}}, c_{\sqrt{3}}; 90^\circ, 90^\circ, 120^\circ\right),$

  in which a_{Si} is the lattice parameter of Si, equal to 5.4309 Å.

  Miller indexes: $h_{\sqrt{3}} k_{\sqrt{3}} l_{\sqrt{3}}$.

  Transformation basis (from Si(111)):

$$M = \begin{pmatrix} 1 & 1 & 0 \\ -1 & 1 & 0 \\ 0 & 0 & 1 \end{pmatrix}$$

Appendix B

Extinction conditions for bulk Si

Here we give the derivation of the extinction conditions for a diamond structure. The diamond structure can be described as simple cubic Bravais lattice, with primitive vectors $a_{Si}\hat{x}$, $a_{Si}\hat{y}$, $a_{Si}\hat{z}$, with an 8-atoms basis:

$$\begin{gathered}(0,0,0); \quad \left(\frac{1}{2},\frac{1}{2},0\right); \quad \left(\frac{1}{2},0,\frac{1}{2}\right); \quad \left(0,\frac{1}{2},\frac{1}{2}\right); \\ \left(\frac{1}{4},\frac{1}{4},\frac{1}{4}\right); \quad \left(\frac{1}{4},\frac{3}{4},\frac{3}{4}\right); \quad \left(\frac{3}{4},\frac{1}{4},\frac{3}{4}\right); \quad \left(\frac{3}{4},\frac{3}{4},\frac{1}{4}\right);\end{gathered} \tag{B–1}$$

The reciprocal lattice of a cubic lattice is still a cubic lattice with reciprocal primitive vector:

$$\boldsymbol{b}_1 = \frac{2\pi}{a_{Si}}\hat{\boldsymbol{x}}, \quad \boldsymbol{b}_2 = \frac{2\pi}{a_{Si}}\hat{\boldsymbol{y}}, \quad \boldsymbol{b}_3 = \frac{2\pi}{a_{Si}}\hat{\boldsymbol{z}}, \tag{B–2}$$

The structure factor is given in Eq. 2–26 for $\boldsymbol{q} = H_{Si}\boldsymbol{b}_1 + K_{Si}\boldsymbol{b}_2 + L_{Si}\boldsymbol{b}_3$, where $H_{Si}K_{Si}L_{Si}$ are the Miller indexes in the cubic basis:

$$F(\boldsymbol{q}) = \sum_{i=1}^{8} f_{Si}(q)e^{i\boldsymbol{q}\boldsymbol{r}_i} \tag{B–3}$$

$\boldsymbol{q}$ is the transferred momentum, $\boldsymbol{r}_i$ are the atomic positions reported in B–2, $f_{Si}(q)$ is the atomic form factor. If we develop Eq. B–3:

$$\begin{aligned}F(\boldsymbol{q}) = f_{Si}(q)\Bigg[1 &+ exp\left(i\frac{\pi}{a_{Si}}(H_{Si}+K_{Si})\right) + exp\left(i\frac{\pi}{a_{Si}}(H_{Si}+L_{Si})\right) + exp\left(i\frac{\pi}{a_{Si}}(K_{Si}+L_{Si})\right) \\ &+exp\left(i\frac{\pi}{2a_{Si}}(H_{Si}+K_{Si}+L_{Si})\right) + exp\left(i\frac{\pi}{2a_{Si}}(H_{Si}+3K_{Si}+3l)\right) \\ &+exp\left(i\frac{\pi}{2a_{Si}}(3H_{Si}+K_{Si}+3l)\right) + exp\left(i\frac{\pi}{2a_{Si}}(3H_{Si}+3K_{Si}+L_{Si})\right)\Bigg]\end{aligned} \tag{B–4}$$

By rearranging the last three terms:

$$\begin{aligned}F(\boldsymbol{q}) = f_{Si}(q) \Bigg[1 + exp\left(i\frac{\pi}{a_{Si}}(H_{Si}+K_{Si})\right) + exp\left(i\frac{\pi}{a_{Si}}(H_{Si}+L_{Si})\right) + exp\left(i\frac{\pi}{a_{Si}}(K_{Si}+L_{Si})\right) \\ +exp\left(i\frac{\pi}{2a_{Si}}(H_{Si}+K_{Si}+L_{Si})\right) + exp\left(i\frac{\pi}{2a_{Si}}(H_{Si}+K_{Si}+L_{Si})\right) exp\left(i\frac{\pi}{a_{Si}}(H_{Si}+K_{Si})\right) \\ +exp\left(i\frac{\pi}{2a_{Si}}(H_{Si}+K_{Si}+L_{Si})\right) exp\left(i\frac{\pi}{a_{Si}}(H_{Si}+L_{Si})\right) \\ +exp\left(i\frac{\pi}{2a_{Si}}(H_{Si}+K_{Si}+L_{Si})\right) exp\left(i\frac{\pi}{a_{Si}}(K_{Si}+L_{Si})\right)\Bigg]\end{aligned} \qquad \text{(B–5)}$$

Now taking $exp\left(i\frac{\pi}{2a_{Si}}(H_{Si}+K_{Si}+L_{Si})\right)$ as a common factor in the last four terms:

$$\begin{aligned}F(\boldsymbol{q}) = f_{Si}(q) \Bigg[\Bigg[1 + exp\left(i\frac{\pi}{a_{Si}}(H_{Si}+K_{Si})\right) + exp\left(i\frac{\pi}{a_{Si}}(H_{Si}+L_{Si})\right) + exp\left(i\frac{\pi}{a_{Si}}(K_{Si}+L_{Si})\right)\Bigg] \\ +exp\left(i\frac{\pi}{2a_{Si}}(H_{Si}+K_{Si}+L_{Si})\right) \Bigg[1 + exp\left(i\frac{\pi}{a_{Si}}(H_{Si}+K_{Si})\right) \\ +exp\left(i\frac{\pi}{a_{Si}}(H_{Si}+L_{Si})\right) + exp\left(i\frac{\pi}{a_{Si}}(K_{Si}+L_{Si})\right)\Bigg]\Bigg]\end{aligned} \qquad \text{(B–6)}$$

Now taking the two terms between square brackets as common factors:

$$\begin{aligned}F(\boldsymbol{q}) = f_{Si}(q) \Bigg[1 + exp\left(i\frac{\pi}{a_{Si}}(H_{Si}+K_{Si})\right) + exp\left(i\frac{\pi}{a_{Si}}(H_{Si}+L_{Si})\right) + exp\left(i\frac{\pi}{a_{Si}}(K_{Si}+L_{Si})\right)\Bigg] \\ \cdot \Bigg[1 + exp\left(i\frac{\pi}{2a_{Si}}(H_{Si}+K_{Si}+L_{Si})\right)\Bigg]\end{aligned} \qquad \text{(B–7)}$$

The first multiplicative terms is the structure factor for an fcc lattice and it is not zero unless $H_{Si}K_{Si}L_{Si}$ have the same parity. Let us see when the second multiplicative term is not zero.

- if $H_{Si}K_{Si}L_{Si}$ are all odd their sum is odd too and the second term in Eq. B–7 becomes:

  $$\left[1 + i(-1)^{(m+3)/2}\right] \qquad \text{with } m = H_{Si} + K_{Si} + L_{Si} \qquad \text{(B–8)}$$

  $(m + 3)/2$ determines the sign of i. Thus, when all indixes are odd, the second term in Eq. B–7 is not zero, just as the first term.

- if all indexes are even, the second instead writes:

  $$\left[1 + (-1)^{m/2}\right] \qquad \text{with } m = H_{Si} + K_{Si} + L_{Si} \qquad \text{(B–9)}$$

  which is different from zero when m is a multiple of 4.

Combining all the rules we have identified, for a diamond structure, diffraction will occur from planes which have indexes with the same parity and for which $H_{Si} + K_{Si} + L_{Si} \neq 4n + 2$.

Appendix C

Structural parameters of thin Si layer models

Tab. C.1 reports some of the structural parameters for Ag-free systems. The meaning of the parameters is described in Fig. C.1, which represents the BL+Si structure; the same definition apply also to the other Ag-free structures. The BL+Si (ML+Si) structure is a silicene bilayer (monolayer) in which Si atoms have been added on the top to form the ($\sqrt{3} \times \sqrt{3}$) reconstruction. z_{out} is the distance between the added atom and the Si which is immediately below. Note that the analogous quantities to z_0, z_1 and z_2 can be defined for bulk Si (“Si bulk"). Concerning the bilayer BL-AA structure (not in Tab. C.1) we do not obtain major differences from the structural parameters already reported by Pflugradt et al. [170].

A second set of structures are silicene layers covered by Si and Ag atoms arranged in analogy to the reconstruction observed when the Si(111) surface is covered by half a silicene layer and nine Ag atoms per unit cell. Indeed, they are the HCT and IET reconstruction described in Section 6.3.1. The two reconstructions terminate one or two Si layers on top of the Ag(111) substrate. Tab. C.2 reports some of the structural parameters for the HCT and IET reconstructions on top of Si bulk (Si+Ag), or in the case they form the termination of a single Si layer (ML+Si/Ag) or two Si layers (BL+Si/Ag) on top of the Ag(111) substrate. The labeling of the distances is represented in Fig. C.2 reporting the Ag-($\sqrt{3} \times \sqrt{3}$) HCT and IET structures on a Si bilayer. The two reconstructions which possess or not the a mirror plane symmetry, are labeled following Si diamond literature [161]. In Tab. C.2 the quantities indicated as d_x are distances between atomic planes, while L are the lengths of the edges of the various equilateral triangles schematized in Fig. C.2. θ_1 and θ_2 are the angles associated with the tilting of the Si trimers and the Ag triangles, respectively, in the IET structure.

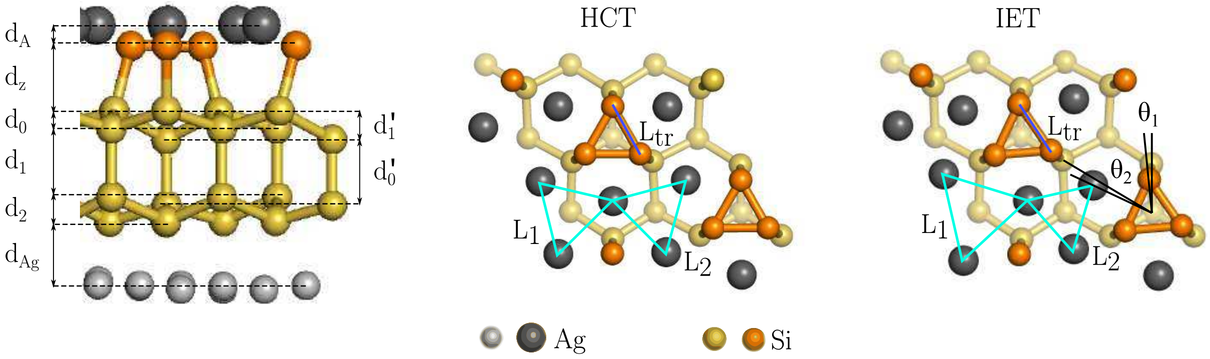

FIGURE C.2: Labels of the structural parameters of the IET and HCT equilibrium structures.

	Si bulk	(4 × 4)	ML+Si	BL+Si	BL+AB
z_{out}			0.133	0.143	
z_{ds}			0.254	0.265	
z_0	0.079	0.079	0.062	0.053	0.062
z_1	0.237			0.244	0.245
z_1'				0.239	
z_2	0.079			0.096	0.077
z_{Ag}		0.218	0.183	0.228	

TABLE C.1: Structural parameters for the Ag-free structures. All distances are in nm.

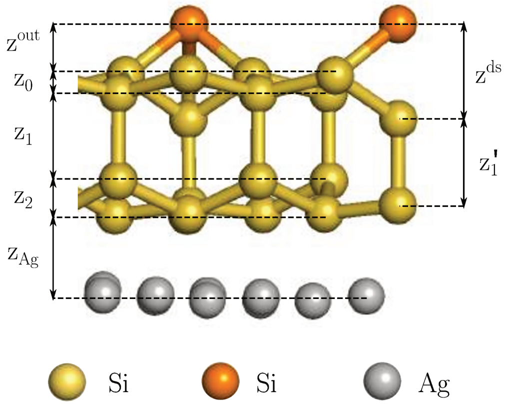

FIGURE C.1: Structural parameters of the Ag-free relaxed structures compared to the ones for Si bulk.

	HCT			IET		
	Si+Ag	ML+Si/Ag	BL+Si/Ag	Si+Ag	ML+Si/Ag	BL+Si/Ag
d_A	0.077	0.072	0.073	0.076	0.080	0.071
d_z	0.230	0.232	0.230	0.230	0.222	0.230
d_0	0.069	0.068	0.065	0.069	0.068	0.065
d_0'	0.100	0.104	0.101	0.100	0.110	0.101
d_1	0.240		0.241	0.240		0.241
d_1'	0.230		0.233	0.230		0.233
d_2	0.086		0.088	0.086		0.088
d_{Ag}		0.239	0.227		0.238	0.233
L_{tr}	0.252	0.252	0.254	0.253	0.254	0.255
L_1	0.351	0.346	0.351	0.302	0.301	0.302
L_2	0.342	0.343	0.351	0.390	0.398	0.398
θ_1				3.8°	3.9°	4.0°
θ_2				5.4°	5.6°	5.5°

TABLE C.2: Structural parameters for the HCT and IET reconstructions on top of Si bulk (Si+Ag), on one Si layer (ML+Si/Ag), or two silicon layers ((BL+Si/Ag). The distances are labeled according to Fig. C.2. All the values are in nm.

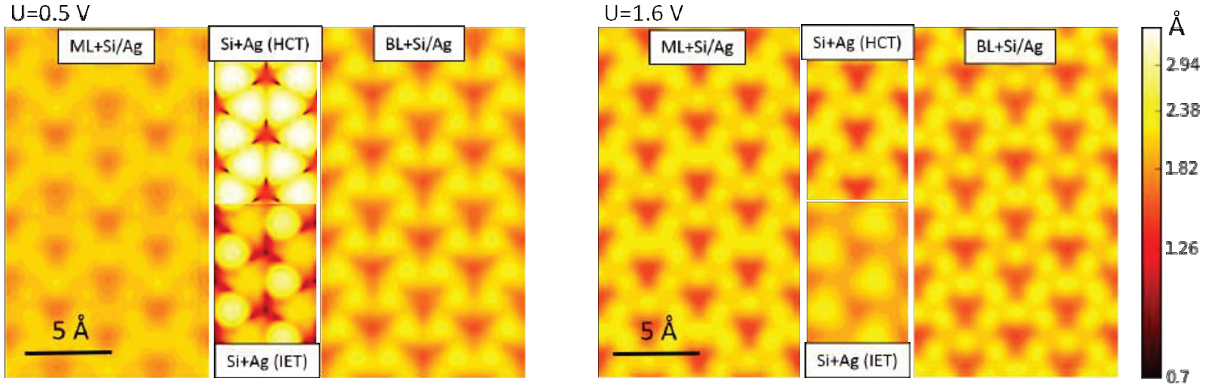

FIGURE C.3: Simulated STM images of various Si/Ag reconstructions for U=0.5 V and (left panel) and U=1.6 V (right panel)

In Fig. C.3, we compare the simulated STM images of the Si/Ag reconstructions at two different voltages (U). Note that for the ML+Si/Ag and BL+Si/Ag we consider only the symmetric configuration (HCT). One should remark that for U=0.5 V, the STM image of the HCT and IET Si+Ag structures are very similar to those reported in the literature [161]. On the other hand, the shape of this image is qualitatively altered by changing U. If we refer to what we have said in Section 6.3.1, the STM image at low voltage shows the characteristic triangular shapes typical of the two Ag-($\sqrt{3} \times \sqrt{3}$) reconstructions, symmetric for the HCT and not symmetric for the IET. On the contrary, the images of the Si/Ag and BL+Si/Ag do not substantially change upon a variation of U and do not show the typical STM appearance. In fact in this case the density of states of the electrons is concentrated around the Ag atoms of the reconstruction and not in-between them as in the case of Si+Ag at U=0.5 V. Thus, in spite of the fact that the atomic structures of the ML+Si/Ag, BL+Si/Ag structures and those of the Ag-($\sqrt{3} \times \sqrt{3}$) reconstructions in bulk Si (Si+Ag) are very similar (see Tab. C.2), the calculated STM images at 0.5 V are quite different.

Bibliography

[1] S. Cahangirov, M. Topsakal, E. Aktürk, H. Şahin, and S. Ciraci, “Two- and One-Dimensional Honeycomb Structures of Silicon and Germanium”, *Physical Review Letters*, vol. 102, p. 236 804, 2009 (cit. on pp. 2, 13, 14, 22, 82, 89, 134, 135).

[2] H. Enriquez, A. Kara, A. J. Mayne, G. Dujardin, H. Jamgotchian, B. Aufray, and H. Oughaddou, “Atomic structure of the $(2\sqrt{3} \times 2\sqrt{3})$ of silicene on Ag(111) surface”, *Journal of Physics: Conference Series*, vol. 491, p. 012 004, 2014 (cit. on pp. 2, 14, 22, 82).

[3] P. Vogt, P. De Padova, C. Quaresima, J. Avila, E. Frantzeskakis, M. C. Asensio, A. Resta, B. Ealet, and G. Le Lay, “Silicene: Compelling Experimental Evidence for Graphenelike Two-Dimensional Silicon”, *Physical Review Letters*, vol. 108, p. 155 501, 2012 (cit. on pp. 2, 14, 17–19, 21, 25, 72, 80, 82, 90, 93).

[4] K. Kawahara, T. Shirasawa, R. Arafune, C.-L. Lin, T. Takahashi, M. Kawai, and N. Takagi, “Determination of atomic positions in silicene on Ag(111) by low-energy electron diffraction”, *Surface Science*, vol. 623, pp. 25–28, 2014 (cit. on pp. 2, 17, 19, 72, 82).

[5] Y. Fukaya, I. Mochizuki, M. Maekawa, K. Wada, T. Hyodo, I. Matsuda, and A. Kawasuso, “Structure of silicene on a Ag(111) surface studied by reflection high-energy positron diffraction”, *Physical Review B*, vol. 88, p. 205 413, 2013 (cit. on pp. 2, 17, 19, 72, 82).

[6] P. De Padova, C. Ottaviani, C. Quaresima, B. Olivieri, P. Imperatori, E. Salomon, T. Angot, L. Quagliano, C. Romano, A. Vona, M. Muniz-Miranda, A. Generosi, B. Paci, and G. Le Lay, “24 h stability of thick multilayer silicene in air”, *2D Materials*, vol. 1, p. 021 003, 2014 (cit. on pp. 4, 92, 93, 97, 101, 119, 146).

[7] P. De Padova, A. Generosi, B. Paci, C. Ottaviani, C. Quaresima, B. Olivieri, E. Salomon, T. Angot, and G. Le Lay, “Multilayer silicene: Clear evidence”, *2D Materials*, vol. 3, p. 031 011, 2016 (cit. on pp. 4, 92, 100, 101, 104, 119, 146).

[8] A. J. Mannix, B. Kiraly, B. L. Fisher, M. C. Hersam, and N. P. Guisinger, “Silicon Growth at the Two-Dimensional Limit on Ag(111)”, *ACS Nano*, vol. 8, pp. 7538–7547, 2014 (cit. on pp. 4, 22, 94, 101, 107, 110, 146).

[9] Y. Borensztein, A. Curcella, S. Royer, and G. Prévot, “Silicene multilayers on Ag(111) display a cubic diamondlike structure and a $(\sqrt{3} \times \sqrt{3})$ reconstruction induced by surfactant Ag atoms”, *Physical Review B*, vol. 92, p. 155 407, 2015 (cit. on pp. 4, 51, 92–94, 97, 101, 110, 114, 146).

[10] T. Shirai, T. Shirasawa, T. Hirahara, N. Fukui, T. Takahashi, and S. Hasegawa, “Structure determination of multilayer silicene grown on Ag(111) films by electron diffraction: Evidence for Ag segregation at the surface”, *Physical Review B*, vol. 89, p. 241 403, 2014 (cit. on pp. 4, 22, 94, 101, 110, 114, 146).

[11] K. Takeda and K. Shiraishi, “Theoretical possibility of stage corrugation in Si and Ge analogs of graphite”, *Physical Review B*, vol. 50, p. 14 916, 1994 (cit. on p. 12).

[12] G. Guzmán-Verri and L. Lew Yan Voon, “Electronic structure of silicon-based nanostructures”, *Physical Review B*, vol. 76, p. 075 131, 2007 (cit. on p. 12).

[13] S. Cahangirov, H. Sahin, G. Le Lay, and A. Rubio, “Introduction to the physics of silicene and other 2d materials”, *Springer International Publishing*, vol. 930, pp. X–96, 2017 (cit. on p. 13).

[14] K. S. Novoselov, A. K. Geim, S. V. Morozov, D. Jiang, M. I. Katsnelson, I. V. Grigorieva, S. V. Dubonos, and A. A. Firsov, “Two-dimensional gas of massless Dirac fermions in graphene”, *Nature*, vol. 438, pp. 197–200, 2005 (cit. on p. 13).

[15] G. Dresselhaus, M. Dresselhaus, and J. Mavroides, “Spin-orbit interaction in graphite”, *Carbon*, vol. 4, pp. 433–440, 1966 (cit. on p. 13).

[16] C.-C. Liu, W. Feng, and Y. Yao, “Quantum spin hall effect in silicene and two-dimensional germanium”, *Phys. Rev. Lett.*, vol. 107, p. 076 802, 2011 (cit. on p. 13).

[17] S. Rachel and M. Ezawa, “Giant magnetoresistance and perfect spin filter in silicene, germanene, and stanene”, *Phys. Rev. B*, vol. 89, p. 195 303, 2014 (cit. on p. 13).

[18] M. Ezawa, “Spin valleytronics in silicene: Quantum spin hall–quantum anomalous hall insulators and single-valley semimetals”, *Phys. Rev. B*, vol. 87, p. 155 415, 2013 (cit. on p. 13).

[19] B. Aufray, A. Kara, S. Vizzini, H. Oughaddou, C. Léandri, B. Ealet, and G. Le Lay, “Graphene-like silicon nanoribbons on Ag(110): A possible formation of silicene”, *Applied Physics Letters*, vol. 96, p. 183 102, 2010 (cit. on pp. 14, 15, 17, 72).

[20] M. R. Tchalala, H. Enriquez, A. J. Mayne, A. Kara, G. Dujardin, M. A. Ali, and H. Oughaddou, “Atomic structure of silicene nanoribbons on Ag(110)”, *Journal of Physics: Conference Series*, vol. 491, p. 012 002, 2014 (cit. on pp. 14–16).

[21] Z. Majzik, M. Rachid Tchalala, M. Švec, P. Hapala, H. Enriquez, A. Kara, A. J. Mayne, G. Dujardin, P. Jelínek, and H. Oughaddou, “Combined AFM and STM measurements of a silicene sheet grown on the Ag(111) surface”, *Journal of Physics: Condensed Matter*, vol. 25, p. 225 301, 2013 (cit. on pp. 14, 17, 72).

[22] H. Jamgotchian, Y. Colignon, B. Ealet, B. Parditka, J.-Y. Hoarau, C. Girardeaux, B. Aufray, and J.-P. Bibérian, “Silicene on Ag(111) : Domains and local defects of the observed superstructures”, *Journal of Physics: Conference Series*, vol. 491, p. 012 001, 2014 (cit. on p. 14).

[23] D. Chiappe, C. Grazianetti, G. Tallarida, M. Fanciulli, and A. Molle, “Local Electronic Properties of Corrugated Silicene Phases”, *Advanced Materials*, vol. 24, pp. 5088–5093, 2012 (cit. on pp. 14, 17, 18, 72).

[24] B. Feng, Z. Ding, S. Meng, Y. Yao, X. He, P. Cheng, L. Chen, and K. Wu, “Evidence of Silicene in Honeycomb Structures of Silicon on Ag(111)”, *Nano Letters*, vol. 12, pp. 3507–3511, 2012 (cit. on pp. 14, 17–19, 22, 72, 92).

[25] H. Jamgotchian, Y. Colignon, N. Hamzaoui, B. Ealet, J. Y. Hoarau, B. Aufray, and J. P. Bibérian, “Growth of silicene layers on Ag(111): Unexpected effect of the substrate temperature”, *Journal of Physics: Condensed Matter*, vol. 24, p. 172 001, 2012 (cit. on pp. 14, 17, 18, 25, 72, 73, 93).

[26] Y.-M. Lin, C. Dimitrakopoulos, K. A. Jenkins, D. B. Farmer, H.-Y. Chiu, A. Grill, and P. Avouris, “100-GHz Transistors from Wafer-Scale Epitaxial Graphene”, *Science*, vol. 327, pp. 662–662, 2010 (cit. on p. 14).

[27] A. Fleurence, R. Friedlein, T. Ozaki, H. Kawai, Y. Wang, and Y. Yamada-Takamura, “Experimental Evidence for Epitaxial Silicene on Diboride Thin Films”, *Physical Review Letters*, vol. 108, p. 245 501, 2012 (cit. on pp. 14, 26, 27).

[28] L. Meng, Y. Wang, L. Zhang, S. Du, R. Wu, L. Li, Y. Zhang, G. Li, H. Zhou, W. A. Hofer, and H.-J. Gao, “Buckled Silicene Formation on Ir(111)”, *Nano Letters*, vol. 13, pp. 685–690, 2013 (cit. on pp. 14, 27).

[29] A. V. Nezhdanov, D. O. Filatov, D. A. Antonov, S. Y. Zubkov, A. I. Mashin, and A. V. Ershov, “The morphology, electron structure, and optical properties of self-assembled silicon nanostructures on the surface of highly oriented pyrolytic graphite”, *Semiconductors*, vol. 45, pp. 56–60, 2011 (cit. on p. 14).

[30] M. De Crescenzi, I. Berbezier, M. Scarselli, P. Castrucci, M. Abbarchi, A. Ronda, F. Jardali, J. Park, and H. Vach, "Formation of Silicene Nanosheets on Graphite", *ACS Nano*, vol. 10, pp. 11 163–11 171, 2016 (cit. on pp. 14, 28, 134–140, 144).

[31] D. Chiappe, E. Scalise, E. Cinquanta, C. Grazianetti, B. van den Broek, M. Fanciulli, M. Houssa, and A. Molle, "Two-Dimensional Si Nanosheets with Local Hexagonal Structure on a MoS $_2$ Surface", *Advanced Materials*, vol. 26, pp. 2096–2101, 2014 (cit. on pp. 14, 28, 134, 135, 140).

[32] R. W. Olesinski, A. B. Gokhale, and G. J. Abbaschian, "The ag-si (silver-silicon) system", *Bulletin of Alloy Phase Diagrams*, vol. 10, pp. 635–640, 1989 (cit. on pp. 14, 17).

[33] R. Bernard, T. Leoni, A. Wilson, T. Lelaidier, H. Sahaf, E. Moyen, L. Assaud, L. Santinacci, F. Leroy, F. Cheynis, A. Ranguis, H. Jamgotchian, C. Becker, Y. Borensztein, M. Hanbücken, G. Prévot, and L. Masson, "Growth of Si ultrathin films on silver surfaces: Evidence of an Ag(110) reconstruction induced by Si", *Physical Review B*, vol. 88, 121411(R), 2013 (cit. on pp. 14, 15, 24, 121).

[34] R. Bernard, T. Leoni, A. Wilson, T. Lelaidier, H. Sahaf, E. Moyen, L. Assaud, L. Santinacci, F. Leroy, F. Cheynis, A. Ranguis, H. Jamgotchian, C. Becker, Y. Borensztein, M. Hanbücken, G. Prévot, and L. Masson, "Growth of si ultrathin films on silver surfaces: Evidence of an ag(110) reconstruction induced by si", *Phys. Rev. B*, vol. 88, p. 121 411, 2013 (cit. on p. 15).

[35] C. Leandri, G. L. Lay, B. Aufray, C. Girardeaux, J. Avila, M. Dávila, M. Asensio, C. Ottaviani, and A. Cricenti, "Self-aligned silicon quantum wires on Ag(110)", *Surface Science*, vol. 574, pp. L9–L15, 2005 (cit. on p. 15).

[36] S. Colonna, G. Serrano, P. Gori, A. Cricenti, and F. Ronci, "Systematic STM and LEED investigation of the Si/Ag(110) surface", *Journal of Physics: Condensed Matter*, vol. 25, p. 315 301, 2013 (cit. on p. 15).

[37] P. De Padova, C. Quaresima, C. Ottaviani, P. M. Sheverdyaeva, P. Moras, C. Carbone, D. Topwal, B. Olivieri, A. Kara, H. Oughaddou, B. Aufray, and G. Le Lay, "Evidence of graphene-like electronic signature in silicene nanoribbons", *Applied Physics Letters*, vol. 96, p. 261 905, 2010 (cit. on pp. 15, 92).

[38] P. Gori, O. Pulci, F. Ronci, S. Colonna, and F. Bechstedt, "Origin of Dirac-cone-like features in silicon structures on Ag(111) and Ag(110)", *Journal of Applied Physics*, vol. 114, p. 113 710, 2013 (cit. on p. 15).

[39] C. Hogan, O. Pulci, P. Gori, F. Bechstedt, D. S. Martin, E. E. Barritt, A. Curcella, G. Prevot, and Y. Borensztein, "Optical properties of silicene, si/ag(111), and si/ag(110)", *Phys. Rev. B*, vol. 97, p. 195 407, 2018 (cit. on p. 15).

[40] Y. Borensztein, G. Prévot, and L. Masson, "Large differences in the optical properties of a single layer of Si on Ag(110) compared to silicene", *Physical Review B*, vol. 89, p. 245 410, 2014 (cit. on p. 15).

[41] G. Prévot, C. Hogan, T. Leoni, R. Bernard, E. Moyen, and L. Masson, "Si nanoribbons on ag(110) studied by grazing-incidence x-ray diffraction, scanning tunneling microscopy, and density-functional theory: Evidence of a pentamer chain structure", *Phys. Rev. Lett.*, vol. 117, p. 276 102, 2016 (cit. on p. 16).

[42] H. Sahaf, C. Léandri, E. Moyen, M. Macé, L. Masson, and M. Hanbücken, "Growth of Co nanolines on self-assembled Si nanostripes", *EPL (Europhysics Letters)*, vol. 86, p. 28 006, 2009 (cit. on p. 16).

[43] B. Feng, H. Li, S. Meng, L. Chen, and K. Wu, "Structure and quantum well states in silicene nanoribbons on Ag(110)", *Surface Science*, vol. 645, pp. 74–79, 2016 (cit. on p. 16).

[44] A. Kara, S. Vizzini, C. Leandri, B. Ealet, H. Oughaddou, B. Aufray, and G. LeLay, "Silicon nanoribbons on Ag(110): A computational investigation", *Journal of Physics: Condensed Matter*, vol. 22, p. 045 004, 2010 (cit. on p. 16).

[45] C. Lian and J. Ni, "The structural and electronic properties of silicon nanoribbons on Ag(110): A first principles study", *Physica B: Condensed Matter*, vol. 407, pp. 4695–4699, 2012 (cit. on p. 16).

[46] G.-m. He, "Atomic structure of Si nanowires on Ag(110): A density-functional theory study", *Physical Review B*, vol. 73, p. 035 311, 2006 (cit. on pp. 16, 17).

[47] J. I. Cerdá, J. Sławińska, G. Le Lay, A. C. Marele, J. M. Gómez-Rodríguez, and M. E. Dávila, "Unveiling the pentagonal nature of perfectly aligned single-and double-strand Si nano-ribbons on Ag(110)", *Nature Communications*, vol. 7, p. 13 076, 2016 (cit. on p. 16).

[48] C. Hogan, S. Colonna, R. Flammini, A. Cricenti, and F. Ronci, "Structure and stability of Si/Ag(110) nanoribbons", *Physical Review B*, vol. 92, p. 115 439, 2015 (cit. on p. 16).

[49] C. Léandri, H. Oughaddou, B. Aufray, J. Gay, G. Le Lay, A. Ranguis, and Y. Garreau, "Growth of Si nanostructures on Ag(001)", *Surface Science*, vol. 601, pp. 262–267, 2007 (cit. on pp. 16, 17).

[50] H. Oughaddou, H. Enriquez, M. R. Tchalala, H. Yildirim, A. J. Mayne, A. Bendounan, G. Dujardin, M. Ait Ali, and A. Kara, "Silicene, a promising new 2d material", *Progress in Surface Science*, vol. 90, pp. 46–83, 2015 (cit. on p. 17).

[51] G. L. Lay, "Physics and electronics of the noble-metal/elemental-semiconductor interface formation: A status report", *Surface Science*, vol. 132, pp. 169–204, 1983 (cit. on p. 17).

[52] B. Lalmi, H. Oughaddou, H. Enriquez, A. Kara, S. Vizzini, B. Ealet, and B. Aufray, "Epitaxial growth of a silicene sheet", *Applied Physics Letters*, vol. 97, p. 223 109, 2010 (cit. on pp. 17, 18, 72).

[53] E. Cinquanta, E. Scalise, D. Chiappe, C. Grazianetti, B. van den Broek, M. Houssa, M. Fanciulli, and A. Molle, "Getting through the Nature of Silicene: An sp ^{2} –sp ^{3} Two-Dimensional Silicon Nanosheet", *The Journal of Physical Chemistry C*, vol. 117, pp. 16 719–16 724, 2013 (cit. on pp. 17, 72, 82).

[54] L. Chen, C.-C. Liu, B. Feng, X. He, P. Cheng, Z. Ding, S. Meng, Y. Yao, and K. Wu, "Evidence for Dirac Fermions in a Honeycomb Lattice Based on Silicon", *Physical Review Letters*, vol. 109, p. 056 804, 2012 (cit. on pp. 17, 22, 24, 72, 92).

[55] C.-L. Lin, R. Arafune, K. Kawahara, Noriyuki Tsukahara, E. Minamitani, Y. Kim, N. Takagi, and M. Kawai, "Structure of Silicene Grown on Ag(111)", *Applied Physics Express*, vol. 5, p. 045 802, 2012 (cit. on pp. 17–19, 21, 22, 72, 77, 80).

[56] R. Arafune, C.-L. Lin, K. Kawahara, Noriyuki Tsukahara, E. Minamitani, Y. Kim, N. Takagi, and M. Kawai, "Structural transition of silicene on Ag(111)", *Surface Science*, vol. 608, pp. 297–300, 2013 (cit. on pp. 17, 18, 22, 72, 77, 92).

[57] A. Resta, T. Leoni, C. Barth, A. Ranguis, C. Becker, T. Bruhn, P. Vogt, and G. Le Lay, "Atomic Structures of Silicene Layers Grown on Ag(111): Scanning Tunneling Microscopy and Noncontact Atomic Force Microscopy Observations", *Scientific Reports*, vol. 3, p. 2399, 2013 (cit. on pp. 17, 18, 22, 72, 77).

[58] C. Grazianetti, D. Chiappe, E. Cinquanta, G. Tallarida, M. Fanciulli, and A. Molle, "Exploring the morphological and electronic properties of silicene superstructures", *Applied Surface Science*, vol. 291, pp. 109–112, 2014 (cit. on pp. 17, 72).

[59] P. Moras, T. O. Mentes, P. M. Sheverdyaeva, A. Locatelli, and C Carbone, "Coexistence of multiple silicene phases in silicon grown on Ag(111)", *Journal of Physics: Condensed Matter*, vol. 26, p. 185 001, 2014 (cit. on pp. 17, 22, 25, 72, 76, 93, 109).

[60] M. R. Tchalala, H. Enriquez, A. J. Mayne, A. Kara, G. Dujardin, M. A. Ali, and H. Oughaddou, "Atomic structure of silicene nanoribbons on Ag(110)", *Journal of Physics: Conference Series*, vol. 491, p. 012 002, 2014 (cit. on pp. 17, 72, 73).

[61] Z.-L. Liu, M.-X. Wang, J.-P. Xu, J.-F. Ge, G. L. Lay, P. Vogt, D. Qian, C.-L. Gao, C. Liu, and J.-F. Jia, "Various atomic structures of monolayer silicene fabricated on Ag(111)", *New Journal of Physics*, vol. 16, p. 075 006, 2014 (cit. on pp. 17, 73, 77).

[62] H. Enriquez, A. Mayne, A. Kara, S. Vizzini, S. Roth, B. Lalmi, A. P. Seitsonen, B. Aufray, T. Greber, R. Belkhou, G. Dujardin, and H. Oughaddou, "Adsorption of silicon on Au(110): An ordered two dimensional surface alloy", *Applied Physics Letters*, vol. 101, p. 021 605, 2012 (cit. on pp. 17, 73).

[63] Z.-L. Liu, M.-X. Wang, C. Liu, J.-F. Jia, P. Vogt, C. Quaresima, C. Ottaviani, B. Olivieri, P. De Padova, and G. L. Lay, “The fate of the $(2\sqrt{3} \times 2\sqrt{3})R30^\circ$ silicene phase on Ag(111)”, *APL Materials*, vol. 2, p. 092 513, 2014 (cit. on pp. 17, 73, 77).

[64] A. Curcella, R. Bernard, Y. Borensztein, A. Resta, M. Lazzeri, and G. Prévot, “Determining the atomic structure of the (4 x 4) silicene layer on Ag(111) by combined grazing-incidence x-ray diffraction measurements and first-principles calculations”, *Physical Review B*, vol. 94, p. 165 438, 2016 (cit. on pp. 17, 73, 94).

[65] R. Bernard, Y. Borensztein, H. Cruguel, M. Lazzeri, and G. Prévot, “Growth mechanism of silicene on Ag (111) determined by scanning tunneling microscopy measurements and *ab initio* calculations”, *Physical Review B*, vol. 92, p. 045 415, 2015 (cit. on pp. 17, 24, 25, 72, 73, 76, 109, 121, 126, 129, 130).

[66] G.-W. Lee, H.-D. Chen, and D.-S. Lin, “Growth mode and structures of silicene on the Ag(1 1 1) surface”, *Applied Surface Science*, vol. 354, Part A, pp. 187–195, 2015 (cit. on pp. 17, 18, 72, 73).

[67] P. De Padova, P. Vogt, A. Resta, J. Avila, I. Razado-Colambo, C. Quaresima, C. Ottaviani, B. Olivieri, T. Bruhn, T. Hirahara, T. Shirai, S. Hasegawa, M. Carmen Asensio, and G. Le Lay, “Evidence of Dirac fermions in multilayer silicene”, *Applied Physics Letters*, vol. 102, p. 163 106, 2013 (cit. on pp. 18, 92).

[68] P. Lagarde, M. Chorro, D. Roy, and N. Trcera, “Study by EXAFS of the local structure around Si on silicene deposited on Ag(1 1 0) and Ag(1 1 1) surfaces”, *Journal of Physics: Condensed Matter*, vol. 28, p. 075 002, 2016 (cit. on pp. 18, 19).

[69] N. Takagi, C.-L. Lin, K. Kawahara, E. Minamitani, N. Tsukahara, M. Kawai, and R. Arafune, “Silicene on Ag(111): Geometric and electronic structures of a new honeycomb material of Si”, *Progress in Surface Science*, vol. 90, pp. 1–20, 2015 (cit. on p. 19).

[70] K.-H. Wu, “A review of the growth and structures of silicene on Ag (111)”, *Chinese Physics B*, vol. 24, p. 086 802, 2015 (cit. on p. 19).

[71] H. Jamgotchian, B. Ealet, H. Maradj, J.-Y. Hoarau, J.-P. Bibérian, and B. Aufray, “A comprehensive analysis of the $(\sqrt{13}\times)\sqrt{13}R13.9^\circ$ type II structure of silicene on Ag(1 1 1)”, *Journal of Physics: Condensed Matter*, vol. 28, p. 195 002, 2016 (cit. on pp. 19, 73, 77, 83, 88, 90).

[72] H. Jamgotchian, B. Ealet, Y. Colignon, H. Maradj, J.-Y. Hoarau, J.-P. Biberian, and B. Aufray, “A comprehensive study of the $(2\sqrt{3} \times 2\sqrt{3})$ reconstruction of silicene on ag(111)”, *Journal of Physics: Condensed Matter*, vol. 27, p. 395 002, 2015 (cit. on pp. 19, 73, 77, 85).

[73] M. Spencer and T. Morishita, “Silicene: Structure, properties and applications”, *Springer International Publishing*, vol. 235, pp. XVI, 276, 2016 (cit. on p. 20).

[74] A. H. Castro Neto, F. Guinea, N. M. R. Peres, K. S. Novoselov, and A. K. Geim, “The electronic properties of graphene”, *Reviews of Modern Physics*, vol. 81, pp. 109–162, 2009 (cit. on p. 20).

[75] C.-L. Lin, R. Arafune, K. Kawahara, M. Kanno, N. Tsukahara, E. Minamitani, Y. Kim, M. Kawai, and N. Takagi, “Substrate-Induced Symmetry Breaking in Silicene”, *Physical Review Letters*, vol. 110, p. 076 801, 2013 (cit. on pp. 21, 72).

[76] S. K. Mahatha, P. Moras, V. Bellini, P. M. Sheverdyaeva, C. Struzzi, L. Petaccia, and C. Carbone, “Silicene on ag(111): A honeycomb lattice without dirac bands”, *Phys. Rev. B*, vol. 89, p. 201 416, 2014 (cit. on pp. 21, 72, 134).

[77] S. Y. Zhou, G.-H. Gweon, J. Graf, A. V. Fedorov, C. D. Spataru, R. D. Diehl, Y. Kopelevich, D.-H. Lee, S. G. Louie, and A. Lanzara, “First direct observation of Dirac fermions in graphite”, *Nature Physics*, vol. 2, pp. 595–599, 2006 (cit. on p. 21).

[78] N. W. Johnson, P. Vogt, A. Resta, P. De Padova, I. Perez, D. Muir, E. Z. Kurmaev, G. Le Lay, and A. Moewes, “The Metallic Nature of Epitaxial Silicene Monolayers on Ag(111)”, *Advanced Functional Materials*, vol. 24, pp. 5253–5259, 2014 (cit. on pp. 21, 22, 72).

[79] P. M. Sheverdyaeva, S. K. Mahatha, P. Moras, L. Petaccia, G. Fratesi, G. Onida, and C. Carbone, "Electronic States of Silicene Allotropes on Ag(111)", *ACS Nano*, vol. 11, pp. 975–982, 2017 (cit. on pp. 21, 134).

[80] J. Sone, T. Yamagami, Y. Aoki, K. Nakatsuji, and H. Hirayama, "Epitaxial growth of silicene on ultra-thin Ag(111) films", *New Journal of Physics*, vol. 16, p. 095 004, 2014 (cit. on pp. 22, 105).

[81] E. Salomon, R. E. Ajjouri, G. L. Lay, and T. Angot, "Growth and structural properties of silicene at multilayer coverage", *Journal of Physics: Condensed Matter*, vol. 26, p. 185 003, 2014 (cit. on pp. 22, 92, 93, 98).

[82] L. Chen, H. Li, B. Feng, Z. Ding, J. Qiu, P. Cheng, K. Wu, and S. Meng, "Spontaneous Symmetry Breaking and Dynamic Phase Transition in Monolayer Silicene", *Physical Review Letters*, vol. 110, p. 085 504, 2013 (cit. on pp. 22, 24).

[83] P. Vogt, P. Capiod, M. Berthe, A. Resta, P. De Padova, T. Bruhn, G. Le Lay, and B. Grandidier, "Synthesis and electrical conductivity of multilayer silicene", *Applied Physics Letters*, vol. 104, p. 021 602, 2014 (cit. on pp. 23, 92, 93, 107, 108).

[84] R. Arafune, C.-L. Lin, R. Nagao, M. Kawai, and N. Takagi, "Comment on "Evidence for Dirac Fermions in a Honeycomb Lattice Based on Silicon"", *Physical Review Letters*, vol. 110, p. 229 701, 2013 (cit. on p. 24).

[85] R. Bernard, Y. Borensztein, H. Cruguel, M. Lazzeri, and G. Prévot, "Growth mechanism of silicene on Ag(111) determined by scanning tunneling microscopy measurements and *ab initio* calculations", *Phys. Rev. B*, vol. 92, p. 045 415, 2015 (cit. on pp. 24, 121).

[86] M. Satta, S. Colonna, R. Flammini, A. Cricenti, and F. Ronci, "Silicon Reactivity at the Ag(111) Surface", *Physical Review Letters*, vol. 115, p. 026 102, 2015 (cit. on p. 25).

[87] G. Prévot, R. Bernard, H. Cruguel, and Y. Borensztein, "Monitoring Si growth on Ag(111) with scanning tunneling microscopy reveals that silicene structure involves silver atoms", *Applied Physics Letters*, vol. 105, p. 213 106, 2014 (cit. on pp. 25, 26, 72, 109, 121).

[88] Y. Yamada-Takamura, Z. T. Wang, Y. Fujikawa, T. Sakurai, Q. K. Xue, J. Tolle, P.-L. Liu, A. V. G. Chizmeshya, J. Kouvetakis, and I. S. T. Tsong, "Surface and Interface Studies of GaN Epitaxy on Si(111) via ZrB_2 Buffer Layers", *Physical Review Letters*, vol. 95, p. 266 105, 2005 (cit. on p. 26).

[89] R. Friedlein, A. Fleurence, K. Aoyagi, M. P. de Jong, H. Van Bui, F. B. Wiggers, S. Yoshimoto, T. Koitaya, S. Shimizu, H. Noritake, K. Mukai, J. Yoshinobu, and Y. Yamada-Takamura, "Core level excitations—A fingerprint of structural and electronic properties of epitaxial silicene", *The Journal of Chemical Physics*, vol. 140, p. 184 704, 2014 (cit. on p. 26).

[90] C.-C. Lee, A. Fleurence, Y. Yamada-Takamura, T. Ozaki, and R. Friedlein, "Band structure of silicene on zirconium diboride (0001) thin-film surface: Convergence of experiment and calculations in the one-Si-atom Brillouin zone", *Physical Review B*, vol. 90, 2014 (cit. on p. 26).

[91] R. Quhe, Y. Yuan, J. Zheng, Y. Wang, Z. Ni, J. Shi, D. Yu, J. Yang, and J. Lu, "Does the Dirac Cone Exist in Silicene on Metal Substrates?", *Scientific Reports*, vol. 4, 2014 (cit. on p. 27).

[92] G. Binnig, H. Rohrer, C. Gerber, and E. Weibel, "Surface studies by scanning tunneling microscopy", *Phys. Rev. Lett.*, vol. 49, pp. 57–61, 1982 (cit. on p. 31).

[93] B. Nieuwenhuys, O. V. Aardenne, and W. Sachtler, "Adsorption of xenon on group viii and ib metals studied by photoelectric work function measurements", *Chemical Physics*, vol. 5, pp. 418–428, 1974 (cit. on p. 34).

[94] J. Bardeen, "Tunnelling from a many-particle point of view", *Phys. Rev. Lett.*, vol. 6, pp. 57–59, 1961 (cit. on p. 35).

[95] J. Tersoff and D. R. Hamann, "Theory of the scanning tunneling microscope", *Phys. Rev. B*, vol. 31, pp. 805–813, 1985 (cit. on pp. 37, 39).

[96] D. Necas and P. Klapetek, "Gwyddion: An open-source software for SPM data analysis", *Central European Journal of Physics*, vol. 10, pp. 181–188, 2012 (cit. on p. 38).

[97] A. Wilson, R. Bernard, Y. Borensztein, B. Croset, H. Cruguel, A. Vlad, A. Coati, Y. Garreau, and G. Prévot, "Critical au concentration for the stabilization of au cu nanoparticles on rutile against dissociation under oxygen", *The Journal of Physical Chemistry Letters*, vol. 6, pp. 2050–2055, 2015 (cit. on p. 38).

[98] A. Wilson, R. Bernard, A. Vlad, Y. Borensztein, A. Coati, B. Croset, Y. Garreau, and G. Prévot, "Epitaxial growth of bimetallic au-cu nanoparticles on tio2(110) followed in situ by scanning tunneling microscopy and grazing-incidence x-ray diffraction", *Phys. Rev. B*, vol. 90, p. 075 416, 2014 (cit. on p. 38).

[99] A.-S. Lucier, H. Mortensen, Y. Sun, and P. Grutter, "Determination of the atomic structure of scanning probe microscopy tungsten tips by field ion microscopy", *Phys. Rev. B*, vol. 72, p. 235 420, 2005 (cit. on p. 40).

[100] R. Feidenhans'l, "Surface structure determination by x-ray diffraction", *Surface Science Reports*, vol. 10, pp. 105–188, 1989 (cit. on p. 41).

[101] B. Warren, *X-ray Diffraction*. 1969 (cit. on p. 42).

[102] O. Robach, Y. Garreau, K. Aïd, and M. B. Véron-Jolliot, "Corrections for surface X-ray diffraction measurements using the Z-axis geometry: Finite size effects in direct and reciprocal space", *Journal of Applied Crystallography*, vol. 33, pp. 1006–1018, 2000 (cit. on pp. 45, 48, 49, 110).

[103] J. Drnec, T. Zhou, S. Pintea, W. Onderwaater, E. Vlieg, G. Renaud, and R. Felici, "Integration techniques for surface X-ray diffraction data obtained with a two-dimensional detector", *Journal of Applied Crystallography*, vol. 47, pp. 365–377, 2014 (cit. on p. 47).

[104] S. Roobol, W. Onderwaater, J. Drnec, R. Felici, and J. Frenken, "BINoculars: data reduction and analysis software for two-dimensional detectors in surface X-ray diffraction", *Journal of Applied Crystallography*, vol. 48, pp. 1324–1329, 2015 (cit. on p. 47).

[105] E. Vlieg, "Integrated intensities using a six-circle surface x-ray diffractometer", *Journal of Applied Crystallography*, vol. 30, 1997 (cit. on p. 48).

[106] M. Yasaka, "X-ray thin-film measurement techniques v. x-ray reflectivity measurement", *Righaku journal*, 2010 (cit. on p. 50).

[107] J. McIntyre and D. Aspnes, "Differential reflection spectroscopy of very thin surface films", *Surface Science*, vol. 24, pp. 417–434, 1971 (cit. on p. 51).

[108] E. D Palik, *Handbook of Optical Constant of Solids II*. 1991, vol. 3 (cit. on p. 51).

[109] P. Lautenschlager, M. Garriga, L. Vina, and M. Cardona, "Temperature dependence of the dielectric function and interband critical points in silicon", *Phys. Rev. B*, vol. 36, pp. 4821–4830, 1987 (cit. on p. 51).

[110] P. Giannozzi, S. Baroni, N. Bonini, M. Calandra, R. Car, C. Cavazzoni, D. Ceresoli, G. L. Chiarotti, M. Cococcioni, I. Dabo, A. D. Corso, S. de Gironcoli, S. Fabris, G. Fratesi, R. Gebauer, U. Gerstmann, C. Gougoussis, A. Kokalj, M. Lazzeri, L. Martin-Samos, N. Marzari, F. Mauri, R. Mazzarello, S. Paolini, A. Pasquarello, L. Paulatto, C. Sbraccia, S. Scandolo, G. Sclauzero, A. P. Seitsonen, A. Smogunov, P. Umari, and R. M. Wentzcovitch, "Quantum espresso: A modular and open-source software project for quantum simulations of materials", *Journal of Physics: Condensed Matter*, vol. 21, p. 395 502, 2009 (cit. on p. 54).

[111] P. Giannozzi, O. Andreussi, T. Brumme, O. Bunau, M. B. Nardelli, M. Calandra, R. Car, C. Cavazzoni, D. Ceresoli, M. Cococcioni, N. Colonna, I. Carnimeo, A. D. Corso, S. de Gironcoli, P. Delugas, R. A. D. Jr, A. Ferretti, A. Floris, G. Fratesi, G. Fugallo, R. Gebauer, U. Gerstmann, F. Giustino, T. Gorni, J. Jia, M. Kawamura, H.-Y. Ko, A. Kokalj, E. Küçükbenli, M. Lazzeri, M. Marsili, N. Marzari, F. Mauri, N. L.

Nguyen, H.-V. Nguyen, A. Otero-de-la-Roza, L. Paulatto, S. Poncé, D. Rocca, R. Sabatini, B. Santra, M. Schlipf, A. P. Seitsonen, A. Smogunov, I. Timrov, T. Thonhauser, P. Umari, N. Vast, X. Wu, and S. Baroni, “Advanced capabilities for materials modelling with q uantum espresso”, *Journal of Physics: Condensed Matter*, vol. 29, p. 465 901, 2017 (cit. on p. 54).

[112] P. Hohenberg and W. Kohn, “Inhomogeneous Electron Gas”, *Physical Review*, vol. 136, B864–B871, 1964 (cit. on pp. 55, 58).

[113] W. Kohn and L. J. Sham, “Self-Consistent Equations Including Exchange and Correlation Effects”, *Physical Review*, vol. 140, A1133–A1138, 1965 (cit. on pp. 57, 58).

[114] D. M. Ceperley and B. J. Alder, “Ground State of the Electron Gas by a Stochastic Method”, *Physical Review Letters*, vol. 45, pp. 566–569, 1980 (cit. on p. 59).

[115] J. P. Perdew and A. Zunger, “Self-interaction correction to density-functional approximations for many-electron systems”, *Physical Review B*, vol. 23, p. 5048, 1981 (cit. on pp. 59, 74).

[116] S. Grimme, “Semiempirical gga-type density functional constructed with a long-range dispersion correction”, *Journal of Computational Chemistry*, vol. 27, pp. 1787–1799, 2006 (cit. on pp. 59, 74, 117).

[117] L. Kleinman and D. M. Bylander, “Efficacious Form for Model Pseudopotentials”, *Physical Review Letters*, vol. 48, pp. 1425–1428, 1982 (cit. on p. 63).

[118] D. Vanderbilt, “Soft self-consistent pseudopotentials in a generalized eigenvalue formalism”, *Physical Review B*, vol. 41, pp. 7892–7895, 1990 (cit. on p. 63).

[119] P. E. Blöchl, “Projector augmented-wave method”, *Physical Review B*, vol. 50, pp. 17 953–17 979, 1994 (cit. on p. 64).

[120] M. Methfessel and A. T. Paxton, “High-precision sampling for Brillouin-zone integration in metals”, *Physical Review B*, vol. 40, pp. 3616–3621, 1989 (cit. on p. 65).

[121] J. A. Scholl David S.; Steckel, “Density functional theory: A practical introduction”, *Wiley onlinelibrary*, 2009 (cit. on p. 66).

[122] L. Bengtsson, “Dipole correction for surface supercell calculations”, *Physical Review B*, vol. 59, p. 12 301, 1999 (cit. on p. 66).

[123] R. P. Feynman, “Forces in Molecules”, *Physical Review*, vol. 56, pp. 340–343, 1939 (cit. on p. 67).

[124] D. B. Lichtenberg, “Application of a generalized Feynman-Hellmann theorem to bound-state energy levels”, *Physical Review D*, vol. 40, pp. 4196–4198, 1989 (cit. on p. 67).

[125] H. Liu, N. Han, and J. Zhao, “Temperature and coverage effects on the stability of epitaxial silicene on Ag(111) surfaces”, *Applied Surface Science*, vol. 409, pp. 97–101, 2017 (cit. on p. 72).

[126] J. Qiu, H. Fu, Y. Xu, Q. Zhou, S. Meng, H. Li, L. Chen, and K. Wu, “From Silicene to Half-Silicane by Hydrogenation”, *ACS Nano*, p. 151 021 074 008 004, 2015 (cit. on p. 73).

[127] M. S. Rahman, T. Nakagawa, and S. Mizuno, “Growth of Si on Ag(111) and determination of large commensurate unit cell of high-temperature phase”, *Japanese Journal of Applied Physics*, vol. 54, p. 015 502, 2015 (cit. on pp. 73, 77).

[128] J. P. Perdew, K. Burke, and M. Ernzerhof, “Generalized gradient approximation made simple”, *Phys. Rev. Lett.*, vol. 77, pp. 3865–3868, 1996 (cit. on p. 74).

[129] V. Barone, M. Casarin, D. Forrer, M. Pavone, M. Sambi, and A. Vittadini, “Role and effective treatment of dispersive forces in materials: Polyethylene and graphite crystals as test cases”, *Journal of Computational Chemistry*, vol. 30, pp. 934–939, 2009 (cit. on pp. 74, 117).

[130] G. Kresse and D. Joubert, “From ultrasoft pseudopotentials to the projector augmented-wave method”, *Physical Review B*, vol. 59, pp. 1758–1775, 1999 (cit. on p. 74).

[131] N. Marzari, D. Vanderbilt, A. De Vita, and M. C. Payne, “Thermal contraction and disordering of the Al(110) surface”, *Physical Review Letters*, vol. 82, pp. 3296–3299, 1999 (cit. on p. 75).

[132] O. Robach, Y. Garreau, K. Aïd, and M. B. Véron-Jolliot, "Corrections for surface x-ray diffraction measurements using the z-axis geometry: Finite size effects in direct and reciprocal space", *Journal of Applied Crystallography*, vol. 33, pp. 1006–1018, 2000 (cit. on p. 78).

[133] B. Croset and G. Prévot, "Elastic relaxations and interactions for vicinal and self-organized surfaces: Role of crystalline anisotropy", *Physical Review B*, vol. 73, p. 045 434, 2006 (cit. on p. 82).

[134] G. Prévot, A. Coati, B. Croset, and Y. Garreau, "Direct observation of elastic displacement modes by grazing-incidence X-ray diffraction", *Journal of Applied Crystallography*, vol. 40, pp. 874–882, 2007 (cit. on p. 88).

[135] S. Cahangirov, V. O. Özçelik, A. Rubio, and S. Ciraci, "Silicite: The layered allotrope of silicon", *Physical Review B*, vol. 90, 2014 (cit. on pp. 92, 93, 104, 111, 119).

[136] L. Tao, E. Cinquanta, D. Chiappe, C. Grazianetti, M. Fanciulli, M. Dubey, A. Molle, and D. Akinwande, "Silicene field-effect transistors operating at room temperature", *Nature Nanotechnology*, vol. 10, pp. 227–231, 2015 (cit. on p. 92).

[137] T. Ohta, A. Bostwick, T. Seyller, K. Horn, and E. Rotenberg, "Controlling the electronic structure of bilayer graphene", *Science*, vol. 313, pp. 951–954, 2006 (cit. on p. 92).

[138] I. Forbeaux, J.-M. Themlin, and J.-M. Debever, "Heteroepitaxial graphite on 6h-SiC(0001): Interface formation through conduction-band electronic structure", *Physical Review B*, vol. 58, pp. 16 396–16 406, 1998 (cit. on p. 92).

[139] P. De Padova, J. Avila, A. Resta, I. Razado-Colambo, C. Quaresima, C. Ottaviani, B. Olivieri, T. Bruhn, P. Vogt, M. C. Asensio, and G. Le Lay, "The quasiparticle band dispersion in epitaxial multilayer silicene", *Journal of Physics-Condensed Matter*, vol. 25, p. 382 202, 2013 (cit. on p. 92).

[140] A. Curcella, Y. Borensztein, R. Bernard, M. Lazzeri, A. Resta, Y. Garreau, and G. Prévot, "Multilayer silicene: Clear evidence of Ag-terminated bulk silicon", *2D Materials*, vol. 4, p. 025 067, 2017 (cit. on pp. 92, 110).

[141] A. Curcella, R. Bernard, Y. Borensztein, M. Lazzeri, and G. Prévot, "The mechanism for the stabilization and surfactant properties of epitaxial silicene", *Nanoscale*, vol. 10, pp. 2291–2300, 2018 (cit. on p. 92).

[142] A. Curcella, R. Bernard, Y. Borensztein, S. Pandolfi, and G. Prévot, "Transition from silicene monolayer to thin Si films on Ag(111): Comparison between experimental data and Monte Carlo simulation", *Beilstein Journal of Nanotechnology*, vol. 9, pp. 48–56, 2018 (cit. on pp. 92, 108, 114).

[143] H. Neddermeyer, "Scanning tunnelling microscopy of semiconductor surfaces", *Reports on Progress in Physics*, vol. 59, p. 701, 1996 (cit. on pp. 92, 112, 119).

[144] H.-D. Chen, K.-H. Chien, C.-Y. Lin, T.-C. Chiang, and D.-S. Lin, "Few-Layer Silicon Films on the Ag(111) Surface", *The Journal of Physical Chemistry C*, vol. 120, pp. 2698–2702, 2016 (cit. on pp. 93, 94, 104, 107).

[145] J. Chen, Y. Du, Z. Li, W. Li, B. Feng, J. Qiu, P. Cheng, S. Xue Dou, L. Chen, and K. Wu, "Delocalized Surface State in Epitaxial Si(111) Film with Spontaneous ($\sqrt{3} \times \sqrt{3}$) Superstructure", *Scientific Reports*, vol. 5, p. 13 590, 2015 (cit. on p. 93).

[146] A. Acun, B. Poelsema, H. J. W. Zandvliet, and R. van Gastel, "The instability of silicene on Ag(111)", *Applied Physics Letters*, vol. 103, p. 263 119, 2013 (cit. on p. 93).

[147] S. Cahangirov, V. O. Özçelik, L. Xian, J. Avila, S. Cho, M. C. Asensio, S. Ciraci, and A. Rubio, "Atomic structure of the ($\sqrt{3} \times \sqrt{3}$) phase of silicene on Ag(111)", *Physical Review B*, vol. 90, 2014 (cit. on pp. 93, 111, 113, 114, 117, 119, 129).

[148] C. Ataca, M. Topsakal, E. Aktürk, and S. Ciraci, "A comparative study of lattice dynamics of three- and two-dimensional mos2", *The Journal of Physical Chemistry C*, vol. 115, pp. 16 354–16 361, 2011 (cit. on p. 93).

[149] K. Kawahara, T. Shirasawa, C.-L. Lin, R. Nagao, N. Tsukahara, T. Takahashi, R. Arafune, M. Kawai, and N. Takagi, "Atomic structure of "multilayer silicene" grown on Ag(111): Dynamical low energy electron diffraction analysis", *Surface Science*, vol. 651, pp. 70–75, 2016 (cit. on pp. 94, 101, 110, 112, 114).

[150] H. Fu, L. Chen, J. Chen, J. Qiu, Z. Ding, J. Zhang, K. Wu, H. Li, and S. Meng, "Multilayered silicene: The bottom-up approach for a weakly relaxed Si(111) with Dirac surface states", *Nanoscale*, vol. 7, pp. 15 880–15 885, 2015 (cit. on p. 94).

[151] G.-W. Lee, H.-D. Chen, and D.-S. Lin, "Bonding and interface formation for Si on Ag(111) by core-level photoemission spectroscopy", *Applied Surface Science*, vol. 354, pp. 212–215, 2015 (cit. on pp. 94, 101, 104, 114).

[152] S. K. Mahatha, P. Moras, P. M. Sheverdyaeva, R. Flammini, K. Horn, and C. Carbone, "Evidence for a diamondlike electronic band structure of Si multilayers on Ag(111)", *Physical Review B*, vol. 92, 2015 (cit. on pp. 94, 101, 104, 114).

[153] Y. Touloukian, R. Kirby, R. Taylor, P. Desai, THERMOPHYSICAL, and E. P. I. A. C. L. IN., *Thermophysical Properties of Matter - the TPRC Data Series. Volume 12. Thermal Expansion Metallic Elements and Alloys*. 1975 (cit. on p. 98).

[154] W. M. Yim and R. J. Paff, "Thermal expansion of AlN, sapphire, and silicon", *Journal of Applied Physics*, vol. 45, pp. 1456–1457, 1974 (cit. on p. 98).

[155] M. S. Paterson, "X-Ray Diffraction by Face-Centered Cubic Crystals with Deformation Faults", *Journal of Applied Physics*, vol. 23, p. 805, 1952 (cit. on p. 99).

[156] Y. Girard, G. Baudot, V. Repain, S. Rohart, S. Rousset, A. Coati, and Y. Garreau, "Structural modifications of Co ultrathin films grown on Au(111) vicinal surfaces", *Physical Review B*, vol. 72, p. 155 434, 2005 (cit. on p. 100).

[157] C. Kamal, A. Chakrabarti, A. Banerjee, and S. K. Deb, "Silicene beyond mono-layers—different stacking configurations and their properties", *Journal of Physics: Condensed Matter*, vol. 25, p. 085 508, 2013 (cit. on p. 100).

[158] I. DeWolf, "Micro-Raman spectroscopy to study local mechanical stress in silicon integrated circuits", *Semiconductor Science and Technology*, vol. 11, pp. 139–154, 1996 (cit. on p. 101).

[159] A. T. Voutsas, M. K. Hatalis, J. Boyce, and A. Chiang, "Raman spectroscopy of amorphous and microcrystalline silicon films deposited by low-pressure chemical vapor deposition", *Journal of Applied Physics*, vol. 78, p. 6999, 1995 (cit. on p. 101).

[160] C. Grazianetti, E. Cinquanta, L. Tao, P. De Padova, C. Quaresima, C. Ottaviani, D. Akinwande, and A. Molle, "Silicon Nanosheets: Crossover between Multilayer Silicene and Diamond-like Growth Regime", *ACS Nano*, vol. 11, pp. 3376–3382, 2017 (cit. on p. 104).

[161] H. Aizawa, M. Tsukada, N. Sato, and S. Hasegawa, "Asymmetric structure of the Si (111) ($\sqrt{3} \times \sqrt{3}$) Ag surface", *Surface Science*, vol. 429, pp. L509–L514, 1999 (cit. on pp. 111, 155, 157).

[162] T. Takahashi and S. Nakatani, "Refinement of the Si(111) ($\sqrt{3} \times \sqrt{3}$) Ag structure by surface x ray diffraction", *Surface science*, vol. 282, pp. 17–32, 1993 (cit. on pp. 111, 113, 114).

[163] H. Tajiri, K. Sumitani, S. Nakatani, A. Nojima, T. Takahashi, K. Akimoto, H. Sugiyama, X. Zhang, and H. Kawata, "X-ray diffraction study of the Si (111) ($\sqrt{3} \times \sqrt{3}$) Ag surface structure", *Physical Review B*, vol. 68, p. 035 330, 2003 (cit. on p. 111).

[164] W. C. Fan, A. Ignatiev, H. Huang, and S. Y. Tong, "Observation and structural determination of ($\sqrt{3} \times \sqrt{3}$) R30° reconstruction of the Si (111) surface", *Physical review letters*, vol. 62, p. 1516, 1989 (cit. on pp. 112, 114, 117).

[165] Z.-X. Guo and A. Oshiyama, "Crossover between silicene and ultra-thin Si atomic layers on Ag (111) surfaces", *New Journal of Physics*, vol. 17, p. 045 028, 2015 (cit. on pp. 112, 114, 117).

[166] E. Vlieg, "*ROD*: a program for surface X-ray crystallography", *Journal of Applied Crystallography*, vol. 33, pp. 401–405, 2000 (cit. on p. 113).

[167] J. P. Perdew, K. Burke, and M. Ernzerhof, "Generalized gradient approximation made simple", *Physical Review Letters*, vol. 77, pp. 3865–3868, 1996 (cit. on p. 117).

[168] J. Bai, H. Tanaka, and X. C. Zeng, "Graphene-like bilayer hexagonal silicon polymorph", *Nano Research*, vol. 3, pp. 694–700, 2010 (cit. on p. 117).

[169] H. Fu, J. Zhang, Z. Ding, H. Li, and S. Meng, "Stacking-dependent electronic structure of bilayer silicene", *Applied Physics Letters*, vol. 104, p. 131 904, 2014 (cit. on p. 117).

[170] P. Pflugradt, L. Matthes, and F. Bechstedt, "Unexpected symmetry and AA stacking of bilayer silicene on Ag(111)", *Physical Review B*, vol. 89, p. 205 428, 2014 (cit. on pp. 117, 155).

[171] V. O. Özçelik, D. Kecik, E. Durgun, and S. Ciraci, "Adsorption of Group IV Elements on Graphene, Silicene, Germanene, and Stanene: Dumbbell Formation", *The Journal of Physical Chemistry C*, vol. 119, pp. 845–853, 2015 (cit. on p. 130).

[172] M. J. Cherukara, B. Narayanan, H. Chan, and S. K. R. S. Sankaranarayanan, "Silicene growth through island migration and coalescence", *Nanoscale*, vol. 9, pp. 10 186–10 192, 2017 (cit. on p. 130).

[173] D. Wall, I. Lohmar, K. R. Roos, J. Krug, M. Horn-von Hoegen, and F.-J. Meyer zu Heringdorf, "Imaging diffusion fields on a surface with multiple reconstructions: Ag/Si(111)", *New Journal of Physics*, vol. 12, p. 103 019, 2010 (cit. on p. 130).

[174] M. Hanbücken, M. Futamoto, and J. Venables, "Nucleation, growth and the intermediate layer in ag/si(100) and ag/si(111)", *Surface Science*, vol. 147, pp. 433–450, 1984 (cit. on p. 130).

[175] T. Yamagami, J. Sone, K. Nakatsuji, and H. Hirayama, "Surfactant role of Ag atoms in the growth of Si layers on Si(111) ($\sqrt{3} \times \sqrt{3}$)-Ag substrates", *Applied Physics Letters*, vol. 105, p. 151 603, 2014 (cit. on p. 130).

[176] C.-H.-T. Chang, T.-Y. Fu, and J.-S. Tsay, "Interaction transfer of silicon atoms forming Co silicide for Co and related magnetic properties", *Journal of Applied Physics*, vol. 117, 17B733, 2015 (cit. on p. 130).

[177] L. Persichetti, F. Jardali, H. Vach, A. Sgarlata, I. Berbezier, M. De Crescenzi, and A. Balzarotti, "Van der Waals Heteroepitaxy of Germanene Islands on Graphite", *The Journal of Physical Chemistry Letters*, vol. 7, pp. 3246–3251, 2016 (cit. on p. 134).

[178] K. G. Nath, I. Shimoyama, T. Sekiguchi, and Y. Baba, "Chemical-state analysis for low-dimensional Si and Ge films on graphite", *Journal of Applied Physics*, vol. 94, pp. 4583–4588, 2003 (cit. on p. 134).

[179] R. van Bremen, Q. Yao, S. Banerjee, D. Cakir, N. Oncel, and H. J. W. Zandvliet, "Intercalation of si between mos2 layers", *Beilstein Journal of Nanotechnology*, vol. 8, pp. 1952–1960, 2017 (cit. on p. 135).

[180] Q. Yao, R. van Bremen, and H. J. W. Zandvliet, "Growth of silicon on tungsten diselenide", *Applied Physics Letters*, vol. 109, p. 243 105, 2016 (cit. on p. 135).

[181] B. Marsen, M. Lonfat, P. Scheier, and K. Sattler, "Energy gap of silicon clusters studied by scanning tunneling spectroscopy", *Phys. Rev. B*, vol. 62, pp. 6892–6895, 2000 (cit. on p. 135).

[182] A. V. Nezhdanov, "The morphology, electron structure, and optical properties of self-assembled silicon nanostructures on the surface of highly oriented pyrolytic graphite", *Semiconductors*, vol. 45, pp. 56–60, 2011 (cit. on pp. 135, 136, 139).

[183] P. Castrucci, F. Fabbri, T. Delise, M. Scarselli, M. Salvato, S. Pascale, R. Francini, I. Berbezier, C. Lechner, F. Jardali, H. Vach, and M. D. Crescenzi, "Raman investigation of air-stable silicene nanosheets on an inert graphite surface", *Nano Research*, pp. 1–11, 2018 (cit. on pp. 135, 139, 140).

[184] E. Scalise, M. Houssa, G. Pourtois, B. v. d. Broek, V. Afanas'ev, and A. Stesmans, "Vibrational properties of silicene and germanene", *Nano Research*, vol. 6, pp. 19–28, 2013 (cit. on p. 135).

[185] J. Zhuang, X. Xu, Y. Du, K. Wu, L. Chen, W. Hao, J. Wang, W. K. Yeoh, X. Wang, and S. X. Dou, "Investigation of electron-phonon coupling in epitaxial silicene by in situ Raman spectroscopy", *Physical Review B*, vol. 91, p. 161 409, 2015 (cit. on p. 135).

[186] T. Kondo, Y. Iwasaki, Y. Honma, Y. Takagi, S. Okada, and J. Nakamura, "Formation of nonbonding π electronic states of graphite due to Pt-C hybridization", *Physical Review B*, vol. 80, p. 233 408, 2009 (cit. on pp. 135, 139, 144).

[187] J. Xhie, K. Sattler, U. Müller, N. Venkateswaran, and G. Raina, "Periodic charge-density modulations on graphite near platinum particles", *Physical Review B*, vol. 43, pp. 8917–8923, 1991 (cit. on pp. 135, 139, 144).

[188] P. Ruffieux, O. Gröning, P. Schwaller, L. Schlapbach, and P. Gröning, "Hydrogen Atoms Cause Long-Range Electronic Effects on Graphite", *Physical Review Letters*, vol. 84, pp. 4910–4913, 2000 (cit. on pp. 135, 139, 144).

[189] H. A. Mizes and J. S. Foster, "Long-Range Electronic Perturbations Caused by Defects Using Scanning Tunneling Microscopy", *Science*, vol. 244, pp. 559–562, 1989 (cit. on pp. 135, 139, 144).

[190] Y. Arnaud and M. Chevreton, "Etude comparative des composés TiX2 (X = S, Se, Te). Structures de TiTe2 et TiSeTe", *Journal of Solid State Chemistry*, vol. 39, pp. 230–239, 1981 (cit. on p. 136).

[191] Y. Baskin and L. Meyer, "Lattice Constants of Graphite at Low Temperatures", *Physical Review*, vol. 100, pp. 544–544, 1955 (cit. on p. 136).

[192] P. A. Young, "Lattice parameter measurements on molybdenum disulphide", *Journal of Physics D: Applied Physics*, vol. 1, p. 936, 1968 (cit. on p. 136).

[193] D. Tománek and S. G. Louie, "First-principles calculation of highly asymmetric structure in scanning-tunneling-microscopy images of graphite", *Physical Review B*, vol. 37, pp. 8327–8336, 1988 (cit. on p. 136).

[194] I. P. Batra, N. García, H. Rohrer, H. Salemink, E. Stoll, and S. Ciraci, "A study of graphite surface with stm and electronic structure calculations", *Surface Science*, vol. 181, pp. 126–138, 1987 (cit. on p. 136).

[195] W. Peng, T. Xu, P. Diener, L. Biadala, M. Berthe, X. Pi, Y. Borensztein, A. Curcella, R. Bernard, G. Prévot, and B. Grandidier, "Resolving the Controversial Existence of Silicene and Germanene Nanosheets Grown on Graphite", *ACS Nano*, vol. 12, pp. 4754–4760, 2018 (cit. on p. 136).

[196] P. L. Giunta and S. P. Kelty, "Direct observation of graphite layer edge states by scanning tunneling microscopy", *The Journal of Chemical Physics*, vol. 114, pp. 1807–1812, 2001 (cit. on p. 136).

[197] Y. Niimi, T. Matsui, H. Kambara, K. Tagami, M. Tsukada, and H. Fukuyama, "Scanning tunneling microscopy and spectroscopy of the electronic local density of states of graphite surfaces near monoatomic step edges", *Physical Review B*, vol. 73, 2006 (cit. on p. 136).

[198] Y. Cai, C.-P. Chuu, C. M. Wei, and M. Y. Chou, "Stability and electronic properties of two-dimensional silicene and germanene on graphene", *Physical Review B*, vol. 88, 2013 (cit. on p. 137).

[199] G. M. Shedd and P. E. Russell, "A simple wave function interference model for the electron-density superstructures observed during scanning tunneling microscopy of perturbed graphite surfaces", *Surface science*, vol. 266, pp. 259–264, 1992 (cit. on p. 139).

[200] N. Takeuchi, J. Valenzuela-Benavides, and L. M. de la Garza, "Electronic superstructures on the graphite surface studied by first-principles calculations", *Surface Science*, vol. 380, pp. 190–198, 1997 (cit. on p. 139).

[201] H. Xu, H. Permana, Y. Lu, and K. Y. S. Ng, "STM study of Mo growth and induced surface structure changes on HOPG", *Surface Science*, vol. 325, pp. 285–293, 1995 (cit. on p. 139).

[202] B. An, S. Fukuyama, K. Yokogawa, and M. Yoshimura, “Characteristics of the $(\sqrt{3} \times \sqrt{3})R30^\circ$ superstructure of graphite by scanning tunneling microscopy”, *Japanese Journal of Applied Physics*, vol. 39, p. 4347, 2000 (cit. on p. 139).

[203] J. C. M. López, M. C. G. Passeggi, and J. Ferrón, “Surface superstructures in highly oriented pyrolytic graphite surfaces after Ar+ bombardment”, *Surface Science*, vol. 602, pp. 671–676, 2008 (cit. on p. 139).

[204] L. Tapasztó, P. Nemes-Incze, Z. Osváth, M. C. Bein, A. Darabont, and L. P. Biró, “Complex superstructure patterns near defect sites of carbon nanotubes and graphite”, *Physica E: Low-dimensional Systems and Nanostructures*, vol. 40, pp. 2263–2267, 2008 (cit. on p. 139).

[205] A. K. Geim and I. V. Grigorieva, “Van der Waals heterostructures”, *Nature*, vol. 499, pp. 419–425, 2013 (cit. on p. 140).

[206] L. Yu, Y.-H. Lee, X. Ling, E. J. G. Santos, Y. C. Shin, Y. Lin, M. Dubey, E. Kaxiras, J. Kong, H. Wang, and T. Palacios, “Graphene/mos2 hybrid technology for large-scale two-dimensional electronics”, *Nano Letters*, vol. 14, pp. 3055–3063, 2014 (cit. on p. 140).

[207] J. Sone, T. Yamagami, K. Nakatsuji, and H. Hirayama, “Si growth at graphene surfaces on 6h-sic(0001) substrates”, *Japanese Journal of Applied Physics*, vol. 55, p. 035 502, 2016 (cit. on p. 141).

[208] X. Lu, M. I. B. Utama, J. Zhang, Y. Zhao, and Q. Xiong, “Layer-by-layer thinning of MoS2 by thermal annealing”, *Nanoscale*, vol. 5, pp. 8904–8908, 2013 (cit. on p. 142).

[209] H. Zhou, F. Yu, Y. Liu, X. Zou, C. Cong, C. Qiu, T. Yu, Z. Yan, X. Shen, L. Sun, B. I. Yakobson, and J. M. Tour, “Thickness-dependent patterning of MoS2 sheets with well-oriented triangular pits by heating in air”, *Nano Research*, vol. 6, pp. 703–711, 2013 (cit. on p. 142).

[210] X. Wang, W. Fan, Z. Fan, W. Dai, K. Zhu, S. Hong, Y. Sun, J. Wu, and K. Liu, “Substrate modified thermal stability of mono- and few-layer MoS2”, *Nanoscale*, vol. 10, pp. 3540–3546, 2018 (cit. on p. 142).

From silicene to Si films and clusters: silicon growth on Ag and layered materials studied by STM, GIXD and DFT

In this work I summarize the studies conducted during my PhD, concerning the synthesis of silicene layers and thin Si films on Ag(111) and Si deposition on layered materials. I present original results which unveil interesting physical phenomena associated with the system under study.

In a first part, I present the outcomes of a combined experimental and theoretical study, based on GIXD measurements and DFT simulations, aimed to determine the exact atomic arrangement of the *silicene monolayer structures on Ag(111)*.

Afterwards I focus on the *atomic structure of Si thin films on Ag(111)*. I show, by means of GIXD measurements, that the Si film has a diamond bulklike structure with stacking faults.

Finally, I determine the atomic structure of the reconstruction observed on top of the aforementioned diamond bulklike Si film by menas of GIXD measurements. Then, by combined STM and DFT studies I give an original picture for *Si growth on Ag(111) above 1 ML Si coverage*.

In the last part of this Thesis, I report STM studies regarding *Si evaporation on several layered materials*: HOPG, MoS_2, $TiTe_2$ and $ZrSe_2$. I show that on each of these substrates and both for room temperature and high temperature growth, Si evaporation results in the formation 3D Si nanoclusters.

Du silicène aux films minces et nanoclusters de Si: croissance du silicium sur Ag et matériaux lamellaires étudiés par STM, GIXD et DFT

Dans cet ouvrage, je résume les études menées au cours de ma thèse concernant la synthèse de monocouches de silicium et de couches minces de Si sur Ag(111) et des dépôts de Si sur des matériaux lamellaires. Je présente des résultats originaux qui ont dévoilé des phénomènes physiques intéressants associés au système étudié.

Dans une première partie, je présente les résultats d'une étude expérimentale et théorique combinée, basée sur des mesures GIXD et des simulations DFT, visant à déterminer la disposition atomique exacte des structures de la *monocouche de silicène sur Ag(111)*.

Ensuite, je me concentre sur *la structure atomique des couches minces de Si sur Ag(111)*. Je montre, au moyen de mesures GIXD, que le film de Si a une structure en forme de diamant avec des défauts d'empilement.

Enfin, je détermine la structure atomique de la reconstruction observée au-dessus du film de Si susmentionné par des mesures de GIXD. Ensuite, par des études combinées de STM et DFT, je donne une image originale de *la croissance de Si sur Ag(111) au-delà de la couverture de 1 ML de Si*.

Dans la dernière partie de cette thèse, je présente des études STM concernant *l'évaporation de Si sur plusieurs matériaux lamellaires*: HOPG, MoS_2, $TiTe_2$ et $ZrSe_2$. Je montre que sur chacun de ces substrats et à la fois pour la température ambiante et la croissance à haute température, l'évaporation du Si entraîne la formation de nanoclusters 3D de Si.